Title
Bed Surface Patchiness in Gravel-Bed Rivers

Author
Nelson, Peter August

Publication Date
2010

Peer reviewed|Thesis/dissertation

Bed Surface Patchiness in Gravel-Bed Rivers

by

Peter August Nelson

A dissertation submitted in partial satisfaction of the
requirements for the degree of
Doctor of Philosophy

in

Earth and Planetary Science

in the

Graduate Division

of the

University of California, Berkeley

Committee in charge:

Professor William E. Dietrich, Chair
Professor Kurt M. Cuffey
Professor Mark T. Stacey

Fall 2010

Bed Surface Patchiness in Gravel-Bed Rivers

Abstract

Bed Surface Patchiness in Gravel-Bed Rivers

by

Peter August Nelson

Doctor of Philosophy in Earth and Planetary Science

University of California, Berkeley

Professor William E. Dietrich, Chair

Gravel-bed rivers commonly display distinct sorting patterns on their beds. Visually, this heterogeneity often appears to form an organization of textural patches or facies. Patches can be distinguished into "free patches," which are zones of sorted material that move freely, such as bedload sheets; "forced patches," which are areas of sorting forced by topographic controls; and "fixed patches" of bed material rendered immobile through localized coarsening that remain fairly persistent through time. The local bed surface grain size, and therefore bed surface patchiness, exerts considerable influence on local bed mobility, bedload transport rates, hydrodynamic roughness, and benthic microhabitats. Despite the ecological and morphodynamic importance of bed surface patchiness, we lack accurate and objective methods to delineate patches, and have little understanding of how patches form, evolve, and interact.

This dissertation investigates the mechanisms responsible for the formation of bed surface patches. First, two sets of flume experiments are used to explore how fixed and free patches respond to reductions in sediment supply, and to show that sediment supply is a primary control on the distribution of fixed patches and the dynamics of bedload sheets. A near-field scale flume experiment is then used to show how bed topography, the flow field, and the sediment transport field interact to form forced patches. Size-selective, cross-stream sediment transport is shown to be a critical mechanism responsible for the development of forced bed surface patches. A high-resolution dataset of spatial grain size distributions collected during this experiment is then analyzed with several clustering methods to develop an objective method of delineating patches. These analyses suggest that rivers have a tendency to form a finite number of patch types that become distributed throughout the reach. Lastly, a two-dimensional morphodynamic model simulating flow, mixed-grain size sediment transport, and bed evolution is presented and used to show that forced patches interact with the evolving bed and, through their effects on the flow field, have a considerable impact on morphologic evolution.

Contents

List of Figures

List of Tables

Acknowledgments

Throughout my academic career, I have been fortunate to receive support, help, and guidance from many people. First and foremost, I would like to thank my advisor, Bill Dietrich. He has been a caring, loyal, and inspiring mentor who has instilled in me an appreciation for good scholarship and a desire to acquire a deeply mechanistic understanding of earth surface processes. Bill's ability to pose interesting and challenging questions is unparalleled, and his generosity with his thoughts and time is admirable.

Many professors and teachers besides Bill have had a considerable influence on my academic upbringing and development. When I was an undergraduate at Princeton, Jim Smith introduced me to research in hydrology and river processes, was a great thesis advisor, gave me a job after graduation, and helped me figure out where to go to graduate school. My work with him, Andy Miller, Mary Lynn Baeck, and Kate Meierdiercks cemented my desire to get into this field. At Berkeley, Michael Manga has been a valued collaborator, and our project studying the formation of spring mounds in the deserts of Australia and New Mexico has provided some welcome diversity to my academic pursuits. I am grateful to the members of my dissertation committee, Kurt Cuffey and Mark Stacey, not only for reading and signing my thesis but also for being two of my favorite teachers at Berkeley. Jim Kirchner has been a valuable resource for statistical knowledge and many aspects of my work have benefitted from my conversations with him. Roland Bürgmann and Doug Dreger rounded out my qualifying exam committee; Roland graciously agreed to join the committee on short notice and saved me from a scheduling nightmare, and I probably would not have passed my exam had Doug not taken me on as a GSI for EPS 50 the previous semester.

All of my work is the product of collaboration, and I have been fortunate to be able to work with some really great people. Thanks to our many long days and nights in assorted hydraulics laboratories, Jeremy Venditti has become a good friend and a valued colleague. Dino Bellugi has been a close friend and his dragging me to nerdy computer science classes has helped to expand my breadth as a scientist and opened my eyes to problems of which I was previously unaware. Chapter 2, a paper coauthored by Bill, Jeremy, Jim Kirchner, Hiroshi Ikeda, Fujiko Iseya, and Leonard Sklar, benefitted from contributions, past or present, from all of them. Aleks Wydzga, Jessica Fadde, Stuart Foster, and John Potter also assisted in the experiments presented in that chapter. The experiments presented in Chapter 3 were a major undertaking and would not have been possible without the efforts of Jeff Marr, Dave Dean, and a small army of University of Minnesota undergraduates. Jon Nelson and Rich McDonald at the USGS hosted me at their office and gave me the code to their model, which became the basis for Chapter 5. Analysis of the output of the model described in Chapter 5 (and also used in Chapter 3) was made much easier thanks to a MATLAB program Carl Legleiter sent me. Chapters 2 and 3, which have been published, were improved by reviews from Peter Wilcock, Andrew Nicholas, Tom Lisle, Jon Nelson, Rob Ferguson, John Pitlick, and Mike Church. Giovanni Seminara and Michele Bolla Pittaluga, at the University of Genoa, took me in for a summer and I look forward to rejoining them for an exciting,

extended stay in Italy.

I have appreciated the friendship and camaraderie of the graduate students in our department, and particularly those in the geomorphology group. I should especially thank Christian Braudrick and Mike Lamb for valuable conversations, stimulating ideas, good humor, and for being great officemates. The Berkeley geomorphology group attracts wonderful people, including (but not limited to) Leslie Hsu, Ken Ferrier, Elowyn Yager, Joel Rowland, Taylor Perron, Toby Minear, Johnny Sanders, Sarah Godsey, Marisa Palucis, Rebecca Leonardson, Kathleen Swanson, Justine Owen, Vicky Lee, Tim Creyts, Noah Finnegan, Daniella Rempe, and Jasper Oshun. I thank them all for their friendship and I am glad our community is still small enough that I can count on seeing them semi-regularly at conferences throughout our careers.

Financially, my work was supported by a National Science Foundation Graduate Research Fellowship, the National Center for Earth-surface Dynamics (NCED), CALFED, Stillwater Sciences, and a grant from the National Science Foundation International Research Experience Program (IREP).

Finally, it is my pleasure to thank my sister Katey, my grandmothers Ginny and Jeunette, my in-laws Jeff, Kristen, and Kyle Dean, and my parents Herb and Cathy, for their unwavering love and support. William Tail provided some much-needed cuteness and snuggles. And no one deserves more thanks then my wife Laurie, whose support for me throughout this endeavor has been unmatched. I know my graduate education required many sacrifices on her part, and I am extraordinarily grateful and lucky to have her in my life.

Chapter 1

Introduction

Rivers have been described as sediment sorting machines [*Church*, 2002]. On the channel-length scale, the most obvious outcome of sorting is fining of bed material in the downstream direction [e.g., *Knighton*, 1980; *Rice and Church*, 1998; *Surian*, 2002; *Moussavi-Harami et al.*, 2004], which has been attributed to selective sorting in channels experiencing net deposition [e.g., *Paola et al.*, 1992; *Ferguson et al.*, 1996; *Gomez et al.*, 2001; *Powell*, 1998] or particle breakdown [e.g., *Kodama*, 1994] and sediment input from hillslopes [*Sklar et al.*, 2006] in the absence of net deposition. At smaller, reach-length scales, river beds frequently display a spatial structure where the sediment mixture comprising the channel bed has been sorted into discrete patches of similar grain size [e.g., *Kinerson*, 1990; *Buffington and Montgomery*, 1999a; *Dietrich et al.*, 2005] (Figure 1.1). These patches can be freely mobile sorting features that migrate downstream, such as bedload sheets [*Whiting et al.*, 1988], (Figure 1.2), or they can be temporally stable features that persist for long periods of time, even though a considerable sediment load may pass over and through them [e.g., *Dietrich et al.*, 2005]. Throughout this dissertation, mobile patches will be referred to as "free patches," temporally stable, persistent patches forced by topographic controls will be referred to as "forced patches," and areas of bed material rendered immobile through localized coarsening that remain fairly persistent through time will be referred to as "fixed patches."

Patches at this scale can be quite important for local sediment transport and fluvial ecology. The likelihood of a particle becoming entrained into bedload transport depends upon the ratio of that particle's size to the local bed surface grain size distribution [e.g. *Wiberg and Smith*, 1987; *Kirchner et al.*, 1990; *Buffington et al.*, 1992; *Buffington and Montgomery*, 1997; *Lamb et al.*, 2008]. Because of this dependency, current standard mixed-grain size bedload transport models [e.g., *Parker*, 1990; *Wilcock and Crowe*, 2003] require the bed

Figure 1.1 *(following page)*: Examples of mapped patches from field studies. (a) Wildcat Creek, CA, as mapped by Laurel Collins in 1988 and presented in *Dietrich et al.* [2005]. (b) Jacoby Creek, CA [from *Kinerson*, 1990].

(a)

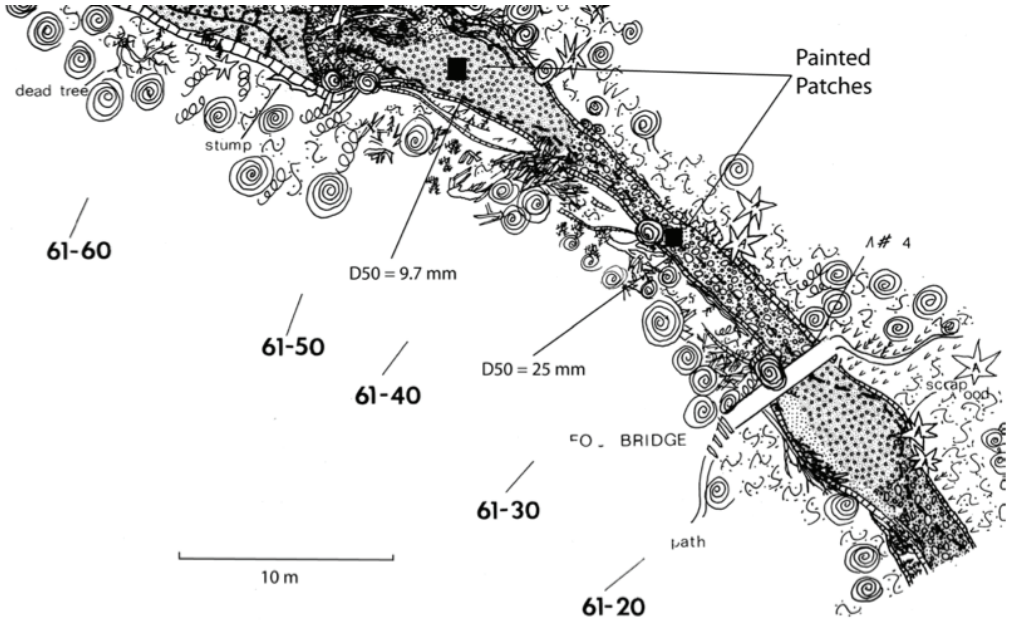
Painted
Patches
dead tree
stump
61-60
D50 = 9.7 mm
61-50
61-40
D50 = 25 mm
scrap wood
BRIDGE
61-30
path
10 m
61-20

(b)

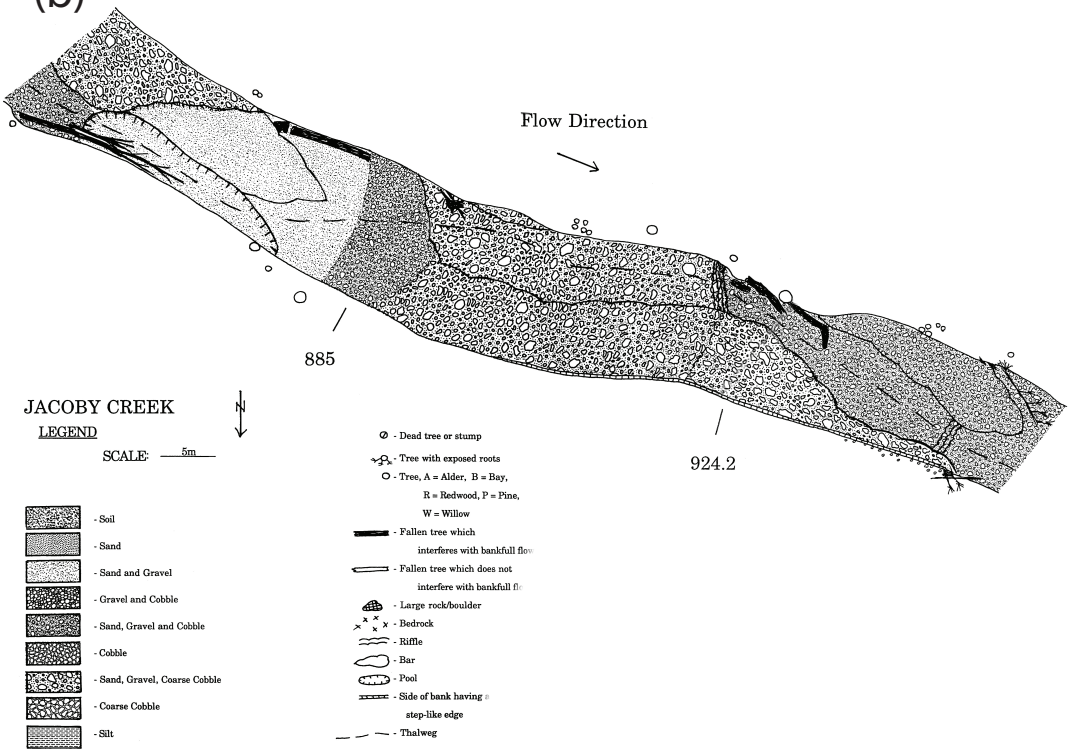
Flow Direction
885
924.2
JACOBY CREEK
LEGEND
SCALE: 5m
N
- Soil
- Sand
- Sand and Gravel
- Gravel and Cobble
- Sand, Gravel and Cobble
- Cobble
- Sand, Gravel, Coarse Cobble
- Coarse Cobble
- Silt
- Dead tree or stump
- Tree with exposed roots
- Tree, A = Alder, B = Bay,
R = Redwood, P = Pine,
W = Willow
- Fallen tree which
interferes with bankfull flow
- Fallen tree which does not
interfere with bankfull flo
- Large rock/boulder
- Bedrock
- Riffle
- Bar
- Pool
- Side of bank having
step-like edge
- Thalweg

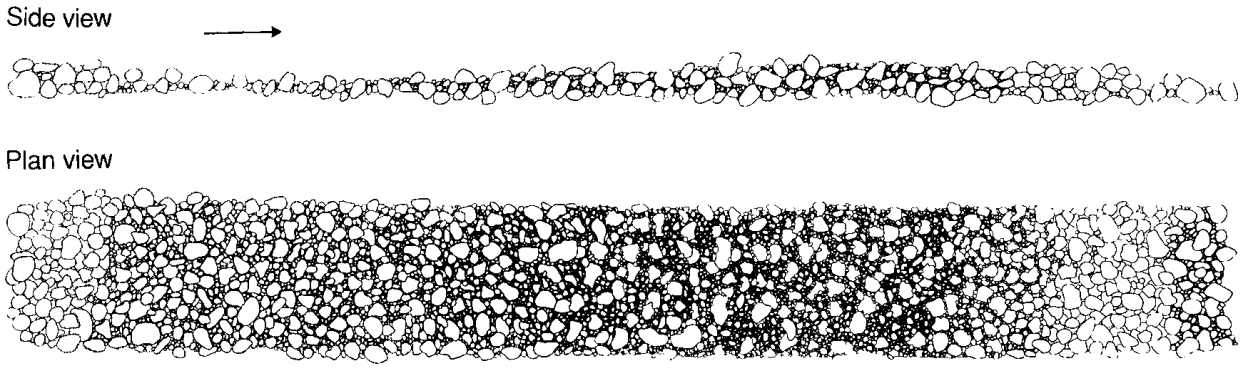

Figure 1.2: Schematic of a bedload sheet [from *Whiting et al.*, 1988]. The arrow is ≈ 5 cm and indicates the direction of flow and sediment transport.

surface grain size distribution as an input parameter; however, applications of these models to real rivers frequently use a spatial average of the grain size distributions of the patchy bed, which can be an important source of error in sediment transport calculations [e.g., *Ferguson*, 2003]. Hydrodynamic calculations of flow in river channels also depend upon a spatial characterization of the channel roughness [*Nelson et al.*, 2003], which is a function of the local bed surface grain size distribution [e.g., *Leopold and Wolman*, 1957; *Dietrich and Whiting*, 1989; *Wilcock*, 1996]. Bed surface patchiness also can control the distribution of biological habitats, since many aquatic organisms prefer microhabitats [*Cummins and Lauff*, 1969; *Rabeni and Minshall*, 1977; *Reice*, 1980] or spawning grounds [*Kondolf and Wolman*, 1993; *Overstreet et al.*, 2010; *Riebe et al.*, 2010] consisting of particular grain sizes.

Despite the prevalence of bed surface patchiness and its importance for sedimentology, engineering, and ecology, we still have little understanding of how patches form, evolve, and interact, nor do we have a method of quantitatively defining what a patch is. This dissertation addresses these issues through studies directed at understanding the mechanisms underlying the formation of bed surface patches in gravel bed rivers. It describes physical experiments investigating the mechanisms responsible for the formation and development of free and forced patches, it explores objective methods of patch delineation, and it presents a morphodynamic model that simulates the coevolution of channel morphology and bed surface patchiness.

In Chapter 2 (previously published as *Nelson et al.* [2009]), two sets of flume experiments (one using bimodal, sand-rich sediment and the other using unimodal, sand-free sediment) are used to explore how fixed and free patches respond to stepwise reductions in sediment supply. At high sediment supply, migrating bedload sheets formed even in unimodal, sand-free sediment, yet grain interactions visibly played a central role in their formation. In both sets of experiments, reductions in supply led to the development of fixed coarse patches, which expanded at the expense of finer, more mobile patches, narrowing the zone of active bedload transport and leading to the eventual disappearance of migrating bedload sheets. Reductions

in sediment supply decreased the migration rate of bedload sheets and increased the spacing between successive sheets. One-dimensional morphodynamic models of river channel beds generally are not designed to capture the observed variability, but should be capable of capturing the time-averaged character of the channel. When applied to our experiments, a 1D morphodynamic model [RTe-bookAgDegNormGravMixPW.xls, Parker (e-book), 2007] predicted the bedload flux well, but overpredicted slope changes and was unable to predict the substantial variability in bedload flux (and load grain size) due to the migration of mobile patches. Our results suggest that: 1) the distribution of free and fixed patches is primarily a function of sediment supply; 2) the dynamics of bedload sheets are primarily scaled by sediment supply; 3) channels with reduced sediment supply may inherently be unable to transport sediment uniformly across their width; and 4) cross-stream variability in shear stress and grain size can produce potentially large errors in width-averaged sediment flux calculations.

In an effort to enhance our empirical understanding of the mechanisms responsible for the formation of forced patches, Chapter 3 (previously published as *Nelson et al.* [2010]) describes a near-field scale flume experiment in which a large (55 m long, 2.74 m wide) straight, sediment recirculating flume was provided a constant water discharge and a unimodal sediment mixture ranging in size from 2-45 mm. A sequence of alternate bars developed and became essentially fixed in space, producing quasi-steady-state bed topography over which we made measurements of local near-bed velocity and sediment transport. The bed developed temporally and spatially persistent forced patches with a general pattern of coarse bar tops and fine pools, which we characterized by visual mapping and with the application of an automated image processing procedure to a high-resolution (1 mm $\times$ 1 mm) digital elevation model of the bed surface. The boundary shear stress field, calculated from velocity measurements and with a quasi-three dimensional hydraulic model (FaSTMECH), displayed substantial variability across the bar unit. Bed surface grain size did not correlate with local boundary shear stress; instead, topographically-forced divergences in the boundary shear stress field were matched by divergences in the sediment transport field. The resultant cross-stream sediment flux was size-selective which in turn forced a bed surface textural response leading to coarse bar tops and fine pools. Our observations suggest that size-selective cross stream bed load transport is a mechanism responsible for the development of forced bed surface patches in gravel-bed channels that have topographically-forced heterogeneous flow fields.

Recent advances in photographic measurement of bed surface grain size distributions are capable of providing data at a spatial resolution high enough to allow us an opportunity to answer the question: what is a patch? Chapter 4 uses the spatial grain size data collected during the experiment described in Chapter 3 to address how patches can objectively and quantitatively be delineated, as opposed to simply mapped by eye. Here we investigate several possible methods of patch delineation in which clustering analysis is applied to this high-resolution grid of spatial grain size distributions. Specifically, we examine three clustering techniques: 1) partitional clustering of grain size distributions with the k-means

algorithm, 2) spatially-constrained agglomerative clustering, and 3) spectral clustering using Normalized Cuts. Because they incorporate spatial and grain size data during the classification process, the agglomerative and spectral clustering methods generated realistic patch maps that, when statistically analyzed, indicated that certain patch types may repeatedly appear at different locations on the bed. Our results suggest that rivers have a tendency to form a finite number of patch types that become distributed throughout the reach.

Finally, Chapter 5 presents a two-dimensional morphodynamic model that is used to examine in greater detail the mechanisms responsible for the development of forced bed surface patches and the coevolution of bed morphology and bed surface patchiness. The model implements standard equations describing depth-averaged channel hydrodynamics, mixed-grain size sediment transport, and bed evolution. We use the conditions and observations from the experiment described in Chapter 3 as our test case, and comparisons between model results and experimental observations suggest that the model predicts bed morphology and sorting patterns similar to the observations. However, discrepancies between model results and observations point to a need for improved treatment of bed stratigraphy and grain interactions in morphodynamic models. We also use the model to explore the coevolution of free and forced bars and bed surface patchiness, and find that, primarily through their interaction with the flow field via roughness feedbacks, forced patches interact with the evolving bed and have a considerable impact on morphologic evolution.

Chapter 2

Response of bed surface patchiness to reductions in sediment supply

2.1 Introduction

The grain size distribution of the surface of channel beds typically displays significant spatial structure. Variations occur at all scales, but once they reach mappable domains they are often referred to as patches or facies of common size distributions [e.g., *Dietrich and Smith*, 1984; *Lisle and Madej*, 1992; *Paola and Seal*, 1995; *Crowder and Diplas*, 1997; *Buffington and Montgomery*, 1999a]. Some patches can be texturally stable for many years (even after considerable bedload flux) and remain in a fixed location in the channel, while other patches may migrate downstream as a distinct grain-size varying pulse of sediment [as reviewed in *Dietrich et al.*, 2005]. The relatively stable (in space) patches appear to arise from shear stress divergences that are forced by topographic controls, such as bar morphology [e.g., *Mosley and Tindale*, 1985; *Laronne and Duncan*, 1992; *Lisle and Hilton*, 1999], flow obstructions such as large woody debris [e.g., *Buffington and Montgomery*, 1999b; *Haschenburger and Rice*, 2004], or immobile accumulations of cobbles or boulders where patches of fine material can accumulate in wake zones [e.g., *Garcia et al.*, 1999; *Laronne et al.*, 2000; *Yager*, 2006]. Theoretical prediction of the size distribution and occurrence of these patches, however, remains challenging [e.g., *Parker and Andrews*, 1985; *Bridge*, 1992; *Lisle et al.*, 2000; *Sun et al.*, 2001a,b; *Julien and Anthony*, 2002]. In systems with decreasing sediment supply, spatially persistent zones of coarse sediment can emerge as a consequence of weaker topographic influences such as grain interactions and general coarsening [*Dietrich et al.*,

This chapter has been published as: Nelson, P. A., J. G. Venditti, W. E. Dietrich, J. W. Kirchner, H. Ikeda, F. Iseya, and L. S. Sklar (2009), Response of bed surface patchiness to reductions in sediment supply, *Journal of Geophysical Research*, *114*, F02005, doi:10.1029/2008JF001144.

1989; *Lisle et al.*, 1993]. Downstream migrating zones of distinct clustering of sediment sizes may organize into thin mappable features referred to as bedload sheets [*Whiting et al.*, 1988]. These features develop from interactions between coarse and fine grains [*Whiting et al.*, 1988; *Dietrich et al.*, 1989; *Tsujimoto*, 1990; *Seminara et al.*, 1996; *Whiting*, 1996]. Following the terminology proposed for bar types [e.g., *Seminara*, 1998], we refer to these end member types of patches as "forced patches" (spatially persistent associated with strong topographic controls), "fixed patches" (spatially persistent due to weak topographic influences and coarsening), and "free patches" (migrating patches, typically bedload sheets in gravel bed rivers) [*Nelson et al.*, 2005]. The occurrence, distribution and dynamics of these patch types have not been systematically mapped.

Field and flume studies suggest that sediment supply and bed texture are dynamically linked. *Dietrich et al.* [1989] proposed that surface armoring depends on sediment supply. They imposed stepwise reductions in sediment supply to a flume with constant water discharge and observed the expansion of coarse, inactive zones on the channel bed. *Lisle et al.* [1993] used the same flume with a much larger width-to-depth ratio to develop alternate bars. Reductions of sediment supply to this channel caused it to incise, the bars became stationary and emerged, and coarse areas of the channel bed expanded while the zone of active bedload transport narrowed. *Buffington and Montgomery* [1999c] used these and other flume data to show that it may be possible to estimate the quantity of sediment supplied to a reach by comparing the grain size of the bed surface to a theoretically competent grain size. *Kinerson* [1990]'s survey of six field sites with varying supply of coarse sediment suggested that the extent of fine patches may correlate with sediment supply. *Clayton and Pitlick* [2008] suggested that an essentially unlimited supply of coarse sediment allowed the Colorado River to maintain an armor layer during flood conditions. It has also been shown that as the supply of fine material is reduced, armor patches and gravel jams can develop [*Gran et al.*, 2006], and elimination of sediment supply can lead to distinct fixed grain arrangements that substantially alter effective bed roughness [*Church et al.*, 1998; *Hassan and Church*, 2000]. Patches of fine sediment may act as major sources of bedload when hydraulic conditions only allow for partial mobility [*Laronne et al.*, 2000]. *Yager* [2006]'s field study of patches of fine material in a steep mountain channel suggested that their area and thickness should shrink and swell with changes in sediment supply.

All commonly-used mixed-grain size bedload transport equations [e.g., *Parker and Klingeman*, 1982; *Parker*, 1990; *Wilcock and Crowe*, 2003, among others] are effectively zero-dimensional (i.e., no spatial or time components) and do not specifically deal with the effects of patchiness. Sediment flux predictions based on average channel attributes (e.g., depth and mean slope) and spatially averaged grain size distributions are unlikely to be accurate where stream beds are spatially patchy [*Paola and Seal*, 1995; *Seal and Paola*, 1995; *Ferguson*, 2003; *Chen and Stone*, 2008]. For the case of steep, coarse-bedded channels where patchy finer sediment passes over rarely mobile coarser sediment [e.g., *Garcia et al.*, 1999; *Laronne et al.*, 2000; *Garcia et al.*, 2007], *Yager et al.* [2007] show that bedload transport estimates can be greatly improved by accounting for drag loss over boulders when estimating the effec-

tive boundary shear stress, and by applying bedload transport equations only to the portion of the bed that is covered with mobile finer sediment. In these systems, the interconnectedness of fine patches and patch-to-patch transport may be of primary importance under low stress conditions [*Laronne et al.*, 2000; *Gran et al.*, 2006]. Discrete particle models that solve the equations of motion for individual sediment grains [e.g., *Schmeeckle and Nelson*, 2003] or that model particle motion with step and exchange rules [e.g., *MacVicar et al.*, 2006] may eventually be able to incorporate and predict patchiness. Thus far, most work has focused mainly on forced patches and their consequences for sediment transport; however, the combined influence of fixed and free patches on bedload transport has not been explicitly explored.

Free patches may be the most active portion of channel, especially if the forced patches are composed of sizes that rarely move. Bedload sheets appear to be the most common occurrence of free patches in the field [*Gustavson*, 1978; *Whiting et al.*, 1988; *Ashmore*, 1991a,b; *Ashworth et al.*, 1992b,a; *Dinehart*, 1992; *Bunte et al.*, 2004] and in flumes during mixed grain size bedload transport [*Iseya and Ikeda*, 1987; *Kuhnle and Southard*, 1988; *Arnott and Hand*, 1989; *Dietrich et al.*, 1989; *Wilcock*, 1992; *Bennett and Bridge*, 1995; *Pender and Shvidchenko*, 1999; *Mikoš et al.*, 2003; *Kuhnle et al.*, 2006; *Lunt and Bridge*, 2007; *Madej et al.*, 2009]. These sorting features have coarse-grained fronts with heights of 1-2 grain diameters and become progressively finer toward their tails. Bedload sheets form and migrate downstream as a consequence of the catch and mobilize process, in which large grains are caught in the wakes of other large grains, followed by infilling of their interstices by smaller particles, which can in turn smooth out hydraulic wakes causing large particles to be remobilized [*Whiting et al.*, 1988]. The sorting patterns across free patches suggest that they pose abrupt changes in roughness and turbulence structure [*Antonia and Luxton*, 1971, 1972; *Best*, 1996]. *Seminara et al.* [1996] proposed that the stress perturbation due to this sorting structure allows for the growth of bedload sheets. *Dietrich et al.* [1989] noted that in response to sediment supply reduction bedload sheets became less frequent and distinct, but did not quantify this observation. Given the growing acknowledgement of and emphasis on the influence of sand on gravel mobility [e.g., *Iseya and Ikeda*, 1987; *Ferguson et al.*, 1989; *Wilcock*, 1998; *Wilcock et al.*, 2001; *Wilcock and Kenworthy*, 2002; *Wilcock and Crowe*, 2003], it is reasonable to ask whether sheets will form in unimodal bed material in which sand is absent. *Gomez et al.* [1989] report secondary dunes of a few grain diameters in height and a few tens of grain diameters in length in experiments with gravel between 6 and 64 mm in diameter. They do not, however, report sorting patterns over these features. In general, it is not well known whether bedload sheets can form in the absence of sand and how sheet characteristics may depend on sediment supply.

In this paper we focus on the relationship between sediment supply and bed surface patchiness and ask three questions: 1) what is the relationship between the distribution of free and fixed patches and relative sediment supply; 2) how are the properties of bedload sheets, specifically wavelength and migration rate, influenced by supply, and 3) how does the presence of fixed and free patches influence the prediction of channel slope, grain size,

and bedload flux in the simplest case of a straight, low width-to-depth ratio flume. To do this we revisit the work of *Dietrich et al.* [1989] and present previously unreported data from those experiments. We build upon this work with a new set of experiments conducted with the same general procedure of a stepwise supply reduction under constant water discharge, but in a larger flume using a unimodal, sand-free sediment. We then use data collected in these two sets of experiments to test the full 1D morphodynamic predictions of bed evolution using the spreadsheet model RTe-bookAgDegNormGravMixPW.xls of G. Parker (1-D sediment transport morphodynamics with applications to rivers and turbidity currents, e-book, 2007, available at http://cee.uiuc.edu/people/parkerg/morphodynamics_e-book.htm). Our analysis shows that as supply is reduced, fixed coarse patches expand at the expense of finer more mobile patches and result in overall bed coarsening. Large, short-term variations in sediment flux are associated with the migration of free patches, the dynamics of which scale with sediment supply. The Parker (e-book, 2007) model predicts average sediment flux fairly accurately and predicts the corresponding median bed surface grain size and slope to within a maximum difference of 30%. Application of common mixed-grain-size sediment transport algorithms to our observed shear stress and areally-averaged bed surface grain size suggests that for some simple cases, spatial grain size averaging may produce reasonable transport estimates.

2.2 Methods

The data presented in this paper were collected during two sets of flume experiments. The first were conducted at the University of Tsukuba in Japan in 1987, and have been described in previous publications [*Dietrich et al.*, 1989; *Kirchner et al.*, 1990]. The second set of experiments was conducted at the University of California, Berkeley Richmond Field Station in Richmond, CA USA in 2005. The procedures for each set of experiments were similar and are described below.

2.2.1 Tsukuba experiments

Dietrich et al. [1989] progressively reduced the sediment supply to a small (7.5 m long, 0.3 m wide) flume, holding the water discharge (0.6 l/s-cm), flume slope (0.0046), and bulk (sediment feed) grain size distribution constant. The width-to-depth ratio was maintained at ~ 3 in order to suppress development of any channel topography and maintain a simple one-dimensional system. The water surface slope, bed slope, and bed surface texture were allowed to equilibrate to the imposed water discharge and sediment supply rate. Sediment was fed into the upstream end of the flume by hand or conveyor belt, and bedload discharged from the end of the flume was collected at 5-minute intervals, weighed, and sieved. The water surface and bed surface slopes were measured every 6 minutes from point gage readings taken at 1-meter intervals along the flume centerline. When equilibrium was achieved—that is, when

the water surface slope stabilized and the rate and size distribution of bedload transported out the end of the flume matched those of the sediment feed—the run was halted. Each run lasted 6 to 8 hours, and these procedures were repeated for two reductions in feed rate. The sediment feed was composed of a bimodal sand-gravel mixture of diameter ranging from 1 mm to 12 mm and with a median grain size (D_{50}) of 3.6 mm (Figure 2.1a). The initial bed median grain size due to just wetting (i.e., flow without significant transport and particle vibration) was about 4.2 mm. Increased flow and high sediment supply quickly fined the bed to a median grain size the same as the supply. In the three runs, sediment was supplied to the channel at successively reduced rates of 17.4, 6.1, and 1.7 g/min-cm. The flow parameters at equilibrium for each run are given in Table 2.1.

During the experiments, the bed organized itself into 3 or 4 distinct patch types (Figure 2.2a and 2.2b; Table 2.2). Patches were classified as "congested" (coarse median grain size D_{50} = 4.68 mm, geometric standard deviation σ = 1.76), "transitional" (D_{50} = 3.63 mm, σ = 2.16), "smooth" (fine - D_{50} = 2.62 mm, σ = 2.16), and "inactive" (coarse zones with no active bedload transport, D_{50} = 5.49 mm, σ = 1.77) (see *Iseya and Ikeda* [1987] for a discussion of the terms). The grain size distributions for smooth, transitional, and congested facies were measured after the experiment from areas of the bed that were fixed onto removable boards with cyanoacrylate glue (see *Kirchner et al.* [1990] for details); the grain size distribution for the inactive facies was taken from a grid-by-number Wolman-style [*Wolman*, 1954] pebble count after the lowest feed rate experiment (1.7 g/min-cm). This sorting was largely longitudinal, forming migrating "congested-smooth" sequences [*Iseya and Ikeda*, 1987] or bedload sheets [*Whiting et al.*, 1988], and during the run the along-flume location of the congested heads of downstream migrating bedload sheets was recorded at 1-2 min intervals. After each run, the entire bed was mapped into these patch types. These patch distributions were used to obtain an area-weighted average grain size distribution for the entire bed surface (Figure 2.1a). We use this area-weighted size as a metric of surface response although its distribution does not actually occur at any particular location on the channel bed.

2.2.2 Berkeley experiments

We performed a similar set of experiments at UC Berkeley's Richmond Field Station (RFS) in Richmond, CA. The Berkeley flume is a 28 m long, 0.86 m wide channel. As in the Tsukuba experiments, the width-to-depth ratio was narrow (~ 4) to suppress the development of bed topography. In these experiments, we performed three stepwise reductions in sediment supply while maintaining a constant water discharge (2.38 l/s-cm), flume slope (0.005) and sediment feed grain size distribution. Sediment was fed into the upstream end of the flume using an automatic screw feeder. The downstream end of the flume was equipped with a sediment trap and a load cell that sampled the sediment discharge rate at 60-second intervals. Sediment that exited the flume was diverted to a separate collection basin and samples were taken from this basin at intervals of between 5 and 20 hours and sieved to

Table 2.1: Hydraulic conditions for each set of experiments.

	Tsukuba			Berkeley			
Sediment feed rate (g/min-cm)	17.4	6.1	1.7	23.3	15.5	9	0
Water discharge (l/cm-s)	0.6	0.6	0.6	2.38	2.38	2.38	2.38
Mean flow depth (cm)	10.2 ± 0.04	10.3 ± 0.02	11.3 ± 0.02	21.8 ± 1.6	22.1 ± 0.9	22.4 ± 1.4	22.8 ± 1.2
Water surface slope $\times 10^{-3}$	5.2 ± 0.2	4.6 ± 0.07	3.5 ± 0.08	4.8 ± 0.08	4.6 ± 0.03	4.0 ± 0.05	3.9 ± 0.05
Bed slope	-	-	-	0.0055	0.0051	0.0048	0.0043
Width-to-depth ratio	2.94	2.91	2.65	3.95	3.90	3.83	3.77
Mean flow velocity (m/s)	0.59	0.58	0.53	1.09	1.08	1.06	1.05
Froude number	0.59	0.58	0.50	0.75	0.73	0.72	0.70
Boundary shear stress (Pa)	5.20 ± 0.21	4.64 ± 0.07	3.88 ± 0.09	10.30 ± 0.78	9.94 ± 0.39	8.85 ± 0.55	8.64 ± 0.48
Boundary shear stress (sidewall corrected) (Pa)	4.89 ± 0.20	4.37 ± 0.07	3.63 ± 0.08	10.14 ± 0.76	9.78 ± 0.38	8.71 ± 0.54	8.50 ± 0.46
D_{50} (bed surface) (mm)	3.74	4.26	4.85	9.61	10.05	10.73	11.82
Armoring ratio	1.03	1.17	1.34	1.19	1.25	1.33	1.47
Shields number	0.086	0.067	0.049	0.066	0.061	0.051	0.045
Width of zone of active transport (cm)	-	-	-	61 ± 10	51 ± 12	46 ± 9	-
Length of run (hr)	7.5	7.5	6	16.0	28.9	27.9	20.7

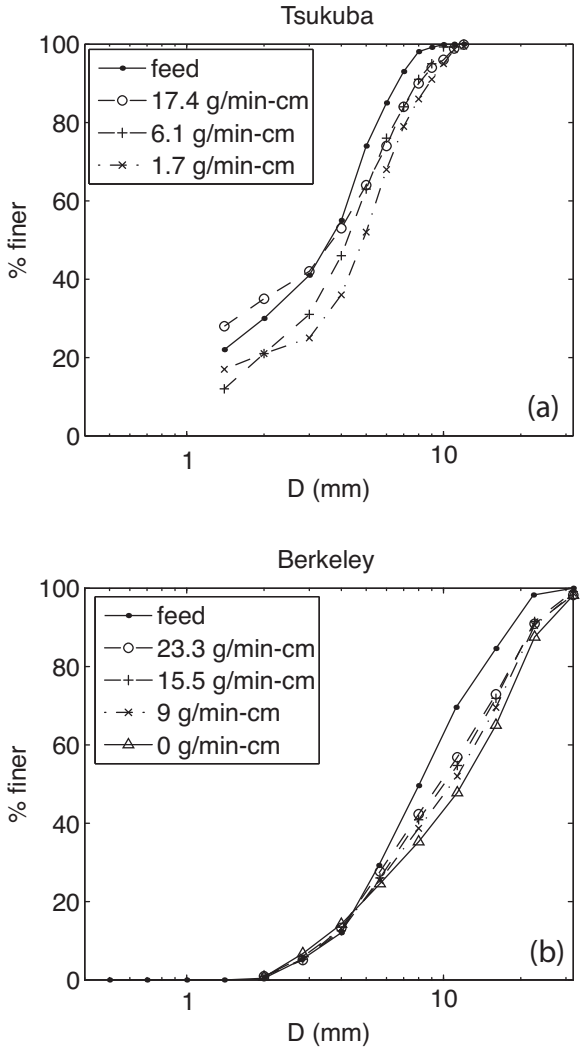

Figure 2.1: Grain size distributions for the bulk (feed) sediment and bed surface for the (a) Tsukuba and b) Berkeley experiments.

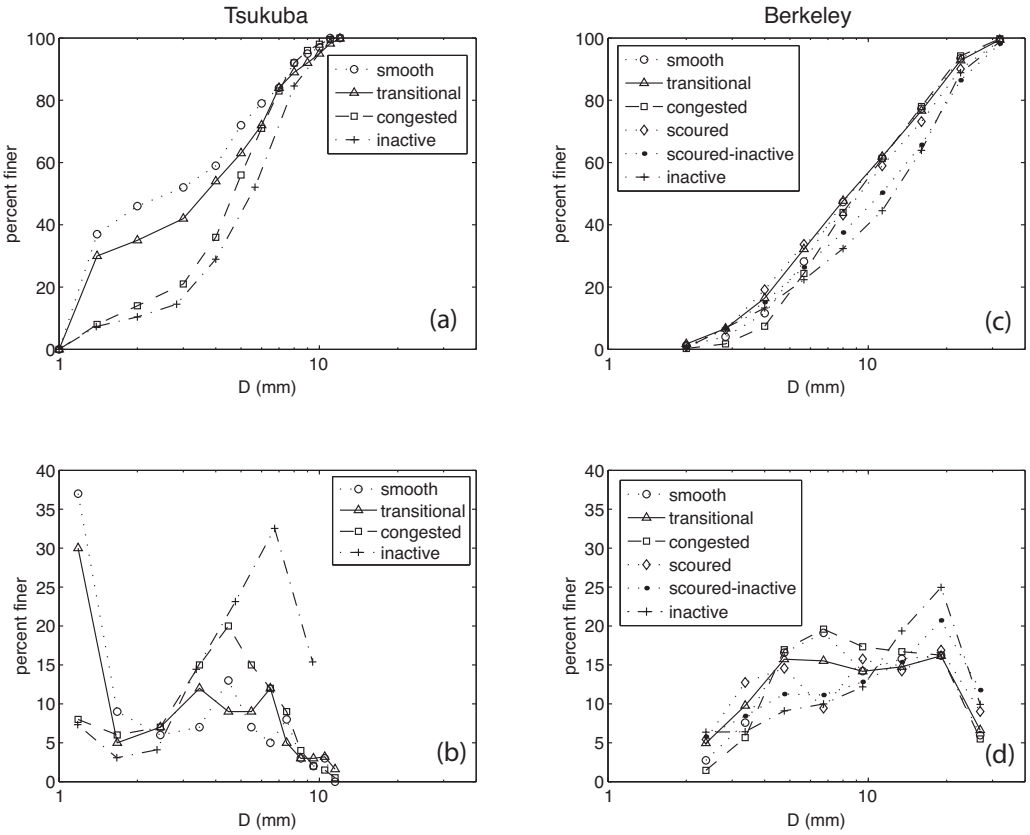

Figure 2.2: Grain size distributions for patch types mapped during each experiment: (a) cumulative and (b) probability distributions from the Tsukuba experiments; (c) cumulative and (d) probability distributions from the Berkeley experiments.

Table 2.2: Grain size characteristics (median grain size D_{50} and geometric standard deviation σ) of patch types mapped in the Berkeley and Tsukuba experiments.

Patch Type	D_{50} (mm)	σ
Tsukuba		
Smooth	2.62	2.16
Transitional	3.63	2.16
Congested	4.68	1.76
Inactive	5.49	1.77
Berkeley		
Smooth	8.54	1.88
Transitional	8.46	1.96
Congested	9.02	1.81
Scoured	9.3	2.05
Scoured-Inactive	11.21	2.05
Inactive	12.47	2.02

obtain the average grain size distribution of the transported sediment. The bed surface and water surface elevation were monitored using an ultrasonic water level sensor and an acoustic echo-sounder that traversed the flume on a mechanized cart that ran along rails above the flume walls. Water and bed surface elevation were measured at 30-60 minute intervals along five longitudinal profiles spaced at 218 mm in the cross-stream direction with the center transect located along the center of the flume. Measurements in the along-channel direction were obtained at an interval of 5 mm. Scans of the bed surface and water surface were performed separately so the echo-sounder did not disturb the water surface measurements. The three center profiles were used to calculate average bed and water surface slopes. Between runs, the flume was drained and a range-finding laser attached to the cart was used to obtain a topographic scan of the bed on a 1 cm $\times$ 1 cm grid. A camera was mounted to the cart and between runs the entire bed was photographed from above.

The grain size distribution of the bulk sediment composing the bed and the sediment feed is presented in Figure 2.1b. We used a unimodal mixture of sand-free gravel ranging in size from 2 to 32 mm with a median grain size of 8 mm. Sediment was fed into the flume at successive rates of 23.3, 15.5, 9 and 0 g/min-cm. The run was halted when equilibrium was reached; that is, when the quasi-steady sediment transport rate exiting the flume as measured by the load cell was equal to the sediment feed rate. Each run lasted between 16 and 29 hours. The flow parameters for the experiments are given in Table 2.1.

During the experiments, the bed was classified (by eye) into patches of similar grain size and sorting, and mapped. As in the Tsukuba experiments, patches ranged from smooth

to congested to inactive, although with the unimodal, sand-free bulk mixture, sorting (the geometric standard deviation) played a more critical role in facies discrimination than in the Tsukuba experiments, where the median grain size was sufficient. Bed areas that appeared to have a bimodal grain size distribution were classified as "scoured," since it appeared that the intermediate-sized material had been stripped from the bed, exposing some finer grains. The coarsest areas that experienced little to no sediment transport were classified as "inactive." However, some areas of the bed that experienced very little sediment transport were distinguishable from the "inactive" facies in that they contained a slightly higher percentage of fine material; these were classified as "scoured-inactive" since they resembled a coarser, inactive version of the "scoured" facies. The grain size distributions of the patch types were later derived by selecting representative photos and performing a digital grain size analysis where a 10×10 grid with a spacing of 5 cm was overlain on the center of the channel in the photo and at each point the intermediate axis of the intersecting grain was recorded. Although grain size distributions obtained from photographic analysis will be affected by grain shape and imbrication [see review in *Bunte and Abt*, 2001], these effects can be minimized in a laboratory setting where the overall sediment characteristics are known, and here the photographic method provided both a time-saving technique and a non-destructive visual archive of the entire bed. Figures 2.2c and 2.2d present the average grain size distribution for each patch type, and Table 2.2 summarizes the calculated median grain size (D_{50}) and geometric standard deviations (σ) for these distributions. The D_{50} of the congested, smooth, and transitional patch types was between 8.46 and 9.02 mm. The congested and transitional patches could be visually distinguished by their degree of sorting; congested patches were the most well-sorted ($\sigma = 1.81$) and transitional patches were relatively poorly-sorted ($\sigma = 1.96$). The scoured, scoured-inactive, and inactive patch types each had similar sorting values ($\sigma \approx 2$) and the major difference between them was in the median grain size; the D_{50} for the scoured patches was 9.3 mm while that of the inactive patches was 12.47 mm. Maps were also constructed of the dry bed at the end of each feed reduction. Similar to the Tsukuba experiment, the photographically-derived patch grain size distributions were combined with patch areas derived from the maps to obtain an area-weighted average grain size distribution of the entire bed at the end of each run.

2.2.3 1D morphodynamic modeling

One-dimensional morphodynamic models cannot account for lateral bed surface heterogeneity; however, the difference between experimental results where patches are documented and 1D model predictions can provide an avenue for quantifying the effect of patches on sediment transport and channel characteristics. To facilitate such a comparison, we simulated the Tsukuba and Berkeley experiments with a one-dimensional morphodynamic model, RTe-bookAgDegNormGravMixPW.xls, which is freely available as an Excel spreadsheet accompanying an e-book (Parker, e-book, 2007). In order to have greater control over the model output (i.e., to allow us to smoothly incorporate stepwise reductions in sediment sup-

ply), we translated the VBA code in the Excel spreadsheet into MATLAB code. The main input parameters to the model include the reach length, the initial grain size distributions of the bed surface, subsurface, and sediment feed, the initial slope, the sediment feed rate, and the water discharge. At each computational node in the modeled reach, the model calculates shear stresses using a normal flow approximation, calculates bedload transport using the surface-based relation of *Parker* [1990] or *Wilcock and Crowe* [2003], and calculates changes in bed surface elevation and grain size using the 1-D Exner equation with the active layer assumption. Here, the Tsukuba experiments (which had a significant sand component) were modeled using the *Wilcock and Crowe* [2003] relation, while the sand-free Berkeley experiments were modeled using both the *Parker* [1990] and *Wilcock and Crowe* [2003] relations. Table 2.3 provides the input parameters used in the modeling.

2.3 Results

2.3.1 Mean hydraulic conditions and bed characteristics

Table 2.1 shows the mean hydraulic conditions at the end of each run for both sets of experiments. In the Tsukuba experiments, as the sediment feed rate was reduced from 17.4 to 6.1 and then to 1.7 g/min-cm, the water surface slope decreased from 0.0052 to 0.0046 and then to 0.0035 (Figure 2.3a), and the mean flow depth varied only slightly, ranging from 10.2 to 11.3 cm. These slope reductions along with the relatively constant depth resulted in a decrease in the boundary shear stress during the experiment, from 5.2 Pa under the 17.4 g/min-cm feed rate to 3.88 Pa under the lowest feed rate of 1.7 g/min-cm (Figure 2.3b). The slope decrease was accompanied by bed degradation, which was greatest at the upstream end because the downstream elevation of the bed was fixed.

In the Berkeley experiments, the mean depth varied only slightly, increasing from 21.8 cm at the highest feed rate of 23.3 g/min-cm, to 22.8 cm at a feed rate of zero. The water surface slope was 0.0048 with the highest sediment feed rate of 23.3 g/min-cm and decreased with each feed reduction, ultimately reaching a value of 0.0039 during the zero-feed run. The bed slope exhibited a similar decrease from 0.0055 at the highest feed rate to 0.0043 during the zero-feed run, although both the bed and water surface slope displayed substantial variability throughout the course of the experiment (Figure 2.4a). These slope reductions decreased the boundary shear stress, which fell from 10.3 Pa at the highest feed rate to 8.64 Pa with zero feed (Figure 2.4b). As in the Tsukuba experiments, the slope decrease was accompanied by bed degradation that was greatest at the upstream end of the flume.

For each experiment, the shear stress τ_b was calculated as $\tau_b = \rho g h S$ where ρ is the density of water, g is gravitational acceleration, h is mean flow depth, and S is the water surface slope. The uncertainties in the depth and slope measurements (the standard error calculated from the repeated measurements) were propagated through the calculation to estimate shear stress uncertainties. Table 2.1 also presents sidewall-corrected shear stress

Table 2.3: Input parameters for morphodynamic model[a].

			Tsukuba			Berkeley			
Variable	Abbreviation	Units	Run 1	Run 2	Run 3	Run 5-1	Run 5-2	Run 5-3	Run 5-4
Sediment feed rate	$qbTf$	$m^2/s \times 10^{-6}$	10.90	3.82	1.07	14.63	9.75	4.88	0
Water discharge	q_w	m^2/s	0.06	0.06	0.06	0.238	0.238	0.238	0.238
Intermittency	I		1	1	1	1	1	1	1
Initial bed slope[b]	$Sfbl$		0.0046	-	-	0.0051	-	-	-
Reach length	L_r	m	7.5	7.5	7.5	30	30	30	30
Time step	dt	days $\times 10^{-5}$	2.6	2.5	1.4	0.12	0.12	0.12	0.12
Number of segments	M		30	30	30	90	90	90	90
Active layer factor[c]	n_a		1	1	1	1	1	1	1
Upwinding coefficient	au		0.75	0.75	0.75	0.75	0.75	0.75	0.75
Output frequency[d]	Mtoprint		2000	3000	3000	120	120	120	120
Output frequency[d]	Mprint		6	6	6	480	868	836	620
Time simulated	Calc time	hr	7.5	10.8	6	16.0	28.9	27.9	20.7

[a]See Parker (e-book, 2007) for details of the model.

[b]Only used in the first run, later runs used the final bed profile from the previous run.

[c]Factor by which surface D_{90} is multiplied to obtain active layer thickness.

[d]Mtoprint is the number of steps until output is recorded; Mprint is the number of printouts after the initial one.

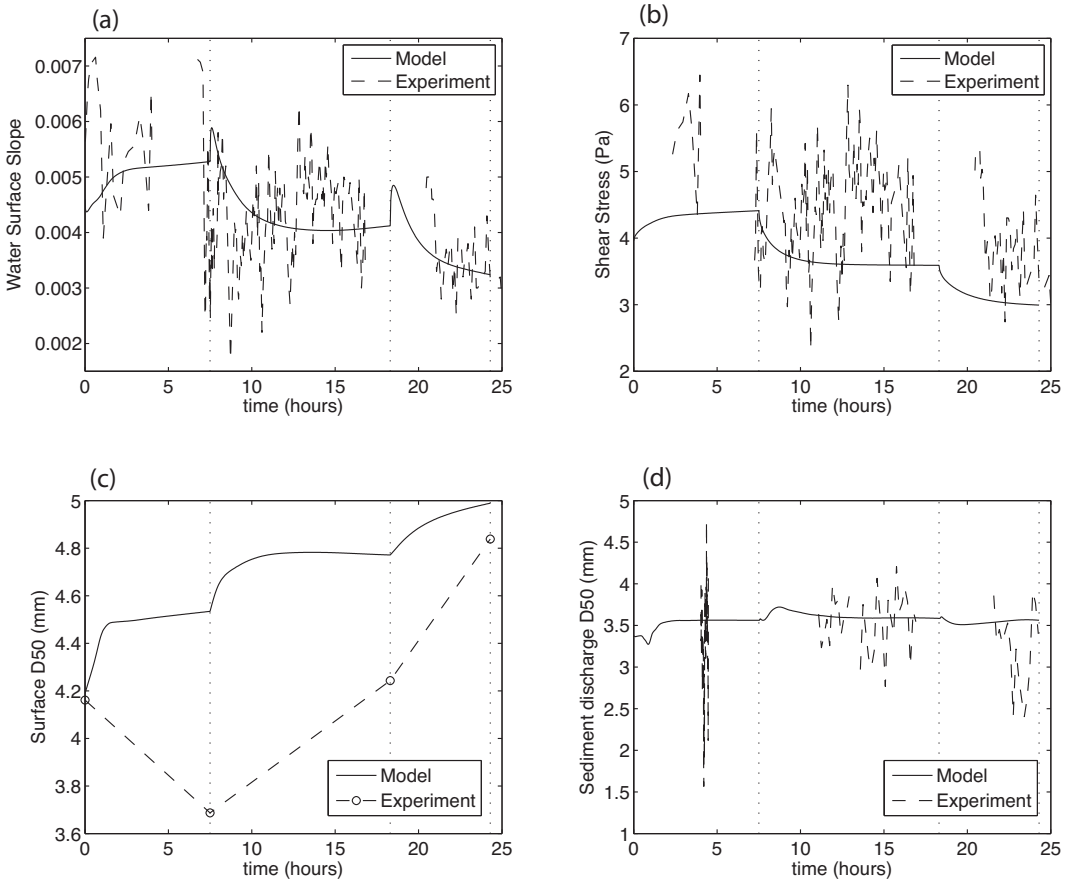

Figure 2.3: Experimental results and model predictions for the Tsukuba experiments for (a) water surface slope, (b) shear stress, (c) median grain size of the bed surface, and (d) median grain size of the sediment discharge.

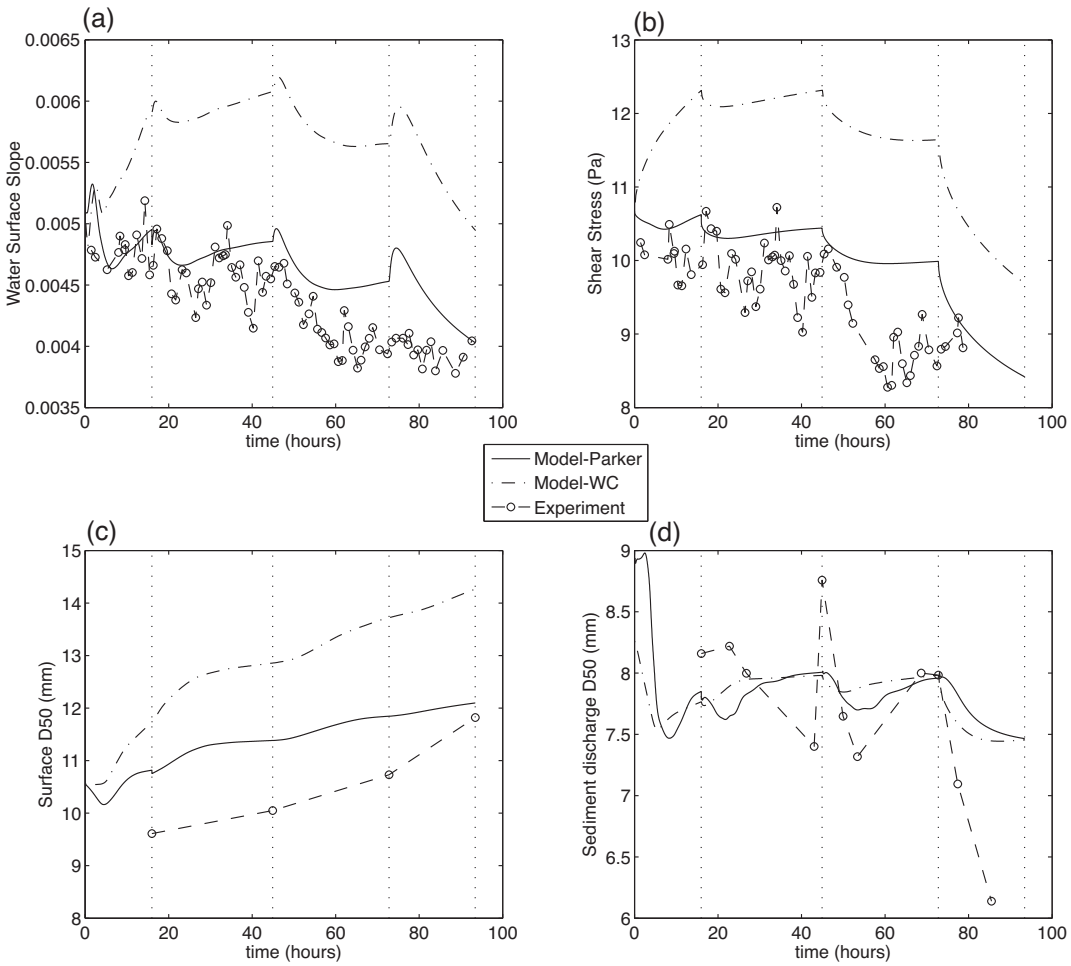

Figure 2.4: Experimental results and model predictions for the Berkeley experiments for (a) water surface slope, (b) shear stress, (c) areally-weighted median grain size of the bed surface, and (d) median grain size of the sediment discharge.

(calculated with the *Williams* [1970] method).

Substantial changes in the surface grain size distribution also accompanied the reduced sediment feed. For both experiments, on a flume-averaged basis, the surface coarsened with each supply reduction. Figures 2.1a and 2.1b show the area-weighted average surface grain size distributions at the end of each run for each experiment. In the Tsukuba experiment, the average median grain size of the bed surface was 3.74 mm at the highest feed rate of 17.4 g/min-cm. After the feed rate was reduced to 6.1 g/min-cm, the surface D_{50} increased to 4.26 mm, and after the feed rate was further reduced to 1.7 g/min, the surface coarsened to a D_{50} of 4.85 mm. As noted above, the initial surface grain size before transport was coarser than the load, but with first introduction of the high feed rate the areally-averaged channel D_{50} fined to nearly that of the load. Assuming that the D_{50} of the subsurface and that of the sediment feed were similar ($D_{50} = 3.65$ mm), these average median surface sizes correspond to armoring ratios (surface D_{50} / subsurface D_{50}) of 1.03, 1.17, and 1.34 for feed rates of 17.4, 6.1, and 1.7 g/min-cm, respectively. Similar overall coarsening was observed in the Berkeley experiments (Table 2.1). Under the highest feed rate of 23.3 g/min-cm, the areally-weighted surface D_{50} was 9.61 mm. The surface coarsened to a D_{50} of 10.05 mm after the feed rate was reduced to 15.5 g/min-cm, then coarsened further to 10.73 mm after the feed rate was reduced to 9 g/min-cm, and finally it coarsened to 11.82 mm after an extended period with no feed. When compared with the D_{50} of the feed (8.06 mm), these values correspond to average armoring ratios of 1.19, 1.25, 1.33, and 1.47 respectively.

2.3.2 Observations of bed surface patchiness

In both the Tsukuba and Berkeley experiments, the bed became organized into patches whose distribution varied with sediment supply. Figures 2.5 and 2.6 are maps representing the bed during each experiment under different sediment feed conditions. In the Tsukuba experiments (Figure 2.5), as mentioned in *Dietrich et al.* [1989], inactive and congested zones expanded as the sediment supply was reduced. Active transport became confined to a corridor down the center of the channel, the width of which narrowed as sediment supply was reduced. At the lowest sediment transport rate the bed ultimately exhibited a virtually uniform pavement. A map of the bed at the lowest sediment feed rate was not made because of this lack of variability.

Similar results were observed in the Berkeley experiments (Figure 2.6). As the supply was reduced, coarse inactive zones along the flume walls expanded at the expense of the finer smooth and transitional areas. These coarse patches along the channel edges were not forced by topography, but were fixed as a consequence of coarse grain interactions and near-wall boundary shear stress reduction (and were present to some degree even at the highest load). Sediment transport was primarily confined to a narrow, finer corridor in the center of the channel. The width of this zone of active transport decreased as the sediment supply was reduced (Table 2.1). Analysis of bed maps indicates that at the highest supply rate of 23.3 g/min-cm, the width of this zone of active transport was 61 ± 10 cm (mean ± 1 standard

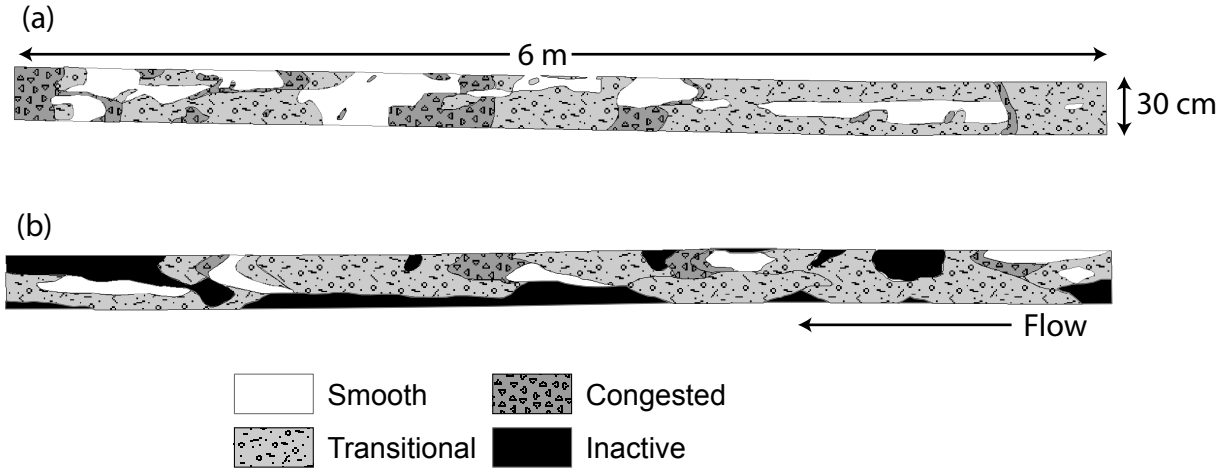

Figure 2.5: Bed facies map of the Tsukuba experiments at the end of the a) 17.4 g/min-cm and b) 6.1 g/min-cm sediment feed runs. The 1.7 g/min-cm run was not mapped as it was uniformly coarse. See text for description of terms in the legend.

deviation), and it narrowed to 51 ± 12 cm at 15.5 g/min-cm, then 46 ± 9 cm at 9 g/min-cm. At 0 g/min-cm, all bed surface heterogeneity had essentially been eliminated and this zone of active transport effectively disappeared as the bed became uniformly coarse. The expansion of the area of the coarse patches at the expense of finer patches led to the increase in average D_{50} over the entire bed surface, as documented above.

2.3.3 Observations of patch dynamics

Free (mobile) patches, typically in the form of bedload sheets, were observed in both the Tsukuba and Berkeley experiments. These sorting features had coarse-grained fronts with heights of about 2 grain diameters and progressively fined toward their tails. In the Tsukuba experiments, coarse gravel particles became trapped in each others wakes and accumulated into congested zones, forming the coarse front of bedload sheets. As sand from the tail advanced and began to bury the upstream portion of the sheet head, coarse material at the tail was exhumed. The interstices of this coarse material were filled with remnant sand from the tail, which altered the local hydrodynamics and allowed the coarse particles to be remobilized. These remobilized coarse particles advanced to the front of the sheet and were deposited, causing the bedform to migrate. Sheets propagated in a similar manner in the Berkeley experiments even in the absence of sand. In the Berkeley experiments, the front of bedload sheets was composed of relatively well-sorted moderately coarse (8-14 mm) gravel, and these fronts advanced when arriving like-sized material was deposited. As fine (3 mm)

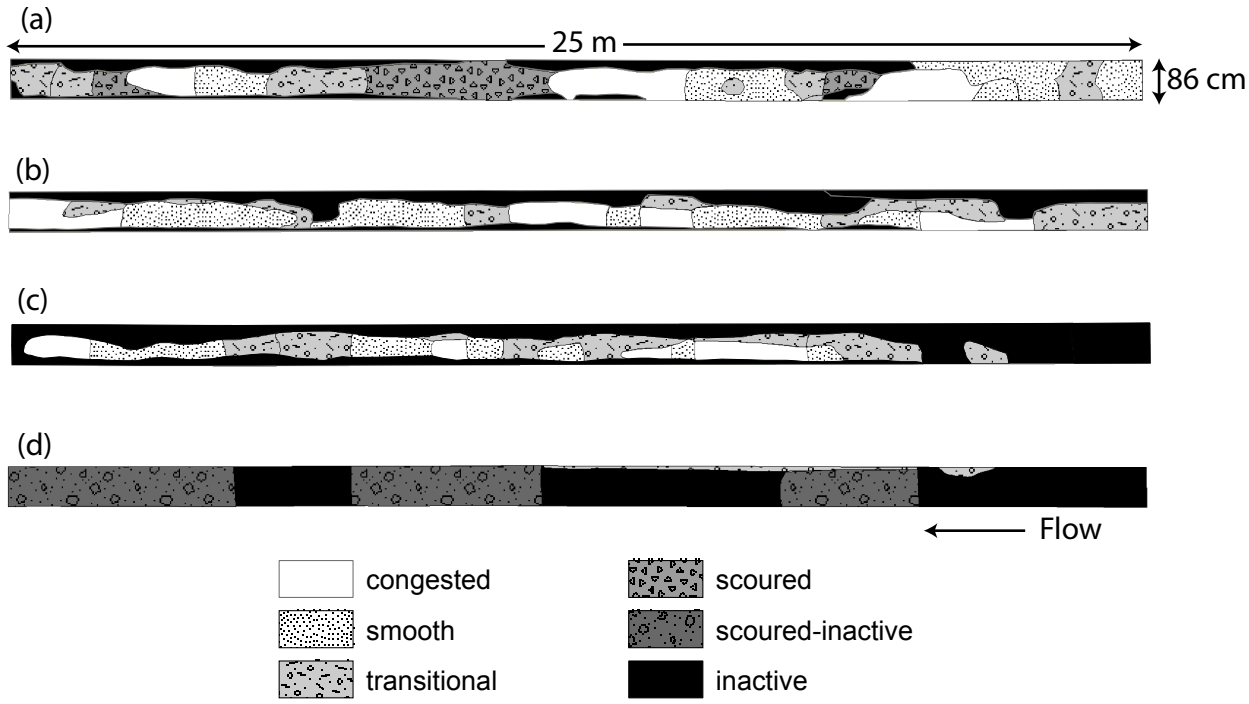

Figure 2.6: Facies map of the bed of the Berkeley experiments at the end of the a) 23.3 g/min-cm, b) 15.5 g/min-cm, c) 9 g/min-cm, and d) 0 g/min-cm sediment feed runs. See text for description of terms in the legend.

gravel from the tail advanced to the front, it exposed coarse material that was remobilized and redeposited at the sheet front. Both of these phenomena illustrate the "catch and mobilize" process described by *Whiting et al.* [1988]. This process, which takes place over the entire length scale of the bedload sheet, creates the downstream-sorted structure of a bedload sheet and also provides a mechanism for its movement. While this phenomenon had previously only been observed in poorly sorted sand-gravel mixtures, our observations in the sand-free Berkeley experiments suggest that the ratio of coarse to fine grain sizes is probably more important to this process than the mere presence or absence of sand. For grain size segregation to emerge, the coarse front must trap the fines and keep them from passing over it. The range of sizes must be wide enough that the small grains can fit into the interstices between the large grains. For an idealized packing geometry where grains are approximated to be tangent circles, the fine grains can fit into the interstices of the coarse grains with no upstream exposure when the diameter of the coarse grains is four times that of the fine grains. This is largely consistent with the characteristics of bedload sheets presented in Table 2.4 and suggests a constraint on the range of sizes that can create bedload sheets. Natural bed surfaces are, however, never really geometrically flat, and it appears to take a critical amount of finer sediment deposition (more than one grain) to cause mobilization. The mobilization effect of the fine grains on the coarse grains is likely related to a hydrodynamic smoothing effect that increases the near-bed velocity and drag on the coarse particles [e.g., *Sambrook Smith and Nicholas*, 2005].

In the Tsukuba experiments, the locations of the coarse fronts of bedload sheets were recorded (Figure 2.7). The lines in Figure 2.8 represent the motion of individual sheets, so by performing linear regression on each line we can determine the migration rate of each individual sheet and the spacing between successive sheet fronts. Figures 2.8 and 2.9 present these data for the duration of the Tsukuba experiments. Although there is substantial variability in the data, it is apparent that, in general, as the supply was reduced the migration rate of sheets decreased and the spacing between sheets increased. Table 2.4 provides average values of sheet migration rate and spacing computed at the end of each run. Unfortunately, the larger spatial and temporal scale of the Berkeley experiments made acquisition of a similarly detailed dataset infeasible. The spacing between sheets, however, was approximated by examining the hand-drawn bed texture maps made during and between runs. These data indicate that, similar to the Tsukuba experiments, the spacing between sheets increased from 6.5 to 9.1 m as the supply was reduced from 23.3 g/min-cm to 9 g/min-cm (Table 2.4). Sheets were absent when the feed rate was reduced to 0 g/min-cm.

2.3.4 Effects of patch dynamics on sediment flux

Figure 2.10 presents measurements of sediment discharge from both experiments. Several important features are readily apparent in both datasets. First is the decline in the mean transport rate after reductions in sediment supply. As can be inferred from Figures 2.1, 2.3c, 2.4c, 2.5, and 2.6, this decline coincided with a general bed coarsening that was a consequence

Table 2.4: Characteristics of bedload sheets in this and other studies[a].

Reference	H (mm)	L (m)	p (min)	L/H (mean)	L/h	U (mm/sec)	D_{16} (mm)	D_{50} (mm)	D_{84} (mm)	q_s^b (kg/m-s)	Shields number	Conditions
Kuhnle et al. [2006]	7-12	0.07-1.06	0.5-1.15	60	3-4	8-27	1.4	1.82	7.5	0.0647-0.0765	0.066-0.078	Recirculating flume
Bennett and Bridge [1995]	4-13	0.6-1.3	9.5 - 16.8	56-338	4-13.5	0.7-1.5	1.1-1.2	2.00	3.5-4.2	0.010-0.043	0.04-0.10	Recirculating flume
Wilcock [1992] (MC50)	6-12	1-2	-	-	-	-	1.8	2.55	6.0	0.018-0.063	0.090	Recirculating flume
Whiting et al. [1988] (Duck Creek)	10-20	0.5-2	-	83	3.6	1.8-3.5	1.3	4.60	8.7	0.038	0.07-0.11	Field
Whiting et al. [1988] (Muddy Creek)	2-4	0.2-0.6	-	133	1.3	6-15	0.4	0.90	1.9	-	0.09-0.18[c]	Field
Bunte et al. [2004]	100-150	-	-	-	-	10	17	69	166	0-0.05	-	Field
Kuhnle and Southard [1988]	2-4	0.5-3	5-26	583	24-49	5-10	1.1	3.03	8.0	0.034-0.098	0.036-0.074	Feed flume
Iseya and Ikeda [1987] (Run 6)	-	1.8	-	-	163.6	7.3 (3.6-11.3)	0.3	0.44	2.5	0.0427	0.5[d]	Feed flume
Pender and Shvidchenko [1999]	9-20	2.2-3.5	-	197	19	0.07-0.18	0.6	3.65	5.9	0.0032 - 0.0063	0.056	Feed flume
Madej et al. [2009]	~ 4	-	-	-	-	10-20	0.4	1	3.2	0.024 - 0.031	0.015	Feed flume
This study - Tsukuba	5-10	1.4	4.8 (2-15)	197	13.5	9.0	1.1	3.63	5.6	0.0290	0.086	Feed flume
This study - Tsukuba	5-10	1.8	11.5 (2-40)	259	17.6	2.6	1.1	3.63	5.6	0.0102	0.067	Feed flume
This study - Tsukuba	5-10	1.8	23.4 (2-120)	254	15.7	3.5	1.1	3.63	5.6	0.0028	0.049	Feed flume
This study - Berkeley	15-30	6.5	-	217	29.8	-	4.3	8.06	15.8	0.0388	0.077	Feed flume
This study - Berkeley	15-30	9.0	-	300	40.8	-	4.3	8.06	15.8	0.0258	0.066	Feed flume
This study - Berkeley	15-30	9.1	-	303	40.5	-	4.3	8.06	15.8	0.0150	0.057	Feed flume
This study - Berkeley	-	-	-	-	-	-	4.3	8.06	15.8	0.0000	0.043	Feed flume

[a] See Notation section for variable definitions.

[b] Sediment transport rate (recirculating flume and field) or sediment feed rate (feed flume).

[c] *Whiting et al.* [1988] estimate shear stress to be 3-6 times critical for coarse sand.

[d] Shields number for *Iseya and Ikeda* [1987] experiment calculated with the D_{50} of the feed sediment, all others calculated with the D_{50} of the bed surface.

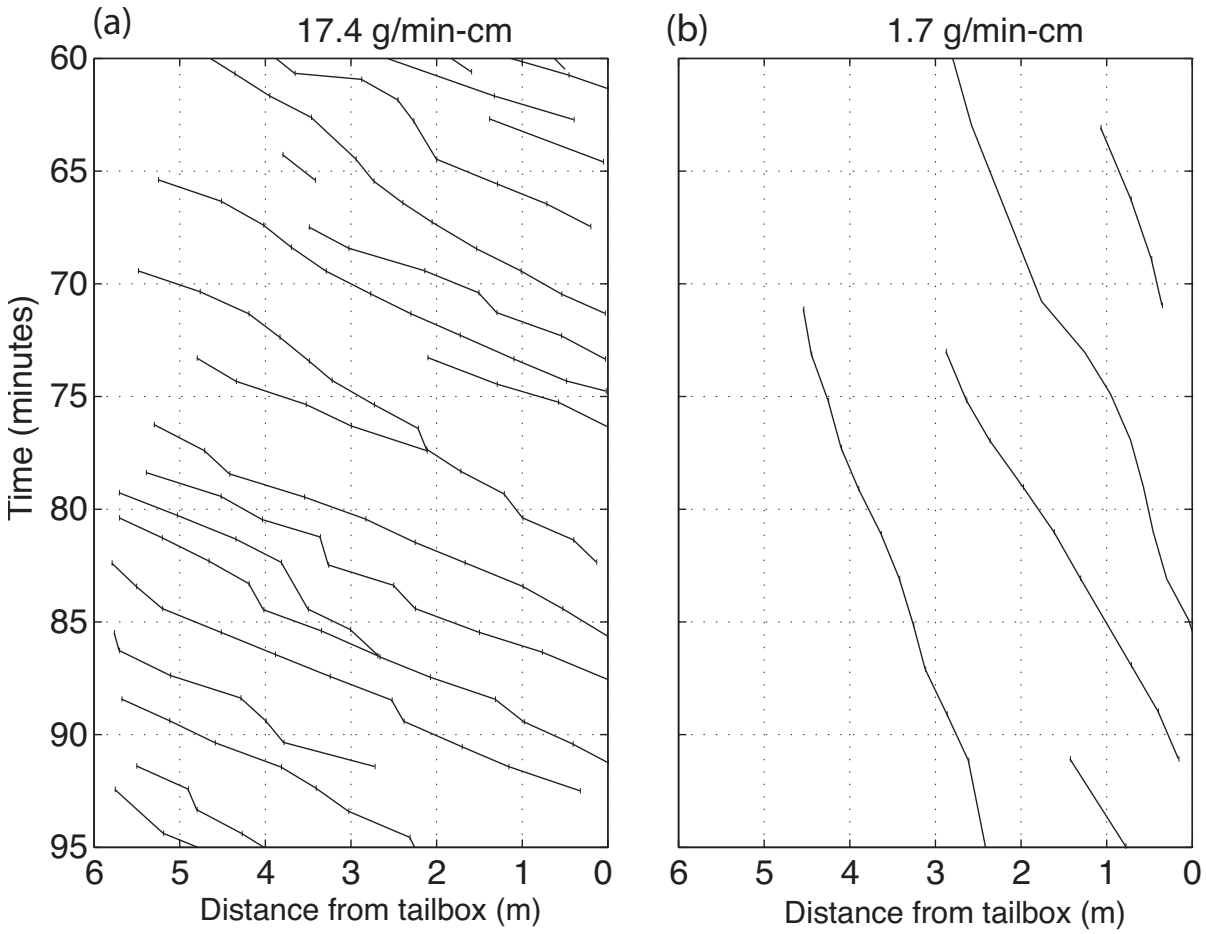

Figure 2.7: Representative observations of the migration of the coarse fronts of bedload sheets during the Tsukuba experiments at a sediment feed of (a) 17.4 g/min-cm and (b) 1.7 g/min-cm.

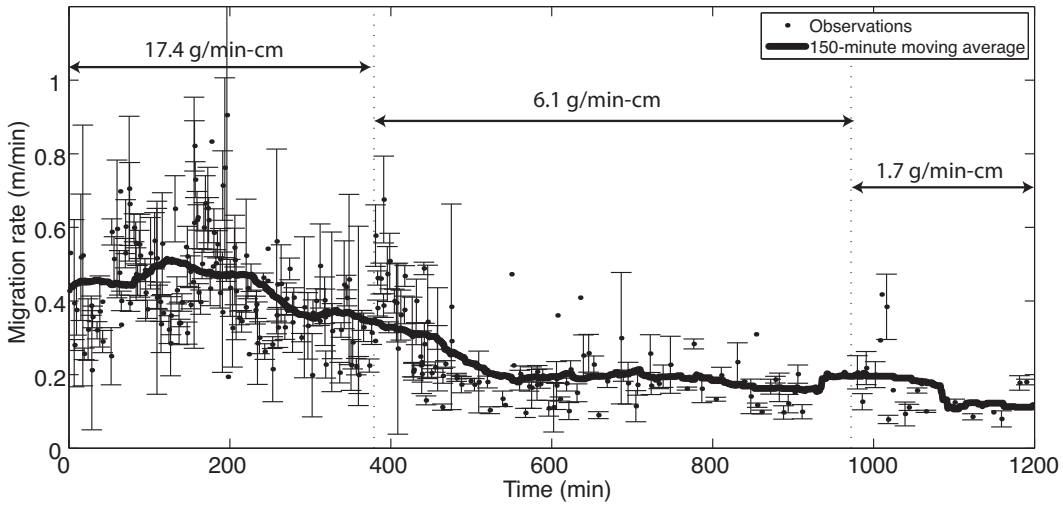

Figure 2.8: Time series of bedload sheet migration rates during the Tsukuba experiments. Each data point is the migration rate of a single sheet calculated from slope of the time-distance trajectory observations shown in Figure 2.7. Dashed lines indicate transitions in the sediment feed rate, and the thick line through the data is a 150-minute moving average. Error bars indicate 95% confidence intervals of the calculated slopes.

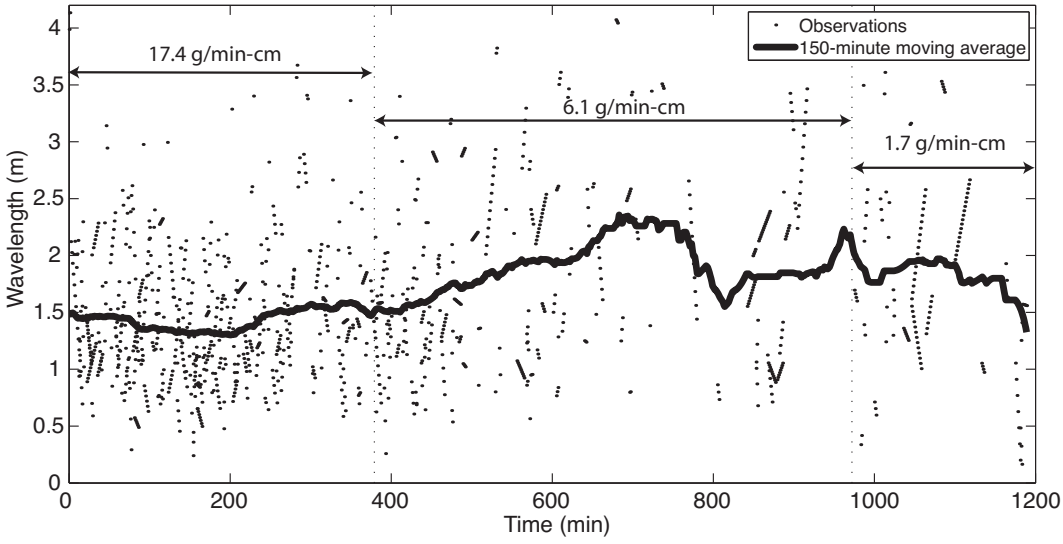

Figure 2.9: Time series of the spacing between bedload sheets calculated from observations of the type presented in Figure 2.7 during the Tsukuba experiments. Data points are the distances between adjacent sheets at a given time, dashed lines indicate transitions in the sediment feed rate, and the line through the data is a 150-minute moving average.

of the expansion of the fixed immobile patches along the flume edges and a reduction of the area occupied by the finer patches. In both experiments, the time-averaged median grain size of the sediment discharged from the flume generally coincided with the median grain size of the feed mixture (Figures 2.3d and 2.4d). A second striking feature of the sediment flux time series in Figure 2.10 is the tremendous short-term variability in sediment discharge during the experiments. During the high-supply Berkeley experiments the instantaneous flux rates spanned nearly two orders of magnitude. The absolute magnitude of these variations in both flumes decreased as the sediment feed rate declined, although the variability relative to the mean flux rate remained relatively constant. In the Tsukuba experiments, sharp increases in sediment flux were primarily the result of increased flux of gravel (rather than sand; see Figure 2.11a). During short-term periods of high sediment flux up to 85% of the load was gravel, while during periods of lower flux the load could be over 50% sand (Figure 2.11b). Because bedload sheets in the Tsukuba experiments had gravelly heads and sandy tails, this suggests that high transport rates coincide with the passage of sheet heads and lower transport rates occur either with the passage of sheet tails or between successive sheets.

2.3.5 1D morphodynamic modeling

Some of the model predictions for the Tsukuba experiments have already been presented in a previous study [*Dietrich et al.*, 2005] and are summarized here in Figures 2.3 and 2.10a. For each feed rate, the surface D_{50} predicted by the model (using the *Wilcock and Crowe* [2003] transport algorithm) is 1.03 to 1.23 times the observed D_{50}; however, the maximum deviation between the model prediction and surface D_{50} is only 0.75 mm, which may be within measurement error (Figure 2.3c). The water surface slopes at the end of each run predicted by the model are between 0.90 and 1.02 times the measured water surface slopes (Figure 2.3a). The model consistently underpredicts the average shear stress; modeled stresses are between 0.77 and 0.85 times the measured stresses (Figure 2.3b). The sediment flux predicted by the model (Figure 2.10a) does not capture any of the short-term variability due to the passage of bedload sheets as discussed above, but it does equilibrate to the feed rate for each phase of the experiment. The average D_{50} of the sediment discharge predicted by the model at equilibrium is equal to that of the sediment feed and is within the range of the experimental observations (Figure 2.3d).

When the *Parker* [1990] algorithm is used to model the Berkeley experiments, the model overpredicts the surface grain size at all feed rates (Figure 2.4c). The predicted surface D_{50} is 1.02 to 1.13 times the observed D_{50} (Figure 2.4c). As was the case for the Tsukuba experiments, the difference between predicted and observed surface D_{50} decreases with decreasing feed rate and hence bed surface patchiness, suggesting that the model performance improves with decreasing bed surface heterogeneity. The water surface slopes predicted by the model are between 1.00 and 1.12 times the observed slopes (Figure 2.4a). The model tended to overpredict shear stress, with modeled shear stresses at equilibrium 1.06 to 1.14 times the measured stress (Figure 2.4b). The models prediction of the Berkeley sediment discharge

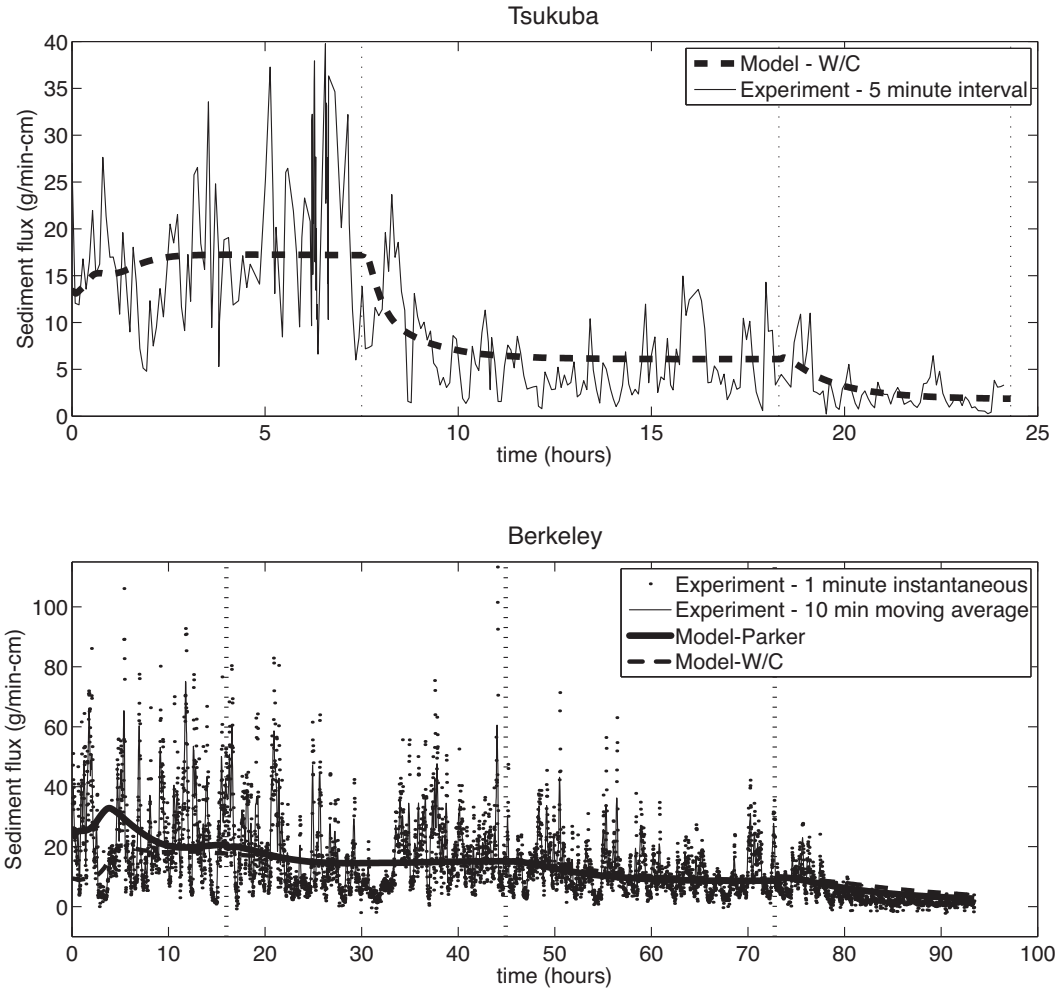

Figure 2.10: Experimental results and model predictions of sediment flux for the (a) Tsukuba and (b) Berkeley experiments. The sediment feed rates are presented within the figure.

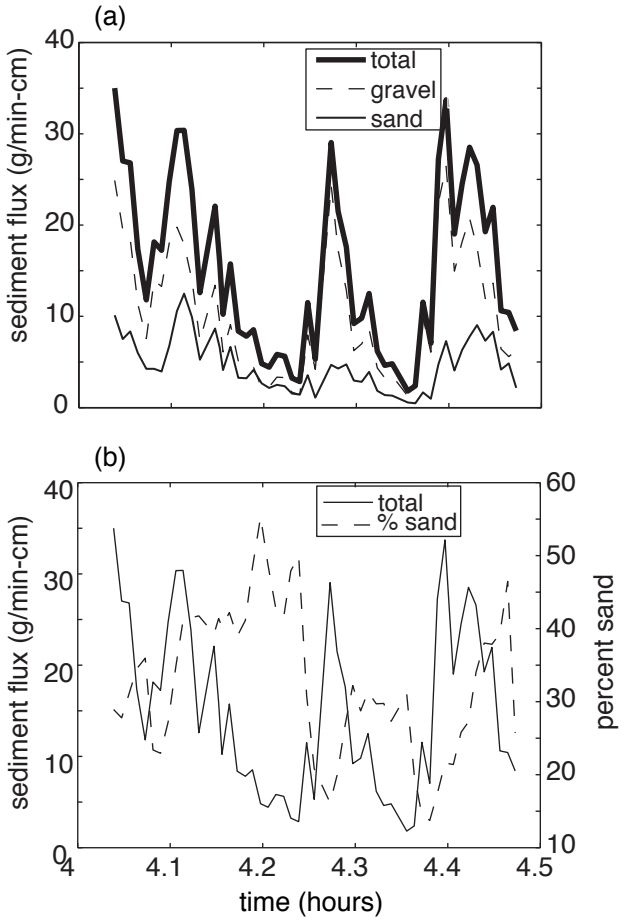

Figure 2.11: Sediment flux during a portion of the 17.4 g/min-cm phase of the Tsukuba experiment. (a) presents the total rate of sediment transport along with the corresponding rates of sand and gravel transport. (b) presents the total sediment transport rate and the percentage of the load that was sand.

was consistent with the average transport rate in the experiment (Figure 2.10b). At the end of the computation, however, the model predicted a sediment discharge of 2.5 g/min-cm while the measured sediment discharged from the flume was less than 1 g/min-cm. Both the predicted and measured D_{50} of the sediment discharge during the feed portions of the experiment tended to equilibrate at the D_{50} of the sediment feed (8 mm), although once the feed was eliminated the measured D_{50} of the sediment discharge decreased more rapidly than that predicted by the model (Figure 2.4d).

Application of the *Wilcock and Crowe* [2003] algorithm in the 1D simulation of the Berkeley experiments yielded results in striking disagreement with the experimental observations. Although the model-predicted sediment discharge matched the average transport rate in the experiment (Figure 2.10b), the model achieved that flux rate by predicting steeper slopes, higher shear stresses, and larger surface grain size than what was observed (Figure 2.4).

The transient response of both simulations shows that after a reduction in sediment supply, the model tends to predict a brief increase in the water surface slope, followed by a decrease in slope, then a small gradual slope increase toward an equilibrium value (Figures 2.3a and 2.4a). The initial increase in water surface slope occurs because immediately following the supply reduction, the bed of the upstream portion of the channel coarsens, which causes the water surface elevation at the upstream end to increase. This bed coarsening and the accompanying depth increase propagates downstream, but as it does so the upstream portion of the channel begins to scour, which causes the water surface slope to drop. Eventually, the downstream portions of the channel also become scoured and the water surface slope experiences a slight recovery.

2.4 Discussion

2.4.1 Sediment supply and patch dynamics

As sediment supply was reduced in the experiments, the resultant surface coarsening did not develop in a uniform manner. Even in the fairly simple conditions of our experiments relatively one-dimensional, low width-to-depth ratio, plane bed the bed displayed remarkable heterogeneity. As supply was reduced, the bed coarsened through the expansion of coarse, fixed patches that first developed along the flume edges, and a constriction of the finer zone of active transport over which free patches (bedload sheets) were moving. As shown in Figures 2.8 and 2.9, the spacing between these sheets and the speed at which they were moving also varied with sediment supply. Only after an extended period of zero feed did the bed become a nearly uniform texture, which in this case was a completely armored, immobile bed.

Table 2.4 summarizes data from this and several other studies in which the measurements of the characteristics of bedload sheets were made. Bedload sheets are similar to bedforms such as ripples or dunes in that their shape and behavior can described in part by a height (H), wavelength (L), and migration rate (U). It is apparent that the height of bedload

sheets scales with the coarse grain diameter, and that they are tens to hundreds of grain diameters in length. Yet, there does not appear to be any consistency in bedload sheet aspect ratio (L/H) or the flow depth to sheet height ratio (h/H). In contrast, dunes have fairly consistent aspect ratios ($L/H = 20$) and scaling with flow depth ($h/H = 5$) in uniform steady flow (see reviews in *Carling* [1999] and *Venditti et al.* [2005]). As is the case for bedload sheets, subaqueous ripples tend to scale with particle diameter ($L \sim 1000D$), but they only form in hydraulically smooth flow and consequently are limited to sediment with $D < 0.7$ mm [*Best*, 1996; *Carling*, 1999; *Venditti et al.*, 2005, and references therein]. Thus, the commonly used methods for scaling bedforms do not apply to bedload sheets. Bedload sheet migration rate decreased and wavelength increased with reductions in sediment supply. This is consistent with the absence of sheets in the low sediment supply channels studied by *Church et al.* [1998] and *Hassan and Church* [2000]. As suggested by *Whiting et al.* [1988], bedload sheets might under certain conditions provide "seeds" for the development of dunes. If flows are competent to carry the load at several times the critical shear stress, it is possible that a threshold sediment supply exists where sheets begin to transform into low amplitude dunes. Indeed, experiments by *Bennett and Bridge* [1995] seem to suggest this is the case. The earlier work seems to be confirmed by the changes in mixed size bedforms observed by *Kleinhans et al.* [2002], where with increasing flow strength and sediment transport, they observed sand ribbons evolve into barchans and eventually dunes.

The dependence of bedload sheet migration rate on sediment supply can in part be explained through a simple mass balance argument. Sediment flux per unit width, q_s, can be expressed as the product of a bedforms migration rate U, height H, and a shape factor which is normally taken to be constant [*Simons et al.*, 1965]. If the height of a bedform remains constant then an increase in q_s translates directly to an increase in U. A similar mass balance argument can be made to explain why sheet spacing decreases with increased sediment supply. It appears [as suggested by *Whiting et al.*, 1988] that for free patches such as bedload sheets to form, it is necessary to reach a critical concentration of coarse particles sufficient to create the sheet front (termed "gravel jams" in *Iseya and Ikeda* [1987]). Since more coarse particles become available with a greater sediment supply, the length of the upstream contributing bed area required to develop the sheet front decreases and sheets can form with greater frequency.

This argument depends on the height of the sheet remaining constant (i.e., 1-2 coarse grain diameters). Studies in which sheets have been documented (Table 2.4) confirm this assumption, but why should an increase in sediment supply produce greater bedform migration rate rather than increase the bedform height? One important feature that distinguishes sheets from subaqueous dunes and ripples is the strong sorting over the bedform. If all grain sizes are mobile and the grain size distribution is wide enough, the mobilization effect of the fine particles on the coarse ones may provide a limit to the bedform height by mobilizing the coarse particles before they can build a slip face. This continual mobilization would then allow the sheet to migrate downstream more rapidly without appreciable gains in height. This process is likely to be limited to a somewhat intermediate range of sediment supply (relative

to channel width) and flow competency, where beyond a certain level sheets may start to frequently merge with each other, forming slip faces and developing dunes. In this framework, then, sediment supply is the primary control on bedload sheet scaling. Hydraulics play a secondary role, in that the flow must be capable of moving the range of grain sizes composing the sheet structure, but must not be so strong as to prevent the initial mutual interactions between coarse particles from forming the sheet front.

2.4.2 Morphodynamic predictions in patchy channels

The presence of sorted patches on the bed poses potential problems for bedload transport calculations because it becomes necessary to average over the width of the bed to get an input grain size. Given the remarkable heterogeneity and sorting we observed in our experiments (Figures 2.5 and 2.6), our uncalibrated application of the Parker (e-book, 2007) one-dimensional morphodynamic model performed quite well, especially for the Berkeley simulation using the *Parker* [1990] algorithm, as some predictions of the median surface grain size, slope, and average sediment flux were nearly within measurement error. It did, however, tend to overpredict changes in slope and underpredict changes in grain size with reductions in sediment supply (Figures 2.3 and 2.4). Of course, since the model includes a sediment feed at the furthest upstream node, if run to equilibrium it has to eventually calculate sediment flux everywhere to be equal to the feed rate. So, a robust evaluation of the models performance must look at the accuracy of its predictions of equilibrium bed states (slope and grain size) and transient conditions.

The surface-based bedload transport relations used in the modeling (*Parker* [1990] and *Wilcock and Crowe* [2003]) calculate sediment flux as a highly nonlinear function of the grain size distribution of the bed surface and the applied shear stress. We can illustrate the relative influence of changes in the bed surface grain size distribution vs. changes in shear stress by calculating sediment transport rates under a wide variety of shear stresses and bed surface grain size distributions. Figure 2.12b presents contours of constant sediment transport rate (in m^2/s) predicted using the *Parker* [1990] algorithm under varying shear stress for 13,071 theoretical bed surface grain size distributions (Figure 2.12a) composed of 2-64 mm material that have varying geometric mean diameters (D_g) but constant geometric standard deviation ($\sigma = 1.9$). The *Parker* [1990] algorithm uses a straining parameter which is a function of σ, so to isolate the effect of changing D_g we only used grain size distributions with $\sigma = 1.9$. Although this results in a population of surface grain size distributions with varying skewness and kurtosis, the impact of this should be minor because higher moments are not used to calculate parameters in the bedload flux algorithm. The transition from one sediment transport rate to another can be accommodated through a pure grain size change, a pure shear stress change (which, for a constant water discharge is likely to manifest itself by changes primarily in slope rather than in depth), or some combination of change in both variables. The shaded area in Figure 2.12 illustrates the potential changes in grain size and shear stress that might accompany a flux change from 0.0002 to 0.0001 m^2/s, if we assume

that supply reductions will inevitably be accompanied by net scour, which can reduce the slope or increase the surface grain size. The precise path taken in response to a supply reduction calculated in a 1D morphodynamic model will be constrained by the conservation of each grain size and depends on the grain size distribution of the feed. The nonlinear nature of sediment transport calculations is readily apparent a 100% change in sediment flux can result from a 40% change in D_g or a 15% change in shear stress. Thus, relatively small changes in slope or grain size can produce large changes in calculated sediment flux, and inversely, large changes in sediment flux (or sediment supply) will result in calculated slope or grain size changes that fall within a relatively narrow range.

In field application, estimates of boundary shear stress (from channel slope and flow depth) and surface grain size distribution are commonly used in bedload transport equations to calculate sediment flux. However, such predictions may be problematic in patchy channels, as several authors [e.g., *Paola and Seal*, 1995; *Ferguson*, 2003] have argued that 1D width-averaged bedload transport calculations tend to underestimate flux if there is cross-stream variance in shear stress that is not exactly compensated by matching changes in grain size. We applied the *Parker* [1990] and *Wilcock and Crowe* [2003] bedload relations to our observed areally-averaged bed surface grain size distributions and shear stresses (Figure 2.13). For the three sediment-feed portions of the Berkeley experiment, the *Parker* [1990] algorithm predicted sediment transport rates within the range of uncertainty. It did overpredict the sediment flux for the zero feed case, suggesting that at very low transport rates the models underlying calibration breaks down. The *Wilcock and Crowe* [2003] model, applied to both experiments, exhibits contradictory behavior it tends to underpredict transport rates for the Berkeley experiment and it tends to overpredict transport rates for the Tsukuba experiment. Given this seemingly inconsistent behavior, we are unable to assign a simple mechanism for its inaccuracy (such as overall underprediction due to lateral patchiness, for instance), but the calculations suggest that our experimental conditions may fall outside the realm of the models applicability. Nonetheless, the rather good performance of the *Parker* [1990] model when applied to the Berkeley experiments suggests that, at least for simple, flume-like conditions, spatial averaging may produce reasonable transport calculations. However, natural gravel beds commonly show greater differences in grain size distributions than observed in our experiments [e.g., *Lisle et al.*, 2000], and one could speculate that for a sinuous channel with larger spatial stress gradients and a wider range of grain sizes spatial averaging may not be sufficient to achieve accurate calculations.

To examine just the effect of cross-stream variability in grain size compared to using an areally-weighted average bed surface grain size distribution in the Parker (e-book, 2007) model, we performed simple calculations in which the channel in each experiment was assumed to be composed of two patch types the "inactive" and "smooth" types (grain size distributions given in Figure 2.2) with the relative proportion of each patch type varying from 0-100% of the channel width. For each bed state, we then used the *Parker* [1990] or *Wilcock and Crowe* [2003] algorithm to calculate the total bedload transport rate for two conditions under the same shear stress: 1) the "actual" case where the transport rate is

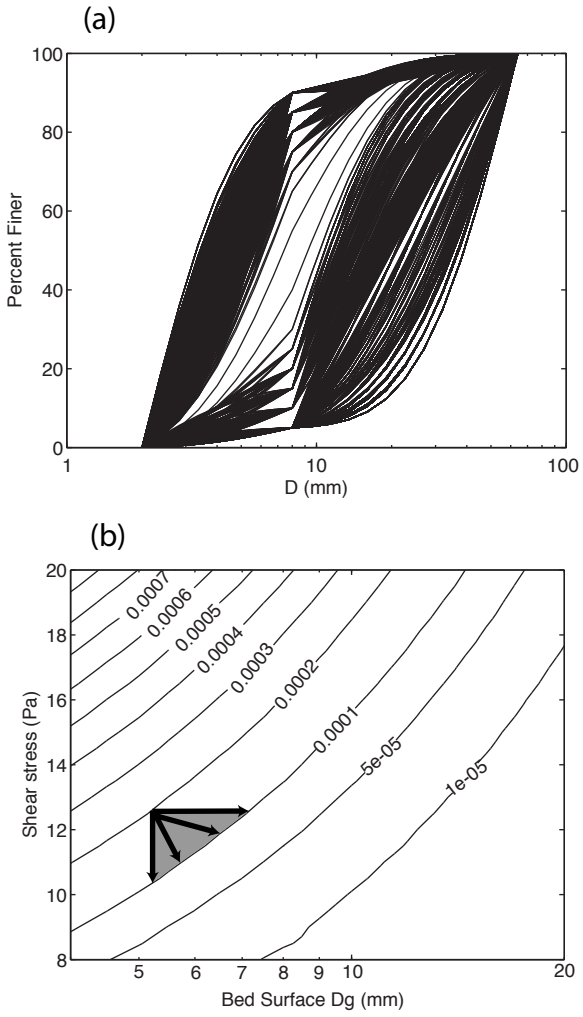

Figure 2.12: (a) Theoretical bed surface grain size distributions ($n = 13071$) with varying geometric mean diameters (D_g) but constant geometric standard deviation ($\sigma = 1.9$). (b) Contours of constant sediment transport rate (in m^2/s) calculated with the algorithm of *Parker* [1990] for the bed surface grain size distributions in (a) and plotted as a function of shear stress and bed surface geometric mean diameter (D_g). The shaded region and arrows represents the region of possible morphodynamic change likely to result from a reduction in sediment supply from 0.0002 m^2/s to 0.0001 m^2/s.

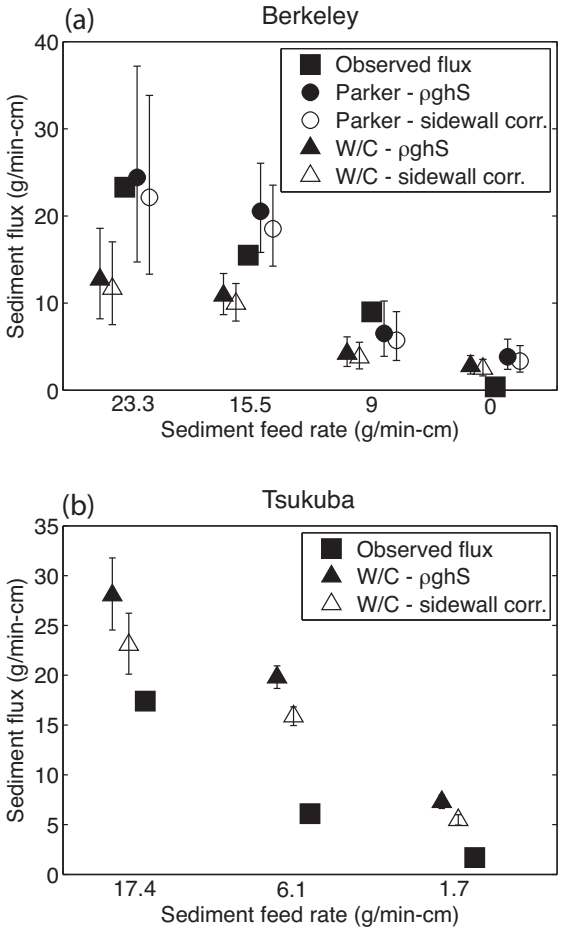

Figure 2.13: Sediment transport rates observed and predicted by the *Parker* [1990] and *Wilcock and Crowe* [2003] models when provided with the experimentally observed areally-averaged bed surface grain size distribution (Figure 2.1) and shear stress. Error bars indicate uncertainty associated with the standard error of the shear stress. Sidewall corrected stresses were calculated with the *Williams* [1970] method.

calculated for each grain size distribution and multiplied by its relative proportion across the bed (a "width-integrated" calculation) and 2) the "1D" case where an areally-averaged grain size distribution is calculated from the proportions of the two patch types and the algorithm is then used to compute the flux rate over that bed state (a "width-averaged" calculation). We assume constant shear stress across the channel typical of our experiments: 4.5 Pa for the Tsukuba case and 10 Pa for the Berkeley case. These calculations are the same for the end-member cases of either 100% smooth or 100% inactive or congested (Figure 2.14). As the bed transitions from 100% smooth to 100% inactive, the calculated sediment transport rate decreases by about 50% for the Berkeley case and about 70% for the Tsukuba case. The difference between the 2-patch calculation and the 1D average calculation is at most about 5%. In the Berkeley case, the flux calculated in the width-averaged calculation is always lower than in the width-integrated calculation, which is consistent with previous work [e.g., *Paola and Seal*, 1995; *Ferguson*, 2003]. In the Tsukuba case, however, the width-averaged calculation predicts a higher flux than the width-integrated calculation when the bed is about 80-100% "inactive" because, for those conditions, the sand content of the average bed grain size distribution increases and thus decreases the critical shear stress through the *Wilcock and Crowe* [2003] sand mobilization parameter. The relatively small effect of grain size variation alone heightens the importance of spatial variation in the boundary shear stress (relative to surface patch texture). For example, under the spatially constant stress conditions, the flux for the 100% "inactive" beds was 25-50% of that for the 100% smooth bed, whereas our observations suggested that this ratio should be close to zero (i.e., the bed was truly inactive and no transport should have been predicted). Again, this disparity is probably due to the local low boundary shear stress over the coarsened near-wall patches. Hence, the results shown in Figure 2.14 underestimate the combined effect of boundary shear stress and grain size variation.

While the 1D Parker (e-book, 2007) model was generally able to predict the mean sediment transport rate for both experiments (Figure 2.11), it was unable to capture the significant short term variability in sediment flux associated with the passage of individual bedload sheets (Figures 2.8, 2.11, and 2.12). Variations in bedload transport rates are very commonly observed in both field and flume studies [e.g., *Carey*, 1985; *Iseya and Ikeda*, 1987; *Kuhnle and Southard*, 1988; *Whiting et al.*, 1988; *Gomez et al.*, 1989; *Ashmore*, 1991a; *Hoey*, 1992; *Lisle et al.*, 1993; *Cudden and Hoey*, 2003; *Bunte and Abt*, 2005; *Whitaker and Potts*, 2007; *Madej et al.*, 2009]. The discrepancy with the model may be a consequence of its simplified hydraulics (the normal flow approximation), or smoothing effects related to the use of upwinding coefficients to calculate spatial derivatives or mixing with the subsurface. The incorporation of more complicated hydrodynamics [e.g., *Seminara et al.*, 1996] or particle-based modeling [e.g., *Schmeeckle and Nelson*, 2003; *MacVicar et al.*, 2006] appears to be necessary to capture this variability. Bedload sheets are an inherent feature of gravel-bed channels, and understanding their dynamics is critical to improving bedload flux models.

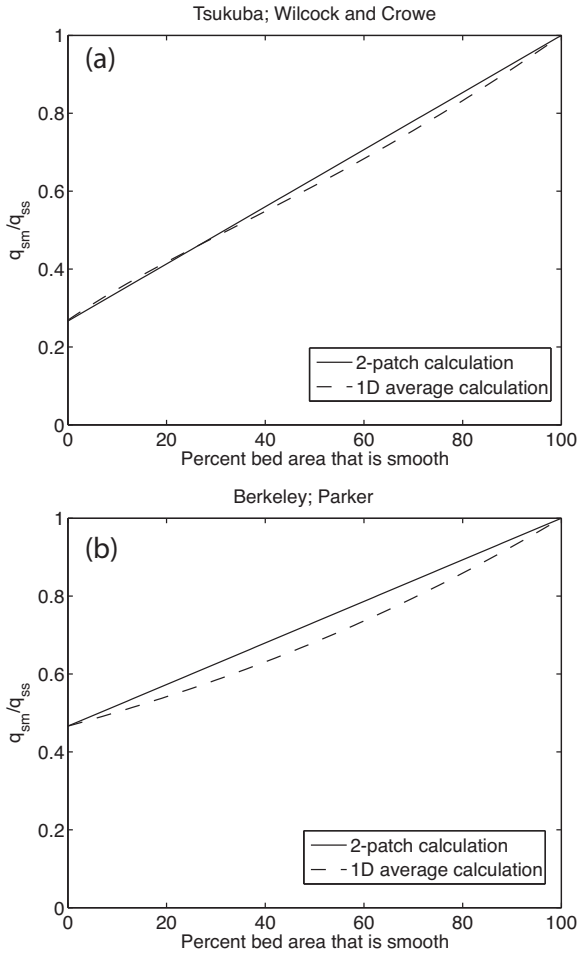

Figure 2.14: (a) Ratio of sediment flux calculated for a shear stress of 4.5 Pa using the *Wilcock and Crowe* [2003] algorithm for a channel composed of a combination of the Tsukuba "smooth" and "inactive" patch types (q_{sm}) (see Figure 2.2a for grain size distributions) to that calculated for a 100% "smooth" channel (q_{ss}). (b) shows the same information as (a), except it uses the *Parker* [1990] model to calculate sediment transport under 10 Pa shear stress on a bed that is a mixture of the Berkeley "smooth" and "inactive" patch types (see Figure 2.2b for grain size distributions).

2.5 Conclusions

Bed surface patches are a fundamental feature of channels with mixed-size sediment. In our experiments, even in the simplest possible case of a straight, low width-to-depth ratio channel with no bed topography subject to constant discharge, the bed became organized into patches of similar grain size and sorting. Freely migrating patches—bedload sheets—formed in both a bimodal sand-gravel mixture and a unimodal sand-free sediment mixture. The primary mechanism of formation and migration of these patches was grain-to-grain interaction via the catch-and-mobilize process, even in experiments using unimodal, sand-free sediment, which suggests that the ratio of grain diameters, rather than the presence of sand, determines a mobilization feedback. The passage of bedload sheets coincides with substantial increases in sediment flux, suggesting that the migration of free patches can be a primary cause of short-term fluctuations in sediment transport rate commonly observed in rivers and flumes.

Sediment supply controls the relative abundance of fixed and free patches and determines the scaling and dynamics of bedload sheets. In both of our experiments, reductions in sediment supply led to an expansion of coarse patches at the expense of finer ones and a narrowing of the corridor through which nearly all bedload transport occurred. Reduced sediment supply led to a decrease in sheet migration rate and an increase in the spacing between sheets. Complete elimination of sediment supply resulted in a nearly total loss of bed surface heterogeneity, a uniformly coarse bed and elimination of bedload sheets.

The 1D Parker (e-book, 2007) morphodynamic model calculated the surface grain size and slope so that it was able to predict the average sediment transport accurately (although short-term fluctuations associated with sheet migration were beyond its capability). Because of the nonlinear relationship between stress, grain size, and sediment transport, the magnitudes of the models over- or under-predictions of slope and grain size were not severe. The model performed best in low-supply conditions where bed surface patchiness was minimized.

Our experiments demonstrate that bed surface patchiness is tied to sediment supply, as patch abundance and the spatial extent of fine bed material increased with increasing supply. It remains challenging to apply 1D models to spatially variable beds using current transport equations. Calculations for our simple experimental conditions suggest that the use of areally-averaged surface grain size may produce reasonable transport predictions, although it is unclear whether averaging would work in a more complicated field scenario. Our experimental results support the idea that bed patchiness conveys information about the sediment supply in a system, and should be an important feature to document in sediment transport studies.

Notation

D	grain size [L].

D_{16}, D_{50}, D_{84}	grain size for which 16, 50, and 84 percent of the grain size distribution is finer, respectively [L].
D_g	geometric mean grain size [L].
dt	time step [T].
g	gravitational acceleration [L T^{-2}].
h	water depth [L].
H	bedform height [L].
I	intermittency [dimensionless].
L	bedform length [L].
Lr	reach length [L].
M	number of model segments [dimensionless].
n_a	active layer factor [dimensionless].
p	bedform period [T].
$q*$	ratio of sediment transport capacity for the surface to that for the subsurface or load [dimensionless].
$qbTf$	sediment feed rate [L^2 T^{-1}].
q_s	sediment flux per unit width [M L^{-1} T^{-1}].
q_{sm}	sediment transport calculated for a mixture of "smooth" and "inactive" or "congested" patch types [L^2 T^{-1}].
q_{ss}	sediment transport calculated for a 100% "smooth" bed [L^2 T^{-1}].
q_w	water discharge [L^2 T^{-1}].
$SfbI$	initial slope [dimensionless].
U	bedform migration rate [L T^{-1}].
ρ	water density [M L^{-3}].
σ	geometric standard deviation [dimensionless].
τ_b	boundary shear stress [M L^{-2} T^{-2}].

Chapter 3

Bed topography and the development of forced bed surface patches

3.1 Introduction

A striking characteristic of most rivers is the patchy nature of their beds. That is, the sediment mixture comprising the channel bed becomes sorted into areas of similar grain size, producing discrete patches of a mappable scale [e.g., *Bluck*, 1971; *Bridge and Jarvis*, 1976; *Forbes*, 1983; *Dietrich and Smith*, 1984; *Kinerson*, 1990; *Wolcott and Church*, 1991; *Lisle and Madej*, 1992; *Paola and Seal*, 1995; *Sambrook Smith and Ferguson*, 1995; *Crowder and Diplas*, 1997; *Buffington and Montgomery*, 1999a; *Dietrich et al.*, 2005; *Yarnell et al.*, 2006; *Nelson et al.*, 2009]. Field studies suggest that some patches remain in a fixed location for an extended period even after passing considerable bed load flux [*Dietrich et al.*, 2005] while others are able to migrate downstream as, for example, bed load sheets [*Whiting et al.*, 1988; *Nelson et al.*, 2009, and references therein]. This variety of patch types led *Nelson et al.* [2009] to classify end member patch types as "free" (downstream migrating sorting features), "fixed" (spatially persistent due to weak, grain scale, topographic controls and local coarsening), and "forced" (spatially persistent due to strong topographic controls such as bar morphology and channel obstructions).

Free patches can be difficult to observe because they occur during periods of high flow and active transport. Forced patches, however, are spatially persistent and observable at low flow, which some have suggested is diagnostic of high-transport conditions [e.g., *Andrews and Erman*, 1986; *Wilcock and DeTemple*, 2005; *Clayton and Pitlick*, 2008]. Forced patches oc-

This chapter has been published as: Nelson, P. A., W. E. Dietrich, and J. G. Venditti (2010), Bed topography and the development of forced bed surface patches, *Journal of Geophysical Research*, *115*, F04024, doi:10.1029/2010JF001747.

cur in virtually all channel morphologies. Strong, persistent sorting patterns are typical of river bends, in which inner point bars tend to be finer than outer pools, with the coarsest bed sediment shifting from the inside to the outside of the bend [*Bluck*, 1971; *Jackson*, 1975; *Bridge and Jarvis*, 1976, 1982; *Dietrich and Smith*, 1983, 1984; *Carson*, 1986; *Whiting and Dietrich*, 1991; *Laronne and Duncan*, 1992; *Whiting*, 1996; *Clayton and Pitlick*, 2008; *Clayton*, 2010]. Straight channels with riffle-pool sequences typically have coarse riffles and fine pools [*Gilbert*, 1914; *Leopold and Wolman*, 1960; *Keller*, 1971; *Lisle*, 1979; *Thompson et al.*, 1996, 1999; *Thompson and Hoffman*, 2001; *Milan et al.*, 2001; *Heritage and Milan*, 2004]. Alternate bars in straight reaches [*Mosley and Tindale*, 1985; *Lisle and Madej*, 1992; *Lisle and Hilton*, 1992; *Whiting*, 1996; *Lisle and Hilton*, 1999] and flumes [*Ikeda*, 1983; *Lisle et al.*, 1991, 1993] tend to have coarse bar tops and fine pools. In high-gradient streams, dynamic patches of fine material form in the wake zones of immobile accumulations of boulders or cobbles [*Garcia et al.*, 1999; *Laronne et al.*, 2000]. The size of these patches appears to be supply dependent, and sediment actively passes through them [*Yager*, 2006].

The development of persistent sorting patterns and forced patches should depend on a number of controlling factors, such as stage-dependent flow fields, channel morphology, including bed topography and planform shape, local sediment supply, the grain size distribution of available sediment, and channel obstructions. However, we still lack a quantitative description of mechanistic processes that explicitly connect these variables, particularly for gravel-bed channels where excess shear stress is low and the sediment is not fully mobile. *Parker and Klingeman* [1982] suggested that gravel beds are armored because equal mobility requires intrinsically less mobile coarse grains to be overrepresented on the bed surface. *Paola and Seal* [1995] proposed that in rivers that typically have spatially variable shear stress fields, bed patchiness arises in response to this spatial variability, creating equal mobility patches of different sizes that differentially pass finer sediment and lead to downstream fining. *Lisle and Hilton* [1999] attributed the coarse bars and fine pools they observed in their relatively straight study reaches to "downstream winnowing," where fine particles winnow out of coarse patches and are deposited somewhere downstream in a fine patch; this requires the coarse fraction to be at least temporarily immobile. Their observations of high shear stress in coarse zones and low stress in fine zones (at low flow) are consistent with this interpretation. Much of the riffle-pool literature [e.g., *Gilbert*, 1914; *Leopold and Wolman*, 1960; *Keller*, 1971; *Lisle*, 1979; *Thompson et al.*, 1996, 1999; *Thompson and Hoffman*, 2001; *Milan et al.*, 2001; *Heritage and Milan*, 2004; *Harrison and Keller*, 2007] suggests that in straight reaches with pools and riffles, a "velocity reversal," where the near bed velocity (and presumably, the boundary shear stress and sediment transport capacity) in the pool exceeds that of the riffle at high discharge but does not exceed it at low discharge, is responsible for the development of coarse riffles and fine pools. Building on this work, *MacWilliams et al.* [2006] suggested pool-riffle sequences are maintained through "flow convergence routing," in which the flow field downstream of a channel constriction converges in riffles at low flow and in pools at high flow, and *Sawyer et al.* [2010]'s field work indicated that this process occurs in large gravel bed rivers. *Lisle and Hilton* [1992] suggested that stage-dependent effects

were responsible for pools filling with sand, the depth of which can serve as a proxy for sediment supply. While these studies have shed light on mechanisms important for the development of forced bed surface patches, none present simultaneous, detailed measurements of stage-dependent flow fields, bed load transport fields, and surface grain size patterns to fully support an explanatory hypothesis.

Sediment supply has been shown to be a critical control on the surface structure of gravel-bed rivers. *Dietrich et al.* [1989] suggested that armoring is largely a result of insufficient sediment supply, and *Nelson et al.* [2009]'s reanalysis of their data and new gravel-only data showed that reductions in sediment supply lead to an expansion of coarse fixed patches, and they found sediment supply to be a primary control on the dynamics and occurrence of free patches. *Lisle et al.* [1991, 1993] also observed that in a flume with bar topography, reducing the sediment supply led to changes in bed surface sorting and emergence of bars. *Kinerson* [1990]'s study of several field sites in northern California suggested that bed surface patchiness is correlated with sediment supply, and *Yarnell et al.* [2006]'s analysis of field and flume studies found that streams with intermediate relative sediment supply values exhibited the greatest habitat heterogeneity (corresponding to bed surface patchiness). *Buffington and Montgomery* [1999c]'s analysis of several flume studies found that the median grain size of the bed surface varied inversely with sediment supply. Hydraulic roughness elements like bank irregularities and large woody debris also can cause the bed surface to become finer than it otherwise would be in their absence [*Buffington and Montgomery*, 1999b].

Planform geometry and cross-channel bed topography interact with the flow and sediment transport fields to produce bed sorting and forced patches. Early models for sorting in channel bends [*Kikkawa et al.*, 1976; *Bridge*, 1977; *Allen*, 1978] assumed that equilibrium channel conditions occur when the local cross-stream effect of particle weight is exactly balanced by drag from secondary circulations. Consequently, these models predict that particles will travel along lines of equal depth such that there is no net cross-stream transport, and the resulting bed surface will exhibit coarse particles in deep water where the inward component of shear stress is greatest and the outward slope is the highest, and the bed will be fine in shallow water where the inward shear and cross-stream slope are lowest. *Parker and Andrews* [1985] developed a model combining a simple representation of flow processes in a bend with the assumption that sorting is solely a result of the cross-stream bed slope, arriving at an analytical solution that predicts coarse sediment follows a path from the inside bank to the outside bank of a bend apex. This model was later incorporated into computer simulations of channel migration [*Sun et al.*, 2001a,b]. In contrast with earlier models, *Dietrich and Smith* [1984], *Dietrich* [1987], and *Dietrich and Whiting* [1989] built upon detailed field measurements of flow and sediment transport to develop a hypothesis that in fully mobile beds, equilibrium occurs when shear stress divergence is balanced by sediment transport divergence. Their observations indicated that shoaling of the flow over the point bar as the shear stress declines forces all sediment toward the pool, but counteracting secondary flows (and effects of currents along oblique dune fronts) preferentially transport finer sediment inward. Net transport of sediment toward the pool matches increasing boundary shear

stress, but the finer sediment is shifted toward the inside bank due to differential transport by inward-directed secondary flows [*Parker and Andrews*, 1985; *Ikeda*, 1989; *Bridge*, 1992]. While these mechanisms have explained observations in sand-bedded channels, it is not clear whether the same reasoning could be used to predict sorting in gravel-bed rivers.

It is tempting to hypothesize that channels locally maintain "threshold" conditions, in which the bed surface locally maintains a grain size distribution (or median grain size) that is just able to be mobilized during a characteristic flood. A standard parameter for grain mobilization is the Shields stress, τ^*,

$$\tau^* = \frac{\tau}{(\rho_s - \rho)gD} \tag{3.1}$$

which attains a critical value τ_c^* at initial motion. Here, τ is the boundary shear stress, ρ_s is the density of the sediment, ρ is the density of water, g is the gravitational constant, and D is the particle diameter. If threshold conditions are achieved and τ_c^* is a constant for all grain sizes, spatial variations in boundary shear stress would be linearly reflected in the surface grain size distribution [*Lisle et al.*, 2000]. This assumption is used to design channels [*Lane*, 1955] and can be used on a watershed scale to make predictions about what the reach-averaged median grain size would be in the absence of external roughness or sediment supply effects [e.g., *Power et al.*, 1998; *Buffington et al.*, 2004]. However, threshold conditions are unlikely to be the norm, as suggested by *Lisle et al.* [2000]'s study where, at several natural channels, they measured bed topography, mapped the surface grain size distribution, and modeled the bed shear stress at bankfull discharge, ultimately finding no correlation between local shear stress and bed grain size. Alternatively, *Dietrich* [1987] and *Dietrich and Whiting* [1989] argued that in gravel bedded meanders with low excess boundary shear stress and low sediment supply, shear stress divergences might be balanced by divergences in sediment transport achieved primarily though bed grain size adjustment rather than erosion or deposition. In this case, bed surface patchiness develops to moderate local bed mobility such that the divergences of stress and sediment flux are in balance. The predictive capability of this hypothesis has yet to be verified due to a limited number of well developed quantitative linkages between topographically-controlled stress fields, the sediment transport field, and the bed surface grain size distribution.

Here we attempt to improve our empirical understanding of these linkages using observations collected during a near field scale flume experiment. We use detailed measurements of the bed surface topography, grain size, and the flow and sediment transport fields over a gravel bed of quasi-steady alternate bars that produced persistent topography and forced patches. Our observations suggest that topographically-forced boundary shear stress divergences are matched by size-selective sediment transport divergences. The resultant changes in local sediment supply are accommodated by local changes in bed surface grain size, forcing the development of patches that allow the maintenance of quasi-steady morphology.

Table 3.1: Hydraulic parameters

Parameter	Value
Discharge [m^3/s]	0.4 ± 0.02
Bed and water surface slope	0.013
Mean depth [cm]	13.5
Width/depth	20
Shear stress [Pa]	17.2
τ^*/τ_c^*	2

3.2 Methods

The observations presented in this paper were collected during a flume experiment conducted in the main channel at St. Anthony Falls Laboratory (SAFL) at the University of Minnesota in Minneapolis, MN. The experiment was part of the larger "StreamLab06" suite of experiments designed to examine the interactions between geomorphology, nutrient cycling, and biomass accumulation. The large scale of the flume enabled us to make local measurements of the bed surface, flow field, and sediment transport field over a bar sequence.

3.2.1 Flume Set Up and Experimental Procedure

The main channel at SAFL is a 2.75 m wide, 80 m long (with a 55 m long test section) rectangular cross-section concrete research channel that has recently been refurbished and reinstrumented. Initially, a homogeneous, flat bed was created by filling the flume with a gravel mixture composed of grains 2-45 mm in diameter with a median grain diameter of 11 mm (Figure 3.1a). Water discharge was held constant throughout the experiment at 400 ± 20 l/s.

Sediment was recirculated throughout the experiment. Bed load exiting the flume was collected in five side-by-side sediment traps which in total spanned the flume width. Each sediment trap was connected to a load cell, which sampled sediment discharge continuously in 1 s intervals. An impeller pump in the floor pit where the sediment traps were located would then return the sediment to the head of the flume [see *Marr et al.*, 2010, for more information on the flume facilities and operation].

Prior theoretical [*Blondeaux and Seminara*, 1985; *Colombini et al.*, 1987; *Lanzoni and Tubino*, 1999] and experimental [e.g., *Lanzoni*, 2000a] work on alternate bars suggests that bar development requires a large width-to-depth ratio and full sediment mobility. *Wilcock and McArdell* [1993] suggested that in a sediment mixture of a grain size range similar to ours, full mobility of all grain sizes occurs when the Shields stress (Equation 3.1) is approximately twice the critical Shields number (assumed to equal 0.045). Considering these suggestions, we chose a design bed slope (0.013) and discharge (0.4 ± 0.02 m^3/s) that resulted in a width-to-depth ratio of 20 and a dimensionless shear stress ratio (τ^*/τ_c^*) of about 2 (see

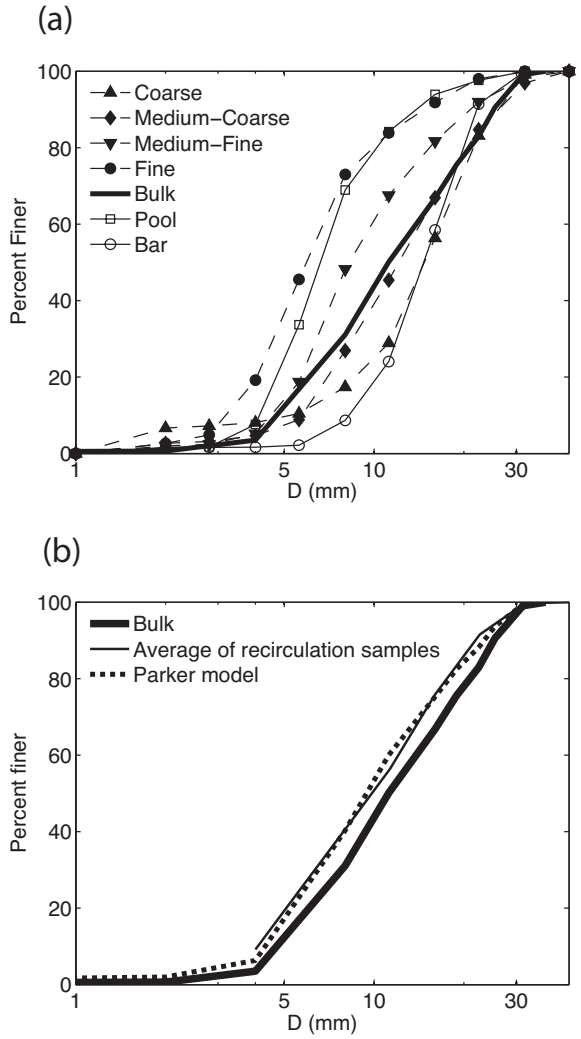

Figure 3.1: (a) Grain size distributions of the bulk sediment mixture, the four mapped patch types, and the bar and pool. (b) Grain size distributions for the bulk sediment mixture used to make the initial bed (thick line) and the average grain size distribution of the recirculation samples (thin line). The dashed line shows the grain size distribution of the bed load predicted by the *Parker* [1990] bed load transport algorithm, using the flume-average shear stress (Table 3.1) and bulk sediment grain size distribution for the bed surface.

Table 3.1 for a summary of the hydraulic conditions during the experiment). Although most gravel bed rivers have slopes smaller than 0.013 [*Parker et al.*, 2007], the width of our flume necessitated a rather steep slope to simultaneously achieve the desired excess stress and large width-to-depth ratio necessary for bar formation. Details regarding the measurement of shear stress are presented in section 3.2.5. To further enhance the development of alternate bars, we constricted the flow at the flume entrance to 2/3 of the channel width, creating a flow perturbation at the inlet that allowed bars to form freely downstream.

We ran the flume with constant discharge and sediment recirculation until the bed topography and bed load flux exiting the channel reached approximately steady-state conditions. The water surface elevation was monitored using an ultrasonic water level sensor that traversed the flume on a mechanized cart that ran along rails above the flume walls. The water surface elevation was repeatedly measured along five longitudinal profiles spaced 500 mm apart in the cross-stream direction with the center transect located along the center of the flume. Measurements in the along-channel direction were obtained at 5 mm intervals. The mechanized cart was also equipped with an acoustic echo sounder that could measure bed surface elevation subaqueously; however, as bed topography developed, the flow became too shallow in some places for this instrument to function, so we relied upon dry-bed topographic scans (described in Section 3.2.3) to obtain bed surface elevation data.

3.2.2 Flow and Sediment Transport Measurements over a Bar Sequence

After the flume developed about a quasi-steady state topography consisting of about 1.5 alternate bar sequences, we made a series of local near-bed velocity, bed surface grain size, and sediment transport measurements over a bar sequence. We made measurements at eleven cross sections, spaced every three meters from $x = 14.5$ m to $x = 44.5$ m (we use x and y as downstream and cross-stream coordinates, respectively), with five points in each cross section spaced 50-60 cm apart (Figure 3.2a). At each point, we used a Pygmy current meter to measure the local velocity 3 cm above the bed. A Pygmy meter was chosen because initial attempts to measure the velocity with an acoustic doppler anemometer (ADV) produced unreliable results. Velocity measurements were taken for an average of 55-60 s [*USBR*, 2001]. Care was taken to ensure the Pygmy meter was oriented orthogonal to the flow, the direction of which was estimated visually with the aid of a string tied to the measurement rod. Although Pygmy meters generally are accurate to better than 3.5 per cent when used between about 6 and 30 cm above the bed, they may suffer from additional errors when placed closer to the bed [*Hubbard*, 1988]; therefore, in the following analysis we assume a 10 per cent uncertainty in measured near-bed velocity. After each velocity measurement, a photograph of the bed was taken with a digital camera placed in a waterproof housing that was attached to a pole. A scale bar was attached to the pole such that it typically appeared along the top of the underwater photographs, which generally covered an area of 7.1 cm by

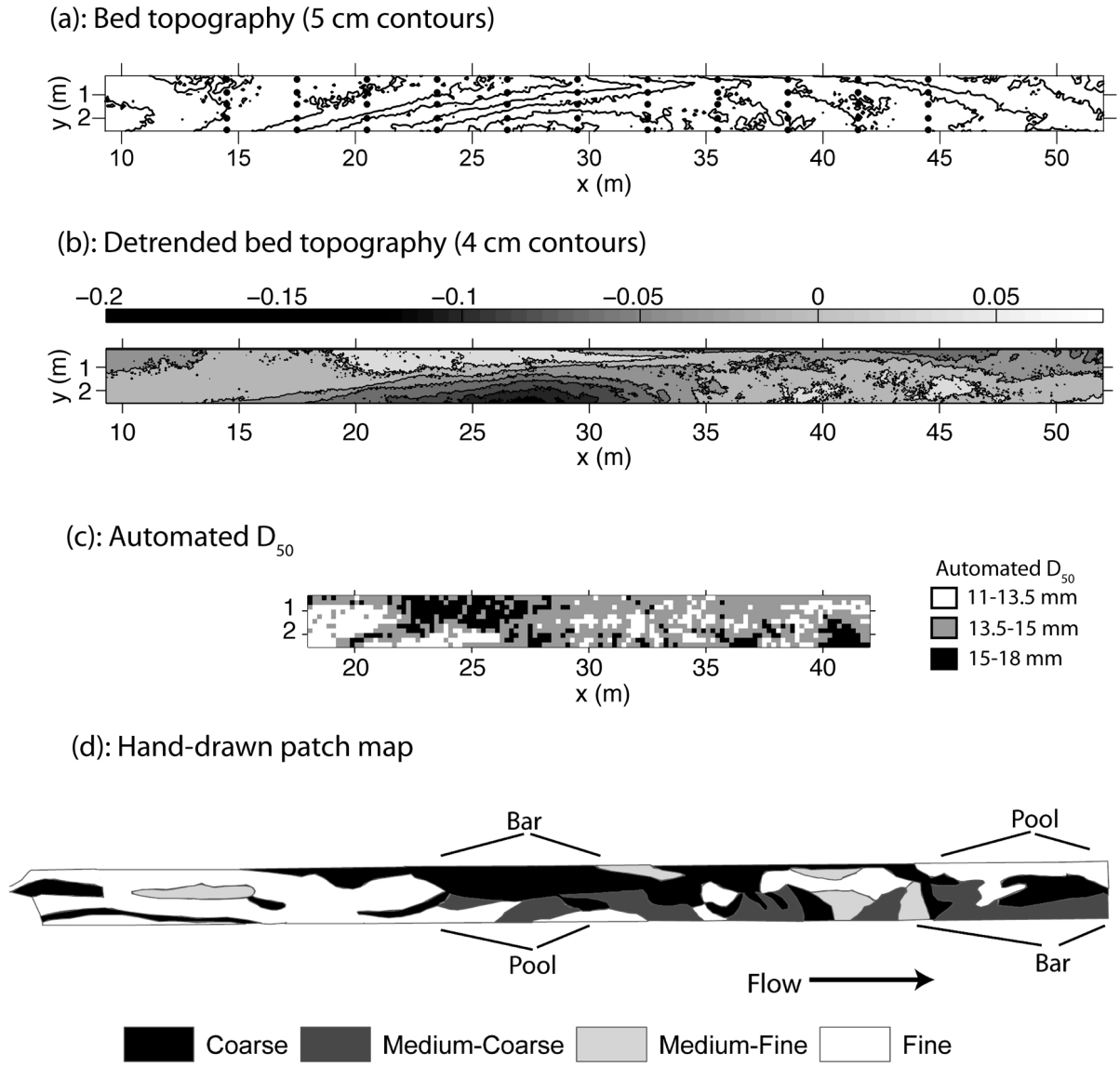

Figure 3.2: (a) Contour map of the quasi-equilibrium bed topography, generated from the 10×10 mm DEM. Flow is from left to right. The dots indicate the locations of velocity and bed load transport measurements at the 11 cross sections. (b) Contour map of the bed topography after subtracting the mean channel slope ($S = 0.013$); dark areas are low (pools) and light areas are high (bar tops). The grayscale bar intervals are shown in units of meters. (c) Map of the local median grain size D_{50} on a 20×20 cm grid, extracted from the 1×1 mm DEM using the automated grain size procedure; darker shading indicates a coarser surface. (d) Hand-drawn patch map. Approximate bar and pool locations are identified. The grain size distribution of each patch type is shown in Figure 3.1a. Each map has the same scale.

5.3 cm. After the experiment, these photographs were analyzed in the lab to characterize the local bed grain size at the time of the velocity measurement. The *b*-axis of each grain (as visible in the photographs - see *Bunte and Abt* [2001] or *Graham et al.* [2010] for a discussion of the possible effects of grain shape and imbrication on grain size distributions derived from photographs) was digitized by hand and the resulting area-by-number grain size distributions were converted to volume-by-weight distributions with the *Kellerhals and Bray* [1971] voidless cube model. Finally, in addition to the local velocity measurements and bed photographs, we measured the local bed load transport at each point on the grid by holding a miniature Helley-Smith-type of sediment sampler (similar to the traps used in *Dietrich and Smith* [1984]), which had a square opening with 5 cm sides and a nylon mesh bag attached to the downstream end to collect the sediment. The sampler was pointed directly upstream, and samples were taken for 60 s, although in some high-transport locations samples were shorter because the bag became filled with sediment. Each sediment sample was bagged, dried, and sieved. Although the bed surface topography appeared to be unchanging, we worked quickly and completed all of the local velocity and bed load transport measurements in under five hours.

3.2.3 Bed Topography Measurements and Bed Surface Patchiness Characterization

After all of the measurements taken while the flume was running were completed, the flume was rapidly drained, preserving the bed state as it existed at the end of the experiment. Bed surface patches were mapped by hand, wherein the bed was classified (by eye) into patches of similar grain size and sorting [e.g., *Nelson et al.*, 2009]. Four patch types were defined: fine (median grain size D_{50} of 5.9 mm, geometric standard deviation σ of 1.79), medium-fine (D_{50} = 8.3 mm, σ = 1.84), medium-coarse (D_{50} = 12.1 mm, σ = 1.92), and coarse (D_{50} = 14.7 mm, σ = 2.11). Figure 3.1a presents the volume-by-weight grain size distributions of these patch types. Eight bed surface samples were collected throughout the StreamLab06 experiments, in which 30×30 cm areas of the bed were painted and all painted particles were collected and sieved. The *Kellerhals and Bray* [1971] method was then used to convert the area-by-weight grain size distributions to the volume-by-weight distributions commonly used in empirical bed load transport formulas. The painted areas were located so that they fell entirely within a particular patch on the hand-drawn map and so that all mapped facies types were represented by physical samples. The samples were averaged to obtain characteristic grain size distributions for each patch type.

In addition to the patch maps, the quasi-equilibrium dry bed surface was characterized with a high-resolution 1×1 mm topographic scan generated by a range-finding laser attached to the motorized cart that traversed the bed. The 1×1 mm digital elevation model (DEM) covered a 24 m swath of the flume, from x = 18 m to x = 42 m. A coarser, 10×10 mm DEM was also generated, covering essentially the entire flume test section from x = 9 m to

$x = 55$ m. A digital camera was also attached to the cart and a sequence of photographs of this larger region of the bed were taken.

3.2.4 Automated bed surface grain size measurements

We also characterized the spatial variability of the bed surface grain size distribution through an automated image analysis procedure. Following the methodology of *Graham et al.* [2005a,b], we used a shaded relief map generated from the 1×1 mm digital elevation model created from the high-resolution laser scan as an input image for automated grain extraction (similar to *McEwan et al.* [2000]). Although the resolution (on a pixels per millimeter basis) of the 1×1 mm DEM was not as high as the resolution of the bed photographs taken from the cart, we found the DEM provided more reliable results than the photographs; that is, the resultant grain size distributions better matched those from surface samples, because the DEM image displayed stronger contrast between grains, the variability within grains due to lithology was eliminated, spatial registration was exact, and there were no perspective issues to correct. Grain size statistics for the portion of the flume covered by the 1×1 mm DEM were calculated on a 20×20 cm grid in the following manner: A 30×30 cm window was centered at each grid point and the hillshade image was cropped to that window size. The *Graham et al.* [2005a] method was then applied to the 30×30 cm neighborhood and the local D_{50} was calculated from its output. While the reader should refer to *Graham et al.* [2005a] for a complete description of their method, a summary of the technique and the parameters we used is described below.

The *Graham et al.* [2005a] method essentially uses pixel intensity to delineate individual sediment grains. It does this by dividing the image into regions, where each region represents a single grain. Because grain boundaries tend to be darker than the grains themselves, the method uses the intensity to detect grain edges. Initially, a median filter is applied to the image (in our case, the 30×30 cm crop of the hillshade DEM) to help blur out image noise and grain imperfections. A morphological bottom-hat filter using a disk structuring element is then applied to the image to enhance the contrast. A double-threshold method is then used to determine which pixels are likely grain edges. Here, two threshold intensities are selected; one threshold corresponding to very dark pixels (which almost certainly are grain edges) and a second, lower threshold corresponding to somewhat dark pixels that are potentially grain edges. Features in the lower threshold image that overlap those in the higher threshold image are then classified as edges. The resulting binary image is then divided into regions using the watershed segmentation algorithm [*Vincent and Soille*, 1991]. Because the watershed segmentation can often produce oversegmented images, *Graham et al.* [2005a] perform an *h-minima* transform to suppress small pits prior to the application of the watershed algorithm. Figure 3.3 shows an example portion of our hillshade DEM at various stages in the grain identification process.

Once the grains have been identified as regions, an ellipse is fit to each region and the minor axis of the ellipse is measured (in pixels). *Graham et al.* [2005a] found this technique

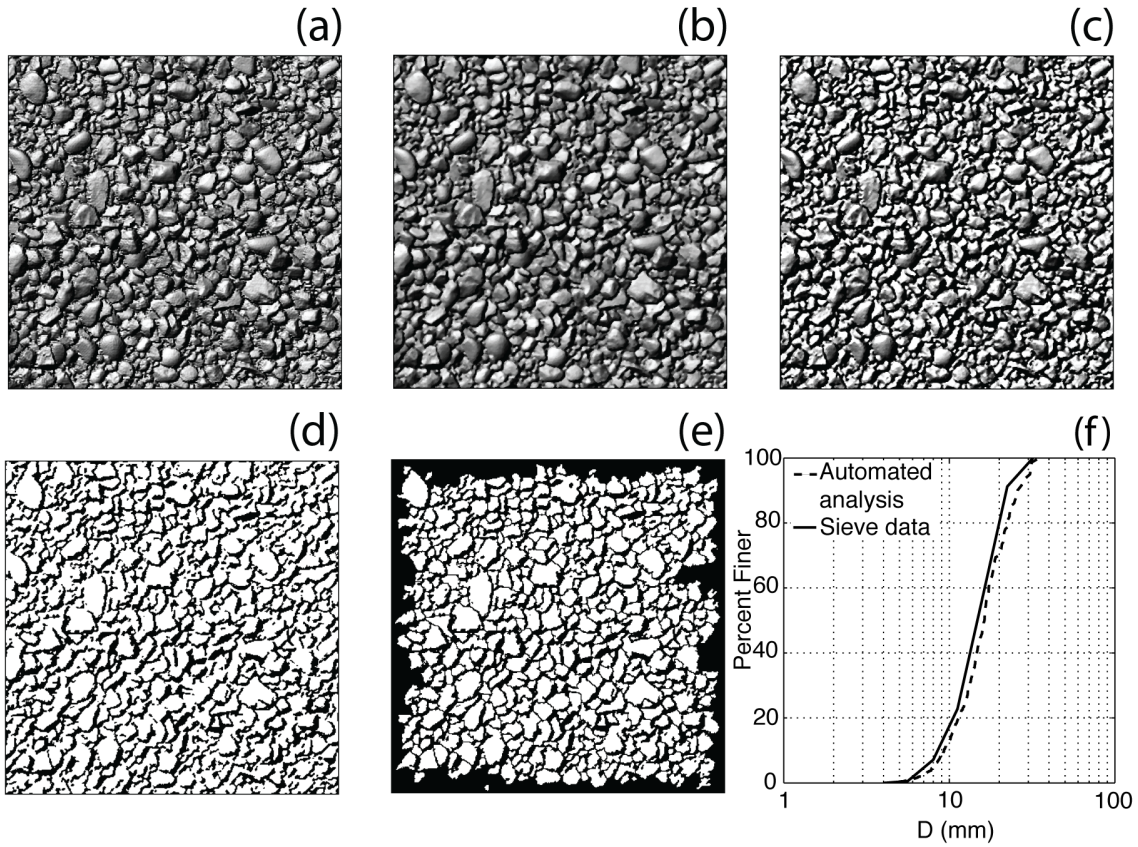

Figure 3.3: Example of steps performed in the automated image analysis, on a 30×30 cm square of the bed from which a surface sample was taken. (a) is the original grayscale image of the 1×1 mm hillshade DEM; (b) is the image after application of a median filter; (c) is after the morphological bottom-hat filter is applied; (d) is after the double-thresholding procedure; (e) is the final segmented image, after application of the *h-minima* transform and the watershed algorithm; (f) compares the volume-by-weight cumulative grain size distributions from the automated analysis and from sieving the surface sample.

Table 3.2: Parameters used in the automated grain size analysis.

Parameter	Value
Median filter size	3 pixels
Structuring element disk radius	5 pixels
Low threshold	1%
High threshold	35%
h-minima threshold	1 pixel

gives a reasonably accurate estimate of the true *b*-axis of each grain. The resulting list of grain diameters is then converted to mm using the known image scale (in our case, 1 pixel = 1 mm), and grain size distributions are generated. Importantly, the grain size distributions must be concatenated at an appropriate level to avoid spurious measurement of image noise [*Graham et al.*, 2005a,b,c]. We concatenated our grain estimated grain size distributions at 4 mm because our experiment involved only gravel and since visual observation (and comparison with surface samples) suggested that the automated results were reasonable to that level.

We found that the *h-minima* transform had positive or negative consequences on the accuracy of the algorithm depending on the type of surface being analyzed. Without the *h-minima* transform, coarse surfaces (such as the one displayed in Figure 3.3a) would be oversegmented by the watershed algorithm, and inclusion of a 1 pixel *h-minima* transform improved the accuracy considerably (e.g. Figure 3.3f). However, finer bed surfaces were better characterized without the *h-minima* transform, since the watershed algorithm tended not to oversegment in these cases. While the importance of the *h-minima* transform is likely related to the 1 mm/pixel scale of our DEM, it does mean that the use of a single *h-minima* parameter for analysis of the entire DEM will produce either too-fine distributions for coarse areas (if *h-minima* = 0) or too-coarse distributions for fine areas (if *h-minima* = 1). Nevertheless, the overall pattern of sorting is essentially the same either way, so for the remainder of this paper, grain size data generated from the automated procedure are presented with *h-minima* = 1. Table 3.2 shows the parameters we used in the image analysis algorithm.

3.2.5 Shear Stress Calculations

Local boundary shear stress was estimated in two ways. First we used the single velocity method described by *Dietrich and Whiting* [1989], in which shear stress is estimated from a single measurement of the near bed velocity. The law of the wall describes the vertical profile of downstream velocity near the boundary:

$$u(z) = \frac{u_*}{\kappa} \ln\left(\frac{z}{z_0}\right) \tag{3.2}$$

where $u(z)$ is the velocity at height z above the bed, z_0 is the roughness height, κ is von Karman's constant ($\kappa = 0.4$), and u_* is the shear velocity, which is defined as

$$u_* \equiv \sqrt{\tau/\rho} \tag{3.3}$$

Here, τ is the boundary shear stress and ρ is the fluid density. Using the law of the wall, the boundary shear stress can be estimated from a single velocity measurement $u(z)$ as

$$\tau = \rho \left[\frac{u(z)\kappa}{\ln(z/z_0)} \right]^2 \tag{3.4}$$

The roughness height, z_0, is commonly parameterized to scale with the coarse grains on the bed; for instance:

$$z_0 = AD_{84} \tag{3.5}$$

Here, D_{84} is the grain size for which 84% of the grains on the bed surface are finer. Following *Leopold and Wolman* [1957], *Dietrich and Whiting* [1989] suggested $A = 0.1$ is a reasonable scaling factor, which we use here. *Wilcock* [1996] found that the single velocity method for estimating u_* was accurate to within about 7%, using a roughness height of $z_0 = 0.095D_{90}$, which is essentially equal to $z_0 = 0.1D_{84}$ used here and $z_0 = 0.09D_{84}$, found by *Wiberg and Smith* [1991]. Using this formulation, we estimated the local shear stress on our grid of velocity measurements using the measured velocity at $z = 3$ cm above the bed, with a D_{84} estimated from the grain size distributions derived from the underwater photographs.

Despite its simplicity, the single-velocity method has been shown to produce more reasonable and reliable estimates of boundary shear stress than other more complicated techniques. *Whiting and Dietrich* [1990] found that the single-velocity method outperformed a method using the slope of the velocity profile because the latter method projected well into the flow and included large scale drag, causing the boundary shear stress to be overestimated. They also pointed out that the near-bed velocity measurement can avoid upstream influences of features such as dunes or bank irregularities, suggesting that instead this method captures primarily the effects of local grain roughness essential to sediment transport. The usefulness of incorporating the local grain size into stress calculations has more recently been confirmed by *Sime et al.* [2007], who found that an unconstrained velocity gradient estimate of shear stress leads to greater error than a grain-size constrained profile. The single-velocity method relies upon the assumption of a logarithmic near-bed velocity profile, which may not occur in areas of high relative roughness ($h/D_{84} >\sim 5$) [*Wiberg and Smith*, 1991; *Bathurst*, 2002; *Katul et al.*, 2002]. Since our flume developed shallow flow over coarse bar tops, the velocity profile there may differ from logarithmic and thus the single-velocity method may over- or under-estimate the local boundary shear stress, but in the absence of velocity profiles over the bar top we proceed with the assumption of a logarithmic profile.

The discrete spacing of velocity measurements, and the lack of data on velocity (and boundary shear stress) direction, suggests that an additional method of modeling the entire

boundary shear stress field, constrained by measurements, is in order. We used a quasi-three-dimensional hydrodynamic model, FaSTMECH (Flow and Sediment Transport and Morphological Evolution of CHannels, available online at http://wwwbrr.cr.usgs.gov/gstl/project-MDSWMS.html), which was developed by the U.S. Geological Survey and has been described in a number of studies [e.g, *Lisle et al.*, 2000; *Kinzel et al.*, 2009]. For a full description of the model, the reader is directed to *Nelson and McDonald* [1995] and the USGS online documentation, but, in summary, the model solves the full vertically-averaged and Reynolds-averaged momentum equations and it incorporates a vertical-structure submodel that computes the vertical velocity profile along the streamlines of the vertically-averaged flow and the secondary flow across those streamlines. The vertically-averaged equations are cast in a channel-fitted coordinate system and are derived and presented in *Nelson and Smith* [1989a]. In its computation of the depth-averaged solution, the model assumes steady, hydrostatic flow and models turbulence with an isotropic eddy viscosity. The vertical submodel takes the solution to the depth-averaged model and an assumed eddy viscosity structure [*Rattray and Mitsuda*, 1974] to calculate the three-dimensional solution. While a fully three-dimensional model might be capable of calculating more reliable estimates of boundary shear stress than a two-dimensional model like FaSTMECH, three-dimensional models inherently require detailed measurements of the three-dimensional flow field for calibration and are highly sensitive to the method of specifying topographic complexity [*Lane et al.*, 1999]. Given the difficulty we encountered in measuring the 3-D velocity field with an ADV (Section 3.2.2), the 2-D modeling capabilities of FaSTMECH are appropriate for this exercise.

The momentum equations are solved over a curvilinear orthogonal finite difference grid, constructed in the graphical user interface MD_SWMS (Multi-Dimensional Surface Water Modeling System) with which FaSTMECH is distributed [*McDonald et al.*, 2005]. The Cartesian grid we used to model the SAFL flume had 8 cm node spacing in both the x and y directions. Elevation data from the 10×10 mm DEM were interpolated onto the grid points.

We provided the model a constant discharge upstream boundary condition of 0.4 m^3/s, and we specified a constant downstream water surface elevation and a constant lateral eddy viscosity of 0.0019 m^2/s. We used spatially-variable roughness in which the drag coefficient C_d was estimated to be a function of the flow depth computed from constant roughness conditions and the local D_{84} estimated from the automated image analysis [e.g., *Nelson et al.*, 2003]. We calibrated the roughness by matching the model-predicted water surface elevation to the five longitudinal water surface profiles collected by the ultrasonic water level sensor during the experiment, and by comparing the model-predicted flow velocity 3 cm above the bed to the pygmy meter velocity measurements; the C_d parameter ranged from 0.0034 to 0.0142. The calculated shear stress field was similar to one calculated with a constant roughness with $C_d = 0.009$, but the variable roughness solution did a better job matching our near-bed velocity measurements. After calibration, the root-mean-square error in our calculated water surface elevation was 0.0146 m and the root-mean-square error between the calculated and measured near-bed velocities was 0.11 m/s. The model's convergence (the per cent deviation between the predicted discharge at a grid cross section and the specified

discharge) was between ±0.07 per cent.

The single-velocity method provides a useful check on the FaSTMECH output. However, because the model provides a continuous estimate of the entire stress field, including the magnitude and direction of the local stress vectors, we focus on and use those estimates throughout our subsequent analysis.

3.3 Observations

3.3.1 Bed Surface Topography and Sorting

Alternate bars began to form shortly after the experiment began and they immediately started to migrate downstream; however, their rate of migration slowed as the bar amplitude became more pronounced and after about 13 hours the bars appeared visually to have stopped migrating. Repeat scans of the water surface indicated that there was little to no change in the water surface (Figure 3.4b), which corroborated the visual observations that a quasi-steady-state condition had developed.

The establishment of quasi-steady conditions was further verified through analysis of the sediment flux exiting the downstream end of the flume (Figure 3.4a). For 15 hours leading up to the bed load and velocity measurements and the 5 hours during which the measurements were taken, the total bed load flux collected in the downstream weigh pans generally ranged from about 0.5 to 2.5 kg/s with occasional deviations from 0.0 to 3.0 kg/s (Figure 3.4a). In spite of this variability, which is an inherent feature of sediment transport [e.g., *Pitlick*, 1988; *Nelson et al.*, 2009; *Singh et al.*, 2009], a linear regression of the time series has a slope of 10^{-5} kg/s/hr, indicating that quasi-steady conditions persisted throughout this period. The four sediment recirculation samples taken during this time (Figure 3.4a) had very similar grain size distributions, the average of which is presented in Figure 3.1b. All grain sizes from the bulk sample were present in the recirculation samples. Interestingly, if the *Parker* [1990] surface-based bed load transport algorithm is provided with the flume-averaged boundary shear stress ($\tau = 17.2$ Pa) and the bulk sediment grain size distribution to characterize the surface, the algorithm calculates a bed load grain size distribution virtually identical to our averaged recirculation samples (Figure 3.1b), suggesting that the *Parker* [1990] algorithm is well-suited for modeling our experiment.

The quasi-steady state bed developed about 1.5 complete bar-pool sequences. Bar heads were located at approximately $x = 11$ m, $x = 35$ m, and $x = 55$ m (Figures 3.2a and 3.2b), indicating a bar wavelength of about 44 m. The furthest upstream bar's location was forced by the placement of sandbags at the flume entrance, and the furthest downstream bar was almost completely developed before reaching the flume outlet. The bar tops were about 25 cm higher than the adjacent pools (Figure 3.2a). By the time we began to make velocity and sediment transport measurements, the bed configuration was essentially unchanging.

In general, the bed surface on bar tops was coarse, and the bed surface in pools was fine

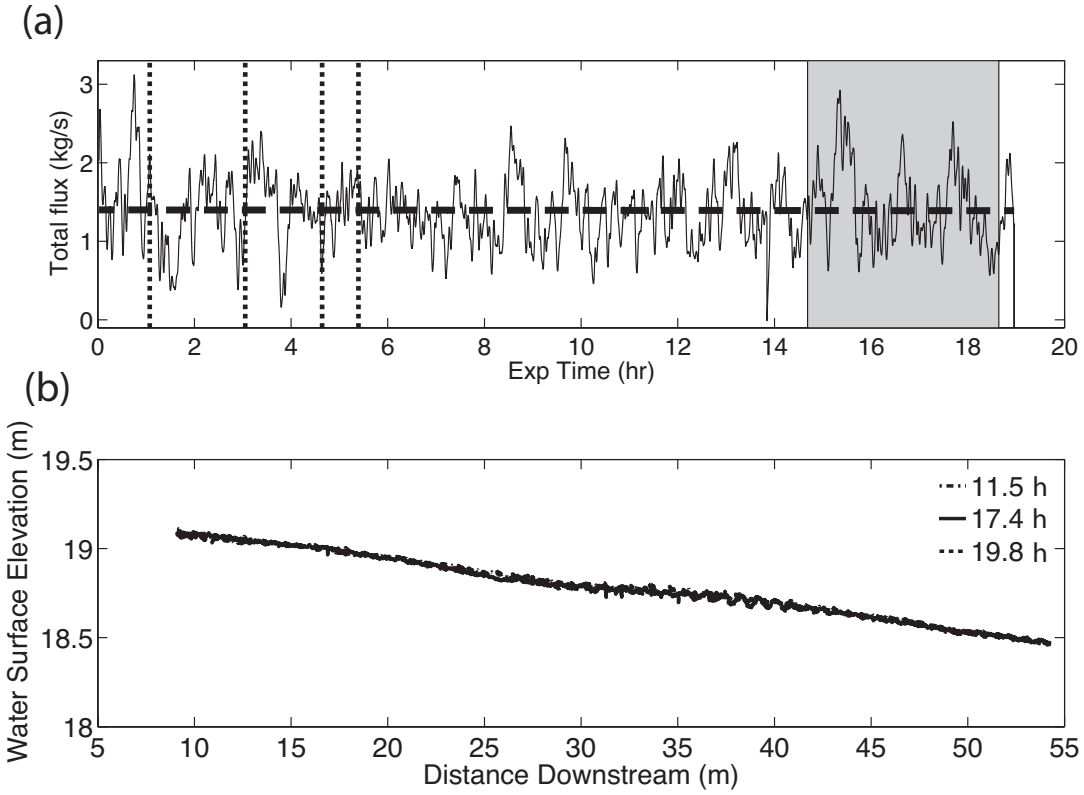

Figure 3.4: (a) Time series of total sediment flux exiting the flume captured by the weigh pans. The dashed horizontal line is a best-fit linear regression to the time series data (slope $\approx 10^{-5}$ kg/s/hr), the four vertical dashed lines indicate collection times for sediment recirculation samples in Figure 3.1b, and the shaded gray region represents the period over which bed load and velocity measurements were taken. (b) Three water surface scans taken along the channel centerline before and after velocity and bed load transport measurements were started. The time of each profile, corresponding to the horizontal axis in (a), is shown in the legend. The substantial overlap of the profiles, along with visual observations of the bed, suggests quasi-steady state conditions.

Table 3.3: Number of cells from the automated grain size analysis (Figure 3.2c) located in each patch class on the hand-drawn patch map (Figure 3.2d).

Automated D_{50}	Coarse	Medium-Coarse	Medium-Fine	Fine
15 - 18 mm	215	58	13	19
13.5 - 15 mm	359	149	62	161
11 - 13.5 mm	65	79	16	230

(Figures 3.2c and 3.2d). Surface samples of the bar top and pool (Figure 3.1a) indicate that the D_{50} of the bar top was 14.6 mm and the D_{50} of the pool was 6.6 mm. The hand-drawn patch map (Figure 3.2d) shows that while there is some local variability in grain size pattern, this general pattern of coarse bars and fine pools predominated in our system.

The map of median grain size generated from the automated image analysis (Figure 3.2c) shows essentially the same pattern as the hand-drawn patch map. This internal consistency is encouraging as it suggests that both methods are effectively capturing the overall sorting structure that developed on the bed. The estimated D_{50} of the bar tops from the automated procedure is generally around 14 - 18 mm, which is consistent with the sieved surface sample. The automated procedure overestimates the D_{50} of the pools to be around 11 - 13 mm, probably due to the inclusion of the *h-minima* threshold everywhere (as discussed in Section 3.2.4). Table 3.3 shows the number of cells from each class of the automated image analysis that are co-located in each class of the hand-drawn patch map, indicating that in general there is good agreement between the two methods. The overall pattern of coarse bars and fine pools prevails regardless of the method used to assess it.

The sorting maps in Figures 3.2c and 3.2d are useful for visualizing the overall sorting patterns on the flume bed, but in reality the transition from one patch to another may not be as sharp as the boundaries on the maps suggest. Figure 3.5 illustrates in detail how the automated image analysis map and the 1×1 mm DEM compare with each other. In general, a visual assessment shows that areas of the bed that are obviously coarse or fine are placed in the appropriate patch category, although the precise location of the boundary depends upon the details of the classification method (in this case, the value of the automated D_{50} at the transition between classes). So, the discrete boundaries in Figures 3.2c and 3.2d might more accurately be thought of as fuzzy boundaries rather than sharp transitions from one patch to another. Research into more sophisticated characterization of objective bed surface patch delineation is ongoing.

3.3.2 Flow Field

The model-predicted stress field is spatially heterogeneous (Figure 3.6a). The zone of maximum shear stress shifts from the left side of the channel (looking downstream) at the upstream end of the flume toward the right side of the flume by about $x = 25$ m. The large

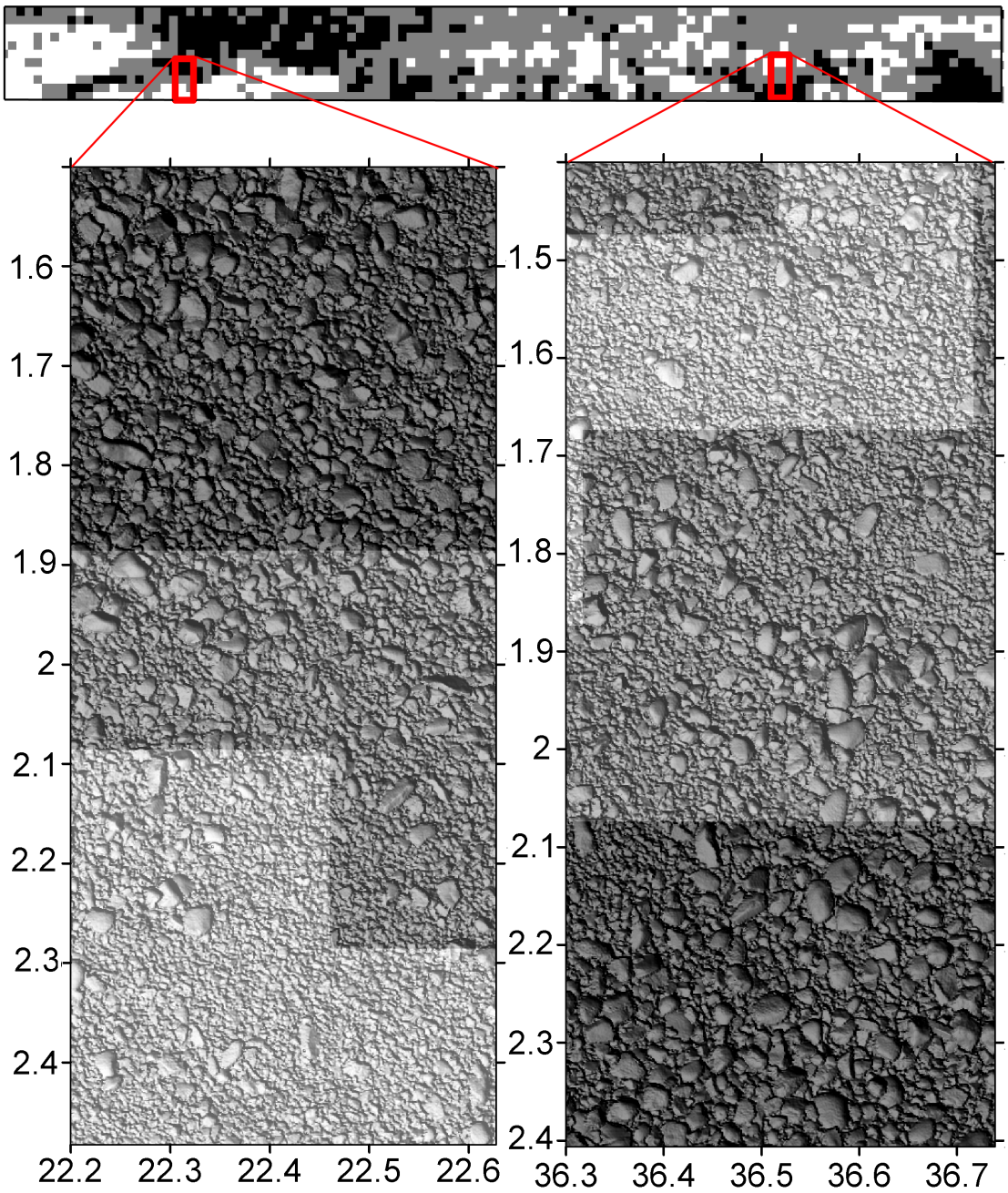

Figure 3.5: Results from the automated image analysis (Figure 3.2c) overlain on portions of the a 1×1 mm DEM. Numbers along the axes indicate cross-stream and downstream position in meters.

bar on the left side of the channel between $x = 20$ and $x = 35$ m directs most of the flow to the right, producing reach-maximum calculated stresses of around 30 Pa in the adjacent pool. Downstream of that bar, the developing bar on the right side of the channel directs flow, and the zone of maximum shear stress, toward the left wall. The oscillations visible in the stress map in Figure 3.6a are not numerical instabilities; they appear instead to be a result of small-scale bedforms present in the scanned topography used to create the computational mesh. Although the water was too turbid to make direct bed surface observations during the experiment, according to the unified bedform phase diagram presented in *Best* [1996], dunes or bed load sheets can be expected for our hydraulic conditions and sediment mixture.

Figure 3.7a compares the model-predicted water surface elevation with the observed profiles for the three middle longitudinal profiles. There is excellent agreement, except at about $x = 31$ m where the echo sounder measured a small (probably transient) wave that was not calculated by the steady state model. Figures 3.7b-e show comparisons between the velocity measured 3 cm above the bed with the pygmy meter and the near-bed velocity computed with FaSTMECH's vertical profile submodel, as well as comparisons between the boundary shear stress calculated with the single velocity measurements and the FaSTMECH-computed boundary shear stress. The error bars on the velocity measurements represent 10% uncertainty, and those on the single-velocity stress measurements are estimated through Gaussian error propagation assuming 10% uncertainty in the measured velocity $u(z)$, 30% uncertainty in the D_{84} estimated from the underwater photographs, and uncertainties of 5 mm for z and 0.02 for A. The agreement in near-bed velocity is generally quite good, and in general there is reasonable agreement between the two methods of computing boundary shear stress despite the uncertainty in many of the parameters used in the single-velocity calculation (Equation 3.4). Because boundary shear stress is modeled as a function of the square of the depth-averaged velocity [*Nelson et al.*, 2003], one should expect it to be more difficult for the model to match stress estimates than velocities.

Figure 3.6 *(following page)*: Shear stress and sediment transport measurements and estimates. (a) The color map is the total boundary shear stress computed in FaSTMECH. Overlain on the map are plots of measured downstream sediment flux per unit width, q_s, the magnitudes of which have been corrected such that the total downstream flux at each cross section equals the mean across all sections (see text). (b) A map of the cross-stream component of the boundary shear stress computed by FaSTMECH. (c) presents cross-stream sediment flux rates (q_n) computed from the q_s data in (a) and Equation 3.8. Positive q_n values are toward the left bank. (d) presents the ratio of the total cross stream sediment flux to total downstream sediment flux at each cross section. Again, positive values are toward the left bank. Note that the x axes of all plots are aligned for easy comparison, and that (a) and (b) cover the same area as the contour map in Figure 3.2. Flow is from left to right.

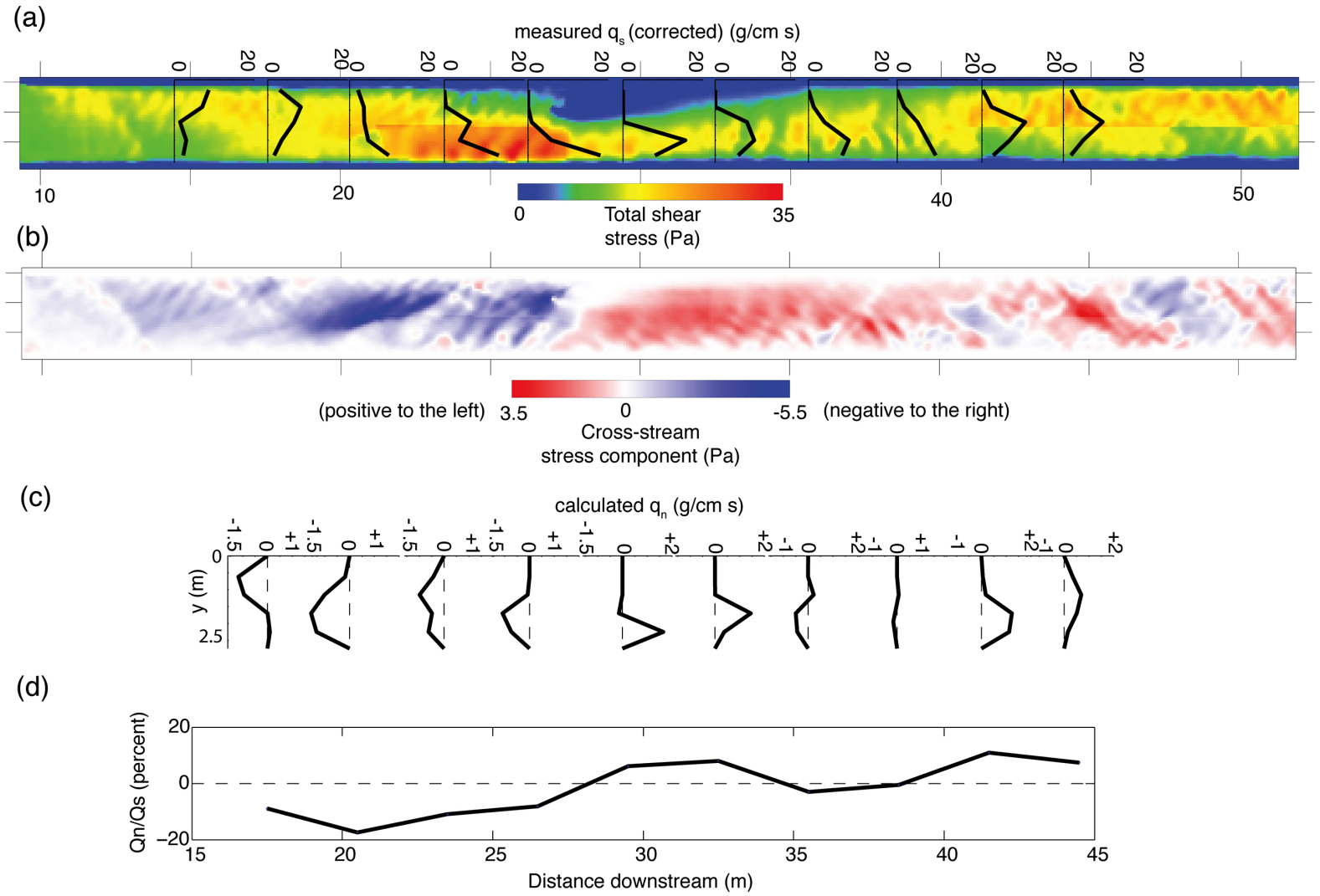
(a)
measured q_s (corrected) (g/cm s)
10
20
40
50
0
Total shear
stress (Pa)
35
(b)
(positive to the left)
3.5
0
-5.5
(negative to the right)
Cross-stream
stress component (Pa)
(c)
calculated q_n (g/cm s)
y (m)
0
2.5
(d)
Qn/Qs (percent)
20
0
−20
15
20
25
30
35
40
45
Distance downstream (m)

Table 3.4: Total downstream sediment flux measured at each cross section ($\int_{-W/2}^{W/2} q_s dy$).

Cross section	x-coordinate [m]	Total downstream sediment flux [g/s]
1	14.5	1284
2	17.5	1777
3	20.5	818
4	23.5	1323
5	26.5	1226
6	29.5	1041
7	32.5	1294
8	35.5	1457
9	38.5	1573
10	41.5	1082
11	44.5	967
Mean		1258
Standard Deviation		278
Coefficient of Variation		0.22

3.3.3 Sediment Transport Field

Table 3.4 presents the total downstream flux Q_s for each section, which were computed from the five measurements taken across each section as $Q_s = \int_{-W/2}^{W/2} q_s dy$, where W is the width of the channel and y is the cross-stream coordinate. The mean value of the measurements, 1258 g/s, is close to the average sediment flux exiting the flume of about 1400 g/s (Figure 3.4a).

There was substantial cross-stream variation in the downstream-oriented sediment transport we measured. Figure 3.6a presents cross-sectional profiles of the downstream sediment transport q_s. To facilitate comparison between cross sections (using a method previously adopted in other studies; e.g., *Dietrich and Smith* [1984]), the data have been corrected such

Figure 3.7 *(following page)*: (a) Measured and model-predicted water surface elevation in the downstream direction for the three middle longitudinal profiles measured with the echo sounder (y = 0.87 m, y = 1.37 m, and y = 1.87 m). (b-e) Comparisons of measured and model-predicted velocity and boundary shear stress for four cross sections. In the velocity plots (top portions of (b-e)), the measured velocities are from 3 cm above the bed surface; the shaded region is the model-predicted velocity between 2-4 cm above the bed and the solid line is the model-predicted velocity at 3 cm above the bed. The bottom portions of (b-e) show boundary shear stress estimated from the single-velocity method (Equation 3.4) and calculated by FaSTMECH.

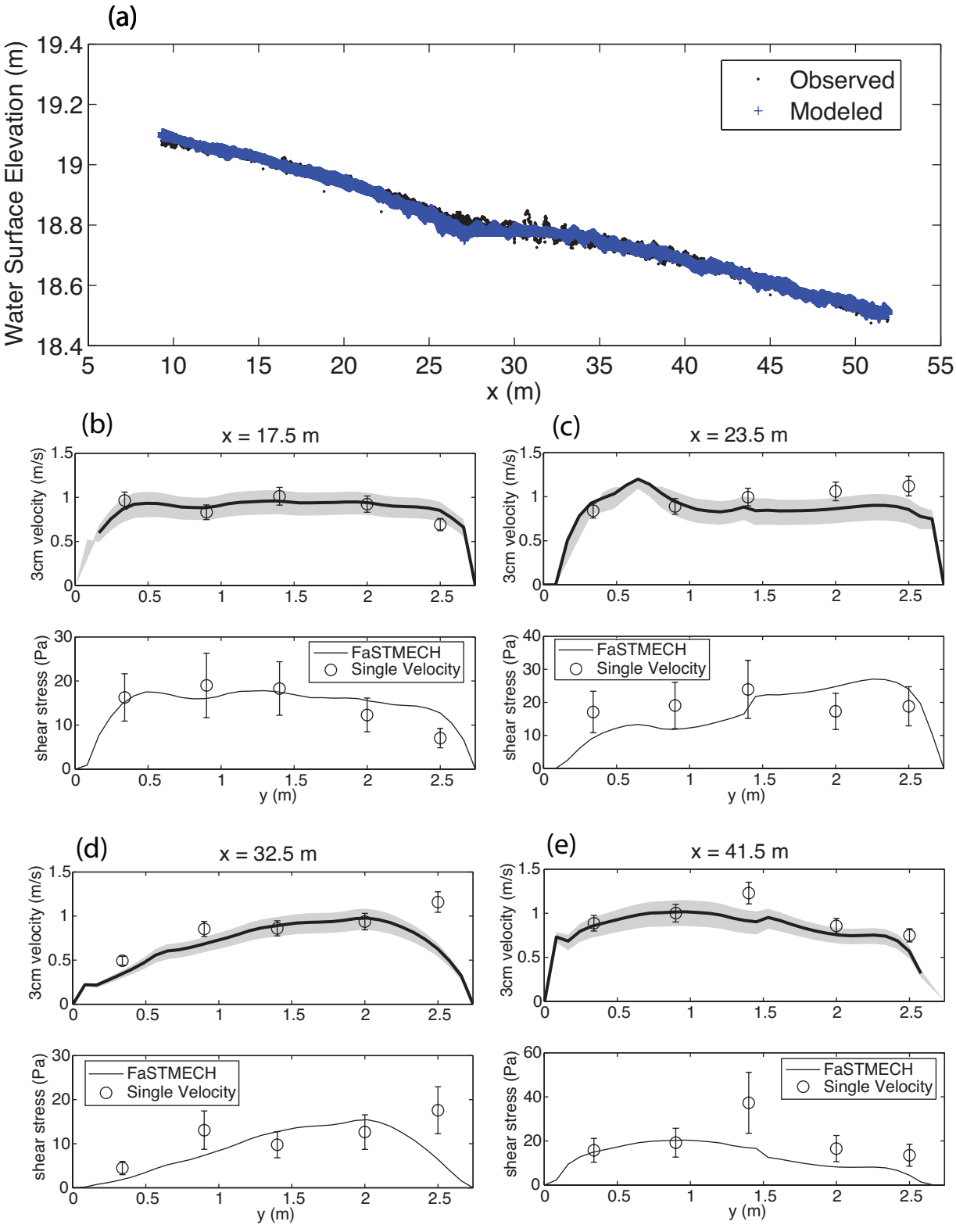
(a)
Water Surface Elevation (m)
x (m)
Observed
Modeled
(b)
x = 17.5 m
(c)
x = 23.5 m
(d)
x = 32.5 m
(e)
x = 41.5 m
3cm velocity (m/s)
shear stress (Pa)
y (m)
FaSTMECH
Single Velocity

that the total downstream transport at each section equals the mean value of 1258 g/s from Table 3.4. The coefficient of variation (standard deviation/mean) of these measurements was 0.22, which, considering the brief duration of measurements and considerable cross-stream variability, we think makes such a correction reasonable for purposes of comparison (*Dietrich and Smith* [1984] observed a coefficient of variation of 0.25 in the downstream sediment flux in their field study of Muddy Creek). Downstream sediment transport tended to follow the zone of maximum shear stress (Figure 3.6a), with the highest measured values in the high-stress pools. Although the bed load measurements were sieved, we present only the total flux data since it is unlikely our samples were large enough to get accurate grain size distributions of the bed load [e.g., *Dietrich and Whiting*, 1989].

Sediment was not moving solely in the downstream direction. Because we oriented our bed load samplers directly upstream, thereby sampling only the downstream component of the local sediment flux q_s, we can calculate the local cross-stream sediment flux q_n if we take advantage of a steady-state assumption. The generalized grain size specific two-dimensional conservation of bed sediment equation can be written as [*Parker*, 2008]

$$(1-\lambda_p)\left[f_{li}\frac{\partial \eta}{\partial t}+\frac{\partial}{\partial t}(L_a F_i)\right]=-\frac{\partial q_{i,s}}{\partial s}-\frac{\partial q_{i,n}}{\partial n} \tag{3.6}$$

where λ_p is the bed porosity, η is the bed elevation, t is time, f_{li} is the fraction of the ith grain size transferred between the surface and the subsurface during aggradation or degradation, L_a is the active layer thickness [e.g., *Hirano*, 1971], F_i is the fraction of the ith grain size on the bed surface, and $q_{i,s}$ and $q_{i,n}$ are the volume bed load transport rates per unit width of the ith grain size in the downstream (s) and cross-stream (n) directions. Following the right-hand rule, we consider the s coordinate to be positive in the downstream direction and the n coordinate to be positive toward the left bank. If we assume steady-state conditions, the time derivatives in Equation 3.6 go to zero and we arrive at a relationship between the downstream and cross stream fractional transport rates:

$$\frac{\partial q_{i,n}}{\partial n}=-\frac{\partial q_{i,s}}{\partial s} \tag{3.7}$$

This equation can be integrated to solve for the cross-stream sediment flux:

$$q_{i,n}=-\int_{-W/2}^{n}\frac{\partial q_{i,s}}{\partial s}dn \tag{3.8}$$

We used Equation 3.8 with our measured downstream bed load transport rates $q_{i,s}$ (corrected to integrate to the mean total flux at each cross section) to calculate the cross-stream bed load transport rates $q_{i,n}$ necessary for steady state. Doing so requires the additional boundary condition of zero flux at the flume walls: $q_{i,n}=0$ at $n=-W/2$ and $W/2$. We evaluated $\partial q_{i,s}/\partial s$ with a forward difference calculation, so the first cross section for which we were able to calculate cross-stream flux was cross section 2 at $x=17.5$ m. Note that in our

experiment, the (s, n) coordinates can be replaced with (x, y) because we are working in a straight flume.

The calculated cross-stream sediment fluxes (summed over all grain sizes) are presented in Figure 3.6c. In the upstream portion of the flume, where there is a prominent bar on the left side of the channel (facing downstream), cross stream transport is primarily to the right. Going downstream, as the bar is passed (and another bar begins to form on the right side of the channel), at around $x = 28$ m, the cross-stream sediment flux changes direction and becomes primarily oriented toward the left bank. This is more readily illustrated in Figure 3.6d, where we have plotted the ratio of the integrated cross-stream flux Q_n ($Q_n = \int_{-W/2}^{W/2} q_n dn$) to the integrated downstream flux Q_s (which, because we are using the corrected data, is the mean value for each section) as a function of distance downstream. In the upstream portion of the channel, there is net transport to the right, and downstream of the bar there is net transport to the left. The magnitude of the Q_n/Q_s ratio is $\pm 18\%$, which is in the range of *Dietrich and Smith* [1984]'s observations at Muddy Creek.

This change in direction of net cross stream transport coincides nicely with the cross-stream component of shear stress predicted by the FaSTMECH model (Figure 3.6b). The model predicts shear stresses oriented to the right in the upstream portion of the channel, changing direction towards the left downstream of $x = 28$ m. The internal consistency between our measured and computed sediment transport rates and the computed shear stress field is an encouraging sign that our observations and modeling are capturing the essential dynamics of our system.

3.4 Discussion

Our flume observations provide an opportunity to examine how topography and the flow and sediment transport fields interact to produce forced patches and persistent sorting. Our observations do not suggest that our flume experiment demonstrated "threshold" conditions; like *Lisle et al.* [2000], we did not find a simple correlation between the local median bed surface grain size and the local shear stress. Instead, our results show that in places the shear stress and grain size appear to be positively correlated (both stress and grain size increasing or decreasing), negatively-correlated (stress increasing while grain size decreases, or vice versa), or insignificantly correlated. We propose that this is a direct consequence of the particular dynamics of the size-selective nature of mixed-grain size gravel transport interacting with topographically-induced steering of the flow [e.g., *Clayton and Pitlick*, 2007].

Figure 3.8 shows FaSTMECH-calculated shear stress and surface D_{50} estimates from the automated grain size analysis along a profile at position $y = 0.8$ m from the left bank (Figure 3.2a). Most of this profile is in an area of the bed classified in the coarser (darker) facies on the hand-drawn patch map (Figure 3.2d), and since the *h-minima* $= 1$ parameter worked well in the coarser areas of the bed (Figure 3.3f), the D_{50} values presented in Figure 3.8 should be reasonable estimates of the magnitude of the actual surface D_{50}. Since much of

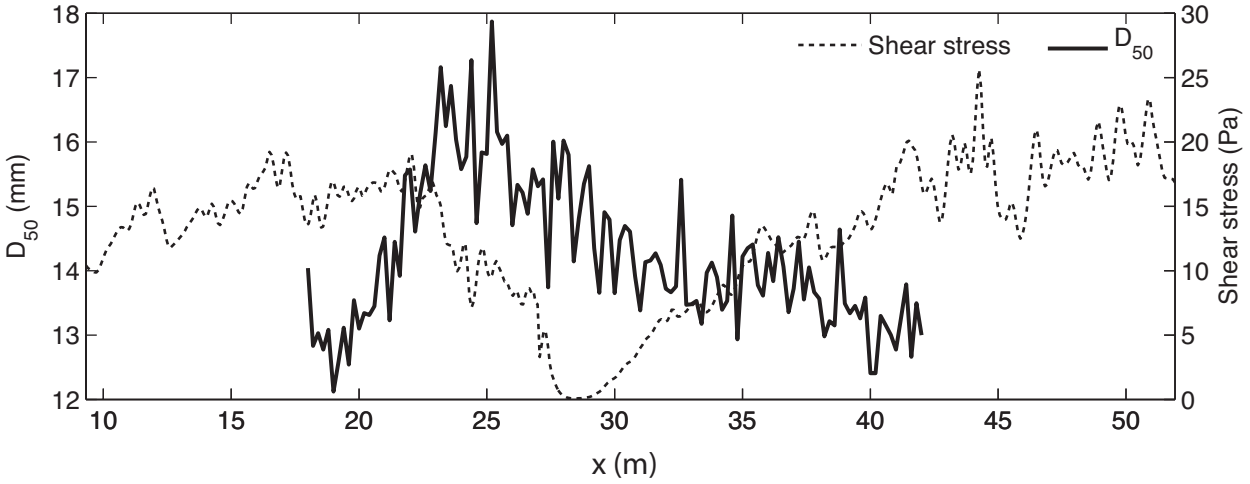

Figure 3.8: Longitudinal profiles of FaSTMECH-computed boundary shear stress (from Figure 3.6a) and bed surface D_{50} generated from the automated image analysis (from Figure 3.2c) along a transect of $y = 0.8$ m.

the transect falls in the same patch type, the variation in D_{50} illustrated by the automated analysis, which can have a significant impact on local sediment transport rates, evidently was not detectable by eye. Along the $y = 0.8$ m profile, between $x = 18$ m and $x = 23$ m the boundary shear stress is essentially constant whereas the median grain size increases. Then from $x = 23$ m to $x = 29$ m the boundary shear stress drops dramatically and the grain size declines. From $x = 29$ m to $x = 41$ m the boundary shear stress increases, but the grain size progressively declines.

An important piece missing from Figure 3.8 is the cross-stream component of the sediment transport field, which covaries with the boundary shear stress field and the surface grain size such that quasi-steady topography and sorting patterns are produced. In their description of fixed bars that developed in a high-gradient flume, *Lisle et al.* [1991] suggested that their stationary bars formed due to deposition of coarse material at the front of the bar preventing bar erosion and causing flow and sediment transport to be directed around the bar due to shoaling and "topographic steering" [e.g., *Dietrich and Smith*, 1984; *Smith and McLean*, 1984; *Nelson and Smith*, 1989a]. Figure 3.6 shows that, in our flume, cross-stream bed load transport away from zones of decreasing boundary shear stress and toward zones of increasing shear stress occurred and this could lead to a dynamically stable bed topography and surface grain size distribution.

Figure 3.9 places the observations of Figure 3.8 in the context of stress-grain size-transport rate relationships built into the *Parker* [1990] surface-based bed load transport model. The procedure used to make the contours of total bed load flux in the figure is similar to that presented in *Nelson et al.* [2009], in which we compute the total bed load transport rate predicted by the algorithm as a function of boundary shear stress and surface geometric

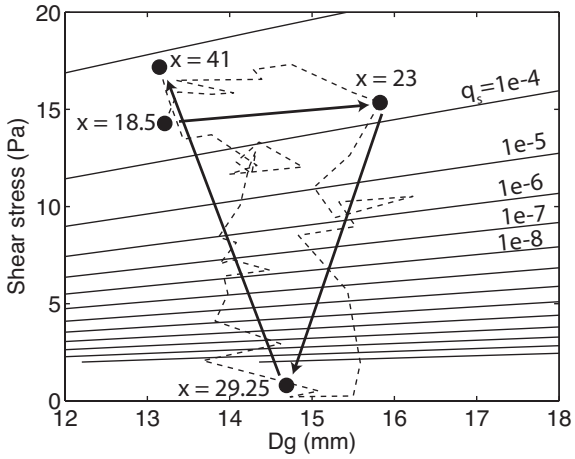

Figure 3.9: Contours illustrating the relationship between the total bed load transport rate, predicted by the *Parker* [1990] model, boundary shear stress, and bed surface grain size. Here, Dg is the geometric mean of the bed surface grain size distribution, and the standard deviation of the bed surface grain size distribution is held constant at $\sigma = 1.7$. Each contour line represents an order of magnitude change in transport rate (in m^2/s). Also shown are shear stress (from FaSTMECH) and bed surface geometric mean grain size (from the automated image analysis) for four locations along the $y = 0.8$ m profile. The arrows show the general pattern in the downstream direction along the $y = 0.8$ m profile, while the dashed line shows the actual trajectory along the profile.

mean grain size for synthetic bed surface distributions that have a wide range of mean grain sizes but constant geometric standard deviation (here, $\sigma = 1.7$, close to the bulk standard deviation of 1.8). The use of thousands of synthetic grain size distributions in this analysis allows us to fully explore the effects of changes in grain size statistics on predicted sediment transport rates. Also shown on the figure are the shear stress (from FaSTMECH) and observed bed surface geometric mean grain size (from the automated image analysis) for four locations along the $y = 0.8$ m transect shown in Figure 3.8, which when connected show the path the transect followed in stress-grain size-flux space. Between $x = 18$ m to $x = 23$ m, lateral sediment transport driven by topographically-induced cross-stream shear stress (Figure 3.6b) reduces the amount of sediment transport necessary to maintain steady conditions. Because the shear stress at $x = 23$ m is virtually the same as that at $x = 18.5$ m, this reduced sediment transport is achieved through bed coarsening (this is further elucidated in the following paragraph). From $x = 23$ m to $x = 29.25$ m, the shear stress declines dramatically due to thinning of the flow and flattening of the water surface slope associated with the slowing and shoaling of the flow around the bar such that essentially no sediment transport is occurring on the top of the bar, and by this point all of the sediment that was being transported upstream has been transported laterally so that it is accommodated by flux through the pool. From $x = 30$ m to $x = 41$ m, the boundary shear stress increases, and here there is a lateral sediment influx driven by cross-stream component of the shear stress oriented toward the left bank (Figure 3.6b). Here, convergence of boundary shear stress is balanced by convergence in sediment transport, and the bed accommodates this increasing sediment flux by becoming finer.

The development of coarse bars and fine pools in our experiment suggests that, along a path moving up the bar, the material moving as cross-stream sediment transport became finer, preferentially shuttling fine sediment into the pools. Unfortunately, because our bed load samples were small, we are unable to present reliably accurate measurements of the grain size distribution of the bed load and therefore cannot experimentally verify that the cross-stream transport became finer along a profile progressing up the bar. However, the *Parker* [1990] and *Wilcock and Crowe* [2003] mixed-grain size bed load transport models can be used to show how, theoretically, the cross-stream flux should be becoming more size-selective. *Wilcock and McArdell* [1993] suggested that the ratio of the fraction of the ith grain size in the load, p_i, to the fraction of the ith grain size on the bed surface, F_i, can be used to assess whether the bed is in a state of full or partial mobility. If p_i/F_i is constant (i.e., equal to 1.0) for all grain sizes D_i, the system is in a state of perfect surface-based equal mobility [*Parker*, 2008]. However, when the ratio becomes smaller as grain size increases, the relative transport of coarse grains is reduced so that partial or selective transport is occurring, or that fine grain size fractions were transported at rates higher than proportionally represented on the bed surface (perhaps due to high supply of fine material), giving the appearance of a cascading trend. Greater deviations from constant p_i/F_i indicate more size-selective conditions.

To explore this for our experiment, we used the FaSTMECH-computed boundary shear

stress and the observed (from automated image analysis) bed grain size distribution to calculate bed load transport from the *Parker* [1990] and *Wilcock and Crowe* [2003] formulas. The algorithms use the shear stress and bed surface grain size distribution as inputs to compute the total transport rate q_T and the grain size distribution of the load p_i, which can then be used with the local bed surface grain size distribution F_i to compute p_i/F_i for each grain size D_i. This type of analysis normally compares conditions of partial vs. equal mobility per grain size fraction at different flow levels [e.g., *Wilcock and McArdell*, 1993; *Clayton and Pitlick*, 2007], whereas for this study, transport conditions are compared spatially, over changes in x. Figure 3.10 shows computed p_i/F_i plots for selected distances downstream along the $y = 0.8$ m transect where the bed surface is coarser than the median size of the bed material (11 mm). Both transport expressions predict that where the boundary shear stress is relatively low compared to the observed grain size of the surface ($x = 26$ and 30 m in Figure 3.10) that deviation from equal mobility is greatest and conversely where the boundary shear stress is relatively large compared to the surface grain size ($x = 20$ and 37 m in Figure 3.10), equal mobility is more closely approximated (though not reached). This effect is more apparent in the *Parker* [1990] algorithm than the *Wilcock and Crowe* [2003] algorithm, particularly for coarse size fractions, perhaps because the *Wilcock and Crowe* [2003] algorithm incorporates a more complex hiding function whose exponent is a function of D_i/D_g, and because it was developed with the intention of capturing mobilization effects of sand on coarse grains while our experimental conditions were sand-free. Nevertheless, where the boundary shear stress rapidly declines (as flow shoals over the top of the bar between $x = 20$ m and $x = 30$ m (Figures 3.2, 3.6, and 3.8) and the bed is coarse, both algorithms suggest that the strongest tendency to transport mostly the finer fraction occurs. Along this path the boundary shear stress is oriented toward the opposite bank (Figure 3.6b) and the mobilized finer sediment is transported across the channel away from the zone of decreasing boundary shear stress (Figure 3.6c). This suggests that the topographically-induced divergence of boundary shear stress leads to differential mobilization of the finer sediment, coarsening of the bed and equilibrium topography, i.e., the formation of a forced bed-surface patch.

Our interpretation is generally in agreement with *Lanzoni and Tubino* [1999]'s description of the implications of heterogeneous sediment on alternate bar formation which emerged from their analytical stability analysis. Their theoretical results suggested that mixed-size sediments might appreciably inhibit bar migration, and that selective transport leads to coarse bars. The alternate bars that developed in *Lisle et al.* [1991, 1993]'s experiments also formed coarse bar tops and became stationary, which they attributed to bar head stabilization by coarse sediment and preferential incision in the pools. Our bars formed sorting patterns similar to those of *Lisle et al.* [1991, 1993], but it is difficult to determine precisely why our bars stopped growing and migrating since, in addition to strong sorting, the upstream bar's location was forced by a physical constriction of the flow at the flume inlet.

Field studies of surface sorting on channel beds suggests that channel curvature can play a role of varying importance for bed sorting patterns. Studies of straight (or nearly straight)

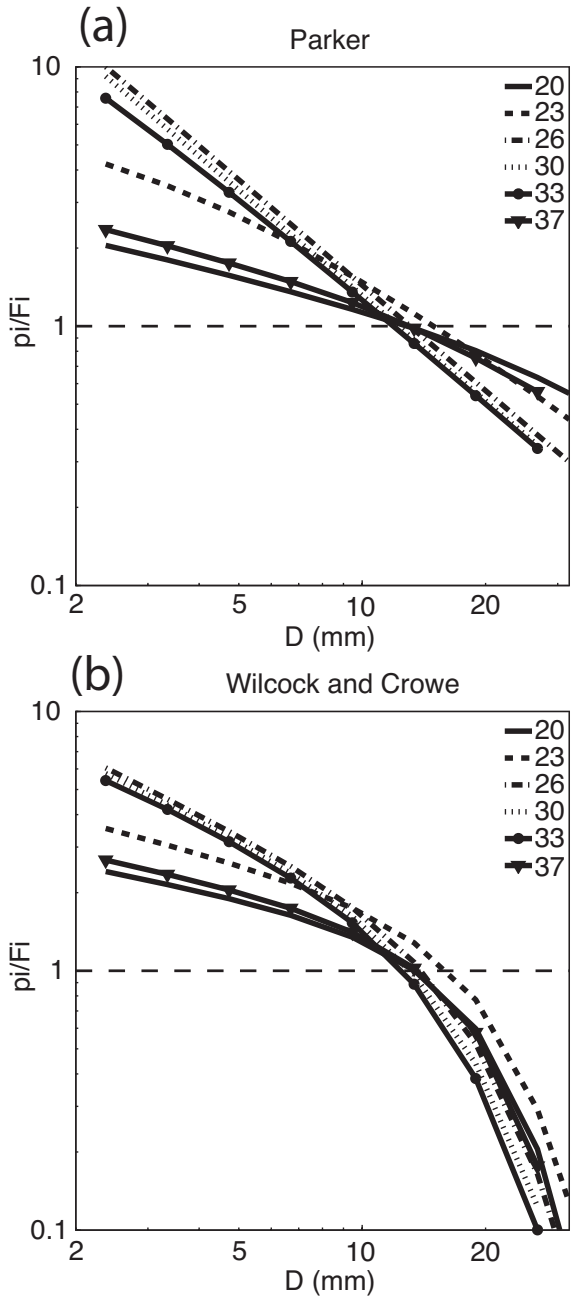

Figure 3.10: p_i/F_i ratios calculated by grain size for various x locations along the $y = 0.8$ m transect using (a) the *Parker* [1990] and (b) *Wilcock and Crowe* [2003] bed load transport algorithms. The legend indicates the x position (in meters) for each line.

reaches with bars in gravel-bed rivers have generally documented surface sorting patterns of coarse bar tops and fine pools [e.g., *Mosley and Tindale*, 1985; *Kinerson*, 1990; *Lisle and Hilton*, 1992; *Lisle and Madej*, 1992]. However, field observations of channel bends with point bars tend to document the opposite pattern of fine bars and coarse pools [*Bluck*, 1971; *Bridge and Jarvis*, 1976, 1982; *Bluck*, 1987; *Whiting and Dietrich*, 1991; *Laronne and Duncan*, 1992; *Carson*, 1986; *Clayton and Pitlick*, 2008; *Clayton*, 2010]. Point bars in curved channels [e.g., *Bluck*, 1971], alternate bars in straight channels [e.g., *Lisle and Madej*, 1992] and unit bars [e.g., *Lunt and Bridge*, 2004] all exhibit slight downstream fining along the bar.

The contradictory sorting patterns observed in straight and curved channels suggests that the presence of curvature induces a shift in the dominant sorting mechanism. In bends, channel curvature creates a strong secondary circulation directed inward at the bed, toward the point bar [*Smith and McLean*, 1984]. For example, following *Parker and Andrews* [1985], *Lanzoni and Tubino* [1999] suggest that cross-stream sediment flux, $q_{i,n}$, can be expressed as:

$$q_{i,n} = \mid \mathbf{q}_i \mid \left\{ \sin\chi - \frac{r}{\beta} \left[\frac{1}{\tau_g^*} f_h \left(\frac{D_i}{D_g} \right) \right]^{1/2} \frac{\partial \eta}{\partial n} \right\} \tag{3.9}$$

Here, $\mathbf{q}_i$ is the sediment flux vector of the ith grain size computed by, say, the *Parker* [1990] model, χ is the angle the boundary shear stress vector makes with the s-axis, β is the width to depth ratio, τ_g^* is the Shields stress computed for D_g, $f_h(D_i/D_g)$ is a reduced hiding function, $\partial\eta/\partial n$ is the cross-stream bed slope, and r is a parameter that varies from 0.5 to 1.5. The term on the right hand side inside the braces represents the effects of friction, lateral bed topography, and hiding effects. The $\sin\chi$ term represents the effects of the transverse component of velocity and the effects of curvature-induced secondary circulations. *Blondeaux and Seminara* [1985] suggested that $\sin\chi$ can be expressed as:

$$\sin\chi = \frac{v}{(u^2+v^2)^{1/2}} - a\frac{h}{r_0+n} \tag{3.10}$$

where u and v are the components of the velocity vector in the s and n directions, h is the flow depth, r_o is the radius of curvature, and a is a scaling parameter ranging from 7 to 12 [e.g., *Engelund*, 1974; *Allen*, 1978; *Bridge and Jarvis*, 1982; *Dietrich and Smith*, 1983]. In straight channels, the $h/(r_0+n)$ term is zero, but in bends it can become quite important. This secondary circulation is opposed by the outward gravitational force on particles provided by the cross-stream slope of the point bar. For fine particles, the effect of the secondary circulation exceeds the gravitational force, causing them to be preferentially transported into a reduced shear stress zone over the bar and transported away. Larger particles, however, roll downslope into the higher shear stress zone in the pool [*Parker and Andrews*, 1985; *Clayton and Pitlick*, 2007]. Curvature effects may be less important in straight channels, which should have weaker secondary circulations and will develop coarse

bars and fine pools because the finer sediment is preferentially transported laterally away from the bar via topographic steering.

The actual importance of curvature on bed sediment sorting for particular location will of course depend on the details of local channel planform, bed topography, and flow regime. Local sorting also is tightly coupled to the details of the bar shape, since the shape of the bar will determine where flow accelerations or decelerations, and consequently shear stress increases or decreases, occur. The shape of our bars resulted in flow deceleration over the bar top, but it is possible that had the upstream end of our bar been wider, the flow could have accelerated and the stress could have increased over the bar, resulting in a different bed surface sorting pattern [e.g., *Whiting and Dietrich*, 1991].

Unlike gravel-bedded channels, sediment transport in sand-bedded channels typically occurs under high excess shear stress conditions in which all grain sizes are fully mobile [*Parker*, 2008]. In these channels, one would expect the coarse sediment to track the zone of highest shear stress, so even relatively straight, alternate bar reaches should have fine bars and coarse pools [*Dietrich and Smith*, 1984].

3.5 Conclusions

Observations of the surface texture of gravel-bed rivers generally indicate that in curved channels the point bar is finer than the adjacent pool, in straight channels alternate bars are coarser than pools, and bars in both straight and curved channels tend to have a coarse to fine texture gradient along the bar top in the downstream direction. Our experiment shows how this pattern of forced bed surface patchiness is a consequence of interactions between channel topography, the flow field, and the sediment transport field.

In our experiment, we developed bed topography and a pattern of forced bed surface patchiness similar to the field case of a straight channel with alternate bars. Our channel reached quasi-steady conditions with an overall sorting pattern of coarse bar tops and fine pools. This pattern did not track the calculated boundary shear stress field; that is, the coarse bar top was not an area of high boundary shear stress and the fine pool bed was not an area of low boundary shear stress.

The development of alternate bars in our channel produced a spatially-variable shear stress field. Thinning and shoaling of the flow over the bar caused the stress over the bar to decrease and flow convergence in the pool produced locally high boundary shear stress there. Sediment was transported laterally off of the bar and into the pool due to the cross-stream component of the flow field. This lateral transport became increasingly size-selective toward the downstream end of the bar as the shear stress on the bar declined, and it caused the local sediment supply along the bar to progressively decrease, which was accommodated locally through bed surface coarsening. Downstream of the bar, an influx of lateral sediment supply due to local stress convergence allowed the bed to fine. Thus, topographically-forced divergences in the boundary shear stress field are matched by divergences in the sediment

transport field, which in turn were accommodated by changes in bed surface texture allowing the channel to maintain quasi-steady state conditions.

Notation

a	scaling parameter for helical flow.
A	parameter relating grain size to roughness height.
D	grain size.
D_{50}, D_{84}	grain size for which 50 and 84% of the grain size distribution is finer.
D_g	geometric mean bed surface grain size.
F_i	fraction of the ith grain size on the bed surface.
f_{li}	fraction of the ith grain size transferred between the surface and the subsurface during aggradation or degradation.
f_h	lateral hiding function.
g	gravitational acceleration.
h	flow depth.
L_a	active layer thickness.
n	cross-stream coordinate (channel fitted).
$q_{i,n}$	cross-stream sediment flux per unit width of the ith grain size fraction.
$q_{i,s}$	downstream sediment flux per unit width of the ith grain size fraction.
q_n	cross-stream sediment flux per unit width.
q_s	downstream sediment flux per unit width.
Q_n	total cross-stream sediment flux.
Q_s	total downstream sediment flux.
r	frictional parameter.
r_0	radius of curvature.
s	downstream coordinate (channel-fitted).
t	time.
u	downstream velocity.
u_*	shear velocity.
W	channel width.
x	downstream coordinate (Cartesian).
y	cross-stream coordinate (Cartesian).
z	height above the bed.
z_0	roughness height.
β	width-to-depth ratio.

χ	angle the boundary shear stress vector makes with the s-axis.
η	bed elevation.
κ	von Karman's constant.
λ_p	bed porosity.
ρ	water density.
ρ_s	sediment density.
σ	geometric standard deviation.
τ	boundary shear stress.
τ^*	non-dimensional Shields stress.
τ_c^*	Shields number for initial motion.
τ_g^*	non-dimensional Shields stress computed with D_g.

Chapter 4

Objective delineation of river bed surface patches from high-resolution spatial grain size data

4.1 Introduction

Gravel bed rivers frequently display considerable spatial heterogeneity in the grain size and sorting of their beds. Visually, this heterogeneity often appears to form an organization of distinct textural patches or facies. For example, Figure 4.1 is a map of Wildcat Creek in Northern California that has formed a pattern of patchiness in which patches of boulders, patches of sand, and patches of gravel are located within a few meters of each other and remain spatially persistent through time, despite passing considerable sediment load [see discussion in *Dietrich et al.*, 2005].

"Free" patches, which are mobile sorted features that move downstream (such as bedload sheets), appear to form primarily through a grain interaction process where coarse and fine grains interact to produce a migrating coarse-to-fine pattern [*Whiting et al.*, 1988; *Nelson et al.*, 2009], although a roughness feedback due to the sorting also suggests that a hydrodynamic mechanism may be important in their formation [*Seminara et al.*, 1996]. The dynamics of free patches depend upon relative sediment supply [*Dietrich et al.*, 1989; *Nelson et al.*, 2009]. Longer-lived sorted areas that are temporally and spatially stable ("forced" patches) emerge as a consequence of the complex interaction between bed topography, the flow field, and the local sediment transport field, wherein topographically-forced local divergences in boundary shear stress are compensated by local divergences in bedload transport, which under low excess stress conditions commonly encountered in gravel bed rivers are achieved through selective transport and local bed surface grain size adjustment [*Nelson et al.*, 2010].

The local bed surface grain size, and therefore bed surface patchiness, is a primary control on local bed mobility and bedload transport rates. Current state-of-the-art bedload

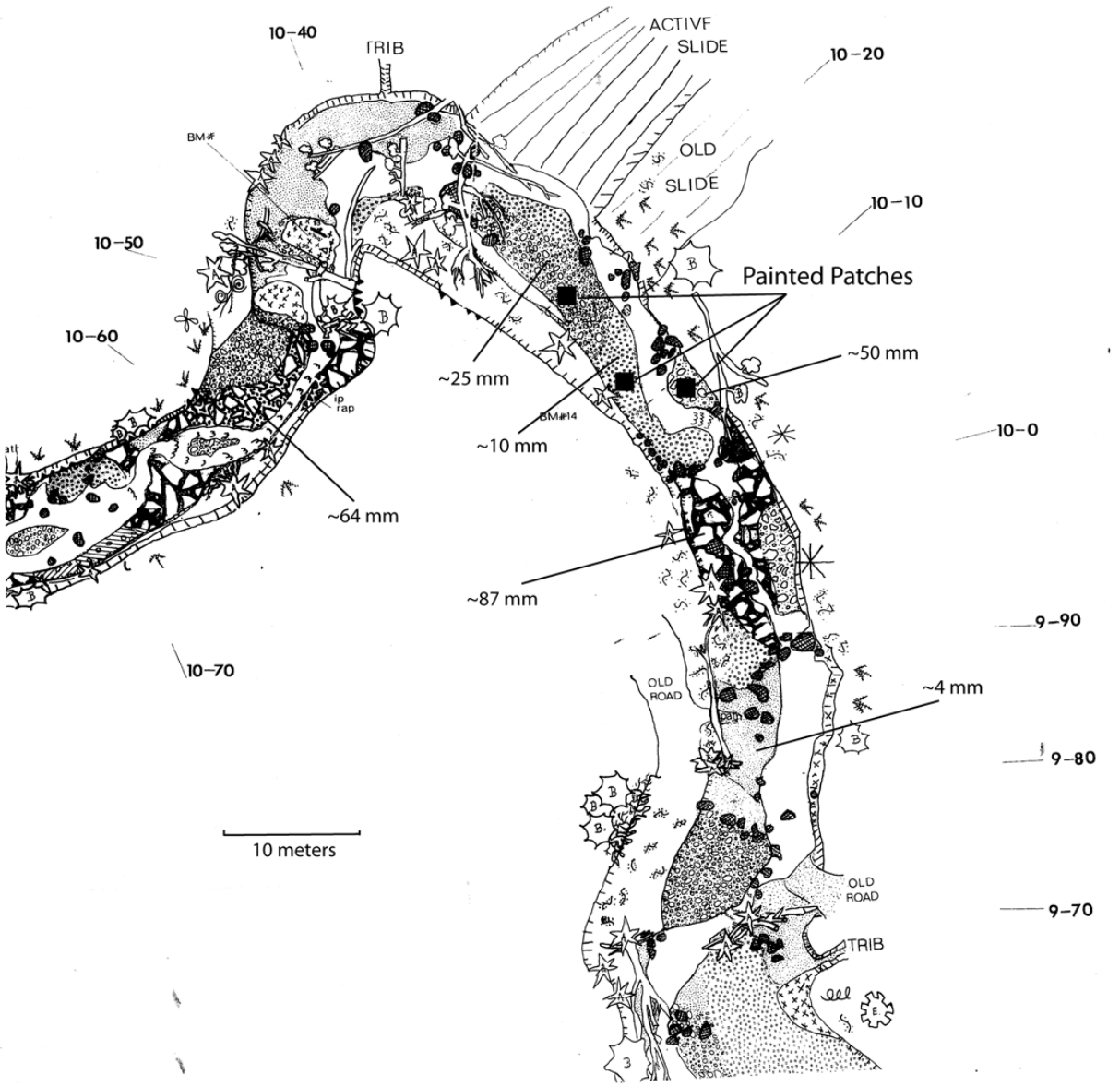

Figure 4.1: Patch map of Wildcat Creek, drawn by Laurel Collins in 1988 [from *Dietrich et al.*, 2005].

transport algorithms [*Parker*, 1990; *Wilcock and Crowe*, 2003] require a bed surface grain size distribution as a model input, in part because they employ empirical "hiding functions" to determine the critical stress for mobility for each grain size as a function of the local bed surface grain size distribution. Bed surface patchiness has been invoked as a potential cause of downstream fining [*Paola and Seal*, 1995] and as an important source of error in one-dimensional bedload transport calculations [*Ferguson*, 2003]. A characteristic local grain size (e.g., the D_{84}, the grain size for which 84% of the sediment is finer) is often used to parameterize local roughness in hydrodynamic calculations for flow and boundary shear stress [e.g. *Leopold and Wolman*, 1957; *Dietrich and Whiting*, 1989; *Wilcock*, 1996]. Patchiness also has biological implications, since many aquatic organisms prefer microhabitats [*Cummins and Lauff*, 1969; *Rabeni and Minshall*, 1977; *Reice*, 1980] or spawning grounds [*Kondolf and Wolman*, 1993; *Overstreet et al.*, 2010; *Riebe et al.*, 2010] consisting of particular grain sizes.

Despite the importance of bed surface patchiness for sediment transport, hydrodynamics, and ecology, a fundamental question remains unanswered: what exactly *is* a patch? In studies where patches are documented, they tend to be visually delineated, but to what extent is there a natural tendency of the human eye to want to pick out patterns? This leads to several fundamental questions about rivers in general: do rivers really exhibit discrete patchiness, or are patches a simplification of a pattern of continuous grain size variation? At what scales do variations in grain size occur on river beds? Do patches interact, or depend on one another in a way that causes them to form? Is there a number of patches (or patch types) that should emerge on a river bed for a particular grain-size mixture and hydraulic conditions?

Meaningful answers to these questions have been elusive in large part because they rely upon spatial grain size information that has required prohibitive effort to collect. Over the past decade, however, significant efforts have been made to generate grain size distributions automatically from digital photographs [e.g., *Butler et al.*, 2001; *Sime and Ferguson*, 2003; *Graham et al.*, 2005a,b] or high-resolution digital elevation models [e.g., *McEwan et al.*, 2000] of river beds. These techniques offer the potential to acquire bed surface grain size data at a spatial resolution high enough to objectively delineate patch boundaries based on grain size data alone, without a subjective visual bias.

In this study, we analyze a high resolution (grain-scale) dataset of bed surface composition from a near-field scale flume experiment in which natural channel topography and sorting patterns from a 2-45 mm gravel mixture were extensively documented. We apply techniques inspired by work in cluster analysis and graph theory to delineate bed surface patches in our dataset and assess each technique's usefulness. Our results suggest that clustering methods can be used to define patch boundaries objectively, and that rivers tend to create a finite number of patch types that may repeatedly emerge at different locations on the bed.

4.2 Background

Although numerous studies document bed patches or facies [e.g., references within *Nelson et al.*, 2009], they tend to be visual maps of a semi-quantitative nature. There have, however, been a few efforts to make patch delineation of stream beds more objective and verifiable. *Crowder and Diplas* [1997] proposed a grid-based statistical approach to locate boundaries between sediment facies. In their procedure, a systematic grid of cells is spread out over the reach without regard to sedimentary units. The arithmetic mean and standard deviation of sediment in each grid cell are estimated from samples collected in a local sub-grid-scale sampling routine, and adjacent subsamples are compared with a standard z-test. If the z-test indicates a statistically significant difference between the two subsamples, they are separated by a facies boundary. While *Crowder and Diplas* [1997]'s method is admirable in its simplicity, their use of the arithmetic mean may be problematic since it can be heavily influenced by the coarsest particles in the sample and therefore is not a robust measure of local grain size.

Buffington and Montgomery [1999a] developed a standard procedure for classifying textural patches that combines visual identification and quantitative grain-size measurement. They advocate visually mapping the bed into sediment facies types that can be represented by two ternary diagrams describing sediment type and grain size, then collecting surface samples of each facies type and comparing with the initial classification, which is then updated. This method can be a valuable tool to use in field studies, but because it still relies upon visual delineation it may not be able to provide a truly objective definition of patchiness or fully answer questions about the scales of textural variability in a stream bed. With high-quality, grain-scale grain-size data becoming available we should be better able to approach these questions from a rigorous and objective standpoint.

Landscape and fluvial ecologists frequently deal with spatial heterogeneity and patchiness. Generally, ecological studies focusing on spatial heterogeneity make use of either categorical maps, where data have already been classified into patches, or point-data analysis, which assumes that system properties are spatially continuous [*Gustafson*, 1998]. In the former case, once data have been classified into categorical maps, they can be further analyzed with categorical indices and metrics, many of which can be automatically generated with software such as FRAGSTATS [*McGarigal et al.*, 2002]. These techniques have been borrowed by fluvial geomorphologists; for instance, FRAGSTATS was used by *Yarnell et al.* [2006] to measure the Shannon's Diversity Index (SHDI) for grain size patch maps of river channels and flumes [e.g., *Kinerson*, 1990; *Lisle et al.*, 1993] and compared with relative sediment supply q^* [*Dietrich et al.*, 1989] to show that increased sediment supply tends to increase habitat heterogeneity. However, the initial classification of the data still can pose a significant challenge. Point-data analysis avoids this problem by assuming that system properties vary continuously in space. These studies then focus on decomposing the spatial heterogeneity present in the data, using techniques such as spatial autocorrelation and semivariograms to define regions of spatial dependence and independence [e.g., *Rossi et al.*, 1992; *Cooper et al.*,

1997]. However, when actual classification of the data is a primary goal (as it is for river bed patch delineation), such techniques are of limited usefulness.

Cluster analysis has been used in a few studies focusing on marine sediments. *Bobertz and Harff* [2004] characterized marine sediment samples with three parameters describing the median, sorting, and skewness of the sample; the samples were then grouped into classes with an agglomerative clustering methods and the clustered samples were compared to the results of a hydrodynamic ocean model. *Hamilton* [2007] used a partitional clustering algorithm to group sediment samples from shallow-marine datasets to find sediment samples and geographical areas with similar characteristics. Although these sorts of techniques do not appear to have been applied to fluvial sedimentary systems, in the following sections we will explore how they can be used to delineate bed surface patches and provide insight on basic principles in fluvial geomorphology.

4.3 Grain size dataset

The core dataset upon which we develop our analysis consists of spatial coordinates and sizes of grains on the channel surface. In particular, we use data collected in the main channel at St. Anthony Falls Hydraulic Laboratory (SAFL) during alternate-bar phase of the StreamLab06 suite of experiments [described in *Nelson et al.*, 2010]. The experiments were conducted in an 80 m long (with a 55 m test section), 2.75 m wide rectangular flume channel to which we supplied a constant water discharge of 0.4 ± 0.02 m^3/s. The bed was initially composed of a unimodal mixture of gravel ranging in diameter from 2 to 45 mm. Sediment was recirculated throughout the experiment, and sandbags were placed at the upstream end of the test section to constrict the flume inlet to 2/3 of the flume width and to encourage alternate bar formation. Approximately 1.5 bar sequences formed, and after a series of local flow and sediment transport measurements were collected, the flume was rapidly drained and a number of dry-bed measurements were taken to characterize the topography and sorting of the bed surface. These data include a hand-drawn facies map of bed surface patches, a series of photographs of the bed surface taken from a camera attached to a mechanized cart that traversed the length of the flume, and a 1×1 mm digital elevation model (DEM) from a laser scan of the middle 2.36 m of the flume ($y = 0.19$ m to $y = 2.55$ m) spanning 24 m of the flume's length ($x = 18$ m to $x = 42$ m). Figure 4.2 shows the hand-drawn patch map where the bed has been visually divided into four patch types: "fine," "medium-fine," "medium-coarse," and "coarse." The bed displayed considerable heterogeneity. *Nelson et al.* [2010] discusses details of the experiment in greater detail and provides an explanation for the observed sorting patterns.

We have developed a dataset of grain sizes and grain locations (x, y, D) using the procedure described in *Graham et al.* [2005a]. The details of our procedure are more fully described in *Nelson et al.* [2010], but a summary of how the dataset was generated follows. We applied the *Graham et al.* [2005a] method to a shaded relief map of the 1×1 mm DEM

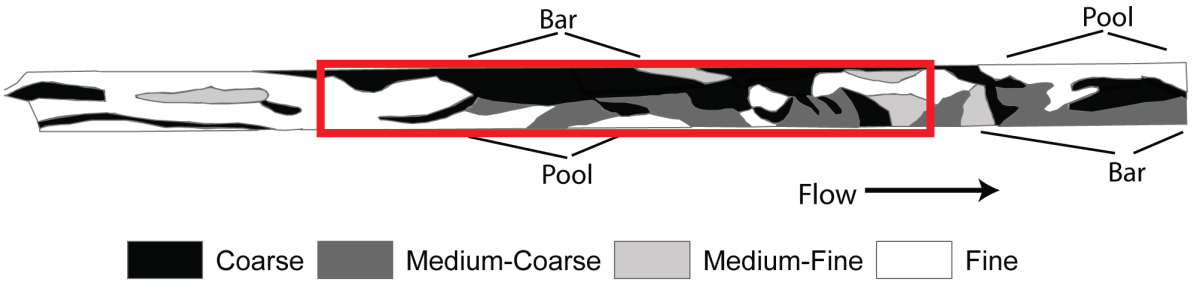

Figure 4.2: Hand-drawn patch map of the bed at the end of the alternate bar phase of the SAFL experiment. The region outlined in red shows the location of the 1×1 mm DEM (from $x = 18$ m to $x = 42$ m).

(rather than photographs of the bed) because it eliminated intragrain heterogeneity due to mineral inclusions, enhanced contrast at grain edges, and provided exact spatial registration. Given an image of a bed of sediment with a known scale, the *Graham et al.* [2005a] method applies image processing filters and a double intensity threshold to detect grain edges and it uses watershed algorithm with an *h-minima* transform to delineate grain regions. Ellipses are fit to the regions, and their semi-major axes (D) and centroids (x, y) are measured to produce a continuous (x, y, D) dataset for our flume. Figure 4.3 shows a portion of the DEM with grain-approximating ellipses overlain on it.

Before attempting to divide our high resolution spatial grain size dataset into patches, it is necessary to use the (x, y, D) data to construct a spatial grid of grain size distributions. We focus our analysis on grids of distributions rather than individual grain measurements for two reasons. First, characterizing sediment mixtures with grain size distributions is a widely-used and readily understood technique in sedimentology and fluvial geomorphology. Second, and more importantly, grain size distributions derived from photographs evidently will always undercount the number of grains when compared to an actual surface sieve sample. For example, *Graham et al.* [2010] manually digitized all of the grains visible in photographs of their study sites (in addition to performing an automated image analysis on the photographs) and compared the data to paint-and-pick surface samples collected after the photos were taken. In all cases, even the manually digitized ones, the photographic analyses identified considerably fewer grains in all size classes than in the paint-and-pick samples. However, this undercounting tended to be uniformly distributed, so the precision of the overall grain size distributions was excellent. This undercounting has been documented in previous photosieving studies as well [*Butler et al.*, 2001; *Graham et al.*, 2005b]. Because undercounting appears to be an unavoidable issue when using photographic grain size data, whereas distributions derived from photographs can provide excellent accuracy

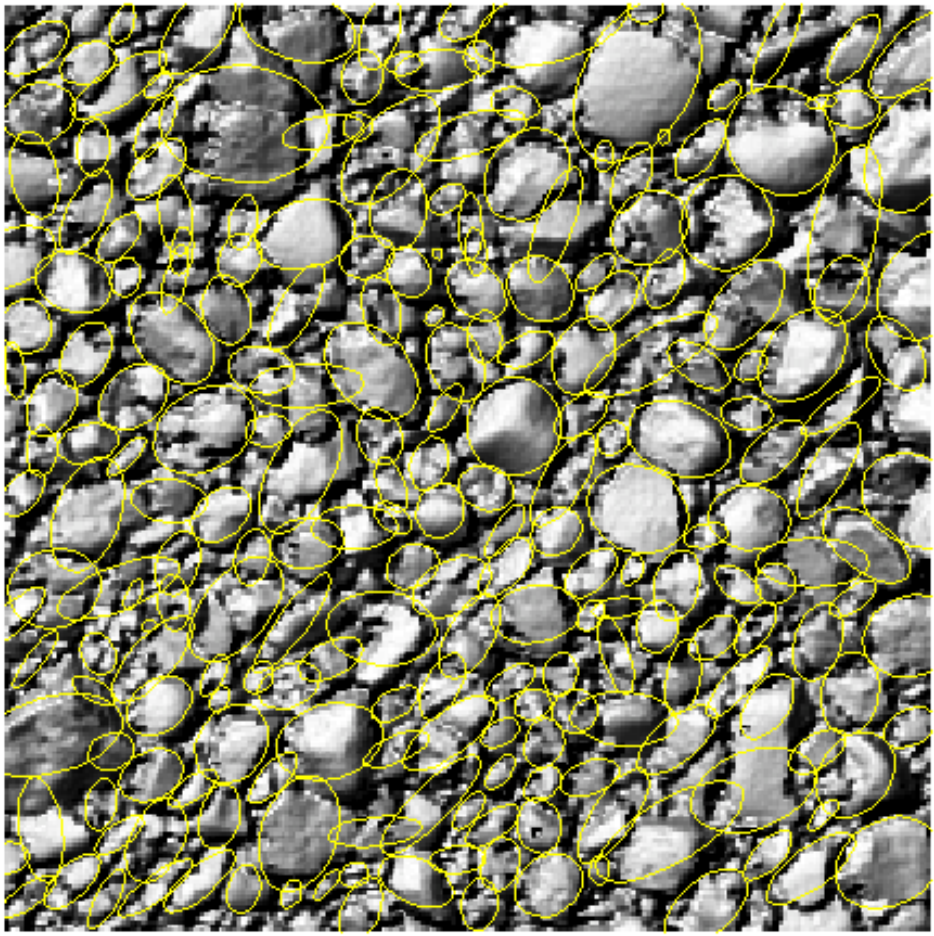

Figure 4.3: Portion of the 1×1 mm DEM with ellipses that best fit the grain regions after applying the *Graham et al.* [2005a] procedure to the image. The region depicted is 25 cm $\times$ 25 cm.

when compared to physical samples, it is probably better to use local grain size distributions rather than raw (x, y, D) data for the purpose of objectively identifying and delineating bed surface patches.

With this in mind, construction of the grid of distributions should adhere to a few rules. Distributions are constructed by dividing the bed into a grid such that each grid point becomes the center of a sampling area. All grains whose centroids lie within the sampling area are used to construct an area-by-number grain size distribution centered at that grid point. Enough grains should be included in the sampling area so that all grain sizes in the population are adequately represented; this places a constraint on the minimum size of the sampling area to be used. Studies examining the statistics of areal grain size distributions have suggested a wide range of acceptable sampling areas: *Diplas and Fripp* [1992] suggested that a sampling area of 100 times the area of the largest particle provides accuracy equivalent to a 100 grain grid sample; *Fripp and Diplas* [1993] suggested that a sampling area 400 times the area of the largest particle is necessary to meet the "low precision" criterion of *De Vries* [1970], and *Petrie and Diplas* [2000]'s more sophisticated approach suggested that areas smaller than 100 times the largest grain's area are acceptable. *Graham et al.* [2010]'s empirical examination of sampling area accuracy indicated that sample areas of around 100 times that of the largest grain produce estimates of the D_{50} within 5% and estimates of the D_{90} within 10%. In general, it seems that choosing a sampling area of 100 times that of the largest particles is a good guideline to follow.

In addition to selecting an appropriate sampling area size, it is necessary to truncate the grain size distributions at a lower bound. Truncation is generally necessary in field sampling (e.g., a *Wolman* [1954] pebble count) since operator bias often results in underrepresentation of fine particles [e.g., *Diplas and Fripp*, 1992; *Fripp and Diplas*, 1993]. Distributions generated from automated analysis of bed photographs also require truncation at a lower threshold because image resolution can impose a lower limit on what grain sizes may be reliably measured [e.g., *Graham et al.*, 2005a,b,c, 2010].

Once the (x, y, D) data have been converted into a spatial grid of grain size distributions, clustering techniques can be used objectively to delineate grain size patches on the bed surface. Several of these techniques are described in the following section.

4.4 Clustering methods

Clustering is of great interest to computer scientists and statisticians concerned with pattern recognition, data mining, image segmentation, and machine learning (among other areas). In a general sense, clustering is the unsupervised classification of patterns (observations, data items, or feature vectors) into groups (clusters) [*Jain et al.*, 1999]. *Jain* [2009] provides the following operational definition of clustering:

> Given a *representation* of n objects, find K groups based on a measure of *similarity* such that the similarities between objects in the same group are high while

the similarities between objects in different groups are low.

Here we outline the notation used in the application of clustering algorithms to spatial grain size data, and describe how partitional clustering, agglomerative clustering, and spectral clustering methods are used to delineate patch boundaries.

4.4.1 Data structure and notation

In the following analyses we apply clustering algorithms to a dataset that consists of a spatial grid of a total of m grain size distributions, $\mathfrak{F} = \{\mathbf{f}_1, \ldots, \mathbf{f}_m\}$. Each distribution $\mathbf{f}_i$ is an *observation* (also referred to as a *pattern* or *feature vector* in the clustering literature), which is a vector describing the ith cumulative or probability grain size distribution. $\mathfrak{F}$ is commonly referred to as a *pattern set*. If the grain size distributions have been discretized into N size classes, the ith distribution can be expressed as $\mathbf{f}_i = (f_{i,1}, \ldots, f_{i,N})$, where $f_{i,k}$ represents the percent of the kth grain size class in $\mathbf{f}_i$ if $\mathbf{f}_i$ is a probability distribution function, or the cumulative percent of the kth grain size class in $\mathbf{f}_i$ if it is a cumulative distribution function. Thus, if $\mathbf{f}_i$ is a probability distribution function, $\sum_{k=1}^{N} f_{i,k} = 100$, and if $\mathbf{f}_i$ is a cumulative distribution function, $f_{i,N} = 100$ and $\sum_{k=1}^{N-1}(f_{i,k+1} - f_{i,k}) = 100$. Each distribution also has spatial coordinates (x, y) which are denoted by the coordinate vector $\mathbf{X}$.

Clustering requires the quantification of the *similarity* between two observations. Similarity can be thought of as a scalar distance d_{ij} between feature vectors $\mathbf{f}_i$ and $\mathbf{f}_j$, which we will define using the Minkowski distance (of order p):

$$\begin{aligned} d_{ij} &= \left\{ \sum_{k=1}^{N} |f_{i,k} - f_{j,k}|^p \right\}^{1/p} \\ &= \|\mathbf{f}_i - \mathbf{f}_j\|_p. \end{aligned} \tag{4.1}$$

Using this notation, d_{ij} is the distance in N-dimensional space between the two grain size distributions $\mathbf{f}_i$ and $\mathbf{f}_j$. If $p = 2$, the measure calculates the Euclidean distance, and if $p = 1$ the measure calculates the "Manhattan" or "taxicab" or "city block" distance. If observations $\mathbf{f}_i$ and $\mathbf{f}_j$ are very similar, d_{ij} will be small, whereas d_{ij} will be large if the distributions are highly dissimilar.

4.4.2 Partitional clustering of the full dataset of grain size distributions

Facies maps of river beds typically divide the bed into a specified number of patch types, each of which has a characteristic grain size. For example, the patch map in Figure 4.2 has four patch types ("fine," "medium-fine," "medium-coarse," and "coarse"), each of which was distinguishable by its apparent grain size distribution. A similar approach can be taken with

a large number of grain size distributions: if one has m grain size distributions whose spatial locations are known and assumes that the distributions comprise k different patch types, each distribution can be assigned to a patch type and then mapped. Such an analysis can be performed using partitional clustering algorithms.

Partitional clustering algorithms find all of the clusters in a dataset simultaneously as a partition of the data and do not impose a hierarchical structure on the clusters [*Jain*, 2009]. The most popular and simplest partitional algorithm is k-means. The k-means algorithm clusters a pattern set (in our case, the entire set of m grain size distributions $\mathfrak{F} = \{\mathbf{f}_1, \ldots, \mathbf{f}_m\}$) into a set of k clusters ($\mathscr{C} = \{c_1, \ldots, c_k\}$) such that the squared error between the empirical mean of a cluster and the points in the cluster is minimized. If μ_α is the mean of cluster c_α (in N-dimensional space), the squared error between μ_α and the points in cluster c_α is defined as:

$$J(c_\alpha) = \sum_{\mathbf{f}_i \in c_\alpha} \|\mathbf{f}_i - \mu_\alpha\|_2^2 \tag{4.2}$$

The goal of k-means is to minimize the sum of the squared error over all k clusters:

$$J(\mathscr{C}) = \sum_{\alpha=1}^{k} \sum_{\mathbf{f}_i \in c_\alpha} \|\mathbf{f}_i - \mu_\alpha\|_2^2 \tag{4.3}$$

The algorithm accomplishes this goal by selecting an initial partition of k clusters and assigning each observation $\mathbf{f}_i$ to its closest cluster center. It then recomputes the cluster centers $\{\mu_1, \ldots, \mu_k\}$, reassigns the observations to the closest cluster centers, and iterates until cluster membership stabilizes. Since the outcome of this procedure is somewhat sensitive to the initial cluster centroids, the routine is usually repeated several times with different starting values and the result that achieves the lowest total error is retained. The procedure also depends on the choice of k, the total number of clusters, which must be determined in advance.

4.4.3 Spatially-constrained agglomerative clustering

Agglomerative clustering differs from partitional algorithms such as k-means because it produces a hierarchy of clusters. In our case, it also differs in that the clustering procedure is spatially constrained. The algorithm is simple and intuitive:

1. Assign each grain size distribution to be its own cluster.

2. Calculate the similarity between clusters, using the distance metric d_{ij} (Equation 4.1).

3. Merge the two *adjacent* (4- or 8-neighborhood) grain size distributions that are the most similar to form a new cluster. The grain size distribution of the new cluster is the area-weighted average of its components.

4. Repeat steps 2 - 3 until all of the grain size distributions comprise a single cluster.

Here, step 3 provides a spatial constraint to the clustering procedure so that grain size patches that emerge from this procedure will be continuously connected.

Agglomerative clustering can be visualized with a dendrogram, which is a binary tree that shows the sequence of clustering. The "leaves" of the tree are the initial nodes (individual grain size distributions); each time a new cluster is formed, they are linked with a horizontal line in the dendrogram. The height of the "branches" can indicate the similarity between the merged clusters, or may only signify the hierarchical order of clustering. A final clustering is achieved by thresholding the dendrogram at a particular level.

4.4.4 Spectral clustering using Normalized Cuts

Spectral clustering takes a different approach than the partitional and agglomerative methods discussed above. In the spectral clustering context, the data are represented as a graph $G = (V, E)$, where the vertices (nodes) V are the individual grain size distributions, and they are connected to each other with edges E. The edges are assigned weights based on a similarity function; that is, the edge between $\mathbf{f}_i$ and $\mathbf{f}_j$ has a weight equal to the similarity between $\mathbf{f}_i$ and $\mathbf{f}_j$. The graph is then partitioned into clusters of nodes by selectively cutting edges such that a cost function is minimized. The intuitive goal of most cost functions is to maximize within-cluster similarity and minimize the association between clusters; therefore, the tendency is to cut edges with low weights (low similarity).

Different algorithms exist to perform the partition; early studies used a minimum cut algorithm, which often results in clusters of imbalanced sizes. The ratio cut algorithm includes a cluster size constraint [*Hagen and Kahng*, 1992]. Normalized Cuts [*Shi and Malik*, 2000] was proposed from an image-segmentation perspective in which the authors advocate segmenting an image from the "big picture downward," so that global impressions of a scene play a role in segmentation rather than purely local cues which may tend to produce bad partitions.

Here, we explore how the Normalized Cuts cost function ($Ncut$) affects clustering of our dataset [*Shi and Malik*, 2000]. Maximizing within-cluster similarity and minimizing similarity between clusters can often naively be achieved by cutting edges such that a single node is isolated, but such a result is usually not the goal of cluster analysis. $Ncut$ seeks to prevent this by minimizing the cost function:

$$Ncut(A, B) = \frac{cut(A, B)}{assoc(A, V)} + \frac{cut(A, B)}{assoc(B, V)} \tag{4.4}$$

where A and B are two disjoint sets into which G is partitioned by removing edges connecting the two parts. $cut(A, B)$ is the total weight of the edges that are removed, and $assoc(\{A, B\}, V))$ is the total connection from all nodes in $\{A, B\}$ to all nodes in the graph. The incorporation of $assoc(A, V)$ and $assoc(B, V)$ into the denominator of the cost function

tends to prevent the clustering of a single node since in that case the denominator is likely to be small, which would make $Ncut(A, B)$ large.

Here, we use a Gaussian to compute the similarity w_{ij}:

$$w_{ij} = \begin{cases} \exp\left(\frac{-d_{ijnorm}}{\sigma_1}\right) \cdot \exp\left(\frac{-\|\mathbf{X}_i - \mathbf{X}_j\|_2}{\sigma_2}\right) & \text{if } \|\mathbf{X}_i - \mathbf{X}_j\|_2 < r \\ 0 & \text{otherwise} \end{cases} \tag{4.5}$$

where $\mathbf{X}_i$ are the (x, y) coordinates of the ith node, r is a threshold Euclidean distance (in the (x, y) plane) beyond which similarity is forced to be zero, d_{ijnorm} is the Minkowski distance between grain size distributions (as described above, equation 4.1) normalized to scale between 0 and 1, and σ_1 and σ_2 are parameters that scale the relative importance of the differences between the grain size distributions and physical distance.

Algorithms to minimize $Ncut$ are presented in *Shi and Malik* [2000] and *von Luxburg* [2007]. A MATLAB implementation of *Shi and Malik* [2000]'s $Ncut$ clustering algorithm is provided online (http://www.cis.upenn.edu/∼jshi/software/) and their algorithm will be used in the analysis that follows. *Shi and Malik* [2000]'s graph segmentation procedure does the following:

1. Given a graph $G = (V, E)$, compute the edge similarity weights w_{ij} and summarize them in the matrices $\mathbf{W}$ and $\mathbf{D}$. $\mathbf{W}$ is an $m \times m$ symmetric matrix where $\mathbf{W}(i, j) = w_{ij}$, and $\mathbf{D}$ is an $m \times m$ diagonal matrix with $\mathbf{d}$ on the diagonal, where $\mathbf{d}(i) = \sum_j w(i, j)$, that is, the total connection from node i to all other nodes.

2. The generalized eigenvalue system $(\mathbf{D} - \mathbf{W})\mathbf{x} = \lambda\mathbf{D}\mathbf{x}$ is solved for eigenvectors $\mathbf{x}$ with the smallest eigenvalues λ.

3. The eigenvector with the second smallest eigenvalue is used to bipartition the graph by finding a splitting point such that $Ncut$ is minimized.

4. The stability of the current cut is checked (the eigenvector is checked to ensure it is not overly smooth, which could produce an uncertain cut), and the segmented parts of the dataset are recursively partitioned until the prespecified number segments is achieved.

As with the other clustering algorithms, the total number of clusters k needs to be decided by the user. This is discussed further in section 4.6.

4.5 Results

The clustering procedures described above were applied to a spatial grid of grain size distributions derived from automated image analysis of the 1×1 mm DEM of the bed at the end of the alternate bar phase of the SAFL experiment [*Nelson et al.*, 2010]. Using

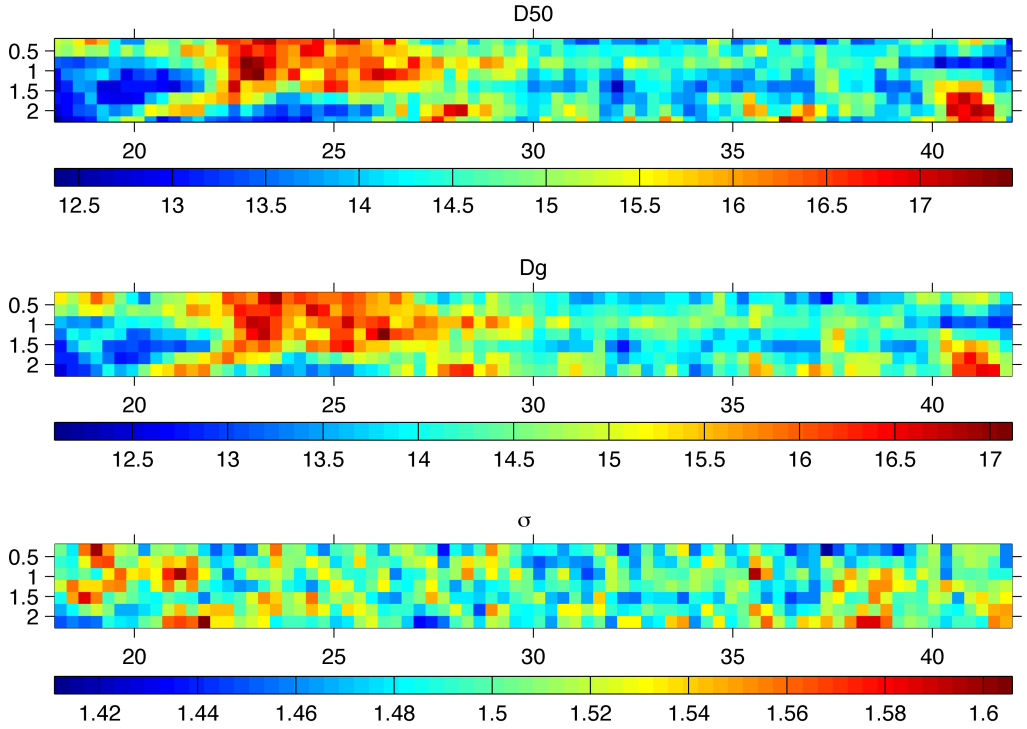

Figure 4.4: D_{50}, D_g, and σ of our test dataset. Color bars for D_{50} and D_g are in mm. The x- and y-coordinates are in meters. Flow was from left to right.

the guideline that sampling area size should be 100 times the area of the largest grain, we chose a sampling area of 0.4 m $\times$ 0.4 m (sufficient for a D_{max} of 45 mm). The grain size distributions were generated on a grid with spacing in the x- and y-directions of 0.3 m, so grains whose centroids fell within 5 cm of the edge of a grid cell contributed to the distribution of that grid cell as well as its neighbor grid cell. This produced a mild spatial smoothing effect while maintaining statistical integrity of each grain size distribution, which is a useful characteristic when the goal is to be able to pick out patch-scale features. The area-by-number distributions were binned into half-ψ intervals ($D = 2^{\psi}$), truncated at 4 mm and converted to volume-by-weight distributions using the voidless cube model of *Kellerhals and Bray* [1971], which are more widely-used in sediment transport relations [e.g., *Parker*, 1990; *Wilcock and Crowe*, 2003]. Figure 4.4 shows the spatial arrangement of the median grain size D_{50}, the geometric mean grain size D_g, and the geometric standard deviation σ of the distributions.

The clustering algorithms described in Section 4.4 were applied to the data in the form

of cumulative distribution functions rather than probability distribution functions. By using cumulative distribution functions, importance is placed on the order of components in $\mathbf{f}$, so the data are essentially treated as curves rather than unrelated multiparameter vectors [e.g., *Hamilton*, 2007]. Clustering algorithms therefore should perform better on cumulative grain size distribution functions rather than frequency distributions. Since the data in Figure 4.4 are what are being classified into clusters, maps of clustered results in the following sections should be compared to Figure 4.4 rather than the hand-drawn map in Figure 4.2. Any discrepancies between Figures 4.2 and 4.4 are due to some combination of visual mapping confusion and inaccuracy of the automated grain size analysis.

4.5.1 *k*-means partitioning

Since the hand-drawn patch map (Figure 4.2) divided the flume bed into four patch types, a natural starting point for partitional clustering is to set the total number of clusters k to 4. k-means was applied 10 times with random initial cluster means to the entire set of cumulative distribution functions, and the result with the lowest total error was retained. Figure 4.5 shows all of the cumulative distribution functions color coded by their k-means-determined patch type, and Figure 4.6 shows each grid cell shaded according to this patch assignment.

The map of k-means-clustered grain size distributions (Figure 4.6) shows some areas of coherent structure, such as the coarse bar top on the left side of the channel between $x = 22$ and $x = 27$ m. However, the lack of spatial consideration during the clustering process is evident: much of the image is quite noisy and unlikely to be considered "patchy."

4.5.2 Spatially-constrained agglomerative clustering

Figure 4.7 shows the dendrogram resulting from spatially-constrained agglomerative clustering on our grid of cumulative distribution functions, using $p = 1$ (Manhattan distance between distributions) and an 8-neighborhood adjacency matrix.

The dendrogram in Figure 4.7 can be thresholded to produce a specified number of patches. Figure 4.8 shows the outcome of thresholding the dendrogram from $k = 2$ to $k = 40$ total clusters.

This technique is generally capable of recovering the general pattern shown on the hand-drawn patch map (Figure 4.2). It does produce some singleton clusters, such as the single cell in the $k = 2$ map, for particular grain size distributions that are very different from all of their neighbors.

4.5.3 Spectral clustering with *Ncut*

The outcome of applying *Ncut* to our set of cumulative distribution functions is highly dependent upon the parameters used to construct the similarity matrix $\mathbf{W}$ (Equation 4.5).

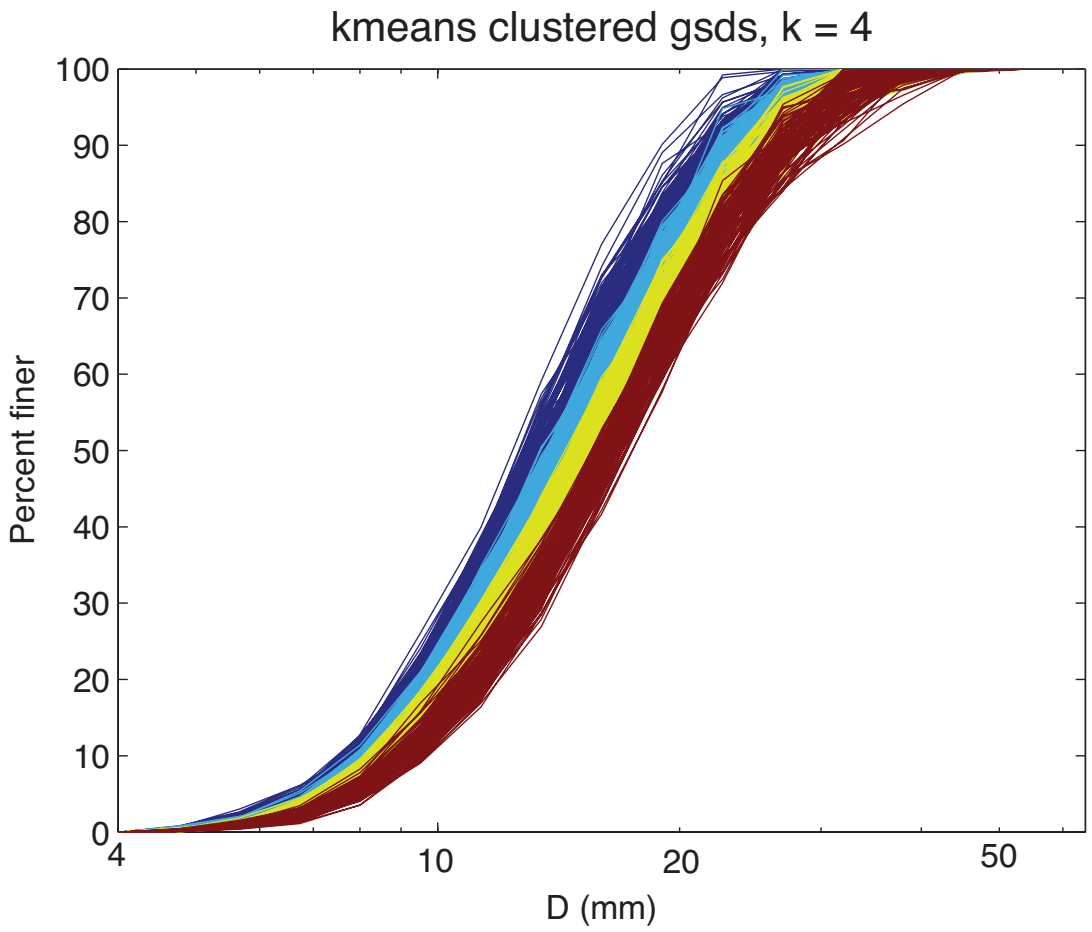

Figure 4.5: Cumulative distribution functions classified by k-means, with $k = 4$. Colors correspond to the map in Figure 4.6.

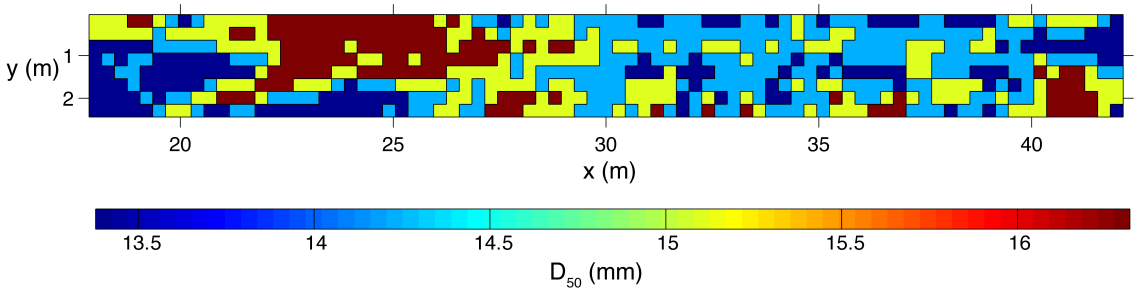

Figure 4.6: Map of the bed of the SAFL flume where the color of each grid cell represents the patch type assigned to its cumulative distribution function by k-means, with $k = 4$. The color corresponds to the patch-average D_{50}, as shown in the color bar (cooler colors belong to finer patch types). The colors also correspond to the distributions plotted in Figure 4.5.

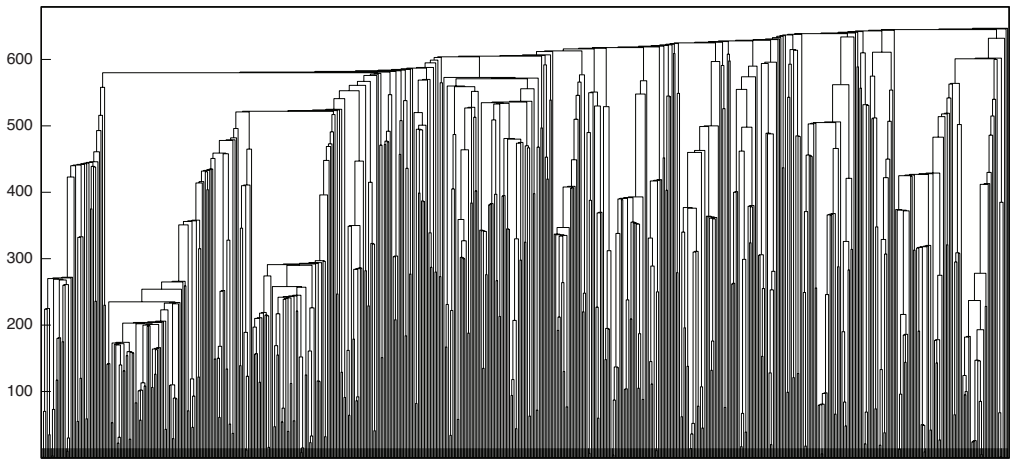

Figure 4.7: Hierarchical dendrogram resulting from spatially-constrained agglomerative clustering of the grid of cumulative distribution functions, using an 8-neighborhood adjacency matrix and $p = 1$. Individual grain size distributions (leaves) lie along the bottom axis; the heights of the branches signify the order of clustering.

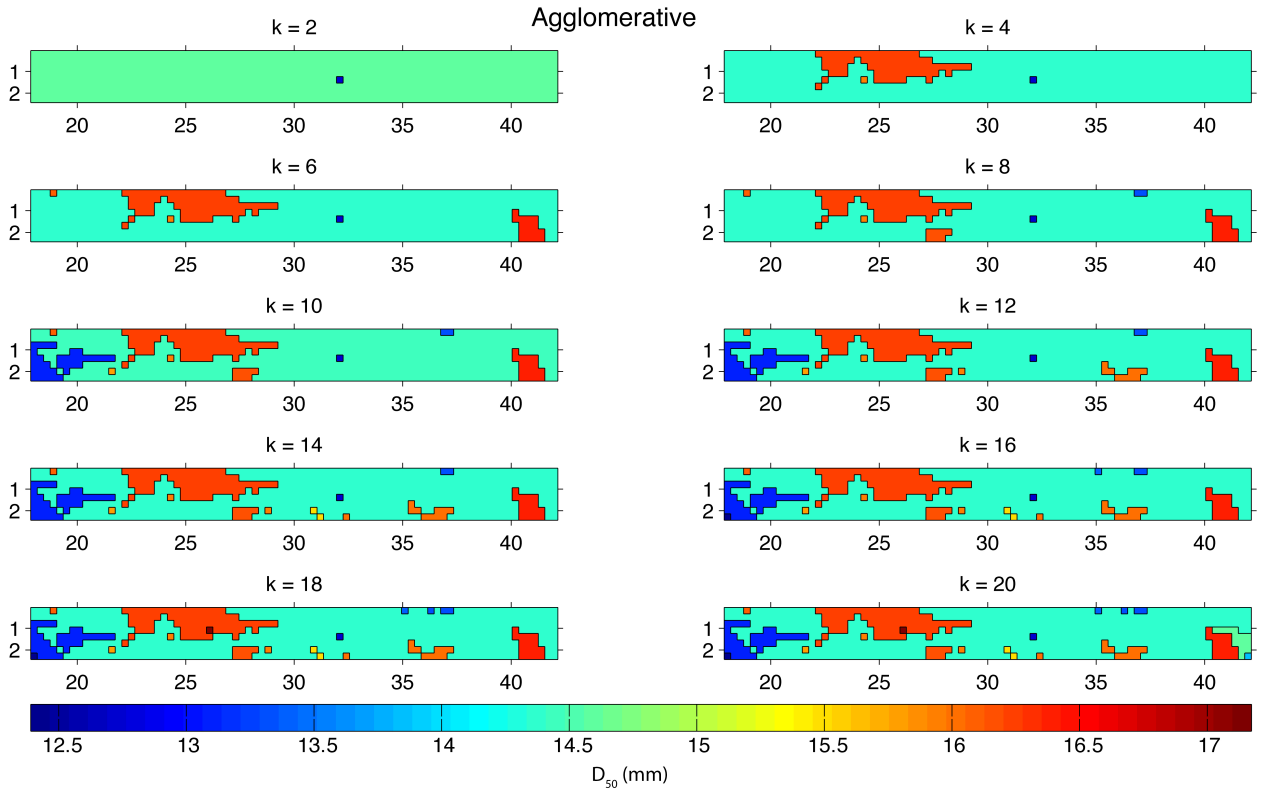

Figure 4.8: Patch maps from agglomerative clustering, for $k = 2$ to 40 total clusters. Patch color corresponds to the patch-averaged D_{50} as shown on the color scale. (Continued on the next page).

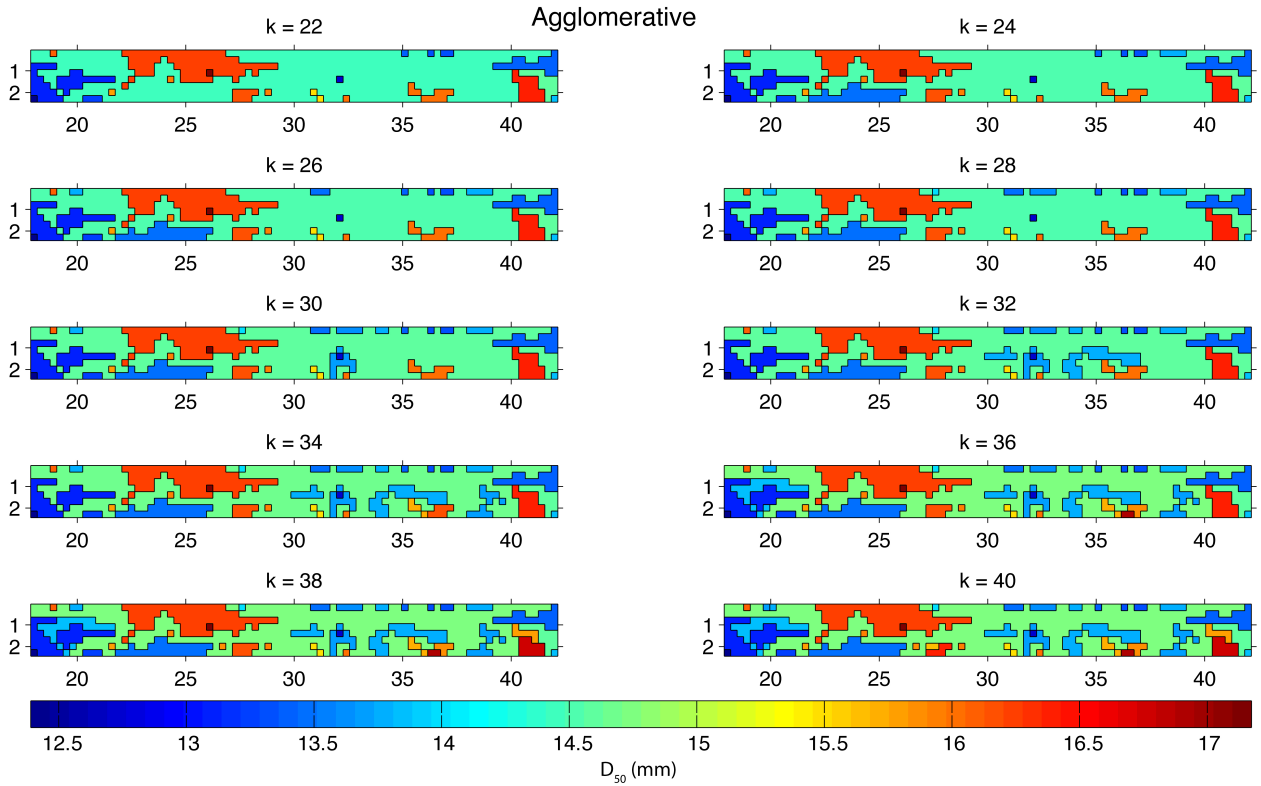

Figure 4.8: (continued)

The parameters σ_1 and σ_2 appear in the denominator of the negative exponentials and they scale the relative importance of d_{ijnorm}, the Minkowski distance between grain size distributions $\mathbf{f}_i$ and $\mathbf{f}_j$, and the relative importance of the (x, y) Euclidean distance between nodes i and j, respectively. It is important to choose values of σ_1 and σ_2 that effectively balance the contribution of grain size and distance to the similarity w_{ij}. If σ_1 is very small, d_{ijnorm} dominates w_{ij} and the algorithm produces spread-out clusters similar to the output of k-means on the set of grain size distributions (Figure 4.6). If σ_2 is very small, the Euclidean distance $\|\mathbf{X}_i - \mathbf{X}_j\|_2$ dominates w_{ij} and the bed becomes divided into k evenly-sized clusters. Additionally, the r parameter dictates the physical distance over which one grain size distribution may be considered to influence another; if r is very small, the outcome is similar to one with σ_2 very small.

After some experimentation with these parameters, we determined that setting $r = 10$ grid cells, $\sigma_1 = 0.008$, $\sigma_2 = 10$, and $p = 1$ (Manhattan distance between distributions) tends to produce clusters that are appropriately influenced by both physical Euclidean distance and the distance between distributions in N-dimensional space. Figure 4.9 depicts the similarity matrix $\mathbf{W}$ calculated for our grid of cumulative distribution functions, which is an $m \times m$ sparse matrix where values closer to 1 indicate greater similarity.

Figure 4.10 shows how the bed is partitioned for a total $k = 2$ to 11 clusters using the similarity function shown in Figure 4.9. The color of the patches in Figure 4.10 corresponds to their patch-averaged D_{50}. One striking difference between *Ncut* and the spatially-constrained agglomerative clustering is that here, in some instances a single patch can have several isolated regions. This is because we allow the similarity w_{ij} to be greater than zero for any two nodes that are separated by less than the distance r, which in this case is 10 grid points. If we chose to set $r = 1$, we would effectively be enforcing the same spatial constraint we used for agglomerative clustering, but doing so would negate many of the advantages of global cues built into the spectral clustering framework.

Normalized Cuts tends to produce distributions of patches similar to the hand-drawn map in Figure 4.2. Although *Ncut* tries to make patches of roughly similar size, it will delineate smaller regions of the bed that have significantly different grain size characteristics than their neighbors (e.g., the coarse patch at about $x = 40$ m). Not all of the patches are single cohesive units, however: because $r = 10$ in our similarity function, a single patch may be several disjoint regions of the bed.

4.6 Discussion

The patch maps produced from the application of these clustering algorithms to our spatial grid of grain size distributions prompt several questions, the most practical of which is: which method is the best choice? Each technique has its own set of advantages and disadvantages. Given a set of grain size distributions, the simplest possible way of classifying them into groups is to partitionally cluster them by comparing only the distribution curves

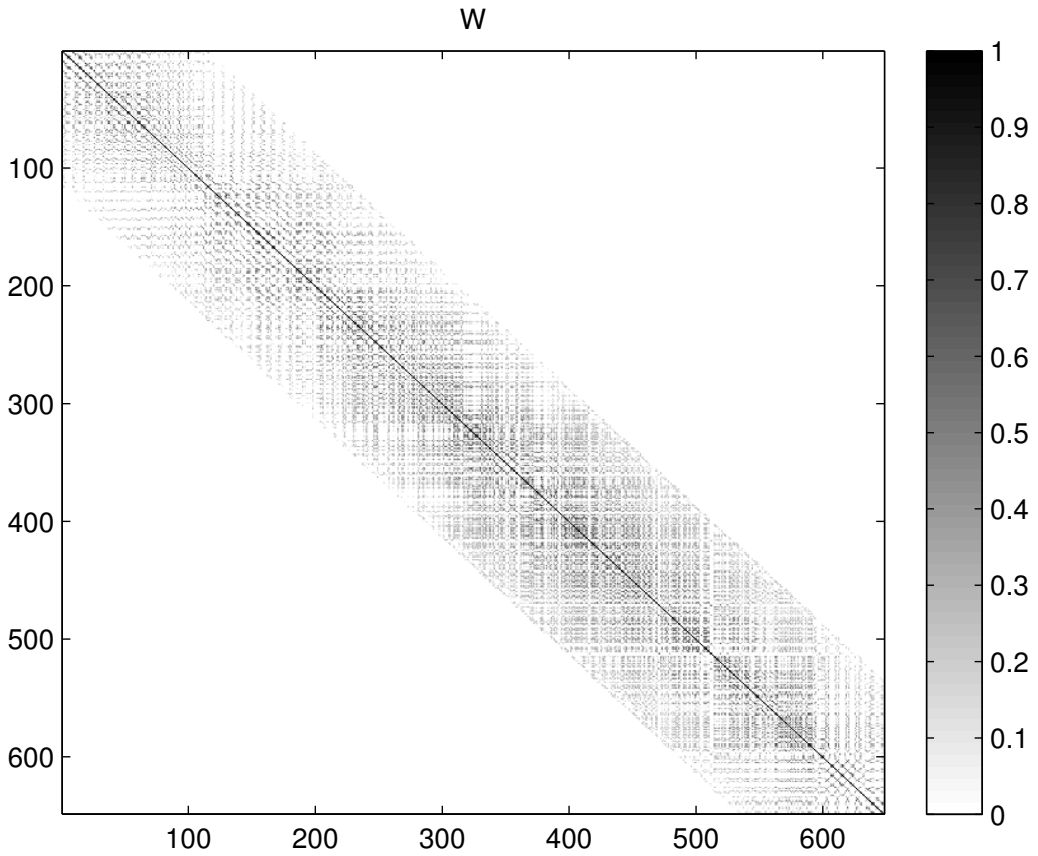

Figure 4.9: Similarity matrix $\mathbf{W}$ constructed with the following parameters: $r = 10$ grid cells, $\sigma_1 = 0.008$, $\sigma_2 = 10$, and $p = 1$ (Manhattan distance between distributions). Darker pixels are entries where w_{ij} is closer to 1, indicating a higher similarity between nodes i and j.

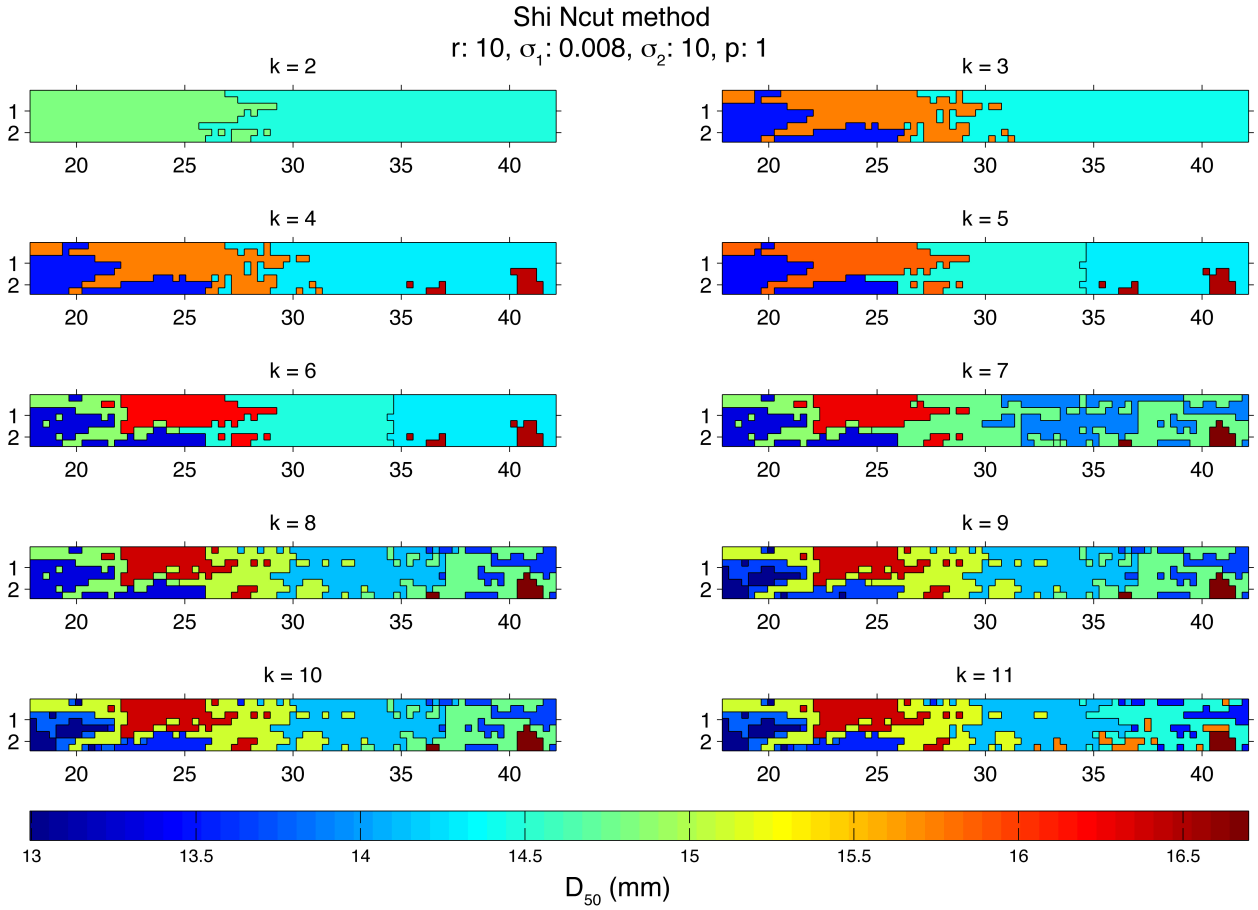

Figure 4.10: Bed discretization resulting from the application of *Ncut* using the similarity matrix shown in Figure 4.9 for $k = 2$ to 11 total clusters. Patches are colored according to their patch-averaged D_{50}, which is shown on the color scale.

and not considering spatial location of each distribution. With this approach, any spatial structure that emerges from mapping the classified distributions is coincidental; in our case, k-means produced a few coherent patches, but much of the bed consisted of a quasi-random scattering different patch types, which is generally not a desired outcome of facies mapping (Figure 4.6). This is not an indictment of the k-means method in general; with the appropriate inclusion of constraints [e.g., *Kulis et al.*, 2005], the k-means algorithm can produce output similar to that of spectral clustering. It suggests, however, that inclusion of spatial coordinates of grain size distributions during classification is necessary if the goal is to divide the bed into coherent patches.

In contrast to our naive partitional approach that ignores spatial location, spatially-constrained agglomerative clustering will only merge neighboring distributions. The spatial constraint ensures that the patches produced by the algorithm will be cohesive, and the hierarchical dendrogram it produces offers the potential to examine multiple scales of grain size variation (e.g., Figure 4.8). However, the procedure is more memory-intensive than the others since the entire dendrogram must be stored, and the method appears to produce singleton clusters more readily than the other methods. Additionally, one must choose where to threshold the dendrogram to produce a final patch map; this can be achieved by thresholding at all levels of the tree, then choose the best result based on a predefined criteria such as a statistical comparison of all clusters produced at a given threshold. This should be fairly efficient since the tree structure of the dendrogram should have $\log(m)$ levels on average.

Because it is a normalized spectral method rooted in graph theory, Normalized Cuts has the advantage of simultaneously satisfying the minimization of dissociation within clusters and maximizing the association within clusters, which is the fundamental goal of cluster analysis. But the method is quite sensitive to the parameters of the similarity function w_{ij}, and it can produce somewhat disjoint patches because the r parameter allows non-adjacent nodes to influence the segmentation process. It also requires a choice of the maximum number of clusters.

All three methods require the user to choose the maximum number of clusters, k, either directly as in k-means or $Ncut$, or indirectly through the choice of where to threshold the dendrogram produced by agglomerative clustering. In general, how to choose k is an unresolved question in clustering analysis. *von Luxburg* [2007] suggests that, in spectral clustering, plotting the lowest eigenvalues and choosing a k that corresponds to a large eigengap may provide useful results, but this technique is generally useful only when there are very distinct clusters in the data. Figure 4.11 shows the lowest 50 eigenvalues of our dataset when *von Luxburg* [2007]'s $Ncut$ algorithm is applied. There are rather large gaps between eigenvalues 4 and 5, between 6 and 7, and between 10 and 11, so one might select $k = 4$, 6, or 10 based on this heuristic. In Figure 4.10, the transition from $k = 4$ to $k = 5$ introduces a partition of the bed at about $x = 35$ m into adjacent regions with very similar D_{50}. Going from $k = 6$ to $k = 7$, that same partition dissolves into a more diffuse boundary, and the difference between $k = 10$ and $k = 11$ is nearly indistinguishable.

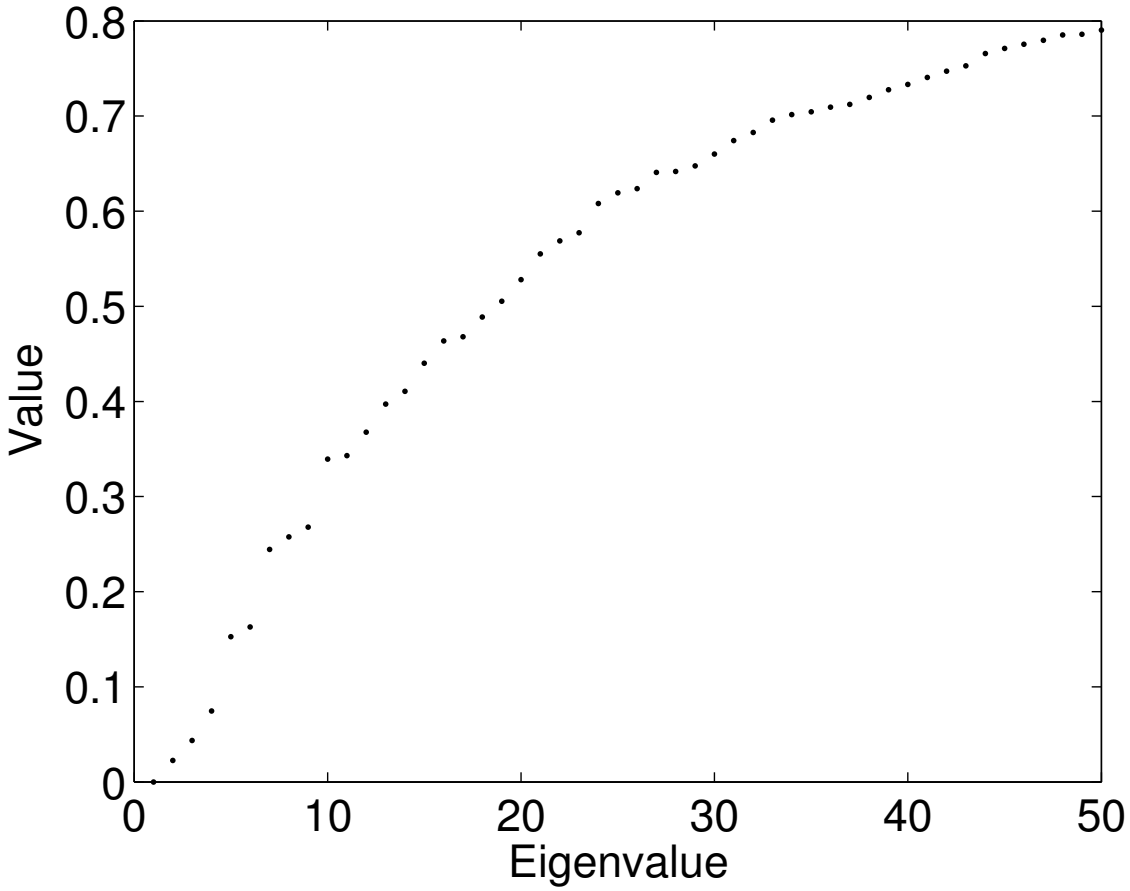

Figure 4.11: The smallest 50 eigenvalues resulting from implementation of the *von Luxburg* [2007] method for *Ncut* spectral clustering. Relatively large gaps between eigenvectors 4 and 5, 6 and 7, and 10 and 11 suggest those may be good choices for the total number of clusters k.

Because clustering algorithms will produce clusters from any dataset, even white noise, a statistical comparison of the patch-averaged grain size distributions can be useful for distinguishing whether the clustering result is meaningful and for informing the choice of k. For each algorithm, the data were classified into k clusters, with k ranging from 2 to 30. The average grain size distribution of each cluster was determined and compared to every other cluster-averaged grain size distribution with the two-sample Kolmogorov-Smirnov goodness-of-fit test [e.g., *Conover*, 1971; *Borradaile*, 2003]. This widely-used nonparametric test compares two frequency distributions and determines the likelihood that they come from the same underlying distribution. The test statistic is the maximum difference between the two cumulative distribution curves, that is:

$$KS = \sup |\mathbf{f}_i - \mathbf{f}_j| \tag{4.6}$$

where KS is the test statistic, $\mathbf{f}_i$ and $\mathbf{f}_j$ are the two cumulative distributions (scaled between 0 and 1), and sup designates the *supremum*. KS is compared at a significance level α to a threshold value KS_α, which is a function of $\sqrt{\frac{n_i n_j}{n_i+n_j}}$, where n_i and n_j are the number of observations contributing to the distributions $\mathbf{f}_i$ and $\mathbf{f}_j$. If α exceeds the asymptotic p-value computed from the samples, the null hypothesis that $\mathbf{f}_i$ and $\mathbf{f}_j$ come from the same distribution can be rejected (that is, if $\mathbf{f}_i$ and $\mathbf{f}_j$ actually do belong to the same distribution, there is a probability α that the data deviate so far from each other that we mistakenly reject the null hypothesis). In our analysis, $\mathbf{f}_i$ and $\mathbf{f}_j$ were generated by retrieving all of the individual (x, y, D) grain size measurements in each patch, allowing n_i and n_j to be known. We also selected a significance level of $\alpha = 0.01$.

Figure 4.12 shows the number of statistically different patch types shown by the Kolmogorov-Smirnov test produced with each clustering algorithm for $k = 2$ to 30. For low values of k, all of the clusters produced by each algorithm are statistically distinct patch types. However, spatially-constrained agglomerative clustering never produces more than five statistically different patch types, even as k increases to 30. The number of distinct patch types produced by *Ncut* spectral clustering begins to diverge from k at $k = 10$ and stabilize to between about 9 and 15 patch types. The number of statistically distinct patch types produced by the k-means implementation, however, only begins to diverge from k once k exceeds 25, and even then it does not indicate an asymptotic leveling-off like the other algorithms.

The divergence from the 1 : 1 relationship between the number of clusters k and the number of statistically distinct patch types is due to the way the algorithms account for spatial location when classifying each grain size distribution. The k-means implementation does not account for spatial location at all and classifies the distributions solely based on grain size data; therefore, that k is generally equal to the number of distinct patch types is a sign that the algorithm is doing its job. Only when k becomes large does it become difficult for the algorithm to partition the data into statistically distinct groups. *Ncut* and our agglomerative clustering implementations, however, do take a grain size distribution's

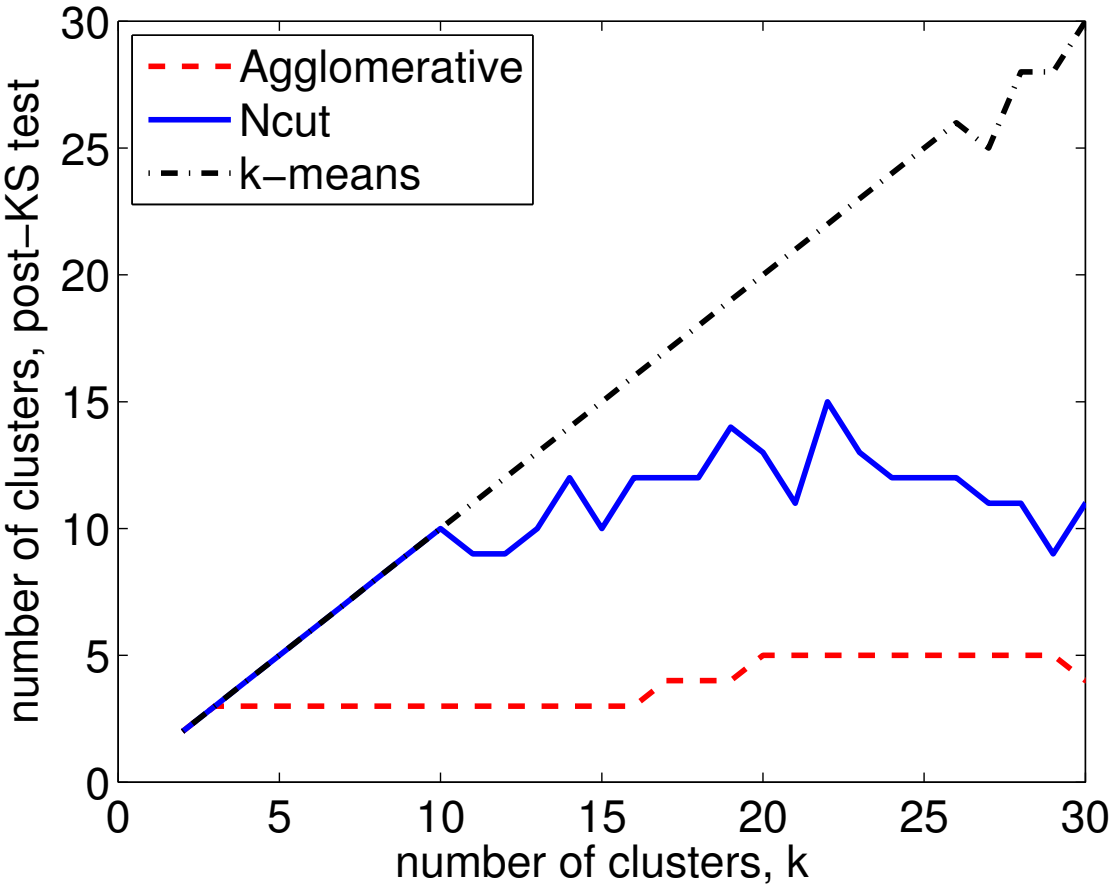

Figure 4.12: Number of statistically different patch types resulting from application of the two-sample Kolmogorov-Smirnov test to all pairs of clusters resulting from each clustering technique for a given value of k.

spatial location into account when classifying it, and this appears to impose a natural limit on the number of patch types produced. Because the criteria for spatial proximity is less rigidly enforced in $Ncut$ than it is for our constrained agglomerative clustering, $Ncut$ produces more patch types. It may not be coincidental that the limiting number of patch types produced by these clustering algorithms corresponds to eigengaps in Figure 4.11.

This analysis suggests a path toward answering a fundamental question about gravel-bedded rivers: is there a tendency in rivers to create certain kinds of patches, or do rivers exhibit a continuous gradation of patchiness that depends almost entirely on local hydrodynamic and sediment supply conditions? Our analyses using spatially-constrained agglomerative clustering and spectral clustering suggest that while local flow and sediment supply conditions are no doubt critical for the formation and maintenance of patches, there nevertheless is a tendency for the channel to form a finite number of patch types that become distributed throughout the reach.

4.7 Conclusions

River beds can display remarkable heterogeneity. Facies maps depicting the distribution of bed surface patches of similar grain size and sorting are a convenient way of describing this complexity, and the growing availability of very high resolution grain size data provides an opportunity to draw boundaries around bed surface patches using objective criteria. The criteria used to classify data into patches should seek to maximize intra-patch similarity while minimizing between-patch similarity.

In this study, we have explored the application of different clustering techniques to a spatial grid of bed surface grain size distributions. The simplest possible method assigns raw grain size distributions to clusters, without regard to their spatial location, using a partitional clustering algorithm. Because this technique tends to produce maps that lack spatially coherent patches, it is apparent that inclusion of information on location needs to be accounted for during the classification process. The techniques we use that include spatial information as well as grain size distribution characteristics, spatially-constrained agglomerative clustering and spectral clustering, produce more consolidated patches than the naive partitional method.

Statistical comparisons of the grain size distributions of the clusters output from the spectral and agglomerative algorithms indicate that a finite number of patch types are present on the channel bed. This suggests that rivers tend to form certain types of patches that may repeatedly emerge at different locations.

Chapter 5

Numerical experiments on the coevolution of bed surface patchiness and channel morphology

5.1 Introduction

The beds of gravel-bedded rivers and flumes commonly display considerable heterogeneity, in which the bed may be organized into patches of distinct grain size and sorting [e.g., *Nelson et al.*, 2009, 2010, and references therein]. Recent flume experiments have shed light on the mechanisms responsible for the formation of free and forced patches. *Nelson et al.* [2009] documented the formation of bedload sheets in both a sand-gravel mixture and a sand-free gravel mixture; in both cases, grain interactions (the "catch-and-mobilize" process) appeared to be responsible for the formation and propagation of bedload sheets. Additionally, the downstream speed of migration of bedload sheets and the spacing between sheets was found to be controlled by the sediment supply. *Nelson et al.* [2010] documented the development of forced patches over an alternate bar sequence in a near-field scale flume experiment using a gravel mixture. Their observations of the surface sorting, bed topography, near-bed flow field, and local sediment transport field suggested that the sorting patterns they observed were the result of topographically-driven stress gradients being compensated by size-selective sediment transport divergences and bed surface coarsening and fining.

Bed surface patches are the manifestation of a complex set of interactions of several driving mechanisms. Bed topography evolves as local erosion and deposition occurs, which is a consequence of spatial gradients in the sediment transport rate. The sediment transport field responsible for bed evolution is controlled by fluid drag forces and gravitational forces acting on a sloping bed. These forces have a highly nonlinear effect on the sediment transport rate. Bed topography also exerts considerable control on the flow field; bed morphology, channel curvature, and flow obstructions cause the flow to deviate from uniform conditions

through topographic steering effects [e.g., *Nelson and Smith*, 1989a], the generation of lateral eddies and secondary circulations associated with helical flow.

These processes all occur in both uniform sediment and in sediment mixtures. However, the presence of multiple grain sizes add several levels of complexity to the uniform system. The sediment transport rate depends on the local bed surface grain size distribution in addition to the local boundary shear stress [e.g., *Parker*, 1990; *Wilcock and Crowe*, 2003]. Local hiding effects due to differing amounts of exposure to fluid drag cause the critical shear stress for sediment motion to be a function of particle size and the ratio of particle's size to its neighbor particles [e.g., *Wiberg and Smith*, 1987; *Kirchner et al.*, 1990; *Buffington et al.*, 1992; *Buffington and Montgomery*, 1997; *Lamb et al.*, 2008]. Depending on the magnitude of the shear stress, the size distribution of the sediment load can differ significantly from that of the bed surface [*Wilcock and McArdell*, 1993]. Gravitationally-driven lateral flux is also affected by grain mixtures since heavier coarse particles are more affected by gravity than fine particles. During sediment transport, grains may interact with each other to form bedload sheets or other bedforms [*Whiting et al.*, 1988; *Dietrich et al.*, 1989; *Nelson et al.*, 2009]. The bed surface grain size distribution also can affect the hydrodynamics by modifying the local roughness [*Leopold and Wolman*, 1957; *Dietrich and Whiting*, 1989; *Wilcock*, 1996], which can affect near bed velocity and consequently particle mobility [e.g., *Venditti et al.*, 2010]. Under conditions of low sediment supply, coarse particles can form clusters of roughness elements that can act to stabilize the bed [*Church et al.*, 1998; *Hassan and Church*, 2000].

Because of the complexity and nonlinearity of these processes, numerical models can be particularly useful for morphological prediction and improved understanding of feedbacks between the processes that underlie morphologic evolution of the river bed. Fluvial systems of uniform sediment have been modeled with considerable success to show how interactions between bed topography and flow lead to bar formation [e.g., *Nelson and Smith*, 1989a,b; *Nelson*, 1990; *Nelson et al.*, 2003] or planform meandering [e.g., *Howard*, 1992, 1996; *Duan and Julien*, 2005] in unisize sediment. However, two-dimensional or three-dimensional models simulating the evolution of river channels composed of gravel mixtures are less prevalent. Some two-dimensional models capable of handling sediment mixtures have been developed [e.g., *Sun et al.*, 2001a,b; *Takebayashi et al.*, 2011], although they have not focused on the coevolution of bed patchiness and bed topography.

Here, we use a morphodynamic model that implements standard, frequently-used flow, mixed-grain sediment transport, and bed evolution equations to simulate the development of alternate bars under steady flow with a gravel mixture to conduct a more detailed investigation of some of these mechanisms. We perform numerical experiments to address the following questions: What are the mechanisms that produce forced patches, and what is the relative importance of each? How do forced patches affect bed morphology? Does morphology drive patchiness, or is there a feedback of patchiness on the morphology? How do patches and the bed co-evolve? And what sets the range of variation of grain size on the bed? Our modeling results provide insight on these questions and highlight potentially important mechanisms that require further research.

5.2 Morphodynamic model

The morphodynamic model we use is a version of FaSTMECH (Flow and Sediment Transport and Morphological Evolution of CHannels) [*Nelson and McDonald*, 1995; *Nelson et al.*, 2003; *McDonald et al.*, 2005] modified to be able to simulate mixed-grain size sediment transport and bed evolution. The hydrodynamic model computes the depth-averaged flow field, which is used to calculate the sediment transport field, which enables the bed elevation and bed surface grain size distribution to be updated.

5.2.1 Hydrodynamic model

The hydrodynamic portion of the FaSTMECH model is fully described in *Nelson and McDonald* [1995], and summarized here. FaSTMECH solves the vertically-averaged equations of mass and momentum in a curvilinear coordinate system [as derived by *Smith and McLean*, 1984]:

$$\frac{1}{1-N}\frac{\partial}{\partial s}(\langle u\rangle h) - \frac{\langle v\rangle h}{(1-N)R} + \frac{\partial}{\partial n}(\langle v\rangle h) = 0 \tag{5.1}$$

$$\begin{aligned}\frac{1}{1-N}\frac{\partial}{\partial s}(\langle u\rangle^2 h) + \frac{\partial}{\partial n}(\langle u\rangle\langle v\rangle h) - \frac{2\langle u\rangle\langle v\rangle h}{(1-N)R} = -\frac{gh}{1-N}\frac{\partial E}{\partial s} \\ + \frac{1}{\rho}\left[\frac{1}{1-N}\frac{\partial}{\partial s}(\langle\tau_{ss}\rangle h) + \frac{\partial}{\partial n}(\langle\tau_{ns}\rangle h) - \frac{2\langle\tau_{ns}\rangle h}{(1-N)R}\right] \\ + \frac{1}{\rho}\left[\frac{1}{1-N}(\tau_{ss})_b\frac{\partial\eta}{\partial s} + (\tau_{ns})_b\frac{\partial\eta}{\partial n} - (\tau_{zs})_b\right]\end{aligned} \tag{5.2}$$

$$\begin{aligned}\frac{1}{1-N}\frac{\partial}{\partial s}(\langle u\rangle\langle v\rangle h) + \frac{\partial}{\partial n}(\langle v\rangle^2 h) - \frac{(\langle u\rangle^2 - \langle v\rangle^2)h}{(1-N)R} = -\frac{gh}{1-N}\frac{\partial E}{\partial n} \\ + \frac{1}{\rho}\left[\frac{1}{1-N}\frac{\partial}{\partial s}(\langle\tau_{ns}\rangle h) + \frac{\partial}{\partial n}(\langle\tau_{nn}\rangle h) - \frac{\langle\tau_{ss}-\tau_{nn}\rangle h}{(1-N)R}\right] \\ + \frac{1}{\rho}\left[\frac{1}{1-N}(\tau_{ns})_b\frac{\partial\eta}{\partial s} + (\tau_{nn})_b\frac{\partial\eta}{\partial n} - (\tau_{zn})_b\right]\end{aligned} \tag{5.3}$$

where s and n are the channel-fitted downstream and cross-stream coordinates, respectively, R is the radius of curvature along the centerline (at $n = 0$), N is a metrical coefficient accounting for the curvilinear coordinate system ($N = n/R$), $\langle u\rangle$ and $\langle v\rangle$ are the depth-averaged streamwise and cross-stream velocities, h is the flow depth, g is gravitational acceleration, E is the water surface elevation, η is the bed elevation, ρ is the density of water,

$\langle \tau_{ss} \rangle$ and $\langle \tau_{ns} \rangle$ are depth-averaged components of the Reynolds stress tensor, and $(\tau_{ss})_b$ and $(\tau_{ns})_b$ are the components of the shear stress evaluated at the bed.

The components of the Reynolds stress tensor are given by

$$\tau_{ss} = 2\rho K \left[\frac{1}{1-N} \frac{\partial u}{\partial s} - \frac{v}{(1-N)R} \right] \tag{5.4a}$$

$$\tau_{nn} = 2\rho K \frac{\partial v}{\partial n} \tag{5.4b}$$

$$\tau_{ns} = \rho K \left[\frac{1}{1-N} \frac{\partial v}{\partial s} + \frac{u}{(1-N)R} + \frac{\partial u}{\partial n} \right] \tag{5.4c}$$

where K is the vertically-averaged kinematic eddy viscosity, which we scale with the free-stream velocity U and the average depth h:

$$K = CUh \tag{5.5a}$$

$$C = \frac{\kappa \sqrt{C_d}}{6} + \alpha \tag{5.5b}$$

The first term in the expression for C represents the commonly-used parabolic depth-averaged eddy viscosity model; κ is von Karman's constant ($\kappa \approx 0.408$), and C_d is a drag coefficient, discussed below. The second term, α, is an empirical correction factor meant to account for lateral separation problems and quasi-two-dimensional unsteadiness; α is expected to take a value between 10^{-3} and 10^{-2} [see *Nelson and McDonald*, 1995].

The boundary shear stress is calculated with a drag coefficient closure:

$$(\tau_{zs})_b = \rho C_d \sqrt{\langle u \rangle^2 + \langle v \rangle^2} \langle u \rangle \tag{5.6a}$$

$$(\tau_{zn})_b = \rho C_d \sqrt{\langle u \rangle^2 + \langle v \rangle^2} \langle v \rangle \tag{5.6b}$$

where C_d is a drag coefficient, which can take on a constant value or it can be spatially variable. If the drag coefficient is chosen to be spatially variable, it can be calculated using the simplifying approximation of a logarithmic velocity profile throughout the water column by combining equation 5.6 with the law of the wall to relate C_d as a function of the depth h and roughness length z_0:

$$C_d = \left[\frac{1}{\kappa} \left(\ln \frac{h}{z_0} - 1 \right) \right]^{-2} \tag{5.7}$$

For sediment mixtures, z_0 can usually be approximated as a function of the coarsest particles on the bed, e.g.,

$$z_0 = \gamma \cdot D_{84} \tag{5.8}$$

where D_{84} is the particle size for which 84% of the bed surface grain size distribution is finer and γ is an empirical parameter generally equal to 0.1 [e.g., *Dietrich and Whiting*, 1989; *Wiberg and Smith*, 1991; *Wilcock*, 1996].

Although the FaSTMECH flow code includes an option to calculate the vertical structure of velocity along streamlines of the vertically-averaged flow to produce a quasi-3D flow field, in the following analyses we use only the simpler depth-averaged 2D result.

5.2.2 Mixed-grain sediment transport calculation

Here we consider the bedload transport of grain size mixtures. A grain size distribution can be discretized into N characteristic grain size classes, where the fraction of sediment of the ith size class in the distribution is denoted f_i' and has a characteristic diameter D_i. Thus,

$$\sum_{i=1}^{N} f_i' = 1. \tag{5.9}$$

For gravel mixtures, the grain size is often expressed on the ψ-scale, where

$$\psi_i = \log_2 D_i \tag{5.10}$$

where D_i is in units of millimeters. The ψ-scale can be used to calculate the geometric mean grain size D_g and the geometric standard deviation σ_g:

$$D_g = 2^{\psi_g}; \qquad \psi_g = \sum_{i=1}^{N} \psi_i f_i' \tag{5.11}$$

$$\sigma_g = 2^{\sigma}; \qquad \sigma = \left[\sum_{i=1}^{N} (\psi_i - \psi_g)^2 f_i' \right]^{1/2}. \tag{5.12}$$

These parameters and this notation will be used extensively in the following sections.

Parker [1990] bedload transport relation

Parker [1990] analyzed *Milhous* [1973]'s flow, sediment transport, and bed surface field data collected at Oak Creek, Oregon, and developed an empirical bedload transport relation for gravel mixtures in which the local bedload transport rate for each grain size can be calculated as a function of the local fluid shear stress and the local bed surface grain size distribution. Although *Parker* [1990]'s relation is an empirical fit to data, it has been shown to work surprisingly well in field and laboratory studies under conditions quite different from the data set upon which it is based [e.g., *Yager et al.*, 2007; *Nelson et al.*, 2009]. The *Parker* [1990] relation calculates the dimensionless grain size specific bedload transport rate W_i^*:

$$W_i^* = \frac{R_p g q_{bi}}{u_*^3 F_i} \tag{5.13}$$

where R_p is the submerged specific gravity of sediment (usually ≈ 1.65), g is gravitational acceleration, q_{bi} is the volumetric bedload transport rate per unit width for the ith grain size class, and F_i is the fraction of the ith grain size class in the bed surface grain size distribution. u_* is the local shear velocity:

$$u_* \equiv \sqrt{|\vec{\tau}_b|/\rho} \tag{5.14}$$

where $|\vec{\tau}_b|$ is the magnitude of the local boundary shear stress vector and ρ is the density of water. The size-specific transport rates q_{bi} can be summed to find the total volumetric transport rate per unit width q_{bT}, and they can be used to calculate the fraction of bedload in each size class p_i:

$$q_{bT} = \sum_{i=1}^{N} q_{bi}; \qquad p_i = \frac{q_{bi}}{q_{bT}}. \tag{5.15}$$

The *Parker* [1990] relation calculates W_i^* as:

$$W_i^* = 0.00218 G(\phi_i) \tag{5.16a}$$

where

$$\phi_i = \omega \phi_{sgo} \left(\frac{D_i}{D_{sg}} \right)^{-0.0951} \tag{5.16b}$$

$$\phi_{sgo} = \frac{\tau_{sg}^*}{\tau_{ssrg}^*} \tag{5.16c}$$

$$\tau_{sg}^* = \frac{u_*^2}{R_p g D_{sg}} \tag{5.16d}$$

$$\tau_{ssrg}^* = 0.0386 \tag{5.16e}$$

$$G(\phi) = \begin{cases} 5474 \left(1 - \dfrac{0.853}{\phi}\right)^{4.5} & \text{for } \phi > 1.59 \\ \exp\left[14.2(\phi - 1) - 9.28(\phi - 1)^2\right] & \text{for } 1 \leq \phi \leq 1.59 \\ \phi^{14.2} & \text{for } \phi < 1 \end{cases} \tag{5.16f}$$

$$\omega = 1 + \frac{\sigma}{\sigma_0(\phi_{sgo})} \left[\omega_0(\phi_{sgo}) - 1\right] \tag{5.16g}$$

where D_{sg} is the local bed surface geometric mean and σ is calculated with equation 5.12 using the bed surface grain size fractions, F_i. ω is a so-called straining parameter that is dependent on the functions $\omega_0(\phi_{sgo})$ and $\sigma_0(\phi_{sgo})$, which are plotted in Figure 5.1.

Equation 5.16b includes a hiding function, in which the mobility of sediment of size D_i is dependent upon the surrounding grain size distribution through the ratio D_i/D_{sg}. The exponent to which this ratio is raised determines how close conditions are to equal mobility, where every grain size is mobilized at the same critical shear stress. For pure equal mobility, the exponent in equation 5.16b would have to be zero; *Parker* [1990]'s relation comes close to the equal threshold condition but still allows for selective transport.

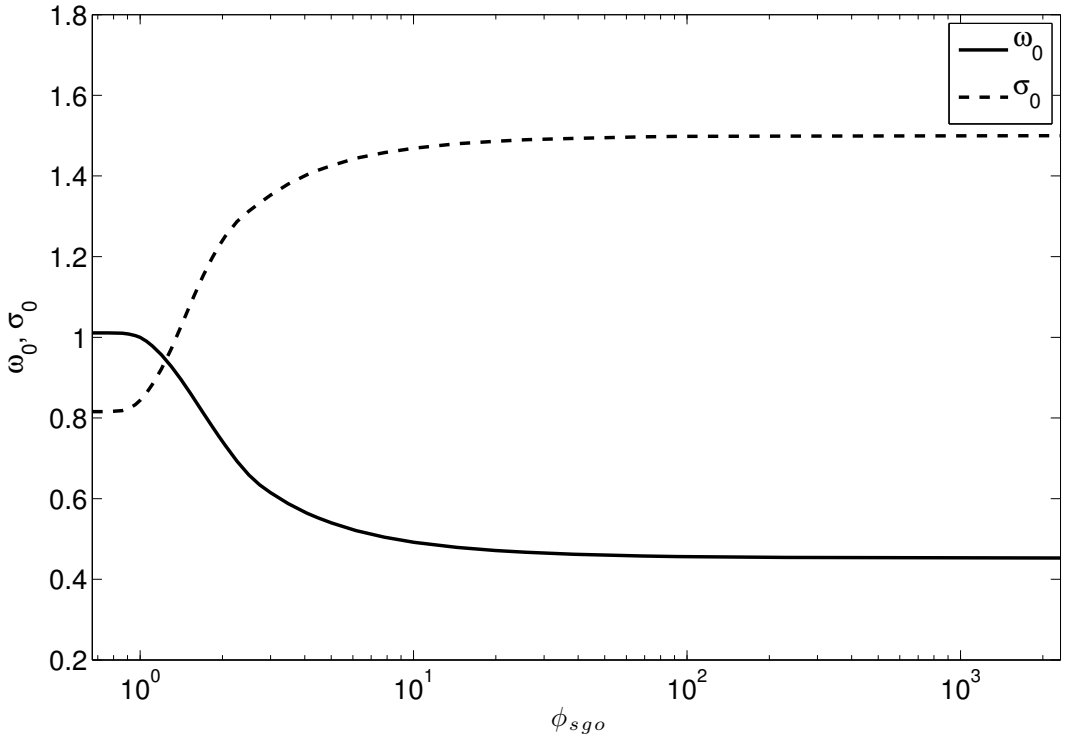

Figure 5.1: Plots of the functions $\omega_0(\phi_{sgo})$ and $\sigma_0(\phi_{sgo})$ for the straining parameter in the *Parker* [1990] relation.

Gravitational correction

Sediment grains traveling as bedload experience fluid drag forces, which bedload transport expressions account for by making the transport rate a function of the boundary shear stress. However, sediment grains also feel the force of gravity, which on a sloping bed can cause the trajectory of sediment motion to deviate from the direction of the boundary shear stress. Additionally, because the gravitational force is proportional to the particle's mass, coarse particles will experience a greater gravitational effect than fine particles. Therefore, in the context of two-dimensional morphodynamic modeling, it is necessary to adjust the sediment transport vector $\vec{q}_{bi} = (q_{is}, q_{in})$ in a way that accounts for grain-size dependent gravitational effects.

The first generation of models accounting for the gravitational effect of a sloping bed on the direction of sediment transport [e.g., *Engelund*, 1974; *Kikkawa et al.*, 1976; *Hasegawa*, 1984; *Parker*, 1984; *Sekine and Parker*, 1992] were developed for transport of a single grain size. *Parker and Andrews* [1985] generalized the linearized Ikeda-Parker formulation [*Parker*, 1984] to mixtures as:

$$\vec{q}_{bi} = |\vec{q}_{bi}| \left[\frac{\vec{\tau}_b}{|\vec{\tau}_b|} - \Gamma \left(\frac{\tau^*_{bi}}{\tau^*_{ci}} \right)^{-n_t} \vec{\nabla}\eta \right] \tag{5.17}$$

where $\vec{\tau}_b = (\tau_{bs}, \tau_{bn})$ and $\vec{\nabla}\eta$ is the vectorial gradient of bed elevation in the (s, n) directions. τ^*_{bi} is the dimensionless shear stress for the ith grain size:

$$\tau^*_{bi} = \frac{|\vec{\tau}_b|}{\rho R_p g D_i}. \tag{5.18}$$

Γ is an empirical coefficient that generally relates friction coefficients and/or sediment exposure [e.g. *Engelund*, 1974; *Kikkawa et al.*, 1976; *Hasegawa*, 1984; *Parker*, 1984; *Sekine and Parker*, 1992] ranging between 1.5 and 5.4, and n_t is generally taken to be 1/2 [*Nelson*, 1990; *Parker*, 2008]. τ^*_{ci} is the critical dimensionless shear stress for incipient motion of the ith grain size, computed with a *Egiazaroff* [1965] hiding relation as modified by *Ashida and Michiue* [1972]:

$$\frac{\tau^*_{ci}}{\tau^*_{cg}} = \begin{cases} \left[\dfrac{\log(19)}{\log\left(19 \frac{D_i}{D_{sg}}\right)} \right]^2 & \text{for } \dfrac{D_i}{D_{sg}} > 0.4 \\ 0.843 \left(\dfrac{D_i}{D_{sg}} \right)^{-1} & \text{for } \dfrac{D_i}{D_{sg}} \leq 0.4. \end{cases} \tag{5.19}$$

Here, τ^*_{cg} is the critical dimensionless shear stress for the geometric mean grain size of the bed surface. The *Parker* [1990] bedload relation does not specify a critical shear stress, but it does incorporate a "reference" dimensionless shear stress τ^*_{ssrg} for which $W^*_i = 0.002$ (equation 5.16e), which we use in place of τ_{cg} in equation 5.19.

If gravitational effects due to the downstream slope of the bed $\partial\eta/\partial s$ can be neglected, and if $q_{in} \ll q_{is}$, equation 5.17 can be expressed:

$$|\vec{q}_{bi}| = q_{is} \tag{5.20a}$$

$$q_{in} = q_{is}\left[\frac{\tau_n}{|\vec{\tau}_b|} - \Gamma\left(\frac{\tau^*_{bi}}{\tau^*_{ci}}\right)^{-n_t}\frac{\partial\eta}{\partial n}\right]. \tag{5.20b}$$

In the following analysis, q_{in} is calculated with equation 5.20b using $\Gamma = 1.5$ and $n_t = 1/2$.

5.2.3 Single grain size sediment transport

While most of the following analyses focus on sediment mixtures, in some cases results are compared to simulations where a single grain size sediment is used. In those cases, we use the *Yalin* [1963] equation to compute sediment transport rates:

$$Q_{tot} = 0.635\sqrt{\frac{|\vec{\tau}_b|}{\rho}}DS\left[1 - \frac{1}{\gamma S}\ln(1+\gamma S)\right] \tag{5.21}$$

where D is the sediment diameter and S is the excess shear stress:

$$S = \frac{|\vec{\tau}_b| - \tau_c}{\tau_c} \tag{5.22a}$$

$$\gamma = 2.45\left(\frac{\rho}{\rho_s}\right)^{0.4}\left(\frac{\tau_c}{(\rho_s-\rho)gD}\right)^{0.5}. \tag{5.22b}$$

The gravitationally-corrected cross stream transport is computed just as in the mixed-grain case (equation 5.20b), except τ^*_b and τ^*_c are not grain-size dependent.

5.2.4 Bed evolution

Once the flow and sediment transport fields have been computed, the Exner equation for conservation of mass of bed sediment can be applied (by grain size) to calculate changes in the bed elevation and bed surface grain size distribution. Spatial variations in sediment transport cause erosion and deposition to occur, and the grain size distribution of the bed surface is the result of mixing of the bedload, bed surface, and subsurface grain size mixtures.

The simplest approach for modeling this evolution is the so-called active layer method, originally proposed by *Hirano* [1971]. Here, the bed is assumed to be composed of a subsurface layer whose grain size distribution does not vary in time, and a surface (active) layer whose grain size distribution can change with time through interaction with the sediment transport field and through mixing with the subsurface layer. *Parker* [1992, 2008] developed

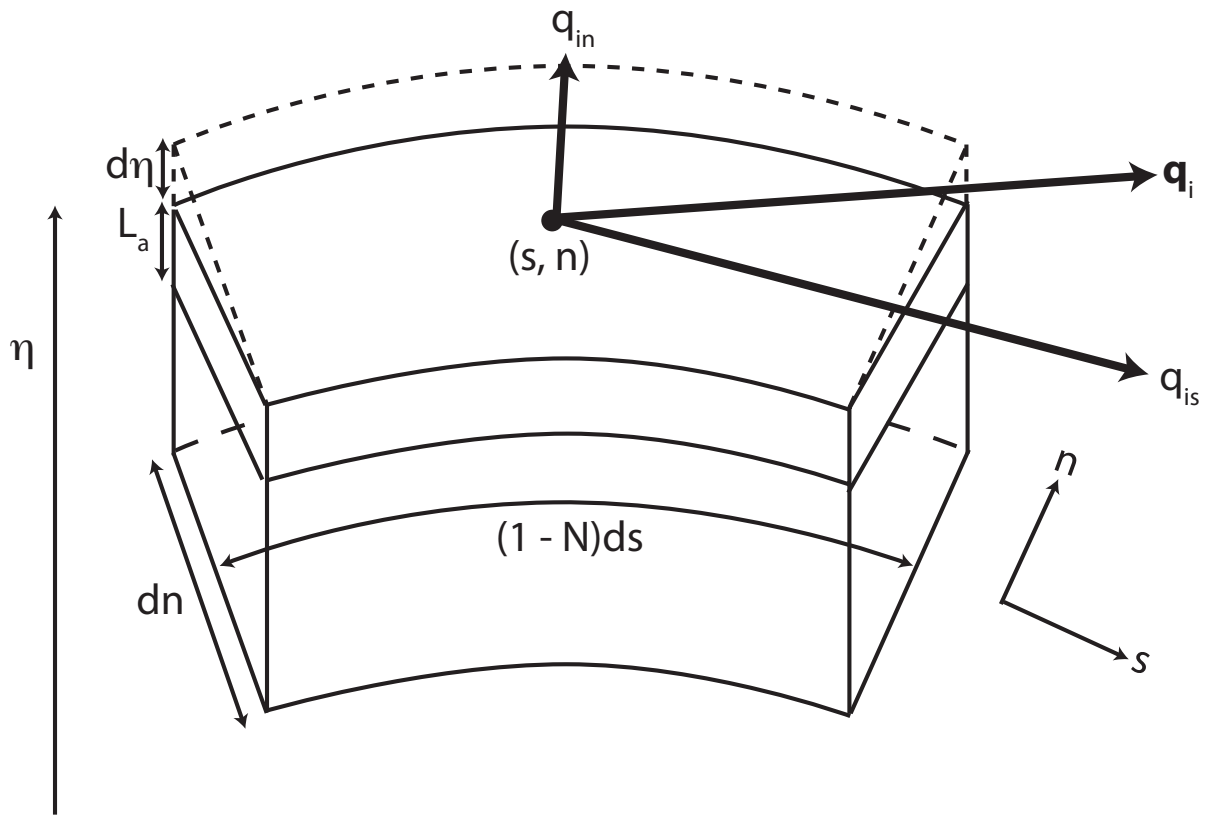

Figure 5.2: Example grid cell at (s, n).

a framework for modeling mixed-grain size bed evolution with the active layer concept, which is summarized here.

Figure 5.2 illustrates the active layer concept. Here, the grid cell centered at (s, n) has a bed elevation η. The thickness of the active layer, L_a, is assumed to be proportional to the diameter of the coarsest grains on the bed, e.g.:

$$L_a = n_a \cdot D_{90} \tag{5.23}$$

where D_{90} is the grain size for which 90% of the sediment in the distribution is finer. n_a is a constant on the order of 1 to 2 [*Parker*, 2008].

The material in the active layer (i.e., the bed surface: $\eta - L_a < z \leq \eta$) is described by a grain size distribution where the fraction of the ith size class is denoted F_i. The active layer is assumed to be well-mixed with no vertical structure. The ith fraction of the subsurface material ($z < \eta - L_a$) is denoted f_i and is assumed not to vary with time. During erosion or deposition, sediment may be exchanged between the active layer and the subsurface. The distribution of sediment that is exchanged at the interface between the active layer and the subsurface is described by exchange fractions denoted f_{li}. If the bed is degrading ($\partial\eta/\partial t < 0$), subsurface material is transferred to the surface layer; if the bed is aggrading, the exchange layer distribution is considered to be a mixture of the surface material and the bedload material [*Hoey and Ferguson*, 1994; *Toro-Escobar et al.*, 1996]:

$$f_{li} = \begin{cases} f_i|_{z=\eta-L_a} & \text{if } \dfrac{\partial\eta}{\partial t} < 0 \\ \alpha F_i + (1-\alpha)p_i & \text{if } \dfrac{\partial\eta}{\partial t} > 0 \end{cases} \tag{5.24}$$

where $0 \leq \alpha \leq 1$. In the analysis below, we set $\alpha = 0.5$.

Equations describing the conservation of bed sediment, by grain size, in the active layer, can now be constructed and used to solve for the evolution of the bed elevation η and the surface grain size distribution F_i. Conservation of the ith grain size fraction in the active layer can be expressed as:

$$(1-\lambda_p)\left[f_{li}\frac{\partial}{\partial t}(\eta - L_a) + \frac{\partial}{\partial t}(F_i L_a)\right] = -\vec{\nabla}\cdot\vec{q}_{bi} \tag{5.25}$$

where λ_p is the bed porosity (assumed here equal to 0.35). In streamwise (s, n) coordinates [e.g., *Smith and McLean*, 1984], the divergence of a vector $(\vec{q}_{bi})$ is

$$\vec{\nabla}\cdot\vec{q}_{bi} = \frac{1}{1-N}\frac{\partial q_{is}}{\partial s} + \frac{\partial q_{in}}{\partial n} - \frac{q_{in}}{(1-N)R}. \tag{5.26}$$

where R is the radius of curvature of the centerline at coordinate $(s, 0)$ and $(1 - N) = (1 - n/R)$ is a scale factor that accounts for variation in the along-stream coordinate with distance from the centerline.

Equation 5.25 can be summed over all grain sizes to arrive at an equation describing the time evolution of the bed elevation η:

$$(1-\lambda_p)\frac{\partial \eta}{\partial t} = -\vec{\nabla}\cdot\vec{q}_{bT}. \tag{5.27}$$

Combining equations 5.25 and 5.27, we arrive at an equation describing the evolution of the surface layer grain size distribution F_i:

$$(1-\lambda_p)\left[L_a\frac{\partial F_i}{\partial t} + (F_i - f_{li})\frac{\partial L_a}{\partial t}\right] = -\vec{\nabla}\cdot\vec{q}_{bi} + f_{li}\vec{\nabla}\cdot\vec{q}_{bT}. \tag{5.28}$$

The above formulation conserves sediment by grain size for the active layer by accounting for exchanges between the bedload layer, the active (surface) layer, and the subsurface layer [e.g., the so-called "three-layer model", *Cui*, 2007]. Because the subsurface layer has no vertical structure in this model, during aggradation, the material transferred to the subsurface does not form a stratigraphic layer that may be exposed during subsequent erosion events. This lack of stratigraphy may have important consequences for predictions of migrating bars, as discussed later.

5.2.5 Discretization and implementation

The modified FaSTMECH code computes flow, sediment transport, and bed evolution as follows. Consider a grid cell on a curvilinear orthogonal grid with the coordinates (s, n). Figure 5.3 illustrates this cell (at location (i, j)) and its neighbor cells, where i increases with s and j increases with n. This cell will serve as a control volume for sediment conservation calculations.

1. FaSTMECH calculates the depth h and depth-averaged velocity components u in the streamwise direction and v in the cross-stream direction (for convenience, we are dropping the $\langle\ \rangle$ from the depth-averaged variables from this point on). Because the calculation is performed on a staggered grid, the velocity components and the depth are not all known at the same location; h is known at the grid center points, u is known at the center of the faces of the control volume surrounding node (i, j) orthogonal to the s-axis, and v is known at the center of the faces of the control volume that are orthogonal to the n-axis (see Figure 5.3). Our notation will follow the convention that $u(i, j)$ is the streamwise velocity at the left edge of the cell and $v(i, j)$ is the cross-stream velocity at the bottom edge of the cell, if s is positive from left to right.

2. The boundary shear stress is calculated at each grid center point by mapping the velocity components to that location. The remapped velocity components (u_{av}, v_{av}) are simply the average values over the grid cell:

$$u_{av}(i, j) = \frac{u(i+1, j) + u(i, j)}{2} \tag{5.29a}$$

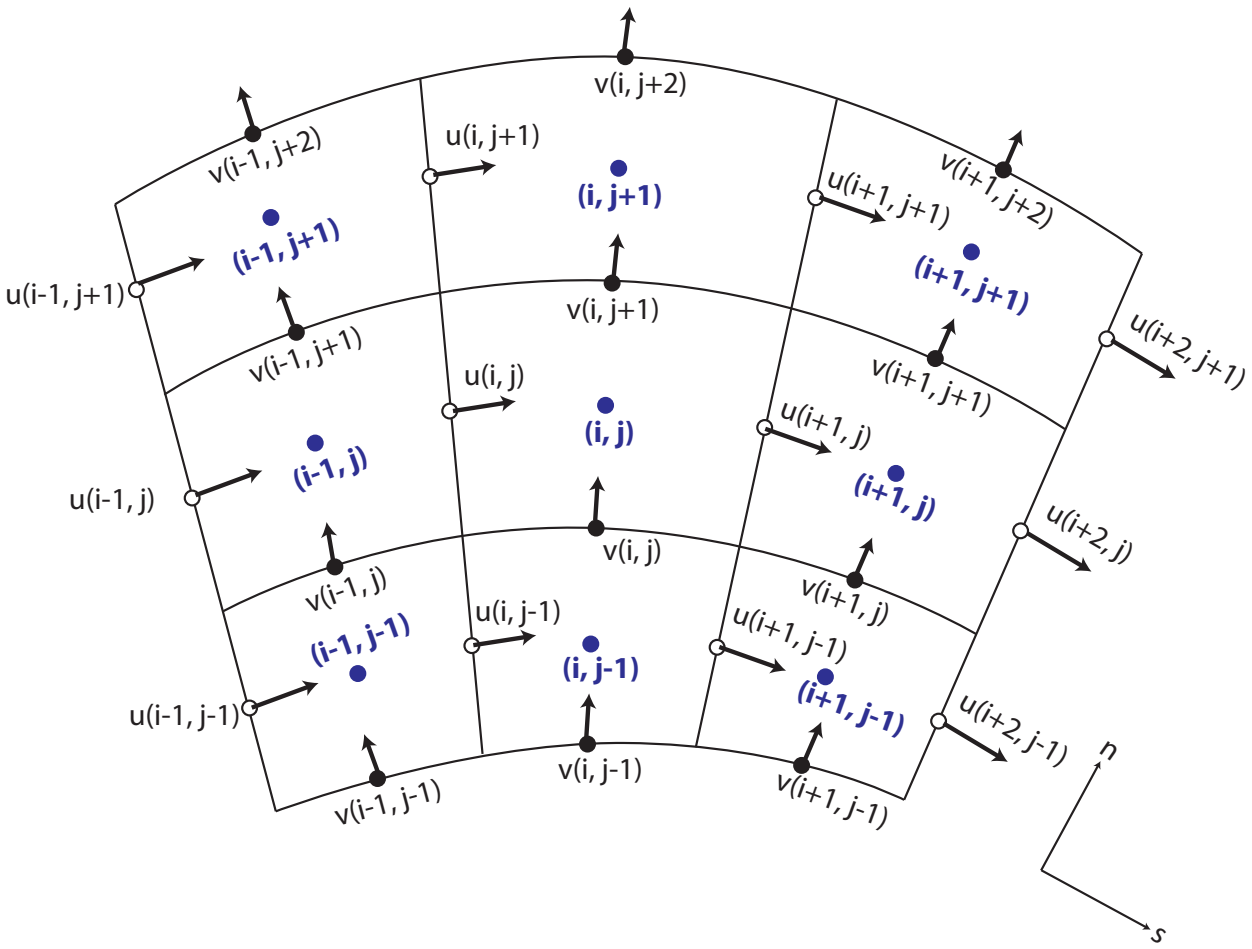

Figure 5.3: Representative portion of a curvilinear orthogonal computational grid. Blue circles are grid center points where h, E, η, and C_d are known; open circles are locations where u is known, and closed black circles are locations where v is known. Discretization values i and j increase with increasing s and n, respectively.

$$v_{av}(i,j) = \frac{v(i,j+1) + v(i,j)}{2} \tag{5.29b}$$

If the grid cell lies on the edge of the mesh, u_{av} and v_{av} take on the values of u and v; e.g., $u_{av}(ns,j) = u(ns,j)$ and $v_{av}(i,nn) = v(i,nn)$, where ns and nn are the number of grid points in the s and n directions, respectively. The boundary shear stress $\vec{\tau}_b = (\tau_s, \tau_n)$ is then calculated as:

$$\tau_s(i,j) = \rho C_d(i,j)\sqrt{u_{av}(i,j)^2 + v_{av}(i,j)^2}u_{av}(i,j) \tag{5.30a}$$

$$\tau_n(i,j) = \rho C_d(i,j)\sqrt{u_{av}(i,j)^2 + v_{av}(i,j)^2}v_{av}(i,j) \tag{5.30b}$$

3. The shear stress components calculated in equation 5.30 are used to calculate the local shear velocity $u_*(i,j)$ (equation 5.14), which is used with the local bed surface grain size distribution $F_i(i,j)$ to calculate the local sediment transport rate by grain size, $|q_{bi}|$ (equation 5.13).

4. The components of the sediment transport vector, q_{is} and q_{in}, are computed. First, q_{is} is calculated as

$$q_{is} = |q_{bi}|\frac{\tau_s}{|\vec{\tau}_b|} \tag{5.31}$$

This is then used in equation 5.20b to compute q_{in}. The cross stream slope, $\partial\eta/\partial n$, is calculated with a center difference:

$$\frac{\partial \eta}{\partial n}(i,j) = \begin{cases} \dfrac{\eta(i,j+1) - \eta(i,j)}{dn} & \text{if } j = 1 \\ \dfrac{\eta(i,j) - \eta(i,j-1)}{dn} & \text{if } j = nn \\ \dfrac{\eta(i,j+1) - \eta(i,j-1)}{2dn} & \text{otherwise} \end{cases} \tag{5.32}$$

where dn is the grid spacing in the n direction.

5. The divergences of sediment fluxes are computed (e.g., equation 5.20b). To enhance computational stability, the spatial derivatives in the s-direction are computed with an upwinding coeffient a_u; e.g.,

$$\frac{1}{1-N}\frac{\partial q_{bT}}{\partial s} = a_u\frac{q_{Ts}(i,j) - q_{Ts}(i-1,j)}{(1-N)ds} + (1-a_u)\frac{q_{Ts}(i+1,j) - q_{Ts}(i,j)}{(1-N)ds}. \tag{5.33}$$

Note that $a_u = 0.5$ corresponds to a center-difference scheme, $a_u = 1$ corresponds to a backward-difference scheme, and $a_u = 0$ corresponds to a forward-difference scheme. Simulations of gravel mixtures using the *Parker* [1990] relation tend to be more stable if $a_u > 0.5$.

The spatial derivatives in the n-direction are computed with a center-difference scheme:

$$\frac{\partial q_{bT}}{\partial n} = \frac{q_{Tn}(i, j+1) - q_{Tn}(i, j-1)}{2dn}. \tag{5.34}$$

If node (i, j) lies on the mesh boundary, the derivatives in equations 5.33 and 5.34 become differences across a single cell.

Conditions at the upstream morphologic boundary (the cross section at which bed evolution is allowed to begin; for instance, the location where we may assume a sediment feed is provided) are slightly more complicated. In the following analyses, we use two options:

a) For simulations using a uniform grain size, we assume completely transport-limited conditions. Here, the calculated shear stress at the upstream morphologic boundary is used to calculate the local sediment transport capacity using the *Yalin* [1963] expression and this becomes the feed condition.

b) For mixed grain size simulations, we use the *Parker* [1990] relation with the local shear stress and bed surface grain size at the upstream boundary to calculate the total local transport capacity at each node on the boundary. The total sediment feed rate at each boundary node is set equal to this value, and the grain size distribution of the sediment feed is forced to be the same at each node. This approximates a well-mixed feed that is laterally distributed so that local erosion or deposition at the boundary is minimized.

6. The flux divergences $\vec{\nabla} \cdot \vec{q}_{bT}$ and $\vec{\nabla} \cdot \vec{q}_{bi}$ may require smoothing to prevent further numerical instabilities that can propagate through a morphodynamic simulation. The divergence at node (i, j) may be adjusted by a weighted average of its adjacent neighbors; for example:

$$\begin{aligned}\vec{\nabla} \cdot \vec{q}_{bT}(i, j) = \Big[&\vec{\nabla} \cdot \vec{q}_{bT}(i, j) + w\vec{\nabla} \cdot \vec{q}_{bT}(i-1, j) + w\vec{\nabla} \cdot \vec{q}_{bT}(i, j-1) \\ &+ w\vec{\nabla} \cdot \vec{q}_{bT}(i+1, j) + w\vec{\nabla} \cdot \vec{q}_{bT}(i, j+1)\Big]/(1+4w).\end{aligned} \tag{5.35}$$

where w is a small (≈ 0.3) weight coefficient. Equation 5.35 represents one smoothing pass and can be repeated as many times as a user specifies.

7. The new bed elevation after a time step of dt ($\eta|_{t+dt}$) is calculated using equation 5.27, which in discretized form is:

$$\eta(i, j)|_{t+dt} = \eta(i, j)|_t - \frac{dt}{1-\lambda_p}\vec{\nabla} \cdot \vec{q}_{bT}(i, j)|_t. \tag{5.36}$$

8. The updated surface grain size distribution after a time step of dt ($F_i|_{t+dt}$) is calculated using equation 5.28, which is discretized as:

$$F_i(i,j)|_{t+dt} = F_i(i,j)|_t + \frac{f_{li}(i,j)|_t \vec{\nabla} \cdot \vec{q}_{bT}(i,j)|_t - \vec{\nabla} \cdot \vec{q}_{bi}(i,j)|_t}{1-\lambda_p} dt - \frac{F_i(i,j)|_t - f_{li}(i,j)|_t}{L_a(i,j)|_t} (L_a(i,j)|_t - L_a(i,j)|_{t-dt}). \tag{5.37}$$

The relevant grain size statistics of the bed surface (D_{50}, D_{sg}, D_{84}, σ) are calculated for the new distribution, and if the roughness is a spatially variable function of the D_{84} (equation 5.8), the local drag coefficient C_d is updated.

9. The calculations are repeated for the next time step, and continued until a specified ending time.

5.3 Simulation conditions

Experiments conducted at St. Anthony Falls Laboratory during the alternate bar phase of StreamLab06 [discussed in *Nelson et al.*, 2010, and chapter 3] serve as the motivation for this work and as the validation dataset for the numerical results. In those experiments, a near-field scale straight, sediment-recirculating, rectangular flume 2.75 m wide with a 55 m long test section was supplied with a steady water discharge of 0.4 ± 0.02 m^3/s. The initial bed was screed flat and composed of a bulk gravel mixture ranging from 2 mm to 45 mm in diameter (Figure 5.4). The initial bed slope was set to 0.0137. At the upstream end of the channel, sand bags were placed on the right side of the flume (looking downstream) so that the upstream flow and sediment supply were constricted to the left 2/3 of the channel width; this obstruction was placed to encourage the formation of alternate bars downstream.

These conditions led to the formation of approximately 1.5 alternate bar sequences that were not migrating. Over one bar sequence, a suite of near-bed velocity and local sediment transport measurements were made and used to infer sorting mechanisms [*Nelson et al.*, 2010]. Water surface profiles were measured during the experiment, and after the flume was rapidly drained a 10×10 mm resolution DEM of the bed was collected with a laser profiler, as well as a higher-resolution 1×1 mm DEM of a 24 m section of the channel. A facies map of the bed was drawn, wherein patches were visually delineated into four patch types ranging from fine to coarse. Spatially, the grain size was also characterized by applying the *Graham et al.* [2005a] automated method to a hillshade image of the 1×1 DEM [see *Nelson et al.*, 2010, and Chapter 3 for details].

Several numerical experiments were conducted to explore the behavior of the model and to gain insight on mechanisms of patch formation. In general, three things were varied in the experiments:

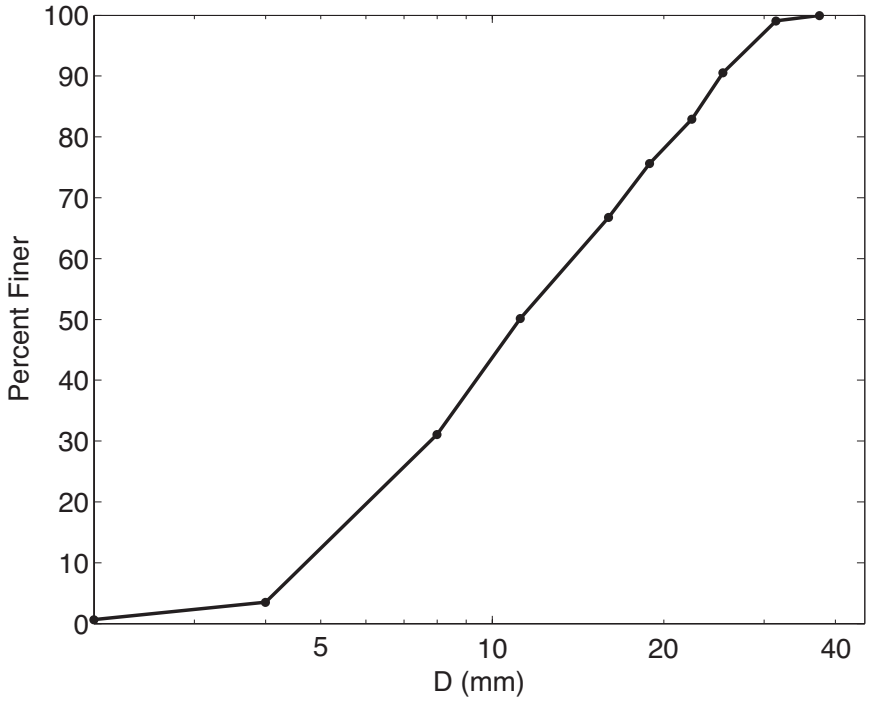

Figure 5.4: Bulk grain size distribution used in the flume and numerical experiments.

1. Presence of an obstruction: In some experiments, an obstruction was created at an upstream point of the grid similar to the sand bags used in the StreamLab06 experiments: a semi-round region on the right side of the channel, extending 1/3 of the grid width, where the grid nodes were prescribed an elevation high enough to prevent them from ever becoming inundated.

2. Grain size - roughness feedback: The effects of grain size and roughness were explored through the use of either a constant drag coefficient or by allowing the roughness length z_0 to be a function of the surface D_{84} (Equations 5.7 and 5.8). In our simulations using constant roughness, C_d was set to 0.017, and simulations with a grain size - roughness feedback use $z_0 = 0.1D_{84}$.

3. Uniform or mixed-grain size sediment: Some simulations were conducted using a uniform grain size of 11 mm and the *Yalin* [1963] expression. For the simulations using gravel mixtures, the bulk grain size distribution shown in Figure 5.4 was used as the initial surface grain size distribution, the subsurface grain size distribution, and the sediment feed grain size distribution.

Table 5.1 summarizes the conditions of each simulation. All simulations were conducted on a 200 m long, 2.75 m wide computational grid, with a grid spacing of about 12.5 cm in the along-stream and cross-stream directions. Comparison with the StreamLab06 experiments is accomplished by looking only at the first 52 m downstream of an obstruction. In all of the model simulations, bed evolution and sediment transport were allowed to start at the 20th downstream cross section (at about $s = 3$ m, where $s = 0$ is the upstream beginning of the grid). Upstream of the morphological boundary, the bed is not allowed to change: $\vec{\nabla} \cdot q_{bi}$ and $\vec{\nabla} \cdot q_{bT}$ are set equal to zero to mitigate upstream boundary effects on the flow calculation and to allow the flow field to develop. In simulations using mixed grain size material, the grain size distribution of the sediment feed was specified to be that of the initial bulk mixture (Figure 5.4). When an obstruction was incorporated into the computational grid, it was placed downstream of this morphologic boundary, centered at approximately $s = 10$ m. In all simulations, the lateral correction factor to the kinematic eddy viscosity, αUh (equation 5.5), was set to a constant value of 0.0014 m^2/s. This corresponds to values for α of around 0.008, which is in the range suggested by *Nelson and McDonald* [1995], who found that values of α between 0.005 and 0.01 provided the best fit to laboratory measurements of flow in a lateral separation eddy. The upwinding coefficient a_u (equation 5.33) was set to 0.5 in Run 4 (uniform sediment) and 0.75 in all other runs (mixed sediment). For mixed grain size runs, the active layer thickness scaling parameter A (equation 5.23) was set to 2. At each time step, four smoothing passes with $w = 0.3$ were applied to the sediment flux divergences (equation 5.35).

Table 5.1: Model run summary.

Name	Grid Length [m]	Grid Width [m]	Obstruction (Y/N)	Sediment Type	Roughness Type
Run 1	200	2.75	Yes	Mixture	Variable
Run 2	200	2.75	No	Mixture	Variable
Run 3	200	2.75	No	Mixture	Constant
Run 4	200	2.75	No	Uniform	Constant
Run 5	200	2.75	Yes	Mixture	Constant

5.4 Results and discussion

5.4.1 Comparison with flume data

Run 1 represents the numerical simulation that most closely approximates conditions present in the StreamLab06 experiment. The simulation uses the sediment mixture supplied to the flume, it incorporates a grain size - roughness feedback, and has an upstream flow obstruction. In the following analyses, we focus only the first 52 m of the numerical grid downstream of the obstruction in Run 1 to maintain a comparison with the flume experiment.

Figure 5.5 shows observations collected during the flume experiment: measured bed topography, detrended bed topography, surface D_{50} resulting from the automated analysis of the 1×1 hillshade DEM, and hand-drawn patch map. Bar heads are apparent at approximately $s = 11$, $s = 30$, and $s = 50$ m. The bar wavelength was long enough (about 40 m) that only one fully developed bar and pool formed in the channel. Although the overall pattern of sorting shown in Figure 5.5c is accurate, the range of grain sizes on the bed surface is larger than what is suggested in Figure 5.5c, since the *h-minima* parameter used in the *Graham et al.* [2005a] method tends to produce grain size distributions coarser than reality for fine areas [see *Nelson et al.*, 2010, and Chapter 3 for more details]. Surface samples suggest that the D_{50} of the patch types mapped in Figure 5.5d are 5.9, 8.3, 12.1, and 14.7 mm for Fine, Medium-Fine, Medium-Coarse, and Coarse, respectively.

Figure 5.6 shows the bed topography, detrended bed topography, and surface D_{50} calculated in Run 1. Here, the s-coordinates have been shifted so that the flow obstruction is centered at $s = 0$ m as it was in the flume experiment, and it only shows data from the n-coordinates for which experimental data exist (between $n = 0.19$ m and $n = 2.55$ m, essentially excluding the outer 20 cm at each edge of the grid); this allows Figures 5.5 and 5.6 to be more easily compared.

The results from the simulation are generally similar to the experimental observations. The bars form at approximately the same locations: in both Figure 5.5 and 5.6 there are local topographic high points at between $s = 25$ and $s = 30$ m on the left side and between

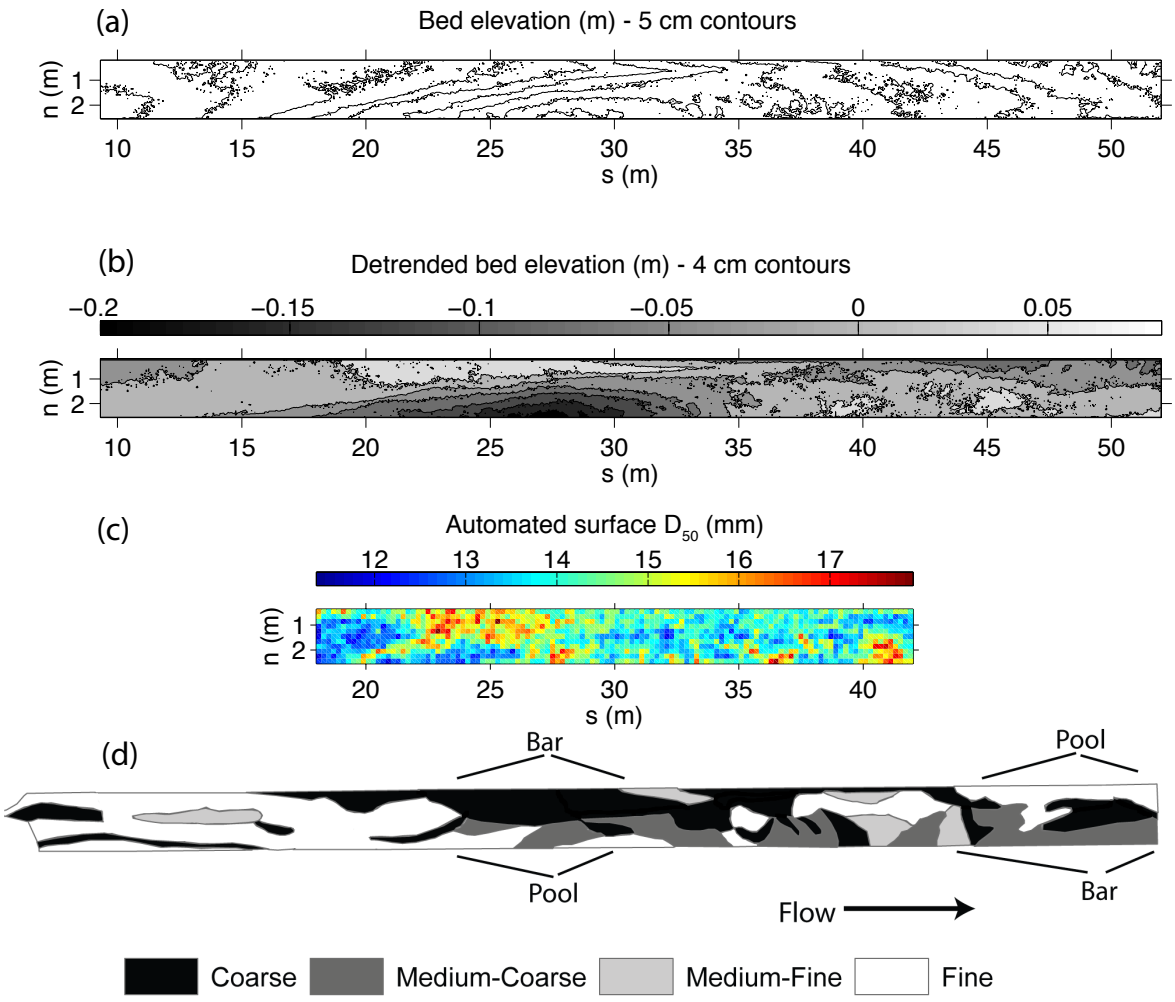

Figure 5.5: Observations from the StreamLab06 flume experiment. (a) Bed topography (5 cm contours); (b) detrended bed topography (4 cm contours - dark areas are low (pools) and light areas are high (bars)); (c) bed surface D_{50} as estimated from the automated analysis of the 1 × 1 mm DEM hillshade image; (d) hand-drawn patch map of the bed.

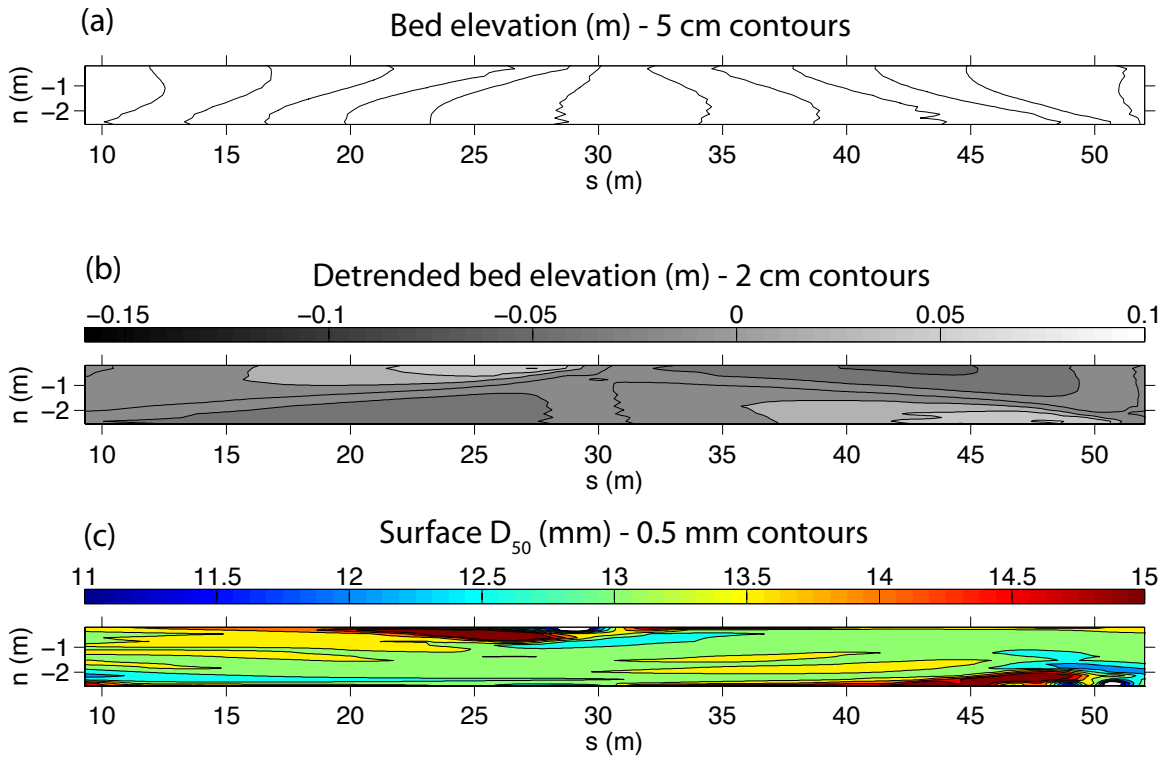

Figure 5.6: Calculated bed and surface grain size from Run 1. The s-axis has been shifted so that the obstruction occurs at $s = 0$, as was the case in the StreamLab06 experiment, and the n axis is confined to the same range (0.19 to 2.55 m) of the measured data plotted in Figure 5.5. (a) Bed topography (5 cm contours); (b) detrended bed topography (2 cm contours - dark areas are low (pools) and light areas are high (bars)); (c) bed surface D_{50}.

$s = 45$ and $s = 50$ m on the right side. The overall pattern of surface sorting is similar to the experiment as well: bar tops are coarser than the adjacent pools, and the coarsest points on the bed in Figures 5.5c and 5.6c occur at about $s = 25$ m. These results provide some confidence that the model reproduces what we see in the flume data.

There are some important discrepancies between the results of the simulation and the experimental observations, however. First, the pools predicted in the model (Figure 5.6b) are not as deep as those from the experiment (Figure 5.5b). This is probably due to the choice of 1.5 for the Γ parameter in the gravitational correction to sediment transport (Equation 5.20b). The studies of sediment transport on lateral slopes from which the form of equation 5.20b is derived [e.g., *Engelund*, 1974; *Ikeda*, 1989; *Sekine and Parker*, 1992] generally focus on uniform sediments much finer than our mixture of coarse gravel, and there is considerable variability in reported values of the Γ parameter [e.g., *Nelson*, 1990; *Sekine and Parker*, 1992]. It is possible that a smaller value of Γ is appropriate for our experimental conditions and would produce morphology closer to our observations. Future work focusing on the transport of gravel mixtures over lateral slopes would be helpful as morphodynamic modeling of gravel-bed rivers progresses.

The other major discrepancy between the simulation results and the experimental observations is that the degree of sorting in the simulation is not as strong as it was in the flume experiment. While the D_{50} of surface samples of the patch types mapped in Figure 5.5d ranged from 5.9 to 14.7 mm, the finest patches produced by the model have a D_{50} of around 11 mm (the median grain size of the bulk mixture), and most of the fine areas have D_{50} of around 12-13 mm (Figure 5.6c). Possible explanations for the model's suppressed surface sorting are discussed later. Additionally, the predicted surface D_{50} (Figure 5.6c) shows some tendency to produce longitudinal stripes of similar grain size; this is probably a numerical artifact that could be mitigated with the inclusion of an additional stochastic lateral sediment transport term [e.g., *Drake et al.*, 1988], which is not accounted for in the model.

We can use the FaSTMECH results from Run 1 to explore the mechanisms responsible for the development of bed surface patches and their co-evolution with bed morphology. Figure 5.7 shows the predicted depth, boundary shear stress field, and load and surface median grain size from Run 1, and Figure 5.8 shows spatial gradients in the sediment transport rate and boundary shear stress. Figure 5.7 shows that τ_s is lowest over the bars, which is where the coarsest bed sediment is found. Clearly, boundary shear stress and the surface D_{50} are not positively correlated with each other, although there does appear to be a positive correlation between τ_s and the bedload D_{50}. Figure 5.8c shows that the divergence of sediment transport is zero everywhere, indicating steady state conditions and the absence of morphologic change. However, there remains a nonzero divergence of boundary shear stress (Figure 5.8f).

How is this nonzero stress divergence compensated so that $\vec{\nabla}\cdot\vec{q}_{bT} = 0$? It appears that this is primarily achieved through lateral sediment transport. Since lateral sediment transport is driven by both cross-stream shear stress and gravitational effects due to the cross-stream

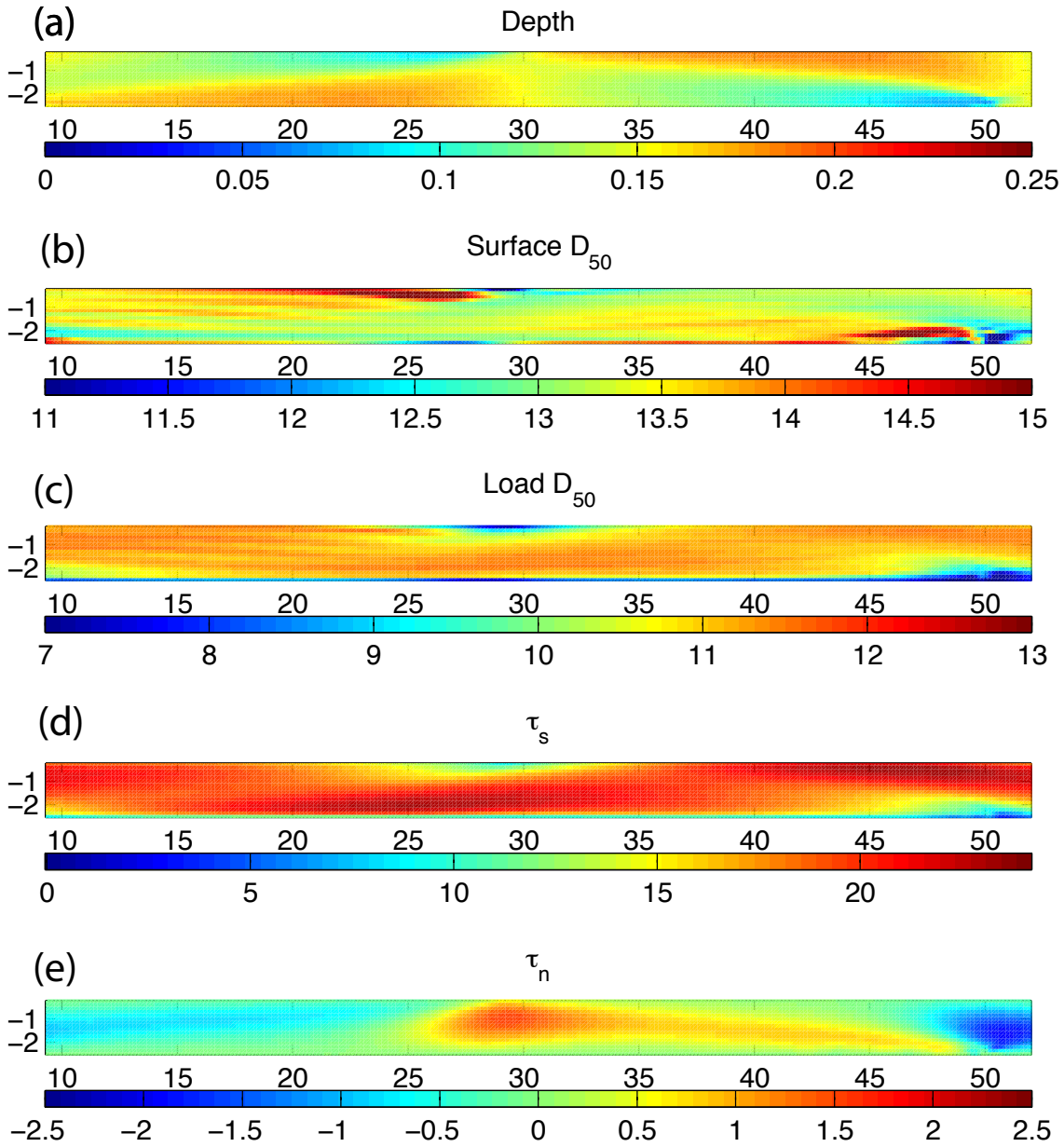

Figure 5.7: Model-predicted (a) depth [m], (b) surface D_{50} [mm], (c) load D_{50} [mm], (d) downstream boundary shear stress [Pa], and (e) cross-stream boundary shear stress [Pa] for Run 1. $\tau_n > 0$ indicates the boundary shear stress is oriented toward the left bank, and $\tau_n < 0$ indicates the boundary shear stress is oriented toward the right bank.

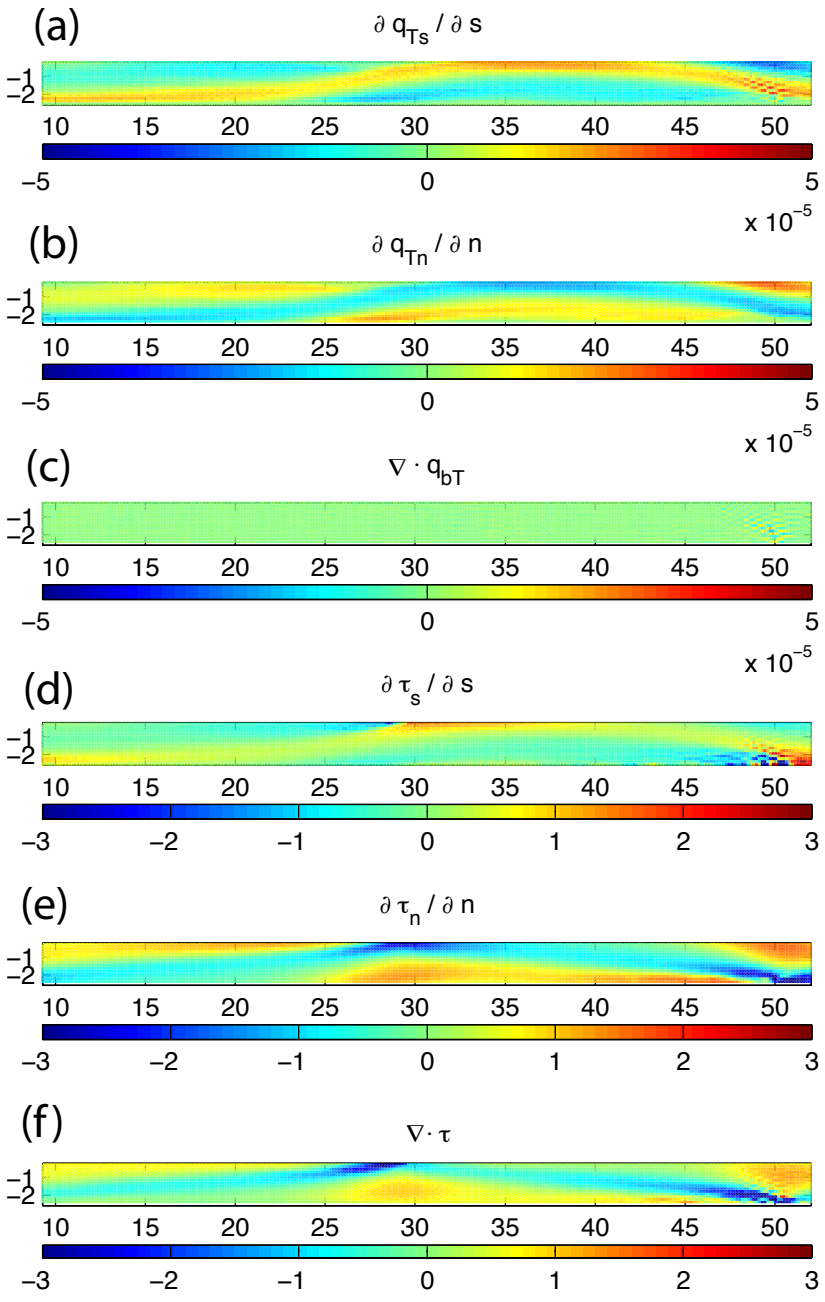

Figure 5.8: Spatial gradients of sediment transport and shear stress for Run 1. $\partial q_{Ts}/\partial s$, $\partial q_{Tn}/\partial n$, and $\vec{\nabla}\cdot\vec{q}_{bT}$ are in units of m/s, and $\partial\tau_s/\partial s$, $\partial\tau_n/\partial n$, and $\vec{\nabla}\cdot\vec{\tau}$ are in units of Pa/m.

bed slope, the bed evolves such that net cross-stream sediment transport imports sediment to areas of positive stress divergence and exports sediment from areas of negative stress divergence. The surface grain size distribution that accommodates locally steady state bed conditions is determined by a combination of the grain size distribution of the sediment arriving at that point, the local stress vector, and the cross-stream bed slope. At steady state, the bed surface grain size distribution and the cross-stream bed slope have co-evolved so that the local sediment influx and local sediment outflux balance each other, by grain size. Because there is low excess shear stress acting on a mixture of coarse gravel, the grain size distribution of these local sediment fluxes reflect varying degrees of size selectivity. For example, consider the bar located on the left side of the channel at about $s = 25$ m. Along the bar, shear stress in the downstream direction decreases as the flow shoals (Figures 5.7a, 5.7c, and 5.8d), causing a net decrease in downstream sediment transport (Figure 5.8a), which is compensated by lateral transport of sediment off of the bar (Figure 5.8b). Sediment transport in the downstream direction along the bar is increasingly size selective due to the decreasing shear stress field, and this selective transport of finer particles (a component of which is laterally transported towards the pool) coarsens the bed (Figure 5.7b), reducing the sediment transport commensurate with the decreasing downstream shear stress. Fine sediment delivered from the bar to the pool enters a converging boundary shear stress field (Figures 5.8d, 5.8e, and 5.8f). Here the relatively high boundary shear stress causes the load to be coarser and the bed surface to be finer than on the bar top (Figure 5.7b).

5.4.2 Coevolution of patchiness and morphology

Our suite of numerical simulations (Table 5.1) enables us to explore how bed surface patches and bed morphology coevolve. A patchy mixed-grain-size bed surface influences the local sediment transport rate through hiding effects, and can influence the flow field through roughness effects, and both of these influences feed back on the evolving bed. But how important are these effects relative to one another?

Bar formation, migration, and wavelength

Figure 5.9 shows the depth field over the entire 200 m domain calculated at the end of all five numerical simulations. Although bars formed in each simulation, there are obvious morphological differences between the runs. Perhaps the most obvious difference is the location of the furthest upstream bar. In Runs 1 and 5, bars form immediately downstream of the obstruction and the entire length of the channel is populated with alternate bars. In Runs 2, 3, and 4, which did not have an obstruction, bars are not apparent until some distance downstream from the inlet. In Run 2, which had a sediment mixture and a grain size - roughness feedback, bars appear at about $s = 110$ m; in Run 3, which had a sediment mixture but constant roughness, bars appear at about $s = 40$ m; and in Run 4, with a uniform sediment and constant roughness, bars begin to form at around $s = 50$ m and are

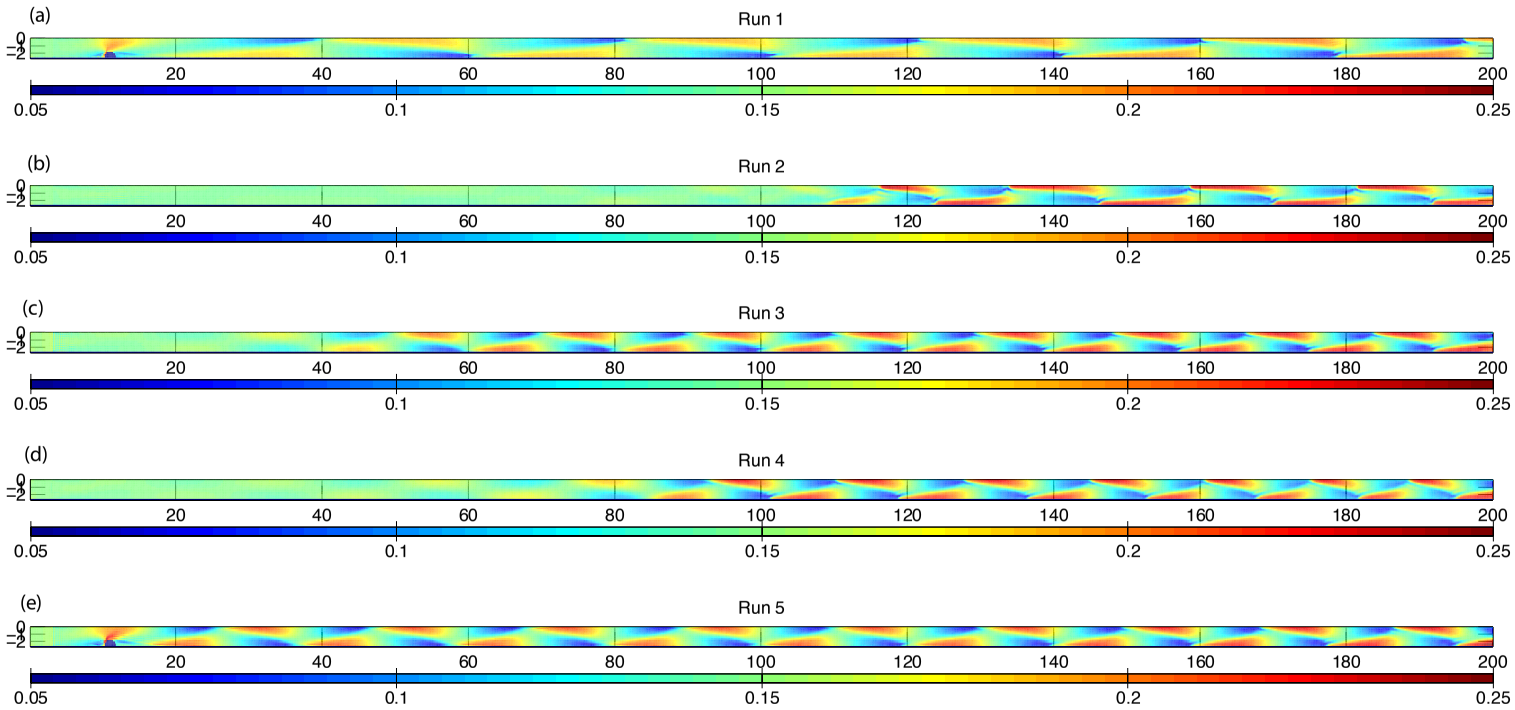

Figure 5.9: Final depth field over the entire domain for all numerical simulations. The color bar scale is in [m]. The conditions of each simulation are summarized in Table 5.1.

fully developed by $s = 80$ m. This suggests that, relative to the case of uniform sediment, the sediment heterogeneity inhibits the initial growth of bars, primarily through roughness feedbacks.

Lanzoni and Tubino [1999]'s analytical linear stability analysis of bar formation in grain size mixtures suggested that relative to the case with uniform sediment, the presence of a sediment mixture leads to a damping of the growth rate and migration speed of bars. Similar to our study, *Lanzoni and Tubino* [1999] incorporated the *Parker* [1990] transport relation, a gravitational cross-stream transport calculation, and a grain size - roughness effect. *Lanzoni and Tubino* [1999]'s work also suggested that the wavelength of mixed-grain-size bars is shorter than that of bars in uniform sediment, although later experiments [*Lanzoni*, 2000b,a] did not find a clear wavelength shortening associated with sediment mixtures. In our numerical experiments, the bars formed in Run 4 (uniform sediment with constant roughness) had a wavelength of about 18 m, while the bars in Run 2 (mixed grain size and variable roughness) appear to have a wavelength of about 15 m when they form, but further downstream a regular wavelength of about 25 m becomes established. This suggests that the length scale of the initial bar-forming instability is shorter for the grain mixture than the uniform sediment (which agrees with the theoretical predictions of *Lanzoni and Tubino* [1999]), but these bars stretch out as they migrate such that their finite amplitude wavelength is significantly longer than that of the uniform sediment.

In all runs except Run 2, the bed tended to evolve toward a steady state where bar migration rates slowed and eventually stopped. The development of fixed bars is not uncommon; in *Ikeda* [1983]'s experiments where a fine gravel mixture was supplied to a very large flume with a 1% slope, alternate bars developed and over time their migration rate slowed and essentially stopped. *Lisle et al.* [1991, 1993]'s experiments in a smaller, steeper flume saw bars became stationary and emerge, which they attributed to bar head stabilization by coarse sediment and incision in the pools. Recent numerical [*Crosato and Desta*, 2009] and theoretical [*Mosselman*, 2009] work has suggested that steady bars can form due to small-amplitude unsteadiness associated with migrating alternate bars, implying that steady bars are an intrinsic instability of alluvial channels.

Roughness effects

The grain size - roughness feedback incorporated in Runs 1 and 2 appears to be a fundamentally important influence on morphological evolution. In Run 2, the bed developed a quasi-steady morphology such that the pattern of bars was visually similar at various points during the simulation; however, the bars in Run 2 were continually re-forming at the upstream end of the channel and bar migration never ceased. As they migrated downstream, the bars would tend to slow down and stretch out, but occasionally pulses of erosion and deposition from upstream would rapidly move through the system, creating a temporal instability that persisted throughout the duration of the simulation. Since the only difference between Run 2, which experienced these instabilities, and Run 3, which did not, was the

grain size - roughness feedback, it appears that this roughness feedback was responsible for this unsteady behavior. The influence of this roughness feedback on bed morphology is especially apparent in a comparison of the simulations with the upstream obstructions, Runs 1 and 5. Unlike Runs 2 - 4, which required a considerable distance to allow bars to develop, the perturbation in Runs 1 and 5 caused deposition immediately downstream, which caused the formation of successive bars along the rest of the channel. The bars are not migrating; they are fixed in place and are effectively tethered to the obstruction. The obvious difference in the bed morphology of Runs 1 and 5 is that the wavelength of the tethered bars in Run 1 (with the grain size - roughness feedback) is about two times larger than that of Run 5.

The grain size - roughness feedback has such a profound influence because it affects the large scale flow, which is nonlinearly coupled to the sediment transport field and the evolving bed surface. A spatially varying drag coefficient, by itself, can produce convective accelerations which cause spatial variation in the fluid velocity and boundary shear stress fields. We examined the magnitude of the effect of a spatially varying drag coefficient on the flow field by imposing the final roughness field from Run 1 on the initial (flat) bed from Run 1 and recalculating the flow field. Since the bed is flat, any deviations from uniform flow are solely due to the spatially variable roughness field. Figure 5.10 shows the roughness, velocity, and shear stress fields for a portion of the bed resulting from this exercise, and Figure 5.11 shows the four convective acceleration terms.

Figures 5.10 and 5.11 show that there is a detectable effect of variable roughness on the overall flow. Most of the influence of the roughness field is reflected in the change in downstream momentum in the streamwise direction (Figure 5.11a) and the change in downstream momentum in the cross-stream direction (Figure 5.11d). There is considerable non-uniformity in the depth-averaged streamwise velocity $\langle u \rangle$ (Figure 5.10b) and boundary shear stress τ_s (Figure 5.10d), and less-pronounced, but noticeable, non-uniformity in the depth-averaged cross-stream velocity $\langle v \rangle$ (Figure 5.10c) and shear stress τ_n (Figure 5.10e). *Whiting and Dietrich* [1991]'s field study of flow over a gravel bar found that even in the absence of strong channel curvature, convective accelerations in both streamwise and cross-stream directions are large; the exercise presented here suggests that channel roughness due to sediment sorting over bars may play a considerable role in producing those convective accelerations. Even in the absence of bar topography, roughness effects from the sorting that develops over bars can significantly affect the overall flow field, especially in the streamwise direction.

Effects of grain mixtures versus uniform sediment

We can take a more detailed look at the effects of sediment mixtures and roughness on the evolution of channel morphology and bed patches by focusing on Runs 2, 3, and 4 (the simulations without obstructions). Figure 5.12 shows the detrended bed topography for 40 m sections of Runs 2, 3, and 4. The bed from Run 2 has bars that are flatter and broader than the beds from Runs 3 and 4, and the pools in Run 2 are deeper and narrower than

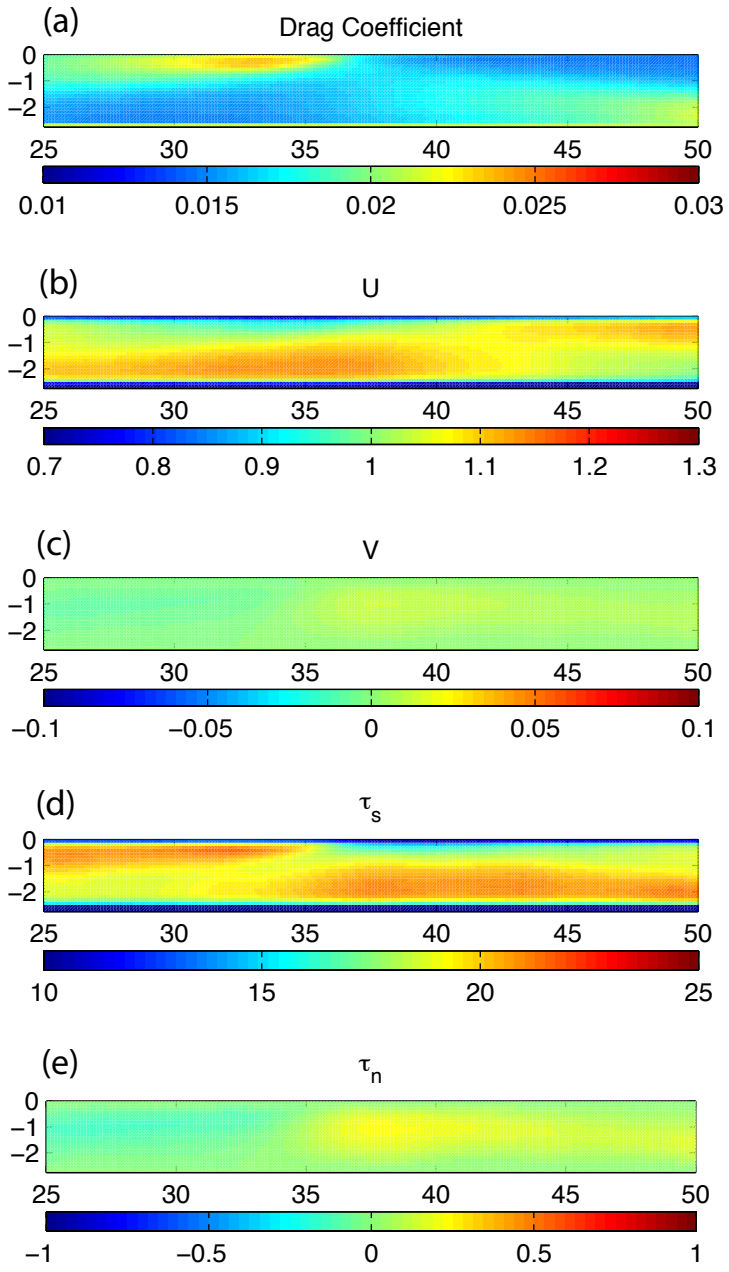

Figure 5.10: Maps of (a) drag coefficient, (b) downstream and (c) cross-stream depth averaged velocity [m/s], and (d) downstream and (e) cross-stream boundary shear stress [Pa] resulting from imposing the final roughness field from the Run 1 simulation on the initially flat bed used in Run 1. Deviations from uniform flow are solely due to roughness effects.

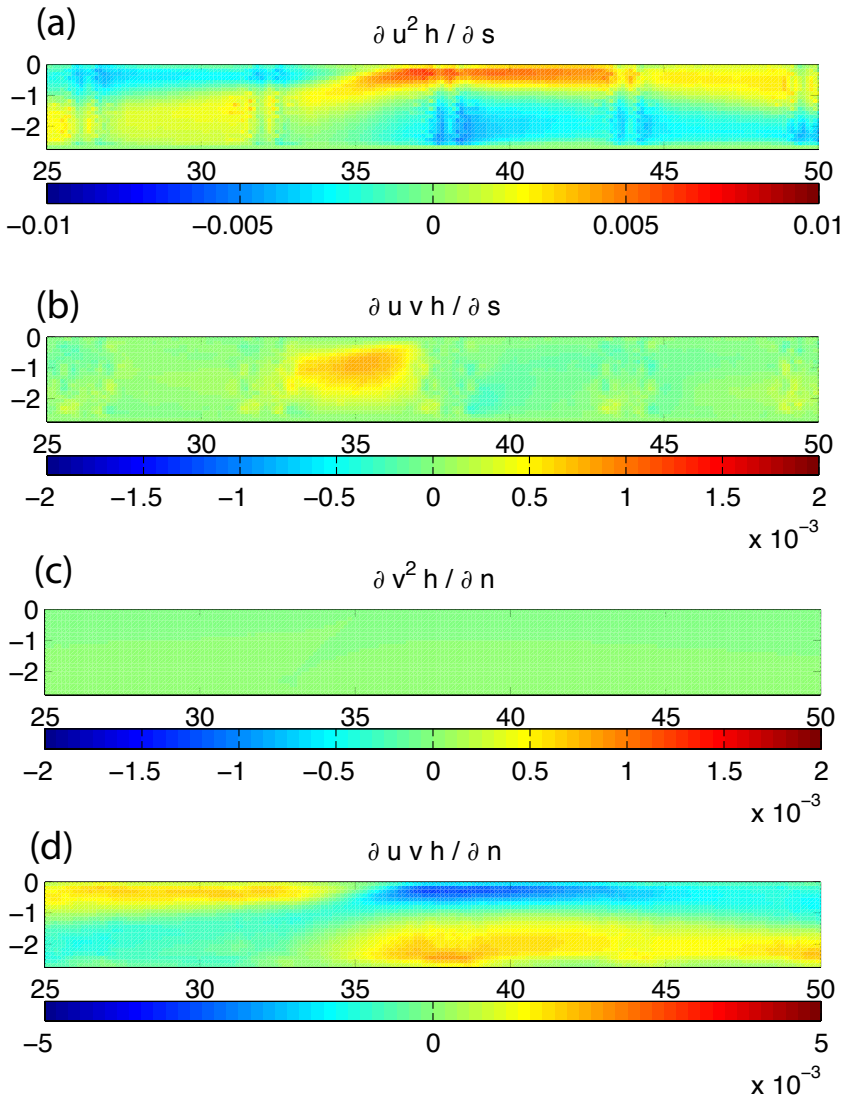

Figure 5.11: Maps of the four components of convective accelerations resulting from imposing the final roughness field from the Run 1 simulation on the initially flat bed used in Run 1. The units for each plot are $[m^2/s^2]$.

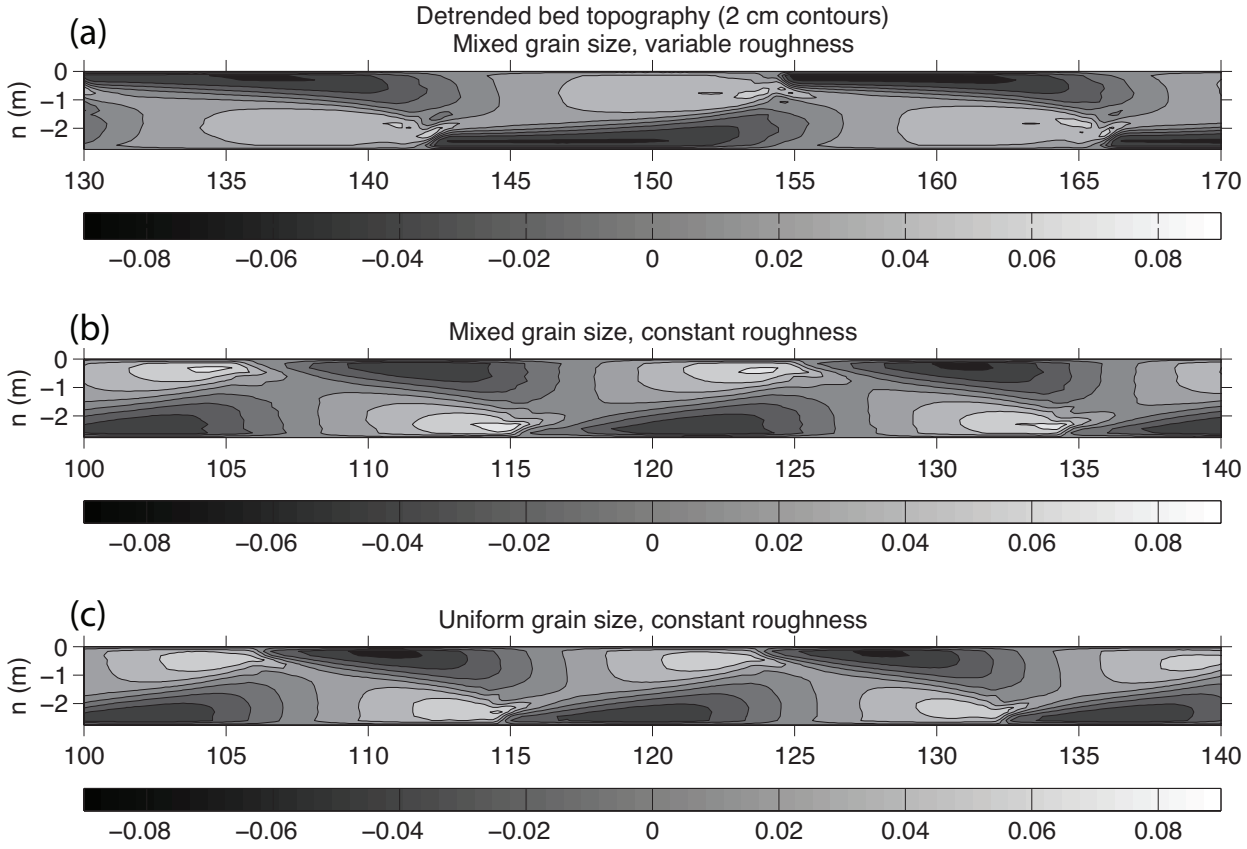

Figure 5.12: Detrended bed topography from Runs 2, 3, and 4. 40 meter portions of the grid are shown to highlight the differences in bar morphology for each run. (a) Mixed grain size, variable roughness (Run 2); (b) Mixed grain size, constant roughness (Run 3); (c) Uniform grain size, constant roughness (Run 4). All plots use a 2 cm contour interval.

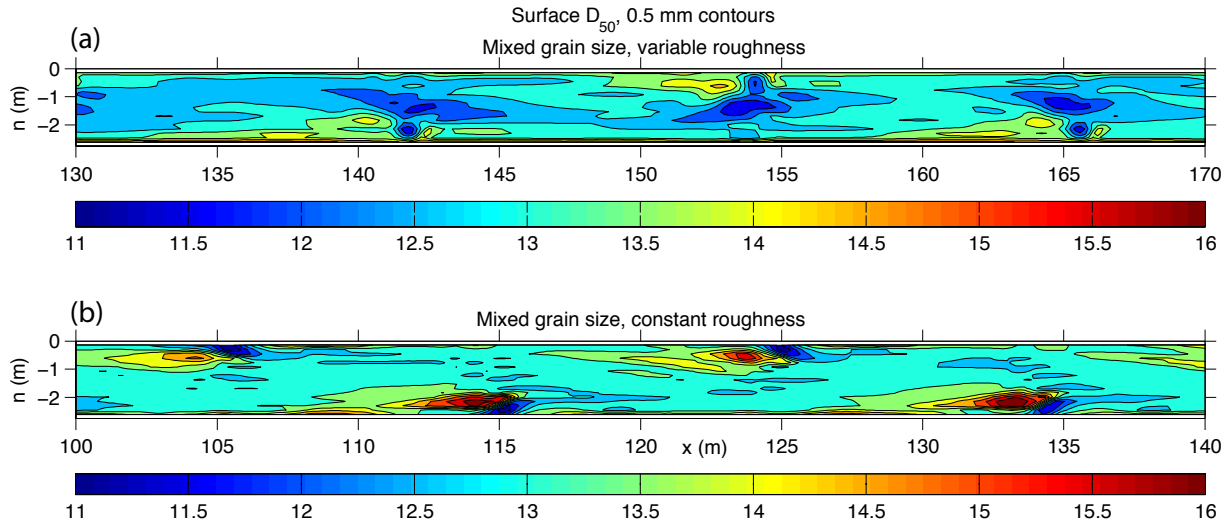

Figure 5.13: Contour plots of the surface D_{50} from (a) Run 2 and (b) Run 3. Contour interval is 0.5 mm. Color scale is in units of [mm].

those from Runs 3 and 4. The bar wavelength of Run 2 (about 24 m) is also longer than those of Runs 3 (about 19 m) and 4 (about 18 m). The bar-pool topography in Runs 3 and 4 is quite similar; the primary difference between the two simulations is that the bar tops in Run 3 come to more of a point than those in Run 4.

Figure 5.13 shows the median surface grain size computed for Runs 2 and 3 for the same 40 m regions shown in Figure 5.12. While both Runs 2 and 3 produced coarse bars and fine pools, the surface patches in Run 2 (Figure 5.13a) do not appear to be as strongly developed as those in Run 3 (Figure 5.13b); the coarse areas on top of the bar in Run 3 are larger and coarser than those in Run 2. Evidently the grain size - roughness feedback leads to a suppression of patchiness.

We can gain insight on why the grain size - roughness feedback leads to the suppression of patches by taking a closer look at the flow and sediment transport fields for Runs 2 and 3. Figures 5.14 and 5.15 show maps of the sediment transport field, shear stress field, and median grain size of the surface and load. The stress fields shown in Figures 5.14 and 5.15 are quite different. In particular, the longitudinal gradients of stress are higher for the constant roughness simulation (Run 3) than they are for the simulation with the grain size - roughness feedback (Run 2). The downstream shear stress, τ_s, stays higher over the bar for a longer distance in Run 2 than it does in Run 3. To better illustrate this, Figure 5.16 shows profiles of τ_s along the $n = -2$ m longitudinal profile for our 40 m region of interest. In both runs, the maximum shear stress occurs in the pool and the minimum shear stress occurs

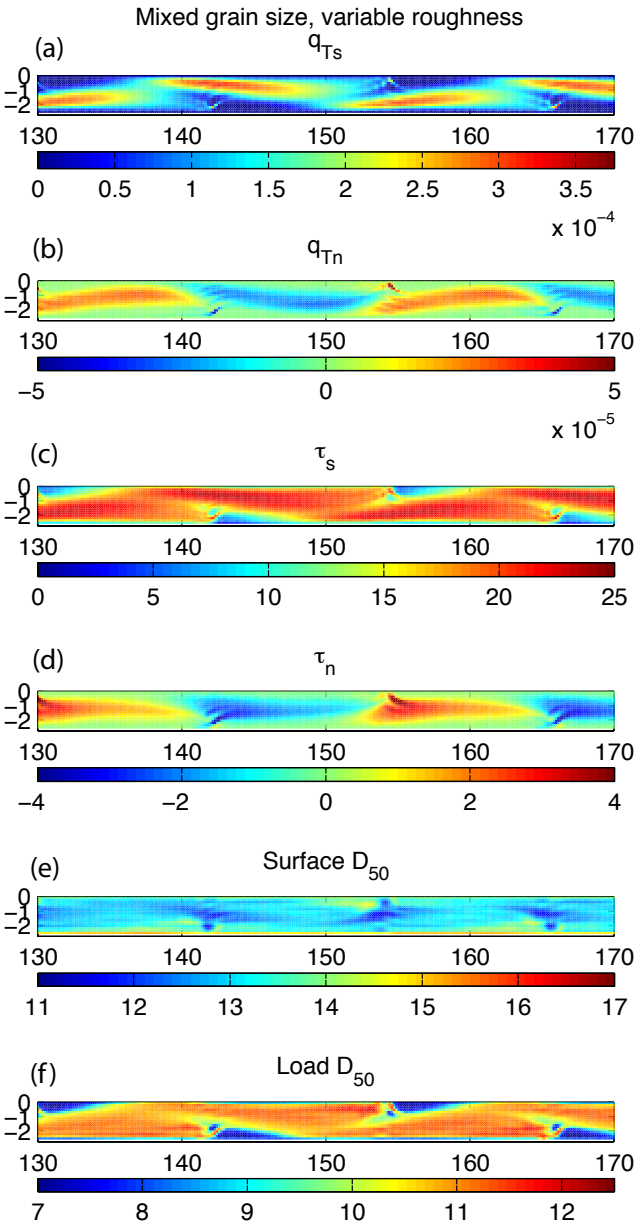

Figure 5.14: Sediment transport rates, boundary shear stress, and grain size predicted for a portion of the numerical grid in the mixed-grain simulation where $z_0 = 0.1D_{84}$ and without an obstruction (Run 2). q_{Ts} and q_{Tn} are sediment transport rates in the s and n directions, respectively [m^2/s], τ_s and τ_n are boundary shear stresses in the s and n directions [Pa], and the median grain sizes of the surface and load are shown in [mm].

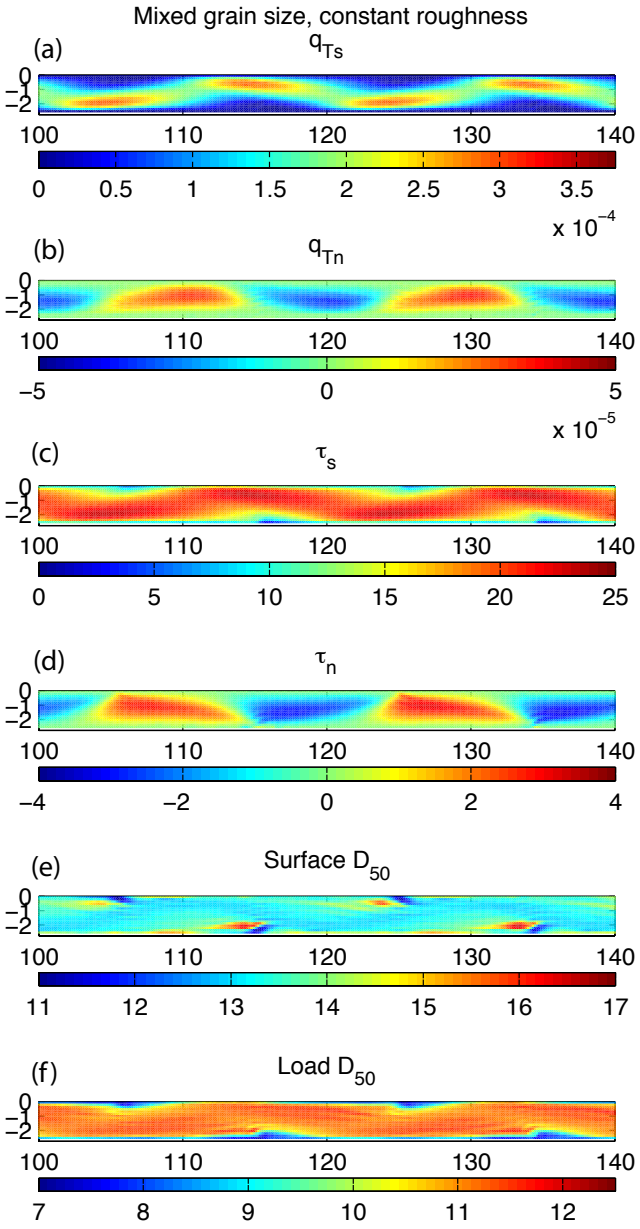

Figure 5.15: Sediment transport rates, boundary shear stress, and grain size predicted for a portion of the numerical grid in the mixed-grain, constant roughness simulation without an obstruction (Run 3). q_{Ts} and q_{Tn} are sediment transport rates in the s and n directions, respectively [m^2/s], τ_s and τ_n are boundary shear stresses in the s and n directions [Pa], and the median grain sizes of the surface and load are shown in [mm].

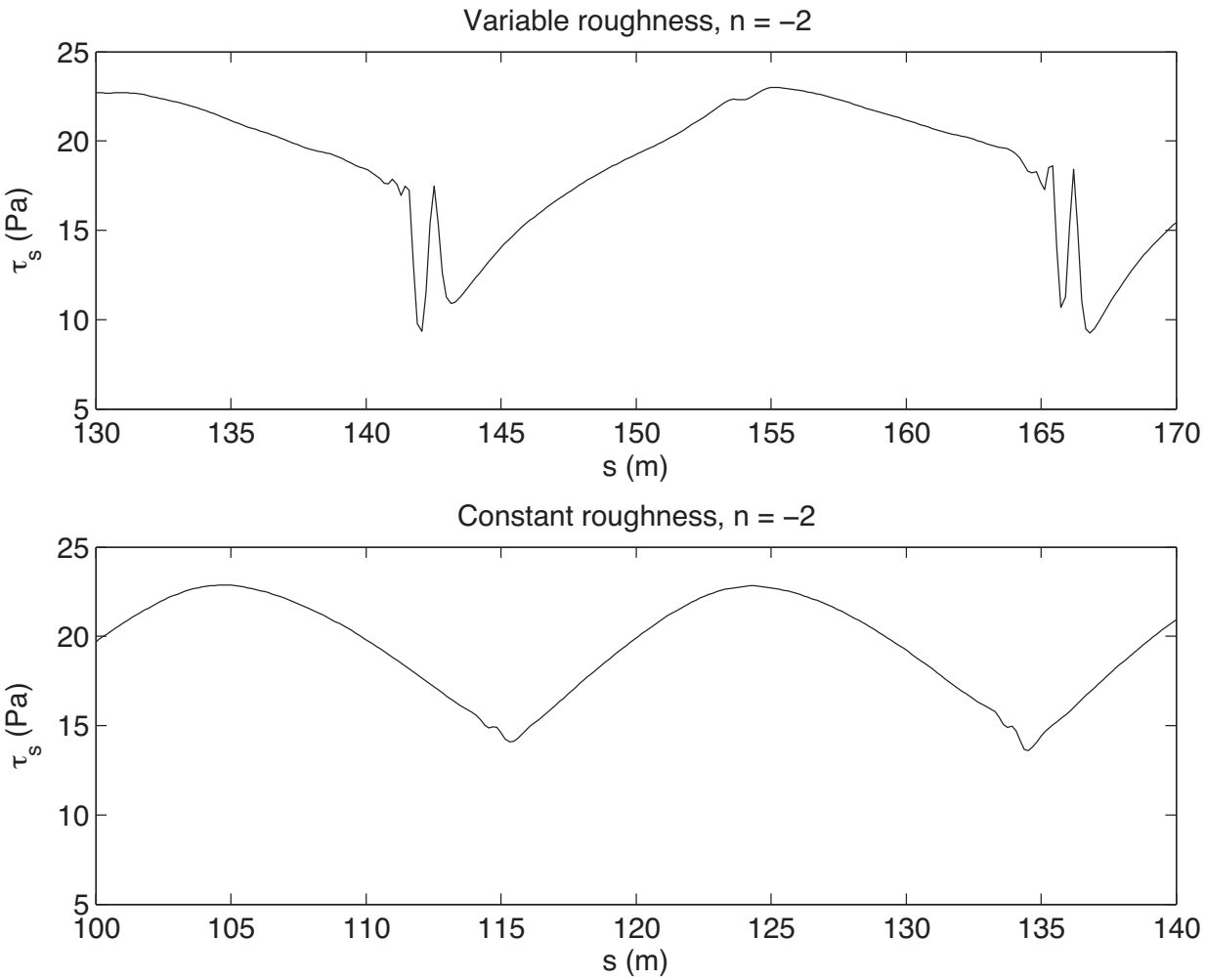

Figure 5.16: Profiles of downstream shear stress τ_s along the $n = -2$ m transect as shown in Figures 5.14 and 5.15. Top figure is the stress profile where the roughness length $z_0 = 0.1D_{84}$ (Run 2) and bottom figure is the stress profile with a constant C_d of 0.017 (Run 3).

immediately downstream of the bar (the spikes the the τ_s profile for Run 2 in Figure 5.16 are due to the small hooks in the bar fronts evident in Figure 5.12a). The stress declines along the profile from the pool to the top of the bar; however, this decline is much more gradual and τ_s is generally higher in Run 2 than in Run 3 (i.e., a decrease in τ_s from 23 to 20 Pa over 10 m compared to a decrease from 23 to 15 Pa over 9 m). The stress stays higher over the bar in the variable roughness case because surface coarsening increases the drag coefficient, which offsets to some degree the effect of decreasing velocity on the boundary shear stress (e.g., Equation 5.6).

For the constant roughness case of Run 3, the rapid decline in shear stress over the bar is compensated through lateral sediment transport (Figure 5.15b), which is achieved through more local relief (pointier bars, Figure 5.12b) and higher cross-stream shear stress (driven by topographic steering) (Figure 5.15d) than in the variable roughness conditions of Run 2. The high shear stress gradient in Run 3 pushes the system into a state of selective transport sooner than in Run 2, so a larger, coarser patch develops on the bar top. In the variable roughness case where $z_0 = 0.1D_{84}$, because the shear stress gradient over the bar is not as high, there is less initial deposition as the bar is being built, producing a flatter bar (Figure 5.12a) that has less of a steering effect on the flow and thus there are lower cross-stream shear stresses over the bar (Figure 5.14d). The overall higher shear stress on the bar in Run 2 results in less selective sediment transport, so the bar coarsens less rapidly and the coarse patch is not as developed.

Other factors

Despite general successes in predicting the overall pattern of patchiness, none of the numerical simulations predict the same *degree* of patchiness (i.e., the total range of variation of grain sizes on the bed) as was observed in the StreamLab06 experiments. In particular, the model does not predict areas of the bed where the median grain size is less than 11 mm, the median grain size of the bulk distribution (also used as a sediment feed in the simulations). There are a few phenomena neglected in the model that may be responsible for this discrepancy.

First is the model's lack of stratigraphy. The locations where the model predicts the finest bed material tend to be immediately downstream of bar heads, where bed scour occurs. In the model, when scour occurs, the exchange fraction f_{li} (equation 5.24) takes on the value of the subsurface grain size distribution, which in these simulations has been set to the bulk grain size distribution. *Parker* [1990]'s model predicts the bed surface to coarsen at low shear stress and fine a high shear stress. The bed surface can be no finer than the grain size distribution of the subsurface material - that which lies below the active layer - and in this model can not change. Hence it is not possible to have grain size patches, as observed in the hand drawn maps, that are well below the median size of the fixed subsurface size distribution. In efforts to avoid problems associated with erosion and deposition, some progress has been made in one-dimensional morphodynamic models using a depth-continuous

sediment continuity model rather than the active layer model used here [e.g., *Parker et al.*, 2000; *Blom and Parker*, 2004]. However, it is unclear to what degree the degree of bed surface patchiness may depend upon subsurface heterogeneity because the subsurface may not really be very heterogeneous. *Kinerson* [1990]'s field study of several gravel bed channels found relatively little variation in the subsurface material despite considerable surface patchiness, in some sites, and measured ratios of the median grain size of the bed surface to that of the subsurface generally fall within the range of 1 to 3 [e.g., *Kinerson*, 1990; *Buffington and Montgomery*, 1999b]. Vertical sorting may be mitigated by variable flow conditions; *Hassan et al.* [2006] found that short asymmetrical hydrographs did not produce substantial vertical sorting. Nonetheless, future modeling efforts incorporating realistic vertical sorting may improve predictions of bed surface patchiness.

Second are the possible effects of grain-to-grain interactions, which are not incorporated into any continuum sediment transport model. Interactions between coarse and fine grains have been shown to produce significant sorting features such as bedload sheets [*Whiting et al.*, 1988; *Nelson et al.*, 2009]. Our model results suggest that there may be bounds to the degree of patchiness associated with topographically-induced sorting mechanisms, but in reality, grain interactions may be occurring and acting on top this sorting, which could form patches finer or coarser than what the model can make on its own. Incorporation of grain interactions into sediment transport relations and bed evolution models is a potentially fruitful area of future research that may lead to improved ability to predict bed surface patchiness.

Finally, although not applicable to the steady flow conditions of our flume experiment, variable stage effects undoubtedly play a significant role in the formation of bed surface patches. In natural channels, as a hydrograph recedes, the bedload progressively fines and fine material is deposited in pools [e.g. *Lisle and Hilton*, 1992, 1999]. If depositional periods during receding flow were the primary method of forming patches of fine bed material, it would be impossible to form patches finer than the sediment supply grain size distribution under steady flow conditions.

5.5 Summary and conclusions

In order to explore mechanisms responsible for the development of bed surface patches in channels with alternate bars, we have developed a two-dimensional morphodynamic model that can be used to simulate the evolution of river beds composed of gravel mixtures. The model calculates the depth-averaged flow field and uses standard relations to calculate the two-dimensional sediment transport field. A simple active layer assumption is then used to calculate the bed elevation and grain size distribution of the bed surface.

Comparisons of model predictions with observations from a near-field scale flume experiment show that the model predicts bed morphology and sorting patterns similar to the experimental observations, although the topography is slightly muted and the degree of

simulated patchiness is not as great as was observed in the flume. These discrepancies highlight the need for an improved treatment of stratigraphy and grain-to-grain interactions in morphodynamic models.

In the flume and in the numerical simulation, steady state conditions developed such that the total divergence of sediment transport was everywhere zero, but the divergence of boundary shear stress was nonzero. Stress divergence and sediment transport divergence over the bars were balanced by stress convergence and sediment flux convergence in the pools, allowing steady state conditions to be maintained. The increasing size selectivity of sediment transport in zones of decreasing shear stress led to the formation of coarse patches on the tops of bars. The pools exhibited high shear stresses and sediment transport rates, so the finer surface grain size there approached that of the sediment load.

Further numerical experiments were performed to explore interactions between bed surface patchiness and morphological evolution. Simulations of the formation of free bars with uniform sediment and mixed sediment with and without a grain size - roughness feedback suggested that bed patches can have demonstrable effect on the flow field, which leads to important feedbacks on the evolving bed morphology and in surface sorting itself. The grain size - roughness feedback modulates topographically-driven divergences of boundary shear stress and forms smaller bars, longer bar wavelengths, and less well-developed patches than simulations using an assumption of constant roughness. Our results suggest that forced-bed surface patches are not a mere byproduct of bed topography, but they interact with the evolving bed and through their effect on the flow field they can profoundly influence morphologic evolution.

Bibliography

Allen, J. R. L. (1978), L. Van Bendegom: A neglected innovator in meander studies, *Mem. Can. Soc. Pet. Geol.*, *5*, 199–209.

Andrews, E. D., and D. C. Erman (1986), Persistence in the size distribution of surficial bed material during an extreme snowmelt flood, *Water Resources Research*, *22*(2), 191–197.

Antonia, R. A., and R. E. Luxton (1971), The response of a turbulent boundary layer to a step change in surface roughness. Part 1. Smooth to rough, *Journal of Fluid Mechanics*, *48*(04), 721–761.

Antonia, R. A., and R. E. Luxton (1972), The response of a turbulent boundary layer to a step change in surface roughness. Part 2. Rough-to-smooth, *Journal of Fluid Mechanics*, *53*(4), 737–757.

Arnott, R. W. C., and B. M. Hand (1989), Bedforms, primary structures and grain fabric in the presence of suspended sediment rain, *Journal of Sedimentary Research*, *59*(6), 1062–1069.

Ashida, K., and M. Michiue (1972), Study on hydraulic resistance and bedload transport rate in alluvial streams, *Transactions, Japan Society of Civil Engineering*, *206*, 59–69.

Ashmore, P. E. (1991a), Channel morphology and bed load pulses in braided, gravel-bed streams, *Geografiska Annaler*, *68*, 361–371.

Ashmore, P. E. (1991b), How do gravel-bed rivers braid?, *Canadian Journal of Earth Sciences*, *28*(3), 326–341.

Ashworth, P., R. Ferguson, and M. Powell (1992a), Bedload transport and sorting in braided channels, in *Dynamics of Gravel-bed Rivers*, edited by P. Billi, R. Hey, C. Thorne, and P. Tacconi, pp. 497–513, John Wiley & Sons, Chichester, UK.

Ashworth, P. J., R. I. Ferguson, P. E. Ashmore, C. Paola, D. M. Powell, and K. L. Prestegaard (1992b), Measurements in a Braided River Chute and Lobe. 2. Sorting of Bed Load During Entrainment, Transport, and Deposition, *Water Resources Research*, *28*(7), 1887–1896.

Bathurst, J. C. (2002), At-a-site variation and minimum flow resistance for mountain rivers, *Journal of Hydrology*, *269*(1-2), 11–26.

Bennett, S. J., and J. S. Bridge (1995), The geometry and dynamics of low-relief bed forms in heterogeneous sediment in a laboratory channel, and their relationship to water flow and sediment transport, *Journal of Sedimentary Research*, *65*(1), 29–39.

Best, J. L. (1996), The fluid dynamics of small-scale alluvial bedforms, in *Advances in Fluvial Dynamics and Stratigraphy*, edited by P. A. Carling and M. R. Dawson, pp. 67–125, John Wiley & Sons, Chichester, UK.

Blom, A., and G. Parker (2004), Vertical sorting and the morphodynamics of bed form–dominated rivers: A modeling framework, *Journal of Geophysical Research*, *109*, F02007, doi:10.1029/2003JF000069.

Blondeaux, P., and G. Seminara (1985), A unified bar-bend theory of river meanders, *Journal of Fluid Mechanics*, *157*, 449–470.

Bluck, B. J. (1971), Sedimentation in the meandering River Endrick, *Scottish Journal of Geology*, *7*, 93–138.

Bluck, B. J. (1987), Bed forms and clast size changes in gravel-bed rivers, in *River Channels: Environment and Process*, edited by K. Richards, pp. 159–178, Institute of British Geographers Special Publication No. 18, Basil Blackwell, Inc., Oxford, UK.

Bobertz, B., and J. Harff (2004), Sediment facies and hydrodynamic setting: a study in the south western Baltic Sea, *Ocean Dynamics*, *54*(1), 39–48.

Borradaile, G. J. (2003), *Statistics of earth science data: their distribution in time, space, and orientation*, 351 pp., Springer Verlag, New York.

Bridge, J. S. (1977), Flow, bed topography, grain size and sedimentary structure in bends: a three dimensional model, *Earth Surface Processes*, *2*, 401–416.

Bridge, J. S. (1992), A revised model for water flow, sediment transport, bed topography and grain size sorting in natural river bends, *Water Resources Research*, *28*(4), 999–1013.

Bridge, J. S., and J. Jarvis (1976), Flow and sedimentary processes in the meandering river South Esk, Glen Clova, Scotland, *Earth Surface Processes*, *1*(4), 303–336.

Bridge, J. S., and J. Jarvis (1982), The dynamics of a river bend: a study in flow and sedimentary processes, *Sedimentology*, *29*(4), 499–541.

Buffington, J. M., and D. R. Montgomery (1997), A systematic analysis of eight decades of incipient motion studies, with special reference to gravel-bedded rivers, *Water Resources Research*, *33*(8), 1993–2029.

Buffington, J. M., and D. R. Montgomery (1999a), A procedure for classifying textural facies in gravel-bed rivers, *Water Resources Research*, *35*(6), 1903–1914.

Buffington, J. M., and D. R. Montgomery (1999b), Effects of hydraulic roughness on surface textures of gravel-bed rivers, *Water Resources Research*, *35*(11), 3507–3521.

Buffington, J. M., and D. R. Montgomery (1999c), Effects of sediment supply on surface textures of gravel-bed rivers, *Water Resources Research*, *35*(11), 3523–3530.

Buffington, J. M., W. E. Dietrich, and J. W. Kirchner (1992), Friction angle measurements on a naturally formed gravel streambed: Implications for critical boundary shear stress, *Water Resources Research*, *28*(2), 411–425.

Buffington, J. M., D. R. Montgomery, and H. M. Greenberg (2004), Basin-scale availability of salmonid spawning gravel as influenced by channel type and hydraulic roughness in mountain catchments, *Canadian Journal of Fisheries and Aquatic Sciences*, *61*(11), 2085–2096, doi:10.1139/F04-141.

Bunte, K., and S. R. Abt (2001), Sampling surface and subsurface particle-size distributions in wadable gravel- and cobble-bed streams for analyses in sediment transport, hydraulics, and streambed monitoring, Gen. Tech. Rep. RMRS-GTR-74, *Tech. rep.*, U.S. Department of Agriculture, Forest Service, Rocky Mountain Research Station, Fort Collins, CO.

Bunte, K., and S. R. Abt (2005), Effect of sampling time on measured gravel bed load transport rates in a coarse-bedded stream, *Water Resources Research*, *41*(11), doi: 10.1029/2004WR003880.

Bunte, K., S. R. Abt, J. P. Potyondy, and S. E. Ryan (2004), Measurement of coarse gravel and cobble transport using portable bedload traps, *Journal of Hydraulic Engineering*, *130*, 879, doi:10.1061/.

Butler, J. B., S. N. Lane, and J. H. Chandler (2001), Automated extraction of grain-size data from gravel surfaces using digital image processing, *Journal of Hydraulic Research*, *39*(4), 1–11.

Carey, W. (1985), Variability in measured bedload-transport rates, *Water Resources Bulletin*, *21*, 39–48.

Carling, P. A. (1999), Subaqueous gravel dunes, *Journal of Sedimentary Research*, *69*(3), 534–545.

Carson, M. A. (1986), Characteristics of high-energy "meandering" rivers; the Canterbury Plains, New Zealand, *Bulletin of the Geological Society of America*, *97*(7), 886–895.

Chen, L., and M. C. Stone (2008), Influence of bed material size heterogeneity on bedload transport uncertainty, *Water Resources Research*, *44*, doi:10.1029/2006WR005483.

Church, M. (2002), Geomorphic thresholds in riverine landscapes, *Freshwater Biology*, *47*(4), 541–557.

Church, M., M. A. Hassan, and J. F. Wolcott (1998), Stabilizing self-organized structures in gravel-bed stream channels: Field and experimental observations, *Water Resources Research*, *34*(11), 3169–3179.

Clayton, J. A. (2010), Local sorting, bend curvature, and particle mobility in meandering gravel bed rivers, *Water Resources Research*, *46*, W02601, doi:10.1029/2008WR007669.

Clayton, J. A., and J. Pitlick (2007), Spatial and temporal variations in bed load transport intensity in a gravel bed river bend, *Water Resources Research*, *43*(2), W02426, doi: 10.1029/2006WR005253.

Clayton, J. A., and J. Pitlick (2008), Persistence of the surface texture of a gravel-bed river during a large flood, *Earth Surface Processes and Landforms*, *33*(5), 661–673, doi: 10.1002/esp.1567.

Colombini, M., G. Seminara, and M. Tubino (1987), Finite-amplitude alternate bars, *Journal of Fluid Mechanics*, *181*, 213–232.

Conover, W. J. (1971), *Practical Nonparametric Statistics*, 462 pp., Wiley, New York.

Cooper, S. D., L. Barmuta, O. Sarnelle, K. Kratz, and S. Diehl (1997), Quantifying spatial heterogeneity in streams, *Journal of the North American Benthological Society*, *16*(1), 174–188.

Crosato, A., and F. B. Desta (2009), Intrinsic steady alternate bars in alluvial channels. Part 1: experimental observations and numerical tests, in *RCEM 2009: River, Coastal and Estuarine Morphodynamics*, edited by C. A. Vionnet, M. H. Garcia, E. M. Latrubesse, and G. M. E. Perillo, pp. 759–765, Taylor & Francis Group, London.

Crowder, D. W., and P. Diplas (1997), Sampling heterogeneous deposits in gravel-bed streams, *Journal of Hydraulic Engineering*, *123*(12), 1106–1117.

Cudden, J. R., and T. B. Hoey (2003), The causes of bedload pulses in a gravel channel: the implications of bedload grain-size distributions., *Earth Surface Processes and Landforms*, *28*(13), 1411–1428, doi:10.1002/esp.521.

Cui, Y. (2007), The Unified Gravel-Sand (TUGS) Model: Simulating sediment transport and gravel/sand grain size distributions in gravel-bedded rivers, *Water Resources Research*, *43*(10), W10436, doi:10.1029/2006WR005330.

Cummins, K. W., and G. H. Lauff (1969), The influence of substrate particle size on the microdistribution of stream macrobenthos, *Hydrobiologia*, *34*(2), 145–181.

De Vries, M. (1970), On the accuracy of bed-material sampling, *Journal of Hydraulic Research*, *8*(4), 523–533.

Dietrich, W. E. (1987), Mechanics of flow and sediment transport in river bends, in *River Channels: Environment and Process*, edited by K. S. Richards, pp. 179–227, Institute of British Geographers Special Publication No. 18, Basil Blackwell, Inc., Oxford, UK.

Dietrich, W. E., and J. D. Smith (1983), Influence of the point bar on flow through curved channels, *Water Resources Research*, *19*(5), 1173–1192.

Dietrich, W. E., and J. D. Smith (1984), Bed load transport in a river meander, *Water Resources Research*, *20*(10), 1355–1380.

Dietrich, W. E., and P. Whiting (1989), Boundary shear stress and sediment transport in river meanders of sand and gravel, in *River Meandering, American Geophysical Union Water Resources Monograph*, vol. 12, edited by S. Ikeda and G. Parker, pp. 1–50, American Geophysical Union, Washington, DC.

Dietrich, W. E., J. W. Kirchner, H. Ikeda, and F. Iseya (1989), Sediment supply and the development of the coarse surface layer in gravel-bedded rivers, *Nature*, *340*, 215–217.

Dietrich, W. E., P. A. Nelson, E. Yager, J. G. Venditti, M. P. Lamb, and L. Collins (2005), Sediment patches, sediment supply, and channel morphology, in *4th Conference on River, Coastal, and Estuarine Morphodynamics, RCEM 2005*, edited by G. Parker and M. H. Garcia, pp. 79–90, A. A. Balkema Publishers, Rotterdam.

Dinehart, R. L. (1992), Evolution of Coarse Gravel Bed Forms: Field Measurements at Flood Stage, *Water Resources Research*, *28*(10), 2667–2689.

Diplas, P., and J. B. Fripp (1992), Properties of various sediment sampling procedures, *Journal of Hydraulic Engineering*, *118*(7), 955–970.

Drake, T. G., R. L. Shreve, W. E. Dietrich, P. J. Whiting, and L. B. Leopold (1988), Bedload transport of fine gravel observed by motion-picture photography, *Journal of Fluid Mechanics*, *192*, 193–217.

Duan, J. G., and P. Y. Julien (2005), Numerical simulation of the inception of channel meandering, *Earth Surface Processes and Landforms*, *30*(9), 1093–1110, doi:10.1002/esp.1264.

Egiazaroff, I. V. (1965), Calculation of nonuniform sediment concentrations, *J. Hydraul. Div. Am. Soc. Civ. Eng*, *91*(4), 225–247.

Engelund, F. (1974), Flow and bed topography in channel bends, *Journal of the Hydraulics Division - ASCE*, *100*, 1631–1648.

Ferguson, R., T. Hoey, S. Wathen, and A. Werritty (1996), Field evidence for rapid downstream fining of river gravels through selective transport, *Geology*, *24*(2), 179–182.

Ferguson, R. I. (2003), The missing dimension: effects of lateral variation on 1-D calculations of fluvial bedload transport, *Geomorphology*, *56*(1-2), 1–14, doi:10.1016/S0169-555X.

Ferguson, R. I., K. L. Prestegaard, and P. J. Ashworth (1989), Influence of sand on hydraulics and gravel transport in a braided gravel-bed river, *Water Resources Research*, *25*(4), 635–643.

Forbes, D. L. (1983), Morphology and sedimentology of a sinuous gravel-bed channel system: lower Babbage River, Yukon coastal plain, Canada, in *Modern and Ancient Fluvial Systems*, edited by J. D. Collinson and J. Lewin, pp. 195–206, Blackwell Scientific, Oxford, UK.

Fripp, J. B., and P. Diplas (1993), Surface sampling in gravel streams, *Journal of Hydraulic Engineering*, *119*, 473.

Garcia, C., J. B. Laronne, and M. Sala (1999), Variable source areas of bedload in a gravel-bed stream, *Journal of Sedimentary Research*, *69*(1), 27–31.

Garcia, C., H. Cohen, I. Reid, A. Rovira, X. Úbeda, and J. B. Laronne (2007), Processes of initiation of motion leading to bedload transport in gravel-bed rivers, *Geophysical Research Letters*, *34*(6), L06403, doi:10.1029/2006GL028865.

Gilbert, G. K. (1914), The transportation of debris by running water, *US. Geological Survey Professional Paper 86*, p. 263 pp.

Gomez, B., R. L. Naff, and D. W. Hubbell (1989), Temporal variations in bedload transport rates associated with the migration of bedforms, *Earth Surface Processes and Landforms*, *14*(2), 135–156.

Gomez, B., B. J. Rosser, D. H. Peacock, D. M. Hicks, and J. A. Palmer (2001), Downstream fining in a rapidly aggrading gravel bed river, *Water Resources Research*, *37*(6), 1813–1823.

Graham, D. J., I. Reid, and S. P. Rice (2005a), Automated sizing of coarse-grained sediments: image-processing procedures, *Mathematical Geology*, *37*(1), 1–28.

Graham, D. J., S. P. Rice, and I. Reid (2005b), A transferable method for the automated grain sizing of river gravels, *Water Resources Research*, W07020, doi: 10.1029/2004WR003868.

Graham, D. J., S. P. Rice, and I. Reid (2005c), Comment: photographic techniques for characterizing streambed particle sizes, *Transactions of the American Fisheries Society*, *134*, 1599–1603, doi:10.1577/T04-146.1.

Graham, D. J., A.-J. . J. Rollet, H. Piégay, and S. P. Rice (2010), Maximizing the accuracy of image-based surface sampling techniques, *Water Resources Research*, *46*, W02508, doi: 10.1029/2008WR006940.

Gran, K. B., D. R. Montgomery, and D. G. Sutherland (2006), Channel bed evolution and sediment transport under declining sand inputs, *Water Resources Research*, *42*, doi: 10.1029/2005WR004306.

Gustafson, E. J. (1998), Quantifying landscape spatial pattern: What is the state of the art?, *Ecosystems*, *1*(2), 143–156.

Gustavson, T. C. (1978), Bed forms and stratification types of modern gravel meander lobes, Nueces River, Texas, *Sedimentology*, *25*(3), 401–426.

Hagen, L., and A. B. Kahng (1992), New spectral methods for ratio cut partitioning and clustering, *IEEE Transactions on Computer-Aided Design of Integrated Circuits and Systems*, *11*(9), 1074–1085.

Hamilton, L. J. (2007), Clustering of cumulative grainsize distribution curves for shallow-marine samples with software program CLARA, *Australian Journal of Earth Sciences*, *54*(4), 503–519.

Harrison, L. R., and E. A. Keller (2007), Modeling forced pool-riffle hydraulics in a boulder-bed stream, southern California, *Geomorphology*, *83*(3-4), 232–248, doi: 10.1016/j.geomorph.2006.02.024.

Haschenburger, J. K., and S. P. Rice (2004), Changes in woody debris and bed material texture in a gravel-bed channel, *Geomorphology*, *60*(3-4), 241–267, doi: 10.1016/j.geomorph.2003.08.003.

Hasegawa, K. (1984), Hydraulic research on planimetric forms, bed topographies, and flow in alluvial rivers, Ph.D. thesis, Hokkaido University, Sapporo.

Hassan, M. A., and M. Church (2000), Experiments on surface structure and partial sediment transport on a gravel bed, *Water Resources Research*, *36*(7), 1885–1896.

Hassan, M. A., R. Egozi, and G. Parker (2006), Experiments on the effect of hydrograph characteristics on vertical grain sorting in gravel bed rivers, *Water Resources Research*, *42*(9), doi:10.1029/2005WR004707.

Heritage, G. L., and D. J. Milan (2004), A conceptual model of the role of excess energy in the maintenance of a riffle–pool sequence, *Catena*, *58*(3), 235–257, doi: 10.1016/j.catena.2004.05.002.

Hirano, M. (1971), River bed degradation with armouring, *Trans. Jpn. Soc. Civ. Eng*, *195*, 55–65.

Hoey, T. (1992), Temporal variations in bedload transport rates and sediment storage in gravel-bed rivers, *Progress in Physical Geography*, *16*(3), 319, doi: 10.1177/030913339201600303.

Hoey, T. B., and R. Ferguson (1994), Numerical simulation of downstream fining by selective transport in gravel bed rivers: Model development and illustration, *Water Resources Research*, *30*(7), 2251–2260.

Howard, A. D. (1992), Modeling channel migration and floodplain sedimentation in meandering streams, in *Lowland Floodplain Rivers: Geomorphological Perspectives*, pp. 1–41, John Wiley & Sons Ltd, Chichester.

Howard, A. D. (1996), Modelling channel evolution and floodplain morphology, in *Floodplain processes*, edited by M. G. Anderson, D. E. Walling, and P. D. Bates, pp. 15–62, John Wiley and Sons, New York.

Hubbard, E. F. (1988), Approval of standard rating for polymer-rotor pygmy meter with cat-whisker head (P-Pygmy or PPG Meter), *USGS Office of Surface Water Technical Memorandum No. 89.01.*

Ikeda, H. (1983), Experiments on bedload transport, bed forms, and sedimentary structures using fine gravel in the 4-meter-wide flume, Environmental Research Center Papers No. 2, *Tech. rep.*, Univ. of Tsukuba, Ibaraki, Japan.

Ikeda, S. (1989), Sediment transport and sorting at bends, in *River Meandering, American Geophysical Union Water Resources Monograph*, vol. 12, edited by S. Ikeda and G. Parker, pp. 103–125, American Geophysical Union, Washington, DC.

Iseya, F., and H. Ikeda (1987), Pulsations in bedload transport rates induced by a longitudinal sediment sorting: a flume study using sand and gravel mixtures, *Geografiska Annaler*, *69*(1), 15–27.

Jackson, R. G. (1975), Velocity-bed-form-texture patterns of meander bends in the lower Wabash River of Illinois and Indiana, *Geological Society of America Bulletin*, *86*(11), 1511–1522.

Jain, A. K. (2009), Data clustering: 50 years beyond K-means, *Pattern Recognition Letters*, *31*, 651–666, doi:10.1016/j.patrec.2009.09.011.

Jain, A. K., M. N. Murty, and P. J. Flynn (1999), Data clustering: a review, *ACM computing surveys (CSUR)*, *31*(3), 264–323.

Julien, P. Y., and D. J. Anthony (2002), Bed load motion and grain sorting in a meandering stream, *Journal of Hydraulic Research*, *40*(2), 125–133.

Katul, G., P. Wiberg, J. Albertson, and G. Hornberger (2002), A mixing layer theory for flow resistance in shallow streams, *Water Resources Research*, *38*(11), 32–1, doi: 10.1029/2001WR000817.

Keller, E. A. (1971), Areal sorting of bed-load material; the hypothesis of velocity reversal, *Bulletin of the Geological Society of America*, *82*(3), 753–756.

Kellerhals, R., and D. I. Bray (1971), Sampling procedures for coarse fluvial sediments, *Journal of the Hydraulics Division*, *97*(8), 1165–1180.

Kikkawa, H., S. Ikeda, and A. Kitagawa (1976), Flow and bed topography in curved open channels, *Journal of the Hydraulics Division - ASCE*, *102*, 1327–42.

Kinerson, D. (1990), Surface response to sediment supply, Master's thesis, University of California, Berkeley.

Kinzel, P. J., J. M. Nelson, and A. K. Heckman (2009), Response of sandhill crane (Grus canadensis) riverine roosting habitat to changes in stage and sandbar morphology, *River Research and Applications*, *25*(2), 135–152, doi:10.1002/rra.1103.

Kirchner, J. W., W. E. Dietrich, F. Iseya, and H. Ikeda (1990), The variability of critical shear stress, friction angle, and grain protrusion in water-worked sediments, *Sedimentology*, *37*(4), 647–672.

Kleinhans, M. G., A. W. E. Wilbers, A. De Swaaf, and J. H. Van Den Berg (2002), Sediment supply-limited bedforms in sand-gravel bed rivers, *Journal of Sedimentary Research*, *72*(5), 629–640.

Knighton, A. D. (1980), Longitudinal changes in size and sorting of stream-bed material in four English rivers, *Bulletin of the Geological Society of America*, *91*(1), 55.

Kodama, Y. (1994), Downstream changes in the lithology and grain size of fluvial gravels, the Watarase River, Japan: evidence of the role of abrasion in downstream fining, *Journal of Sedimentary Research-Section A-Sedimentary Petrology and Processes*, *64*(1), 68–75.

Kondolf, G. M., and M. G. Wolman (1993), The sizes of salmonid spawning gravels, *Water Resources Research*, *29*(7), 2275–2285.

Kuhnle, R. A., and J. B. Southard (1988), Bed load transport fluctuations in a gravel bed laboratory channel, *Water Resources Research*, *24*(2), 247–260.

Kuhnle, R. A., J. K. Horton, S. J. Bennett, and J. L. Best (2006), Bed forms in bimodal sand-gravel sediments: laboratory and field analysis, *Sedimentology*, *53*(3), 631–654, doi: 10.1111/j.1365-3091.2005.00765.x.

Kulis, B., S. Basu, I. Dhillon, and R. Mooney (2005), Semi-supervised graph clustering: a kernel approach, in *Proceedings of the 22nd International Conference on Machine Learning*, Bonn, Germany.

Lamb, M. P., W. E. Dietrich, and J. G. Venditti (2008), Is the critical Shields stress for incipient sediment dependent on channel-bed slope?, *Journal of Geophysical Research*, *113*, F02008, doi:10.1029/2007JF000831.

Lane, E. W. (1955), Design of stable channels, *Transactions of the American Society of Civil Engineers*, *120*, 1234–1260.

Lane, S. N., K. F. Bradbrook, K. S. Richards, P. A. Biron, and A. G. Roy (1999), The application of computational fluid dynamics to natural river channels: three-dimensional versus two-dimensional approaches, *Geomorphology*, *29*(1-2), 1–20.

Lanzoni, S. (2000a), Experiments on bar formation in a straight flume. 2. Graded sediment, *Water Resources Research*, *36*(11), 3351–3364.

Lanzoni, S. (2000b), Experiments on bar formation in a straight flume. 1. Uniform sediment, *Water Resources Research*, *36*(11), 3337–3350.

Lanzoni, S., and M. Tubino (1999), Grain sorting and bar instability, *Journal of Fluid Mechanics*, *393*, 149–174.

Laronne, J., and M. Duncan (1992), Bedload transport paths and gravel bar formation, in *Dynamics of Gravel-bed Rivers*, edited by P. Billi, R. Hey, C. Thorne, and P. Tacconi, pp. 177–202, John Wiley & Sons, Chichester, UK.

Laronne, J. B., C. Garcia, and I. Reid (2000), Mobility of patch sediment in gravel bed streams: Patch character and its implications for bedload, in *Gravel-Bed Rivers V*, edited by M. P. Mosley, pp. 249–280, New Zealand Hydrological Society, Inc., Wellington, New Zealand.

Leopold, L. B., and M. G. Wolman (1957), River channel patterns: braided, meandering and straight, *US Geol. Survey Prof. Paper*, *282*, 39–85.

Leopold, L. B., and M. G. Wolman (1960), River meanders, *Geological Society of America Bulletin*, *71*(6), 769–793.

Lisle, T., and M. Madej (1992), Spatial variation in armouring in a channel with high sediment supply, in *Dynamics of Gravel-bed Rivers*, edited by P. Billi, R. Hey, C. Thorne, and P. Tacconi, pp. 277–293, John Wiley & Sons, Chichester, UK.

Lisle, T. E. (1979), A sorting mechanism for a riffle-pool sequence, *Geological Society of America Bulletin*, *90*(2), 1142–1157.

Lisle, T. E., and S. Hilton (1992), Volume of fine sediment in pools: An index of sediment supply in gravel-bed streams, *Water Resources Bulletin*, *28*(2), 371–383.

Lisle, T. E., and S. Hilton (1999), Fine bed material in pools of natural gravel bed channels, *Water Resources Research*, *35*(4), 1291–1304.

Lisle, T. E., H. Ikeda, and F. Iseya (1991), Formation of stationary alternate bars in a steep channel with mixed-size sediment: A flume experiment, *Earth Surface Processes and Landforms*, *16*(5), 463–469.

Lisle, T. E., F. Iseya, and H. Ikeda (1993), Response of a channel with alternate bars to a decrease in supply of mixed-size bed load: A flume experiment, *Water Resources Research*, *29*(11), 3623–3629.

Lisle, T. E., J. M. Nelson, J. Pitlick, M. A. Madej, and B. L. Barkett (2000), Variability of bed mobility in natural, gravel-bed channels and adjustments to sediment load at local and reach scales, *Water Resources Research*, *36*(12), 3743–3755.

Lunt, I. A., and J. S. Bridge (2004), Evolution and deposits of a gravelly braid bar, Sagavanirktok River, Alaska, *Sedimentology*, *51*(3), 415–432, doi:10.1111/j.1365-3091.2004.00628.x.

Lunt, I. A., and J. S. Bridge (2007), Formation and preservation of open-framework gravel strata in unidirectional flows, *Sedimentology*, *54*(1), 71–87, doi:10.1111/j.1365-3091.2006.00829.x.

MacVicar, B. J., L. Parrott, and A. G. Roy (2006), A two-dimensional discrete particle model of gravel bed river systems, *Journal of Geophysical Research*, *111*, F03009, doi: 10.1029/2005JF000316.

MacWilliams, M. L., J. M. Wheaton, G. B. Pasternack, R. L. Street, and P. K. Kitanidis (2006), Flow convergence routing hypothesis for pool-riffle maintenance in alluvial rivers, *Water Resources Research*, *42*, W10427, doi:10.1029/2005WR004391.

Madej, M. A., D. G. Sutherland, T. E. Lisle, and B. Pryor (2009), Channel responses to varying sediment input: A flume experiment modeled after Redwood Creek, California, *Geomorphology*, *103*(4), 507–519, doi:10.1016/j.geomorph.2008.07.017.

Marr, J. D., S. R. Johnson, C. Hill, and C. Ellis (2010), StreamLab06: Overview of experiments, instrumentation, and data collection, *Project Report 539*, National Center for Earth Surface Dynamics, St. Anthony Falls Laboratory, University of Minnesota.

McDonald, R. R., J. M. Nelson, and J. P. Bennett (2005), Multi-dimensional surface-water modeling system user's guide, *U.S. Geological Survey Technical Methods*, *6-B2*, 136.

McEwan, I. K., T. M. Sheen, G. J. Cunningham, and A. R. Allen (2000), Estimating the size composition of sediment surfaces through image analysis, *Proceedings of the Institute of Civil Engineers, Water and Maritime Engineering*, *142*(4), 189–195.

McGarigal, K., S. A. Cushman, M. C. Neel, and E. Ene (2002), FRAGSTATS: spatial pattern analysis program for categorical maps, http://www.umass.edu/landeco/research/-fragstats/fragstats.html.

Mikoš, M., G. Pender, T. Hoey, A. Shvidchenko, and G. Petkovšek (2003), Numerical simulation of graded sediment transport, *Water & Maritime Engineering*, *156*(1), 47–51.

Milan, D. J., G. L. Heritage, A. R. G. Large, and M. E. Charlton (2001), Stage dependent variability in tractive force distribution through a riffle–pool sequence, *Catena*, *44*(2), 85–109.

Milhous, R. T. (1973), Sediment transport in a gravel-bottomed stream, Ph.D. thesis, Oregon State University, Corvallis.

Mosley, M. P., and D. S. Tindale (1985), Sediment variability and bed material sampling in gravel-bed rivers, *Earth Surface Processes and Landforms*, *10*(5), 465–482.

Mosselman, E. (2009), Intrinsic steady alternate bars in alluvial channels. Part 2: Theoretical analysis, in *RCEM 2009: River, Coastal and Estuarine Morphodynamics*, edited by C. A. Vionnet, M. H. Garcia, E. M. Latrubesse, and G. M. E. Perillo, pp. 767–770, Taylor & Francis Group, London.

Moussavi-Harami, R., A. Mahboubi, and M. Khanehbad (2004), Analysis of controls on downstream fining along three gravel-bed rivers in the Band-e-Golestan drainage basin NE Iran, *Geomorphology*, *61*(1-2), 143–153.

Nelson, J. M. (1990), The initial instability and finite-amplitude stability of alternate bars in straight channels, *Earth-Science Reviews*, *29*, 97–115.

Nelson, J. M., and R. R. McDonald (1995), Mechanics and modeling of flow and bed evolution in lateral separation eddies, in *USGS Directors Approved report submitted to the USGS Grand Canyon Monitoring and Research Center*, p. 39, Flagstaff, AZ.

Nelson, J. M., and J. D. Smith (1989a), Flow in meandering channels with natural topography, in *River Meandering, American Geophysical Union Water Resources Monograph*, vol. 12, edited by S. Ikeda and G. Parker, pp. 69–102, American Geophysical Union, Washington, DC.

Nelson, J. M., and J. D. Smith (1989b), Evolution and stability of erodible channel beds, in *River Meandering, American Geophysical Union Water Resources Monograph*, edited by S. Ikeda and G. Parker, pp. 321–378, American Geophysical Union, Washington, DC.

Nelson, J. M., J. P. Bennett, and S. M. Wiele (2003), Flow and sediment-transport modeling, in *Tools in Fluvial Geomorphology*, edited by G. M. Kondolf and H. Piégay, pp. 539–576, John Wiley & Sons, Chichester.

Nelson, P. A., J. G. Venditti, and W. E. Dietrich (2005), Response of bed surface patchiness to reductions in sediment supply, *Eos Trans. AGU*, *86*(52), Fall Meet. Suppl., Abstract H51H-04.

Nelson, P. A., J. G. Venditti, W. E. Dietrich, J. W. Kirchner, H. Ikeda, F. Iseya, and L. S. Sklar (2009), Response of bed surface patchiness to reductions in sediment supply, *Journal of Geophysical Research*, *114*, F02005, doi:10.1029/2008JF001144.

Nelson, P. A., W. E. Dietrich, and J. G. Venditti (2010), Bed topography and the development of forced bed surface patches, *Journal of Geophysical Research*, *115*, F04024, doi:10.1029/2010JF001747.

Overstreet, B. T., C. S. Riebe, J. K. Wooster, and F. K. Ligon (2010), Limits on salmon spawning in coarse-bedded rivers, Abstract COS 48-4, 95th ESA Annual Meeting, Pittsburgh, Penn., August 1-6.

Paola, C., and R. Seal (1995), Grain size patchiness as a cause of selective deposition and downstream fining, *Water Resources Research*, *31*(5), 1395–1408.

Paola, C., G. Parker, R. Seal, S. K. Sinha, J. B. Southard, and P. R. Wilcock (1992), Downstream fining by selective deposition in a laboratory flume, *Science*, *258*(5089), 1757.

Parker, G. (1984), Discussion of Lateral Bed Load Transport on Side Slopes, *Journal of Hydraulic Engineering*, *110*(2), 197–199.

Parker, G. (1990), Surface-based bedload transport relation for gravel rivers, *Journal of Hydraulic Research*, *28*(4), 417–436.

Parker, G. (1992), Some random notes on grain sorting, in *Grain Sorting Seminar*, 117, pp. 19–76, Eidgenőssische Technische Hochschule Zűrich.

Parker, G. (2008), Transport of gravel and sediment mixtures, in *Sedimentation Engineering, ASCE Manual No. 110*, edited by M. H. Garcia and G. Parker, pp. 165–252, American Society of Civil Engineers, Reston, VA.

Parker, G., and E. D. Andrews (1985), Sorting of bed load sediment by flow in meander bends, *Water Resources Research*, *21*(9), 1361–1373.

Parker, G., and P. C. Klingeman (1982), On why gravel bed streams are paved, *Water Resources Research*, *18*(5), 1409–1423.

Parker, G., C. Paola, and S. Leclair (2000), Probabilistic Exner sediment continuity equation for mixtures with no active layer, *Journal of Hydraulic Engineering*, *126*(11), 818–826.

Parker, G., P. R. Wilcock, C. Paola, W. E. Dietrich, and J. Pitlick (2007), Physical basis for quasi-universal relations describing bankfull hydraulic geometry of single-thread gravel bed rivers, *Journal of Geophysical Research*, *112*, F04005, doi:10.1029/2006JF000549.

Pender, G., and A. Shvidchenko (1999), The observation of bedload sheets in laboratory experiments, *Proceedings of the 28th Congress of the International Association for Hydraulic Research*.

Petrie, J., and P. Diplas (2000), Statistical approach to sediment sampling accuracy, *Water Resources Research*, *36*(2), 597–605.

Pitlick, J. (1988), Variability of bed load measurement, *Water Resources Research*, *24*(1), 173–177.

Powell, D. M. (1998), Patterns and processes of sediment sorting in gravel-bed rivers, *Progress in Physical Geography*, *22*(1), 1, doi:10.1177/030913339802200101.

Power, M. E., W. E. Dietrich, and K. O. Sullivan (1998), Experimentation, observation, and inference in river and watershed investigations, in *Experimental Ecology*, edited by W. J. Resetarits and J. Bernardo, pp. 113–132, Oxford University Press, New York.

Rabeni, C. F., and G. W. Minshall (1977), Factors affecting microdistribution of stream benthic insects, *Oikos*, pp. 33–43.

Rattray, M., Jr., and E. Mitsuda (1974), Theoretical analysis of conditions in a salt wedge, *Estuarine and Coastal Marine Science*, *2*, 373–394.

Reice, S. R. (1980), The role of substratum in benthic macroinvertebrate microdistribution and litter decomposition in a woodland stream, *Ecology*, *61*(3), 580–590.

Rice, S., and M. Church (1998), Grain size along two gravel-bed rivers: statistical variation, spatial pattern and sedimentary links, *Earth Surface Processes and Landforms*, *23*(4), 345–363.

Riebe, C. S., B. T. Overstreet, J. K. Wooster, and F. K. Ligon (2010), A new tool for assessing salmon spawning substrates in coarse-bedded rivers, Abstract H43D-1292 presented at 2010 Fall Meeting, AGU, San Francisco, Calif., 13-17 Dec.

Rossi, R. E., D. J. Mulla, A. G. Journel, and E. H. Franz (1992), Geostatistical tools for modeling and interpreting ecological spatial dependence, *Ecological Monographs*, *62*(2), 277–314.

Sambrook Smith, G. H., and R. I. Ferguson (1995), The gravel sand transition along river channels, *Journal of Sedimentary Research*, *65*(2), 423–430.

Sambrook Smith, G. H., and A. P. Nicholas (2005), Effect on flow structure of sand deposition on a gravel bed: Results from a two-dimensional flume experiment, *Water Resources Research*, *41*, W10405, doi:10.1029/2004WR003817.

Sawyer, A. M., G. B. Pasternack, H. J. Moir, and A. A. Fulton (2010), Riffle-pool maintenance and flow convergence routing observed on a large gravel-bed river, *Geomorphology*, *114*(3), 143–160, doi:10.1016/j.geomorph.2009.06.021.

Schmeeckle, M. W., and J. M. Nelson (2003), Direct numerical simulation of bedload transport using a local, dynamic boundary condition, *Sedimentology*, *50*(2), 279–301.

Seal, R., and C. Paola (1995), Observations of downstream fining on the North Fork Toutle River near Mount St. Helens, Washington, *Water Resources Research*, *31*, 1409–1419.

Sekine, M., and G. Parker (1992), Bed-load transport on transverse slope. I, *Journal of Hydraulic Engineering*, *118*(4), 513–535.

Seminara, G. (1998), Stability and morphodynamics, *Meccanica*, *33*(1), 59–99.

Seminara, G., M. Colombini, and G. Parker (1996), Nearly pure sorting waves and formation of bedload sheets, *Journal of Fluid Mechanics*, *312*, 253–278.

Shi, J., and J. Malik (2000), Normalized cuts and image segmentation, *IEEE Transactions on pattern analysis and machine intelligence*, *22*(8), 888–905.

Sime, L. C., and R. I. Ferguson (2003), Information on grain sizes in gravel-bed rivers by automated image analysis, *Journal of Sedimentary Research*, *73*(4), 630–636.

Sime, L. C., R. I. Ferguson, and M. Church (2007), Estimating shear stress from moving boat acoustic Doppler velocity measurements in a large gravel bed river, *Water Resources Research*, *43*, W03418, doi:10.1029/2006WR005069.

Simons, D., E. Richardson, and C. Nordin (1965), Bedload equation for ripples and dunes, *U.S. Geol. Surf. Prof. Paper*, *462-H*, 1–9.

Singh, A., K. Fienberg, D. J. Jerolmack, J. Marr, and E. Foufoula-Georgiou (2009), Experimental evidence for statistical scaling and intermittency in sediment transport rates, *Journal of Geophysical Research*, *114*, F01025, doi:10.1029/2007JF000963.

Sklar, L. S., W. E. Dietrich, E. Foufoula-Georgiou, B. Lashermes, and D. Bellugi (2006), Do gravel bed river size distributions record channel network structure, *Water Resources Research*, *42*(6), doi:10.1029/2006WR005035.

Smith, J. D., and S. R. McLean (1984), A model for flow in meandering streams, *Water Resources Research*, *20*(9), 1301–1315.

Sun, T., P. Meakin, and T. Jøssang (2001a), A computer model for meandering rivers with multiple bed load sediment sizes, 1. Theory, *Water Resources Research*, *37*(8), 2227–2242.

Sun, T., P. Meakin, and T. Jøssang (2001b), A computer model for meandering rivers with multiple bed load sediment sizes, 2. Computer simulations, *Water Resources Research*, *37*(8), 2243–2258.

Surian, N. (2002), Downstream variation in grain size along an Alpine river: analysis of controls and processes, *Geomorphology*, *43*(1-2), 137–149.

Takebayashi, H., S. Tsukawaki, I. Sim, T. Sambath, and S. Sotham (2011), Characteristics of bed deformation and size distribution of bed material at Chaktomuk in Cambodia, in *Proceedings of the 11th International Symposium on River Sedimentation*.

Thompson, D. M., and K. S. Hoffman (2001), Equilibrium pool dimensions and sediment-sorting patterns in coarse-grained, New England channels, *Geomorphology*, *38*(3-4), 301–316.

Thompson, D. M., E. E. Wohl, and R. D. Jarrett (1996), A revised velocity-reversal and sediment-sorting model for a high-gradient, pool-riffle stream, *Physical Geography*, *17*(2), 142–156.

Thompson, D. M., E. E. Wohl, and R. D. Jarrett (1999), Velocity reversals and sediment sorting in pools and riffles controlled by channel constrictions, *Geomorphology*, *27*(3-4), 229–241.

Toro-Escobar, C. M., C. Paola, and G. Parker (1996), Transfer function for the deposition of poorly sorted gravel in response to streambed aggradation, *Journal of Hydraulic Research*, *34*(1), 35–53.

Tsujimoto, T. (1990), Instability of longitudinal distribution of fluvial bed-surface composition, *Jour. Hydroscience and Hydraulic Engineering, JSCE*, *7*(2), 69–80.

USBR (2001), Water Measurement Manual, *Tech. rep.*, United States Department of the Interior Bureau of Reclamation.

Venditti, J. G., M. Church, and S. J. Bennett (2005), Morphodynamics of small-scale superimposed sand waves over migrating dune bed forms, *Water Resources Research*, *41*, doi:10.1029/2004WR003461.

Venditti, J. G., W. E. Dietrich, P. A. Nelson, M. A. Wydzga, J. Fadde, and L. Sklar (2010), Mobilization of coarse surface layers in gravel-bedded rivers by finer gravel bed load, *Water Resources Research*, *46*(7), W07506, doi:10.1029/2009WR008329.

Vincent, L., and P. Soille (1991), Watersheds in digital spaces: an efficient algorithm based on immersion simulations, *IEEE Transactions on Pattern Analysis and Machine Intelligence*, *13*(6), 583–598.

von Luxburg, U. (2007), A tutorial on spectral clustering, *Statistics and Computing*, *17*(4), 395–416.

Whitaker, A., and D. Potts (2007), Coarse bed load transport in an alluvial gravel bed stream, Dupuyer Creek, Montana, *Earth Surface Processes and Landforms*, *32*, 1984–2004, doi:10.1002/esp.1512.

Whiting, P. J. (1996), Sediment sorting over bed topography, in *Advances in Fluvial Dynamics and Stratigraphy*, edited by P. Carling and M. Dawson, pp. 204–228, John Wiley & Sons, Chichester, UK.

Whiting, P. J., and W. E. Dietrich (1990), Boundary shear stress and roughness over mobile alluvial beds, *Journal of Hydraulic Engineering*, *116*(12), 1495–1511.

Whiting, P. J., and W. E. Dietrich (1991), Convective accelerations and boundary shear stress over a channel bar, *Water Resources Research*, *27*(5), 783–796.

Whiting, P. J., W. E. Dietrich, L. B. Leopold, T. G. Drake, and R. L. Shreve (1988), Bedload sheets in heterogeneous sediment, *Geology*, *16*(2), 105–108.

Wiberg, P. L., and J. D. Smith (1987), Calculations of the Critical Shear Stress for Motion of Uniform and Heterogeneous Sediments, *Water Resources Research*, *23*(8), 1471–1480.

Wiberg, P. L., and J. D. Smith (1991), Velocity distribution and bed roughness in high-gradient streams, *Water Resources Research*, *27*(5), 825–838.

Wilcock, P. (1992), Experimental investigation of the effect of mixture properties on transport dynamics, in *Dynamics of Gravel-bed Rivers*, edited by P. Billi, R. Hey, C. Thorne, and P. Tacconi, pp. 109–139, John Wiley & Sons, Chichester, UK.

Wilcock, P. R. (1996), Estimating local bed shear stress from velocity observations, *Water Resources Research*, *32*(11), 3361–3366.

Wilcock, P. R. (1998), Two-fraction model of initial sediment motion in gravel-bed rivers, *Science*, *280*(5362), 410–412.

Wilcock, P. R., and J. C. Crowe (2003), Surface-based transport model for mixed-size sediment, *Journal of Hydraulic Engineering*, *129*(2), 120–128, doi:10.1061/(ASCE)0733-9429(2003)129:2(120).

Wilcock, P. R., and B. T. DeTemple (2005), Persistence of armor layers in gravel-bed streams, *Geophysical Research Letters*, *32*(8), L08402, doi:10.1029/2004GL021772.

Wilcock, P. R., and S. T. Kenworthy (2002), A two-fraction model for the transport of sand/gravel mixtures, *Water Resources Research*, *38*(10), 1194–1205, doi: 10.1029/2001WR000684.

Wilcock, P. R., and B. W. McArdell (1993), Surface-based fractional transport rates: Mobilization thresholds and partial transport of a sand-gravel sediment, *Water Resources Research*, *29*(4), 1297–1312.

Wilcock, P. R., S. T. Kenworthy, and J. C. Crowe (2001), Experimental study of the transport of mixed sand and gravel, *Water Resources Research*, *37*(12), 3349–3358.

Williams, G. (1970), Flume width and water depth effects in sediment-transport experiments, *U.S. Geol. Surf. Prof. Paper*, *562-H*, 1–37.

Wolcott, J., and M. Church (1991), Strategies for sampling spatially heterogeneous phenomena; the example of river gravels, *Journal of Sedimentary Research*, *61*(4), 534–543.

Wolman, M. G. (1954), A method of sampling coarse river-bed material, *Transactions of the American Geophysical Union*, *35*(6), 951–956.

Yager, E. M. (2006), Prediction of sediment transport in steep, rough streams, Ph.D. thesis, University of California, Berkeley.

Yager, E. M., J. W. Kirchner, and W. E. Dietrich (2007), Calculating bed load transport in steep boulder bed channels, *Water Resources Research*, *43*, W07418, doi: 10.1029/2006WR005432.

Yalin, M. S. (1963), An expression for bed-load transportation, *J. Hydraul. Div. ASCE*, *89*(3), 221–250.

Yarnell, S. M., J. F. Mount, and E. W. Larsen (2006), The influence of relative sediment supply on riverine habitat heterogeneity, *Geomorphology*, *80*(3-4), 310–324, doi: 10.1016/j.geomorph.2006.03.005.